



ScuDo

Scuola di Dottorato ~ Doctoral School
WHAT YOU ARE, TAKES YOU FAR



Doctoral Dissertation
Doctoral Program in Aerospace Engineering (32th Cycle)

Electric VTOL preliminary design and wind tunnel tests

Alessandro Bacchini

* * * * *

Supervisors

Prof. Giulio Romeo, Supervisor
Prof. Enrico Cestino, Co-Supervisor

Politecnico di Torino
March, 2020

This thesis is licensed under a Creative Commons License, Attribution - Noncommercial - NoDerivative Works 4.0 International: see www.creativecommons.org. The text may be reproduced for non-commercial purposes, provided that credit is given to the original author.

I hereby declare that, the contents and organisation of this dissertation constitute my own original work and does not compromise in any way the rights of third parties, including those relating to the security of personal data.

.....
Alessandro Bacchini
Turin, February 29, 2020

Summary

Electric vertical takeoff and landing aircraft have the potential to transform the transportation industry. They fly over traffic directly to their destination, drastically reducing commuting time. Electric motors and batteries developed for electric cars power them, and propellers and ducted fans generate the thrust required for vertical and horizontal flight. Although many start-ups and many established companies are designing and testing their prototypes, there is little academic published data. Most designs are kept secret to shield them from the competitors.

The goal of this research is to investigate the broad field of eVTOL design and focus on one of its aspects, the retraction of the lift+cruise takeoff propellers inside the fuselage to reduce drag. First, an analytical toolset of equations is collected to evaluate eVTOL performances. Next, VTOL configurations from the 1950s up to the present day are presented, and the three main eVTOL configurations are compared, assessing the performances of a prototype for each one of them. Then, the power sources available are presented, discussing batteries, fuel cells, and hybrids. Finally, the propeller retraction system is investigated building and testing in the wind tunnel a model. Two exotic eVTOL designs are also discussed. The eVTOL for the exploration of Titan highlighted the effects of gravity and the density on its performances. The supersonic eVTOL showed the procedure to derive power source requirements from an existing design.

This work successfully highlights the crucial aspects of eVTOL design. The eVTOL range depends not only on the specific energy of the batteries but also on the lift to drag ratio and on the battery-mass ratio. Efficient hover requires a large disk actuator area, and coaxial rotors and ducted fans are valid alternatives to the standard rotor. eVTOL wing can be designed for an efficient cruise with no takeoff and landing distance requirements as conventional airplanes have.

The configuration comparison showed that each configuration is best suited to a different mission. Multirotors are efficient in hover and best suited to short-range missions. Vectored thrust eVTOLs are efficient in cruise and best suited to long-range missions. Lift plus cruise eVTOLs are a compromise, but they are slowed down by the drag of the lift propellers.

The power sources were analyzed, evaluating their specific energy and specific power. The high efficiency of the battery and the factors affecting its life are discussed. The specific fuel consumption of the fuel cells is computed. Hydrogen storage is crucial to the fuel cell system specific energy. Cryogenic liquid storage

offers the best gravimetric efficiencies, but it poses the biggest challenges. Metal-hydrides and other chemical compounds are options with lower gravimetric efficiencies than compressed hydrogen. The structural analysis of a compressed hydrogen tank was performed, evaluating its gravimetric efficiency. Hybrids were discussed, including internal combustion engine plus battery, gas turbine plus battery, and fuel cell, battery, and supercapacitor.

The lift propellers retraction system is investigated, building a model based on the Mini Talon drone and testing it in the wind tunnel. The drag reduction measured is around 30%, and this value is used to estimate the performances of a passenger eVTOL and a surveillance drone employing it. The Kitty Hawk Cora data is used to evaluate the passenger eVTOL performances with the retraction system, and the range and the cruise speed found were higher than the baseline. The advantages for a surveillance drone are limited because it is designed to watch over its target area for as long as possible, and an increase in flight speed has minor advantages.

Acknowledgment

I want to thank my supervisors Prof. Enrico Cestino and Prof. Giulio Romeo, for their continuous support during these years of Ph.D. Their experience has guided me and made this dissertation possible. I would also like to thank Prof. Dries Verstraete for hosting me at the University of Sydney and supervising my work there. His expertise guided me and helped me perform the tests.

I wish to thank all my colleagues and friends at Politecnico di Torino and the University of Sydney for the fantastic time spent together. I want to express my deepest gratitude to Benjamin Van Magill for 3D-printing the models, to Dr. Derrick Ho for teaching me how to solve all the mechanical problems I faced and Dr. Tamas Bykerk for teaching me how to use the wind tunnel. To all my friends Filippo, Denis, Matteo, Luca, Matteo, Nicoletta, and Andrea at Polito and Amrit, John, Louis, and Tomas at Usyd, thank you for the beautiful memories.

My family, Mum, Dad, and Elena have inspired and supported me during my Ph.D. studies. I am grateful to them for all the opportunities they gave me, for everything they taught me, and for the amazing time spent together.

I wish to thank all my volleyball friends for having had a lot of fun together, and my high school friends Gnuz, Pippo, Tommi, Nico, Ale, Dello, Cesta, Fogli, Cesco, Pasku, and Salo for their long time friendship.

Finally, I would like to thank my girlfriend Roneda, for having supported and loved me deeply during the last seven years.

Contents

| | |
|---|----|
| Acknowledgment | v |
| List of tabels..... | ix |
| List of figures..... | xi |
| 1. Introduction..... | 1 |
| 1.1 Electric VTOL | 1 |
| 1.1.1 Advantages of the electric propulsion..... | 3 |
| 1.1.2 Zee Aero..... | 3 |
| 1.1.3 Joby Aviation | 5 |
| 1.1.4 Lilium..... | 8 |
| 1.1.5 E-Hang | 8 |
| 1.1.6 Aurora Flight Sciences | 9 |
| 1.1.7 Airbus A ³ | 10 |
| 1.1.8 Uber Elevate..... | 11 |
| 1.1.9 NASA Greased Lightning..... | 11 |
| 1.1.10 Pipistrel 801 | 12 |
| 1.2 Research objectives..... | 13 |
| 1.3 Overview by chapter..... | 13 |
| 1.4 Unique and novel contributions..... | 14 |
| 1.5 Research Publications | 15 |
| 1.5.1 Journal papers..... | 15 |
| 1.5.2 Conference papers | 15 |
| 2. Performances | 16 |
| 2.1 Comparison with existing alternatives..... | 16 |
| 2.1.1 Helicopters | 16 |
| 2.1.2 Land transportation | 18 |
| 2.2 Electric airplane range | 20 |
| 2.2.1 Lift to drag ratio and flight speed..... | 23 |
| 2.2.2 Battery-mass ratio | 25 |
| 2.2.3 Tradeoff between payload and battery mass, and the energy cost of an eVTOL mission. | 27 |
| 2.3 Take-off and landing..... | 28 |
| 2.3.1 Nonideal effects and the figure of merit | 30 |
| 2.3.2 Minimum disk actuator area required to hover | 33 |
| 2.3.3 Hover on other planets | 36 |

| | | |
|--------|--|-----|
| 2.3.4 | eVTOL for Titan | 38 |
| 2.4 | Transition from hover to forward flight..... | 40 |
| 2.4.1 | Energy required for the transition phase | 42 |
| 2.4.2 | Power required at every flight speed..... | 44 |
| 2.5 | Chapter conclusion | 45 |
| 3. | Configurations | 47 |
| 3.1 | The golden era of the VTOL..... | 47 |
| 3.1.1 | Tailsitter | 48 |
| 3.1.2 | Vectored Thrust..... | 49 |
| 3.1.3 | Deflected slipstream..... | 52 |
| 3.1.4 | Tilt Jet..... | 52 |
| 3.1.5 | Tiltrotor | 53 |
| 3.1.6 | Tilt-prop | 56 |
| 3.1.7 | Tilt-duct..... | 56 |
| 3.1.8 | Tilt-wing..... | 58 |
| 3.1.9 | Lift + cruise | 61 |
| 3.1.10 | Lift + lift/cruise | 63 |
| 3.1.11 | Ejector | 65 |
| 3.1.12 | Fan..... | 68 |
| 3.1.13 | Tip jet and compound helicopter..... | 69 |
| 3.2 | Electric VTOLs..... | 73 |
| 3.2.1 | Wingless..... | 73 |
| 3.2.2 | Lift plus Cruise..... | 75 |
| 3.2.3 | Vectored Thrust..... | 77 |
| 3.2.4 | Hoverbikes | 82 |
| 3.2.5 | Electric Rotorcraft..... | 83 |
| 3.3 | Configuration comparison | 84 |
| 3.3.1 | Wingless: E-Hang 164 | 84 |
| 3.3.2 | Lift plus Cruise: Kitty Hawk Cora | 88 |
| 3.3.3 | Vectored thrust: Lilium Jet..... | 92 |
| 3.3.4 | Reference mission performances | 95 |
| 3.4 | Chapter conclusion | 99 |
| 4. | Power sources | 100 |
| 4.1 | Batteries | 101 |
| 4.1.1 | Battery classification | 102 |
| 4.1.2 | Factors that affect battery life | 103 |
| 4.1.3 | Battery design..... | 105 |
| 4.2 | Fuel Cells | 105 |

| | | |
|------------|---|-----|
| 4.2.1 | Fuel cell specific fuel consumption..... | 106 |
| 4.2.2 | Hydrogen storage | 107 |
| 4.2.3 | Fuel cell stack weight and efficiency | 109 |
| 4.3 | Hybrids..... | 110 |
| 4.3.1 | Internal combustion engine and battery hybrid..... | 110 |
| 4.3.2 | Gas turbine and battery hybrid..... | 111 |
| 4.3.3 | Fuel cell, battery, and supercapacitor triple hybrid..... | 112 |
| 4.3.4 | Supersonic electric jet | 115 |
| 4.4 | Chapter conclusion | 119 |
| 5. | Wind tunnel tests | 120 |
| 5.1 | Problem statement..... | 120 |
| 5.2 | Experimental setup | 122 |
| 5.2.1 | Model selection | 122 |
| 5.2.2 | Motors and propellers | 122 |
| 5.2.3 | CAD models..... | 127 |
| 5.2.4 | Wind tunnel tests..... | 128 |
| 5.3 | Test results | 139 |
| 5.4 | Effect of the drag reduction on passenger eVTOLs and surveillance drones | 165 |
| 5.4.1 | Effect of the drag reduction on passenger eVTOLs..... | 165 |
| 5.4.2 | Effect of the drag reduction on surveillance drones..... | 167 |
| 5.4.3 | Considerations regarding scaling up the drag reduction from model to full-size eVTOLs..... | 169 |
| 5.5 | Chapter conclusion | 169 |
| 6. | Conclusion | 170 |
| 6.1 | Contributions to knowledge..... | 170 |
| 6.2 | Future Work..... | 172 |
| References | | 173 |

List of Tables

| | |
|---|----|
| Table 1: Parameters of the Cessna 172 used to model aircraft power consumption. | 19 |
| Table 2: Parameters of the Fiat Punto used to model car power consumption..... | 19 |
| Table 3: Parameters of the Frecciarossa 1000 used to model train power consumption..... | 19 |
| Table 4: Power required to hover of six popular helicopters..... | 29 |
| Table 5: Interference factor values for coaxial rotors..... | 29 |
| Table 6: Figure of merit of quadrotor motors and propeller computed from the Cobra Motors data. | 32 |
| Table 7: Data used for hover computations. | 35 |
| Table 8: Gravity acceleration, atmospheric density, the $\frac{g^3}{2\rho}$ parameter, and the $\sqrt{\frac{g^3}{2\rho}}$ parameter on Earth, Mars, and Titan. | 37 |
| Table 9: eVTOL for Titan mass balance. | 39 |
| Table 10: Data used for transition computations. | 43 |
| Table 11: E-Hang 184 specifications from E-Hang’s website. | 84 |
| Table 12: E-Hang 184 data computed with Figure 83 and Table 11 data. | 86 |
| Table 13: Kitty Hawk Cora specifications from Kitty Hawk’s website. | 88 |
| Table 14: Kitty Hawk Cora propeller area..... | 89 |
| Table 15: Kitty Hawk Cora mass and battery data. | 89 |
| Table 16: Kitty Hawk Cora hover performances..... | 89 |
| Table 17: Kitty Hawk Cora geometry data used to compute the drag..... | 90 |
| Table 18: Lilium Jet geometry..... | 93 |
| Table 19: Lilium Jet mass and battery data. | 93 |
| Table 20: Lilium Jet hover performances..... | 94 |
| Table 21: Data used in the computations for the reference missions performances. | 96 |
| Table 22: Takeoff, landing, acceleration, and deceleration..... | 96 |
| Table 23: Mission 1: 7 km urban mission..... | 96 |
| Table 24: Mission 2: 30 km extra-urban mission. | 96 |
| Table 25: Mission 3; 100 km long-range mission. | 97 |
| Table 26: Performances comparison..... | 97 |
| Table 27: Summary of the energy and time required for the three reference missions. | 97 |

| | |
|--|-----|
| Table 28: Gong's triple hybrid architecture specifications. | 114 |
| Table 29: Supersonic electric jet mass breakdown. | 115 |
| Table 30: Supersonic eVTOL data. | 117 |
| Table 31: High subsonic eVTOL data. | 118 |
| Table 32: Summary of the battery and motor properties required for the supersonic and the high subsonic eVTOL, and the present values. | 118 |
| Table 33: Mini Talon VTOL mass budget. | 123 |
| Table 34: Mini Talon reference data. | 140 |
| Table 35: Drag reduction values found. | 142 |
| Table 36: Kitty Hawk Cora data used to compute the eVTOL with propellers retraction system performances. | 165 |
| Table 37: Mini Talon VTOL data used to compute the eVTOL drone with propellers retraction system performances. | 168 |

List of Figures

| | |
|---|----|
| Figure 1: Zee Aero proof of concept at NASA Ames 2013. | 3 |
| Figure 2: Kitty Hawk Cora | 4 |
| Figure 3: Kitty Hawk Flyer..... | 4 |
| Figure 4: Kitty Hawk Heaviside | 5 |
| Figure 5: Joby Aviation Lotus | 6 |
| Figure 6: Joby Aviation S2 | 6 |
| Figure 7: Joby Aviation S4. | 7 |
| Figure 8: Joby Aviation S2 and S4 compared to the Robinson R22 and R44 helicopters. | 7 |
| Figure 9: The Lilium Jet | 8 |
| Figure 10: E-Hang 216 | 9 |
| Figure 11: Aurora Flight Sciences Pegasus passenger aerial vehicle. | 10 |
| Figure 12: Aurora Flight Sciences LightningStrike XV-24A..... | 10 |
| Figure 13: A ³ Vahana Alpha One | 11 |
| Figure 14; NASA Greased Lightning. | 12 |
| Figure 15: Pipistrel 801..... | 12 |
| Figure 16: Road transport comparison, power required by car, train, and airplane, at different speeds. | 20 |
| Figure 17: Range of an electric airplane for different L/D, varying the specific energy of the battery and at different values of the battery-mass ratio..... | 22 |
| Figure 18: Lift to drag ratios of different aircraft and rotorcraft types [27]. | 24 |
| Figure 19: Flight speed of different aircraft and rotorcraft types [27]..... | 25 |
| Figure 20: Empty weight, fuel, and payload fraction of existing aircraft, rotorcraft, and VTOLx [27]. | 26 |
| Figure 21: Energy cost to perform the maximum range trip at different empty weight fractions (mempty/m) varying the battery to total mass ratio (mbattery/m). | 28 |
| Figure 22: Figure of merit, experimental, and theoretical data at different thrust coefficient. Data source: [35]..... | 31 |
| Figure 23: Figure of merit of the FMS 70 mm ducted fan. | 32 |
| Figure 24: Thrust system area required function of the battery specific power for various battery to total mass ratios. | 35 |
| Figure 25: Thrust system area required function of battery specific-power for various total mass..... | 36 |

| | |
|--|----|
| Figure 26: Thrust system area required function of the battery to total mass ratio for various total mass..... | 36 |
| Figure 27: Power required and power available for the eVTOL on Titan..... | 40 |
| Figure 28: Free body diagram of the transition from hover to forward flight for two VTOLs. Configuration A has a smaller wing surface while configuration B has a bigger wing surface..... | 42 |
| Figure 29: Energy required to get from hover to cruise speed function of the wing surface..... | 44 |
| Figure 30: Power required for any flight speed..... | 45 |
| Figure 31: V/STOL wheel [41]..... | 48 |
| Figure 32: Convair XFY Pogo..... | 49 |
| Figure 33: Underside view of the Hawker Siddeley P1127 prototype..... | 50 |
| Figure 34: The Harrier Jet..... | 51 |
| Figure 35: Bell X-14..... | 51 |
| Figure 36: Ryan VZ/3 Vertiplane..... | 52 |
| Figure 37: Bell 65 Air Test Vehicle..... | 53 |
| Figure 38: Trascendental Model 1G..... | 54 |
| Figure 39: Bell XV-3..... | 54 |
| Figure 40: Bell XV-15..... | 54 |
| Figure 41: V-22 Osprey..... | 55 |
| Figure 42: Agusta Westland AW609..... | 55 |
| Figure 43: Bell V-280 Valor..... | 55 |
| Figure 44: Curtiss-Wright X-19..... | 56 |
| Figure 45: Doak VZ-4..... | 57 |
| Figure 46: Bell X-22..... | 58 |
| Figure 47: Vertol 76 VZ-2..... | 59 |
| Figure 48: Hiller X-18..... | 60 |
| Figure 49: Ling-Temco-Vought (LTV) XC-142..... | 60 |
| Figure 50: Canadair CL-84..... | 61 |
| Figure 51: Short SC 1..... | 62 |
| Figure 52: Mirage III V..... | 62 |
| Figure 53: Yak 38..... | 64 |
| Figure 54: EWR VJ 101..... | 64 |
| Figure 55: VFW VAK 191..... | 65 |
| Figure 56: Dornier Do 31..... | 65 |
| Figure 57: Lockheed XV-4A Hummingbird in hover..... | 66 |
| Figure 58: Augmentor system, view of the Hummingbird's fuselage from above..... | 67 |

| | |
|--|-----|
| Figure 59: Rockwell International's XfV-12A..... | 67 |
| Figure 60: Ryan XV-5A. | 68 |
| Figure 61: Vanguard Omniplane. | 69 |
| Figure 62: McDonnell XV-1..... | 70 |
| Figure 63: Fairey Rotodyne. | 70 |
| Figure 64: Lockheed AH-56 Cheyenne. | 71 |
| Figure 65: Kamov Ka-22 Vintokryl..... | 71 |
| Figure 66: Sikorsky–Boeing SB-1 Defiant..... | 72 |
| Figure 67: Volocopter VC200 and 2X..... | 74 |
| Figure 68: Alauda Airspeeder prototype. | 74 |
| Figure 69: Ascendance Flight Technologies Atea prototype..... | 75 |
| Figure 70: AutoflightX V600. | 76 |
| Figure 71: Elroy Air cargo drone..... | 76 |
| Figure 72: Zuri eVTOL design. | 77 |
| Figure 73: Agusta Westland Project Pero..... | 78 |
| Figure 74: Mobi-one tilt-wing design..... | 78 |
| Figure 75: Bell Nexus eVTOL..... | 79 |
| Figure 76: Beta Technologies Alia prototype..... | 79 |
| Figure 77: Dufour Aerospace aEro 2. | 80 |
| Figure 78: Opener Blackfly. | 80 |
| Figure 79: Overair Butterfly. | 81 |
| Figure 80: Hoversurf Scorpion. | 82 |
| Figure 81: Kitty Hawk Flyer..... | 82 |
| Figure 82: Aquinea Volta. | 83 |
| Figure 83: E-Hang 184 specs and dimensions, from E-Hang’s website [62]. Dimensions in the top view are in millimeters. | 85 |
| Figure 84: Kitty Hawk Cora geometry. | 88 |
| Figure 85: Lilium jet geometry..... | 93 |
| Figure 86: Lilium Jet 5-seater geometry..... | 95 |
| Figure 87: Energy required for the three reference missions..... | 97 |
| Figure 88: Time required for the three reference missions..... | 98 |
| Figure 89: Ragone plot showing specific power and specific energy of different types of batteries, fuel cells, ultra-capacitors, and internal combustion engines. Courtesy of Andrew Gong and Dries Verstraete, [79] [80]..... | 100 |
| Figure 90: Li-ion 18650 cell. | 102 |
| Figure 91: Li-ion 4s battery. | 102 |
| Figure 92: Effect of the depth of discharge on a LiAl / MnO ₂ coin-type battery at 20°C from Linden's handbook of batteries, chapter 34 [23]..... | 104 |

| | |
|--|-----|
| Figure 93: Effect of the number of cycles and the depth of discharge on the residual energy of li-ion batteries from Linden's handbook of batteries, chapter 35 [23]. | 104 |
| Figure 94: Effect of the discharge rate on the capacity of 18650 type e C/LiCoO2 li-ion batteries, from Linden's handbook of batteries, chapter 35 [23]. The discharge capacity (Ah) is on the x-axis. | 105 |
| Figure 95: Effect of the temperature on a 18650-type C / LiCoO2 battery discharged at 0.2C. From Linden's handbook of batteries, chapter 35 [23]..... | 105 |
| Figure 96: Ragone plot of fuel cell configurations at 50% fuel cell efficiency, 2kW/kg stack specific power, 6 kW/kg fuel subsystem. The two lines correspond to a tank gravimetric efficiency of 5% and 7.5%. | 110 |
| Figure 97: Rolls-Royce eVTOL. | 112 |
| Figure 98: Spectronik fuel cell characteristics. Courtesy of Andrew Gong [79]. | 115 |
| Figure 99: Mini Talon hover performances computed with eCalc. | 124 |
| Figure 100: Cobra Motors CM-2217/20 Multirotor motor, Kv=950, motor propeller performances specified by the producer. | 125 |
| Figure 101: Cruise motor performances computed with eCalc. | 126 |
| Figure 102: Cobra Motors 2820/14, Kv=840, motor propeller performances specified by the producer. | 127 |
| Figure 103: CAD models of the original Mini Talon produced by X-UAV and the modified Mini Talon with the propellers retraction system. | 128 |
| Figure 104: Assembled models. The Mini Talon 2 is on top, the Mini Talon 1 is on the low left and the Mini Talon 3 on the low right. | 130 |
| Figure 105: Parts used to assemble the fourth model. Starting from the top left and proceeding clockwise there are the 3D printed tail, the 3D printed wings, the fuselage provided by Krossblade, and the wing junction inside the fuselage. | 131 |
| Figure 106: University of Sydney 7 ft by 5 ft low-speed wind tunnel | 132 |
| Figure 107: Mini Talon 1 in the University of Sydney 7 by 5 wind tunnel..... | 133 |
| Figure 108: Mini Talon 2, propellers retracted..... | 133 |
| Figure 109: Mini Talon 2, propellers out 30°..... | 134 |
| Figure 110: Mini Talon 2, propellers out 60°..... | 134 |
| Figure 111: Mini Talon 2, propellers out 90°..... | 135 |
| Figure 112: Mini Talon 3, propellers parallel to the airflow. | 135 |
| Figure 113: Mini Talon 3, propellers perpendicular to the airflow. | 136 |
| Figure 114: Mini Talon 3 without propellers..... | 136 |
| Figure 115: Mini Talon 3 without propellers and motors..... | 137 |
| Figure 116: Krossblade Skyproowler, propellers out. | 137 |
| Figure 117: Krossblade SkyProwler, propellers retracted. | 138 |
| Figure 118: Me in the wind tunnel with the SkyProwler model..... | 138 |

| | |
|---|-----|
| Figure 119: Mini Talon 2, lift coefficient, 10 m/s. | 143 |
| Figure 120: Mini Talon 2, lift coefficient, 12.5 m/s. | 143 |
| Figure 121: Mini Talon 2, lift coefficient, 15 m/s. | 144 |
| Figure 122: Mini Talon 2, lift coefficient, 17.5 m/s. | 144 |
| Figure 123: Mini Talon 2, drag coefficient, 10 m/s. | 145 |
| Figure 124: Mini Talon 2, drag coefficient, 12.5 m/s. | 145 |
| Figure 125: Mini Talon 2, drag coefficient, 15 m/s. | 146 |
| Figure 126: Mini Talon 2, drag coefficient, 17.5 m/s. | 146 |
| Figure 127: Mini Talon 2, lift to drag ratio, 10 m/s. | 147 |
| Figure 128: Mini Talon 2, lift to drag ratio, 12.5 m/s. | 147 |
| Figure 129: Mini Talon 2, lift to drag ratio, 15 m/s. | 148 |
| Figure 130: Mini Talon 2, lift to drag ratio, 17.5 m/s. | 148 |
| Figure 131: Mini Talon 2, drag polar, 10 m/s. | 149 |
| Figure 132: Mini Talon 2, drag polar, 12.5 m/s. | 149 |
| Figure 133: Mini Talon 2, drag polar, 15 m/s. | 150 |
| Figure 134: Mini Talon 2, drag polar 17.5 m/s. | 150 |
| Figure 135: Mini Talon 3, lift coefficient, 10 m/s. | 151 |
| Figure 136: Mini Talon 3, lift coefficient, 12.5 m/s. | 151 |
| Figure 137: Mini Talon 3, lift coefficient, 15 m/s. | 152 |
| Figure 138: Mini Talon 3, lift coefficient, 17.5 m/s. | 152 |
| Figure 139: Mini Talon 3, drag coefficient, 10 m/s. | 153 |
| Figure 140: Mini Talon 3, drag coefficient, 12.5 m/s. | 153 |
| Figure 141: Mini Talon 3, drag coefficient, 15 m/s. | 154 |
| Figure 142: Mini Talon 3, drag coefficient, 17.5 m/s. | 154 |
| Figure 143: Mini Talon 3, lift to drag ratio, 10 m/s. | 155 |
| Figure 144: Mini Talon 3, lift to drag ratio, 12.5 m/s. | 155 |
| Figure 145: Mini Talon 3, lift to drag ratio, 15 m/s. | 156 |
| Figure 146: Mini Talon 3, lift to drag ratio, 17.5 m/s. | 156 |
| Figure 147: Mini Talon 3, drag polar, 10 m/s. | 157 |
| Figure 148: Mini Talon 3, drag polar 12.5 m/s. | 157 |
| Figure 149: Mini Talon 3, drag polar, 15 m/s. | 158 |
| Figure 150: Mini Talon 3, drag polar, 17.5 m/s. | 158 |
| Figure 151: Krossblade SkyProwler, lift coefficient, 10 m/s. | 159 |
| Figure 152: Krossblade SkyProwler, lift coefficient, 20 m/s. | 159 |
| Figure 153: Krossblade SkyProwler, lift coefficient, 30 m/s. | 160 |
| Figure 154: Krossblade SkyProwler, drag coefficient, 10 m/s. | 160 |
| Figure 155: Krossblade SkyProwler, drag coefficient, 20 m/s. | 161 |
| Figure 156: Krossblade SkyProwler, drag coefficient, 30 m/s. | 161 |

| | |
|---|-----|
| Figure 157: Krossblade SkyProwler, lift to drag ratio, 10 m/s. | 162 |
| Figure 158: Krossblade SkyProwler, lift to drag ratio, 20 m/s. | 162 |
| Figure 159: Krossblade SkyProwler, lift to drag ratio, 30 m/s. | 163 |
| Figure 160: Krossblade SkyProwler, drag polar, 10 m/s. | 163 |
| Figure 161: Krossblade SkyProwler, drag polar, 20 m/s. | 164 |
| Figure 162: Krossblade SkyProwler, drag polar, 30 m/s. | 164 |
| Figure 163: Range function of the flight speed for different drag reductions and retraction system weights, computed using Kitty Hawk Cora's data. | 166 |
| Figure 164: Endurance function of the flight speed for different drag reductions and retraction system weights. | 168 |

Chapter 1

Introduction

eVTOL, or electric vertical takeoff and landing aircraft, is the new technology enabling the so-called “flying cars”. The power electronics developed for electric cars are combined with the best aerodynamics designs and sophisticated computer algorithms to drive propellers that provide the thrust for vertical takeoff and cruise. With little more than the technology and the materials of an electric car, eVTOL promises to make people fly to their destination, avoiding traffic and saving time.

During the last ten years, many companies and startups developed and tested eVTOL prototypes. The academic community has followed providing studies on eVTOLs. Most papers have focused on the design of a single eVTOL, and general analyses on eVTOL performances and configurations were limited. This research effort started on the broad theme of eVTOL design. The first studies were dedicated to performances and configurations. Eventually, we came by the retractable takeoff propellers concept, and we studied it in more detail. This dissertation aims to present this work, on eVTOL performances, configurations, power sources, and on the wind tunnel tests conducted to evaluate the retractable takeoff propellers concept.

The remainder of the introduction will present a literature review on the eVTOL and its technology. The recent history of the researches, the companies, and the startups trying to bring eVTOLs to market is presented with a comparison with existing alternatives and the history of the golden era of the military eVTOL. The introduction ends with an overview of the research objectives, the novel contributions to literature, and an overview by chapter of the dissertation.

1.1 Electric VTOL

The electric vertical takeoff and landing is an aircraft that uses electric propulsion to take off vertically like a helicopter and fly to its destination. Brushless electric motors drive propellers, rotors, or ducted fans that generate the thrust to take off vertically and to fly horizontally. Li-ion batteries usually provide the power, but hybrids using jet turbines, internal combustion engines, and fuel cells have also been considered. Most eVTOLs have a wing that enables efficient cruise flight generating the lift required to stay aloft in exchange for the drag that it produces. Some eVTOLs do not have a wing and are either electrified helicopters or scaled-up multirotors. Among the eVTOLs that have a wing, some use the same propulsion system for hover and cruise tilting it with a specific mechanism, and

others have a dedicated propulsion system for cruise and another propulsion system for takeoff and landing.

eVTOLs and electric cars share many technologies. The Li-ion battery is the same, like the motors and the power electronics. The capability to fly is provided by standard aerospace technology, wings, propellers, rotors, and ducted fans. However, an eVTOL is not merely an electrified airplane. That would be environmentally friendly but practically of limited use. The limited specific energy of the batteries affects the range of aircraft even more than the range of a car. Many universities and companies have replaced the conventional power plant of different aircraft with an electric motor and batteries or fuel cells. Some examples are the Politecnico di Torino Enfica [1], the Airbus E-fan [2]. The aircraft's noise is reduced, and its pollution brought to zero, but its range and performances are reduced. Until the life-cycle cost of the electric drivetrain is higher than that of a conventional one, there is little incentive for this change. The applications for which a conventional electric airplane can already be better than an internal combustion engine airplane are pilot training and recreational flights. These missions start and end from the same airport and last only a few minutes. The range requirement is minimal, and batteries can satisfy it. As the cost of the electric energy is lower than the cost of the fuel, an electric plane can balance the higher initial cost with lower operating energy costs. Over their lifetime, electric planes for pilot training can be cheaper than conventional ones. One example of such a plane is the Alpha Electro [3] produced by the Slovenian company Pipistrel.

The main advantage of electric propulsion applied to airplanes is the capability to take off and land vertically. This can be achieved by adding motors and propellers to generate the vertical thrust. The battery does not have to change, and it can provide the power required, which is transported to the motors by electrical cables. The history of the past VTOL prototypes showed that driving the power from an internal combustion engine or a turbine mechanically to propellers for the vertical thrust is more complicated. This topic will be discussed in detail in chapter 3.

Mechanical transmissions are complex, fragile, and require much maintenance. An example is the helicopter tail rotor, its transmission is very complex, and it is a single point of failure. Also, having multiple internal combustion engines or gas turbines, one for each propeller, is not as advantageous as having multiple small electric motors. The efficiency of small internal combustion engines or turbines depends on their scale [4]. Big ones are efficient, while small ones are not. Conversely, electric motors are not scale-dependent. Small engines can be as efficient as large ones.

1.1.1 Advantages of the electric propulsion

Mark Moore has stated the advantages of electric propulsion in his paper describing the Puffin tailsitter VTOL [5]. He listed the following advantages: elimination of engine noise and emissions, reduction in engine cooling and radiated heat, reduction in vehicle vibration levels, improvement in reliability and operating costs, variable speed output at full power for improved cruise efficiency at low tip-speed, elimination of high/hot sizing penalty, and reduction of engine-out penalties. Mark Moore has worked for NASA for over 30 years performing conceptual design studies of advanced aircraft. With his Puffin paper, he has turned the attention of many researchers and engineers to eVTOLs. In another article [6], Moore outlined the misconceptions about electric propulsion, describing how 400 Wh/kg batteries would be enough to provide the required range at lower operating costs. In this paper, he does not underline the importance of the VTOL capability enabled by electric propulsion. Still, he finally left NASA to work for Uber Elevate in 2017, focusing on eVTOLs.

1.1.2 Zee Aero

Zee Aero is the first name of the startup funded in March 2010 by Stanford professor Ilan Kroo with the financial support of Google's Larry Page [7]. They realized a proof of concept based on the original patent by Ilan Kroo with eight propellers for vertical takeoff, two pusher propellers for cruise, and two wings to generate lift. The front wing is a large low canard. The rear wing is attached to the top of the tail and ends in two long vertical winglets orientated towards the bottom of the vehicle that provides latero-directional stability. Figure 1 shows the Zee Aero proof of concept at NASA Ames in 2013.



Figure 1: Zee Aero proof of concept at NASA Ames 2013.

The work on the proof of concept demonstrator led to the development of the two-seat Z-P2, which became the Cora shown in Figure 2. It has a standard wing and tail without a canard. The aspect ratio of the wing is increased to improve the lift to drag ratio. In 2018 the company was renamed Kitty Hawk, and in 2019, it expanded its prototype line, adding the Flyer and the Heaviside. The Flyer, shown in Figure 3, is an electric hoverbike that can be flown without a pilot license because it is built under US FAR Part 103 ultralight regulations. The Heaviside, shown in Figure 4, is a single-seat eVTOL with six tiltable propellers on the wing and two tiltable propellers on the front canard. Its wing is forward-swept, and it has both the canard and a conventional tail.



Figure 2: Kitty Hawk Cora



Figure 3: Kitty Hawk Flyer



Figure 4: Kitty Hawk Heaviside

1.1.3 Joby Aviation

JoeBen Bevirt founded Joby Aviation in 2009. Joby worked on the Lotus UAV, the S2 and S4 eVTOL, and the NASA projects Leaptech and X-57 Maxwell.

The Lotus (Figure 5) was a VTOL UAV designed in partnership with NASA. It mounts three propellers, two on the wingtips, and one on the tail. All three propellers generate the thrust for hover, the tail propeller tilts, and it pushes the Lotus during the cruise. The propellers on the wingtips fold, the two blades stop parallel on the same side of the rotation axis, outside of the wing, increasing its surface and aspect ratio. This design was initially considered for personal air transportation, but subscale testing showed that the manufacturing compromises necessary for the folding propeller technology and propeller dynamics concerns make this design practical only for small scales [8].

The S2 in Figure 6 is a two-seat tilt-prop which uses eight propellers on the wing and four on the tail for takeoff and landing. Each one of these propellers can tilt and fold onto their nacelle, which hosts the tilting mechanism and the electric motor. Four additional pusher propellers are used for cruise. Two are on the wingtips, and the remaining two are on the tips of the V tail [9]. From experience acquired with the S2, Joby developed the S4, a four-seat variant employing six larger propellers for hover. The six larger propellers of the S4 shown in Figure 7 have a total disk area larger than the area of the twelve propellers of the S2. The larger disk area reduces the power required for hover, reducing the effects of the increased payload, and improving hover efficiency.



Figure 5: Joby Aviation Lotus



Figure 6: Joby Aviation S2

The S2 might be considered a lift plus cruise eVTOL because it has 12 foldable propellers for hover and four pusher propellers for cruise in the wingtips and at the edges of the V-tail. The S4, instead, can tilt four of its six propellers and fold the remaining two. It is considered a vectored thrust eVTOL. Figure 8 shows the comparison between the disk actuator surface of the Robinson R-22, R-44, and the Joby S-2 and S-4. The weight of the 16 electric motors, the limited disk actuator area for hover, and aero-propulsive interactions close to the ground might explain why the S-4 was selected over the S-2. The S-4 can also carry four passengers plus the pilot reducing the cost per trip.

The NASA Leaptech (Leading Edge Asynchronous Propeller Technology) project investigates the effects of distributed propulsion testing a modified wing with 18 propellers driven by li-ion batteries mounted on a specially modified truck

[10]. NASA is applying the lessons learned during this project to the design of the X-57 distributed electric propulsion aircraft, modifying a Tecnam P2006T.



Figure 7: Joby Aviation S4.

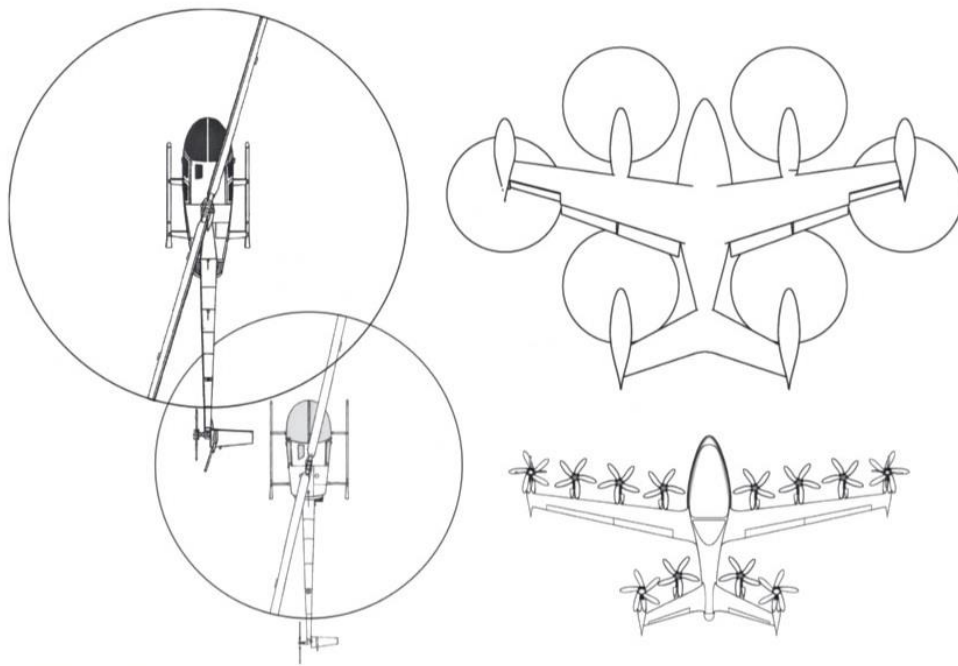


Figure 8: Joby Aviation S2 and S4 compared to the Robinson R22 and R44 helicopters.

1.1.4 Lilium

Lilium is a German startup founded in 2015 by Daniel Wiegand, Sebastian Born, Patrick Nathen, and Matthias Meiner. It has designed and flight-tested a two-seat electric jet in 2017 and modified to carry a pilot and four passengers. The five-seat version first flew in 2019.

The Lilium Jet (Figure 9) is powered by 36 electric ducted fans, 12 mounted on the trailing edge of each wing, and six mounted on the trailing edge of each canard. These motors can tilt and provide the required thrust for hover and cruise. During the transition, they blow the wing increasing its maximum lift coefficient.



Figure 9: The Lilium Jet

1.1.5 E-Hang

E-Hang is a Chinese drone manufacturer producing aerial vehicles for cinematography, photography, and survey missions. It is now expanding its business, providing solutions for logistics and passenger transportations with its new line of autonomous aerial vehicles. The E-Hang 184 is their first eVTOL able to carry a passenger. It is a scaled-up multirotor with four couples of contra-rotating propellers. From this prototype, they developed the 216 (Figure 10), which has sixteen contrarotating propellers on eight arms and can carry two passengers.



Figure 10: E-Hang 216

1.1.6 Aurora Flight Sciences

Aurora Flight Sciences is an American company working on private and public research projects. Boeing acquired it in 2017 after they designed the Pegasus Passenger Aerial vehicle and LightningStrike XV-24A.

The Pegasus is a lift+cruise eVTOL (Figure 11) with eight propellers for hover and a pusher propeller for forward flight. The takeoff propellers are mounted on two booms aligned to the flight direction, which also support the two vertical fins. The booms act as landing gear and are connected to the fuselage by two canard surfaces on the front and by the horizontal tail surface on the rear.

The LightningStrike (Figure 12) is a design founded by the American agency DARPA to demonstrate high-speed and VTOL capabilities in a drone. A 20% scale, 147 kg, prototype was built, while the full-scale vehicle was never realized. The project was stopped because the subscale prototype reached the program's main objectives. The original design would have been powered by a hybrid powertrain consisting of the Rolls-Royce AE-1107C turboshaft, also used by the V-22, and lithium batteries. The thrust would have been produced by eighteen electric ducted fans on the wing and six on the canard. The final vehicle was to weight around five tons, cruise at 550 km/h, hover with 75% efficiency, have a lift to drag ratio of at least 10, and carry a useful load of 40% of the gross weight.



Figure 11: Aurora Flight Sciences Pegasus passenger aerial vehicle.



Figure 12: Aurora Flight Sciences LightningStrike XV-24A

1.1.7 Airbus A³

A³ is an Airbus subsidiary located in the Silicon Valley that is developing a passenger eVTOL. Its prototype, called Vahana (Figure 13), has two tilt-wings with four propellers mounted on the leading edge of each wing. The propellers are driven by eight 45 kW electric motors powered by batteries. The batteries weigh 272 kg, about a third of the total weight. The Vahana Alpha One flew for the first time in January 2018.



Figure 13: A³ Vahana Alpha One

1.1.8 Uber Elevate

Uber Elevate is a service under development by the American ridesharing company Uber. The objective is to provide on-demand urban air transportation, a faster alternative to the standard Uber rides able to fly over traffic. Uber Elevate was announced in 2016 with a whitepaper [11] written by Jeff Holden and Nikhil Goel. In the whitepaper, they describe the vision of urban air transportation and the advantages that it would have been able to fly over traffic, reducing the time required to go from one place to the other. They also explore the market feasibility barriers and the economic model. Uber then hired many eVTOL experts, including Mark Moore and Eric Allison, and started to build the digital and physical infrastructure to enable aerial ridesharing. Different partners, including Boeing, Karem Aircraft, Bell Aerospace, Embraer, Pipistrel, Joby Aviation, Hyundai, and Jaunt Air Mobility, gathered around Uber to produce suitable eVTOL designs.

Every year since 2017, Uber organizes the Uber Elevate summit to promote urban air mobility and show the advancements in the enabling technologies.

1.1.9 NASA Greased Lightning

The Greased Lightning (Figure 14) is a hybrid diesel-electric tilt-wing aircraft. The NASA project started in 2013 to investigate eVTOL design taking advantage of the new technologies for drone propulsion and control. The Greased Lightning prototype has a ten-foot wingspan, ten electric engines, and weighs 25 kg. The prototype flew in 2015, showing its ability to take off vertically and transition to horizontal flight [12]. The Greased Lightning project is being followed by the Langley Aerodrome No. 8, a tandem wing with four propellers on each tilt-wing similar to the Vahana.



Figure 14: NASA Greased Lightning.

1.1.10 Pipistrel 801

Pipistrel is a Slovenian light aircraft manufacturer producing internal combustion engine aircraft and two all-electric planes, the Taurus Electro, and the Alpha Electro [3]. The former is the first electric motor-glider to achieve serial production. It was modified in 2011 to take part in the NASA Green Flight Challenge, and it won [13]. The latter is an all-electric trainer that takes advantage of the low cost of electricity to have low operating costs.

Pipistrel unveiled its 801 eVTOL (Figure 15) design in 2019. It has eight ducted lift fans in the wing roots and one tractor propeller in the tail. It was initially designed to carry one pilot plus four passengers, but, as of the 26th of November 2019, Pipistrel declared they would be focusing on a similar cargo drone [14].



Figure 15: Pipistrel 801.

1.2 Research objectives

The main objective of this research is to investigate the design of eVTOL. Although in recent years, many eVTOLs have been designed and tested, there is a lack of comprehensive study on eVTOL design, performances, and configurations. New eVTOL designs appear every year, and it is difficult to understand their merits. Are these designs already mature? Is there room for improvement?

In light of these considerations, the following aims have been investigated:

- To study the eVTOL performances and gather a set of analytical tools for this purpose.
- To analyze the different configurations of present and past configurations with the analytical tools developed.
- To analyze the possible power sources for eVTOL, evaluating the two more significant parameters for eVTOL design, the specific power, and the specific energy.
- To investigate possible improvements in eVTOL design.

To complete these objectives, the past and present designs are studied, from the golden era VTOLs up to the present day eVTOLs. An analytical toolset is created with different equations based on the momentum theory and elementary physics. This toolset is refined with experiments on electric ducted fan propulsion for drone models, and it is used extensively to evaluate the performances of the different eVTOL models. The power sources are investigated, analyzing their main peculiarities from existing publications. The fuel cells are also studied from first principles deriving their specific fuel consumption and the energy stored in hydrogen and computing the possible gravimetric efficiency of compressed hydrogen with structural analytical formulas. Possible improvements in eVTOL design are investigated on the lift-plus-cruise eVTOL design. Finally, the lift propellers retraction system is studied. The drag is measured in the wind tunnel, and the performances of an eVTOL using this system is estimated.

1.3 Overview by chapter

An overview by chapter is presented here to guide the reader through the dissertation:

Chapter 2 – Performances. This chapter presents the analytical toolset used to evaluate the performances of eVTOL. The eVTOL is compared to alternative modes of transportation, including the car, the train, and the helicopter. The eVTOL performances are evaluated in cruise, hover, and transition. The range of the eVTOL is computed, and the parameters affecting it are discussed. The power required to hover is computed, and the minimum area to provide enough thrust for vertical takeoff is derived. The power required during the transition phase is

computed. These tools are applied to the design of an eVTOL for the exploration of Titan.

Chapter 3 – Configurations This chapter presents all the VTOL and eVTOL configurations. It starts with the classification of the VTOL of the 1950s and 1960s and then compares the three main present-day eVTOL configurations, the multirotor, the lift plus cruise, and the vectored thrust.

Chapter 4 – Power sources This chapter discusses the power sources available to eVTOLs. First, batteries are presented discussing their technology and the factors affecting their lift. Then, fuel cells are discussed computing the energy stored in hydrogen, their specific fuel consumption, and the gravimetric efficiency achievable with compressed hydrogen. Three different hybrids are analyzed: internal combustion engine and battery, gas turbine and battery, fuel cell, battery, and supercapacitor. The chapter ends with the computation of the power source parameters required to build a supersonic eVTOL.

Chapter 5 – Wind tunnel tests This chapter investigates the propellers retraction system for lift plus cruise eVTOLs. A propeller retraction system is designed and built on the Mini Talon drone. It is tested in the University of Sydney 7 ft x 5 ft wind tunnel, and the performances of a passenger eVTOL and a surveillance drone employing it are computed.

Chapter 6 – Conclusions This chapter provides a conclusion to the dissertation, highlighting the novel contributions and areas of possible future work.

1.4 Unique and novel contributions

This dissertation presents novel contributions in the field of eVTOL design. These include:

- The *first comprehensive scientific work on the design of eVTOLs*. Previous articles and dissertations dealt with a single concept, while here we are studying the design of eVTOLs as generally as possible.
- The presentation of analytical tools to compute the *performances of eVTOLs* in hover, transition, and cruise.
- An in-depth discussion on *eVTOL configurations*. Designs from the 1950s to the present are presented, and the most popular configurations are compared, evaluating their performances and their ability to complete reference missions.
- An overview of the *propulsion technology to power eVTOLs*. This topic has already been discussed in numerous publications dealing with one technology at a time. Here, different power sources, including batteries, fuel cells, and hybrids, are discussed and compared for their application

in eVTOL propulsion. The parameters analyzed are specific power and specific density.

- A detailed *study of the system to retract takeoff propellers into the fuselage* or wing of eVTOLs employing dedicated propellers for hover. This study has been conducted experimentally *with wind tunnel tests*, which allowed us to measure the drag savings enabled by such a system.

1.5 Research Publications

Key results presented in this dissertation have been published in peer-reviewed journals and presented at conferences. A list of publications is shown below:

1.5.1 Journal papers

- Bacchini, A.; Cestino, E. Electric VTOL Configurations Comparison. *Aerospace* 2019, 6, 26 [15].
- Bacchini, A., Cestino, E. (2019). Key aspects of electric vertical take-off and landing conceptual design. *Proceedings of the Institution of Mechanical Engineers, Part G: Journal of Aerospace Engineering*. <https://doi.org/10.1177/0954410019884174> [16].
- Alessandro Bacchini, Enrico Cestino, Dries Verstraete, and Benjamin Van Magill. Impact of takeoff propeller drag on the performance of lift+cruise eVTOL aircraft. (Under submission)

1.5.2 Conference papers

- Bacchini, A; Cestino, E; Romeo, G. A reduced-order model to estimating propeller/wing interaction in solar-powered aircraft preliminary design, 2017, 7th EASN international conference, Innovation in European Aeronautics Research, Warsaw, Poland [17].

Chapter 2

Performances

In this chapter, the eVTOL is compared to its main existing alternatives, and its performances are computed. The typical mission of an eVTOL consists of takeoff, transition to horizontal flight, cruise, transition to hover, and landing. The range and the flight speed are the indicators used to evaluate performances in cruise. The hover is analyzed using the disk actuator theory. The transition is discussed computing the energy required to complete the transition from hover to cruise flight and the power required at every flight speed of the transition. Part of the contents of this chapter has been published in the article: “Key aspects of electric vertical take-off and landing conceptual design” [16].

2.1 Comparison with existing alternatives

To be economically sound, an electrical VTOL must be better than existing alternatives: helicopters, road transport, and rail transport. First, helicopters are discussed, then VTOLs are compared to road and rail transport.

2.1.1 Helicopters

The main alternative to the eVTOL is the helicopter. Ultra-rich people around the world already use it to move conveniently over the traffic and to reach their destinations quickly. However, its cost is out of reach for everybody else. Jet airplanes are costly too, and only a few of the rich can afford a private jet. However, most people living in developed countries can afford an airplane ticket on most airlines and travel conveniently around the world because the costs are shared between many passengers over the lifetime of the airplane. Similarly, during the sixties and seventies, some companies tried to establish commercial helicopter services.

The most popular helicopter airline was the New York Airways, which was founded in 1949 as a mail and cargo carrier. In 1953, it started to carry passengers [18] and, at its peak, it was carrying half a million passengers every year. Its main heliports were at La Guardia, JFK, and Newark airports, downtown Manhattan, and on the rooftop of the Pan Am building located directly above the Grand Central Station. At first, it employed the Sikorsky S-55, S-58, and S-61 helicopters; then, it moved to the larger twin rotors Boeing Vertol V-44 and Boeing Vertol 107. This last helicopter was powered by two turboprops, each capable of powering the entire helicopter, making it safe enough to fly over highly populated areas. The interiors

of the Vertol 107 were designed in the same fashion as the B-707 jet. Each row had two seats on the left of the central corridor and one seat on the right.

In 1963 a Vertol 107 crashed killing all its three passengers and three crew members. A mechanical failure caused the accident due to contaminated lubricants. In 1977 a terrible accident happened on the top of the Pan Am building. A landing gear arm of the S-61 failed due to high-cycle fatigue. The helicopter rolled on its side, killing four people waiting on the rooftop. One blade flew off the roof and smashed onto an office window on the side of the Pan Am building. Another piece fell 60 stories down to the street, killing a 29-year-old woman as she was commuting back home [19]. The airline ceased flying in 1979 after its third accident. An S-61 experienced a fracture of one of the tail-rotor blades while it was climbing out of the Newark international airport. The helicopter managed to land, but three people died, and thirteen were severely wounded.

In Los Angeles, San Francisco, and Chicago, similar scheduled services operated through the sixties and seventies. Financial issues and a series of fatal crashes forced these companies out of business as well. The remaining helicopter airlines operate sightseeing tours or luxury rides.

The main problems affecting the helicopter are its cost and the noise it generates. The cost of helicopter operations consists of fuel, pilot, and maintenance. The propellant cost caused financial issues for the existing helicopter airlines during the seventies because of the surge in oil prices due to the 1973 oil crisis. Helicopters require much propellant because the rotary-wing is less aerodynamically efficient in forward flight than fixed-wing airplanes. The cost of the pilot is high because it requires years of training. This cost can be avoided if the helicopter can fly by itself. Many researchers have worked on this problem, and autonomous helicopter flight in the upright flight regime has seen considerable progress. However, the only way to perform autonomously more complex maneuvers is using neural networks [20]. Helicopters require many hours of maintenance because they are highly complex mechanical machines. The transmission, the main rotor, and the tail rotor are single points of failure and need to be inspected routinely.

The noise generated by helicopters has three spectral components, the engine, the main rotor, and the tail rotor. The engine noise of an eVTOL is lower because electric motors are quiet. The main rotor generates significant noise not only during takeoff and landing but also during the cruise. The noise generated by a propeller varies as an exponent of the tip speed, which, in a helicopter in cruise, must be high enough for the retreating blade to generate enough lift. eVTOLs do not have this problem because they usually have a wing to generate lift during the cruise, and the primary source of noise is the propeller that pushes them forward. Likewise, eVTOLs do not have a tail rotor that generates additional noise. Takeoff and landing are the critical mission phases when eVTOLs create more noise. Smaller rotors and distributed electric propulsion give more freedom to the designer to reduce noise, but smaller rotors produce higher frequency sounds. These travel shorter distances than low-frequency ones because they are attenuated by the atmosphere. On the

other hand, human hearing is more sensitive to mid-high frequencies than to low ones [6] [11].

Finally, the helicopter is affected by the retreating blade problem, which limits its maximum flight speed. This problem is caused by the difference in force produced by the advancing blade and by the retreating blade. Aerodynamic forces are proportional to the square of the airspeed. The advancing blade is invested by its rotational speed plus the flying speed, while the retreating blade is invested by an airspeed equal to the difference of these two terms. The retreating blade flies at a higher angle of attack to produce as much lift as the advancing blade. As the flight speed increases, the angle of attack must increase. At a certain speed, the retreating blade gets to such a high angle of attack that it stalls. At this speed, it is not possible to compensate for the difference of lift, and the helicopter must fly slower than this speed. The retreating blade problem is the reason behind the limitation of the helicopter's maximum speed.

2.1.2 Land transportation

Flying has a significant advantage compared to road and rail transport: traffic jams are not a problem because the aircraft moves in tridimensional space, and it flies directly to its destination.

In this section, the power required for three different transportation systems is computed to compare the energy costs of the car, the train, and the eVTOL. The Fiat Punto is used to represent the car, while the train is represented by the Frecciarossa 1000, and the eVTOL is represented by the Cessna 172 aircraft (Table 1, Table 2, and Table 3). Figure 16 shows the power required per passenger at different speeds for the car, the train, and the aircraft. The aircraft power required is computed for a given velocity in level, unaccelerated flight [21]:

$$T_{req} = D \quad (1)$$

$$P_{req} = T_{req} \cdot V = D \cdot V \quad (2)$$

$$P_{req} = \frac{1}{2} \rho V^2 S C_D \cdot V \quad (3)$$

$$C_D = C_{D0} + k C_L^2 \quad (4)$$

$$P_{req} = \frac{1}{2} \rho V^3 S C_{D0} + \frac{W^2}{\frac{1}{2} \rho V S} \left(\frac{1}{\pi \epsilon A R} \right) \quad (5)$$

The power required for the car and train is the sum of two factors: rolling resistance and aerodynamic resistance [22]. Equations (6) and (7) also consider the component of the weight when the ground is not level:

$$F_{res} = \left[mg \cos(\alpha) - \frac{1}{2} \rho V^2 A_{CS} C_L \right] (f_0 + k V^2) + \frac{1}{2} \rho V^2 A_{CS} C_D \quad (6)$$

$$+ mg \sin(\alpha) \quad (7)$$

$$P_{req} = F_{res} \cdot V$$

Table 1: Parameters of the Cessna 172 used to model aircraft power consumption.

| | |
|------------------------------|-------------------------|
| Air density (ρ) | 1.225 kg/m ³ |
| Wing surface (S) | 16.2 m ² |
| C_{D0} | 0.03 |
| Weight | 1100 kg |
| Oswald factor (ϵ) | 0.8 |
| Aspect ratio (AR) | 7.32 |
| Number of passengers | 4 (including one pilot) |

Table 2: Parameters of the Fiat Punto used to model car power consumption.

| | |
|---------------------------------|--|
| Weight | 1000 kg |
| Cross-section area (A_{CS}) | 2 m ² |
| C_L | 0 |
| C_D | 0.3 |
| f_0 | 0.01 |
| k | $6.5 \cdot 10^{-6} \text{ s}^2/\text{m}^2$ |
| Number of passengers | 4 |

Table 3: Parameters of the Frecciarossa 1000 used to model train power consumption.

| | |
|---------------------------------|--|
| Weight | 500 tons |
| Cross-section area (A_{CS}) | 12 m ² |
| C_L | 0 |
| C_D | 1.8 |
| f_0 | 0.002 |
| k | $6.5 \cdot 10^{-6} \text{ s}^2/\text{m}^2$ |
| Number of passengers | 440 |

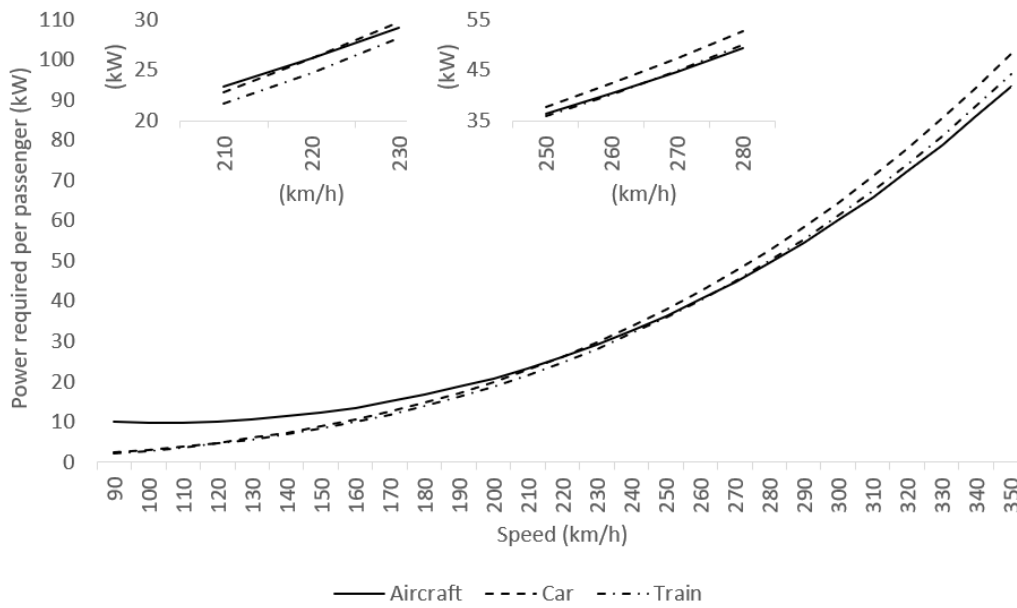


Figure 16: Road transport comparison, power required by car, train, and airplane, at different speeds.

This analysis shows that besides the great advantage of being able to fly over traffic directly to its destination, the eVTOL has comparable energy costs to the car and the train for high cruise speeds. As Figure 16 shows, at low speeds, the car and the train are more efficient than the airplane. The train is more efficient than the car because the rolling resistance between two hard surfaces, the steel of the train’s wheels and the rail, is lower than the rolling resistance of the tires on the tarmac, and because it has a smaller frontal section per passenger. At higher speeds, the aircraft becomes competitive with the car and the train. Considering our assumptions, it becomes more efficient than the car at about 220 km/h and more efficient than the train at about 265 km/h. In practice, we find that considering the typical car (Table 2) with four passengers, a trip by car usually is cheaper than a train ticket. The price of the train ticket comprises not only the cost of the energy, but also the cost of the railway personnel, the train itself, and the infrastructure. In computing the cost of a trip by car, we do not usually consider the cost of the car itself and the insurance. When there are fewer passengers and considering the cost of the car and the cost of insurance, the car is more expensive than the train.

2.2 Electric airplane range

The main parameter affecting the mission capabilities of an eVTOL is its range, or how far it can fly before needing to recharge its batteries. The flight speed is another important performance indicator. The faster an eVTOL flies, the less time is required to complete a trip. The customer saves time, and more trips can be performed in a day. However, flying faster requires more power, reducing the range available.

The range of an eVTOL can be computed with the Breguet equations modified for electric flight. In an internal combustion aircraft, fuel burns during the flight, and the total weight reduces. In an electric aircraft, the weight remains constant

because the energy is provided by the batteries, which change their chemical composition but not their mass.

The range is found multiplying flight speed and flight time:

$$R = v_{\infty} \cdot t \quad (8)$$

The flight time of a battery-powered aircraft corresponds to the time required to drain the battery:

$$t = \frac{m_{battery} \cdot E^*}{P_{battery}} \quad (9)$$

Where E^* is the specific energy of the battery, and $P_{battery}$ is the power supplied by the battery. Inserting it into the range equation yields:

$$R = v_{\infty} \cdot \frac{m_{battery} \cdot E^*}{P_{battery}} \quad (10)$$

The power drawn by the battery is related to the power required for forward flight, $P_{aircraft}$:

$$P_{battery} = \frac{P_{aircraft}}{\eta_{total}} \quad (11)$$

The power required for forward flight is proportional to the aircraft weight, lift to drag ratio and flight speed:

$$P_{aircraft} = D_{aircraft} \cdot v_{\infty} = \frac{m \cdot g}{\frac{L}{D}} \cdot v_{\infty} \quad (12)$$

Combining the two previous equations and inserting them in the range equation:

$$R = v_{\infty} \cdot \frac{m_{battery} \cdot E^*}{\frac{L}{D} \cdot \eta_{total} \cdot v_{\infty}} \quad (13)$$

This equation can be simplified to the range equation for battery-electric flight:

$$R = E^* \cdot \eta_{total} \cdot \frac{1}{g} \cdot \frac{L}{D} \cdot \frac{m_{battery}}{m} \quad (14)$$

Figure 17 shows the range of an electric aircraft computed with equation (14) for different lift to drag ratios, varying the specific energy of the battery, and at different battery-mass ratio.

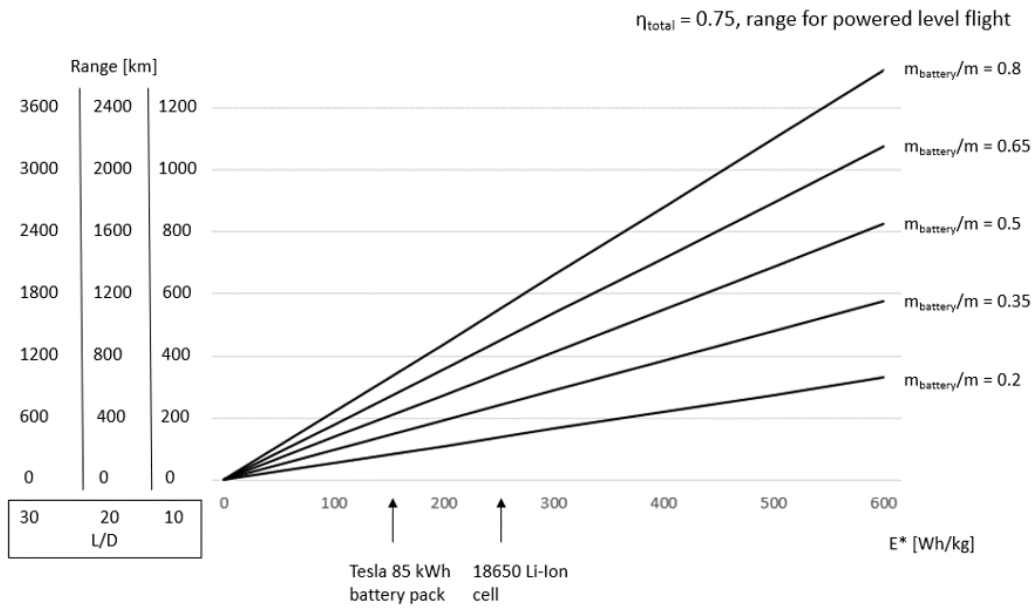


Figure 17: Range of an electric airplane for different L/D, varying the specific energy of the battery and at different values of the battery-mass ratio.

Equation (14) shows that the range of an electric aircraft is affected by the specific energy of the batteries E^* , the propulsive efficiency η_{total} , the gravity acceleration g , the lift to drag ratio $\frac{L}{D}$, and the battery-mass ratio $\frac{m_{battery}}{m}$.

The specific energy of the batteries E^* measures the energy that can be stored in a fixed amount of battery weight. The present li-ion technology has a specific energy of around 200 Wh/kg, with larger packs that require thermal control having lower specific energy [23]. Innovative technologies like lithium-sulfur batteries have demonstrated higher energy densities of about 400 Wh/kg [24] but with a lower specific power. Fuel cells can provide electricity combining hydrogen and oxygen into water at higher energy densities than batteries. Like lithium-sulfur batteries, fuel cells have lower specific power than batteries. Hybrid drivetrains combining internal combustion engines and batteries, or gas turbines and batteries can be a valid alternative with higher energy densities. Chapter 4 will dive into this topic, and it will deal extensively with all the power sources available for eVTOLs.

The propulsive efficiency can be expressed as the product of the efficiency of the electric motor and the efficiency of propeller, rotor, or ducted fan used to produce the thrust for forward flight. The efficiency of the electric motors is around 0.95, and propellers and ducted fans can be designed to reach efficiencies of about 0.8. A reasonable value for the total propulsive efficiency, also suggested in [25], is 0.75. The efficiency of a fixed-pitch propeller depends on the flying speed. Variable pitch propeller can change the propeller blade pitch to keep the efficiency high at every flight speed.

The range of an electric aircraft is inversely proportional to the gravity acceleration. For this reason, the flight might be a practical means of exploration on Titan, where the gravity acceleration is seven times lower than the Earth's, and

the atmospheric pressure is around 1.4 atm. On Titan, an electric aircraft powered by a radioisotope generator, like the one powering the Curiosity rover now on Mars, could fly for years. The flight might become practical on Mars too. The gravity is a third of the Earth's gravity, and the atmospheric pressure a hundred times lower. Electric planes might be able to fly long-range, but they will have to overcome the problem of a very high stall speed due to the low atmospheric density.

The lift to drag ratio is a measure of the overall aerodynamic efficiency. At subsonic speeds, it depends on the aspect ratio and the wetted area. Many eVTOLs have a sizeable wetted area due to the motors and propellers for vertical takeoff, which reduce the lift to drag ratio. Different design solutions exist to overcome this problem. The same system can be used for vertical takeoff and cruise flight, for example, tilting the wing like the Greased Lightning and the Lilium Jet do. Another idea that will be discussed more broadly in chapter 5 is to retract the takeoff propellers into the fuselage.

The battery-mass ratio affects the range profoundly. It can be increased, reducing the weight of the remaining components of the eVTOL, for instance, with electric motors that are lighter but can generate the same power, or a lighter structure that can withstand the same loads. The battery-mass ratio can be improved, reducing the payload too. However, the payload cannot be reduced indefinitely because there is no value in moving a battery pack from a place to the other without being able to carry anything else. This tradeoff will be discussed in section 2.2.3.

Figure 17 shows the results of equation (14). On the x-axis, there is the battery specific energy and on the y-axis the range. The different lines correspond to different battery-mass ratios, and the different scales on the y-axis correspond to different lift to drag ratios. The two marks on the x-axis indicate 157 kWh/kg, the specific energy of the Tesla Model S 85 kWh battery pack [26], and 250 kWh/kg, the specific energy of a 18650 lithium-ion cell. The Model S battery pack shows the performances of a consumer product in a high-power application. It is lower than the specific energy of the single 18650 cell because the battery pack comprises the casing, connections, thermal management system, and digital control. Figure 17 shows that an electric aircraft employing the Model S battery pack, with a battery-mass ratio of 0.5 and a lift to drag ratio of 10 would have a range of about 200 km.

2.2.1 Lift to drag ratio and flight speed

The results in Figure 17 show that each term in equation (14) needs to be optimized to produce an eVTOL with a useful range. The lift to drag ratio and the battery-mass ratio are the two parameters that can be directly controlled by the eVTOL designer. Figure 18 shows the lift to drag ratio of different aircraft and rotorcraft types. The values shown help to understand better the results of the range computations shown in Figure 17.

Gliders have the best lift to drag ratios ranging from 50 to 70. The Rutan Voyager and the Global Flyer were designed by Burt Rutan to fly around the world non-stop. Their high aspect ratio was essential to achieve such a high range and

endurance. The Rutan Voyager was built in 1983, and was the first aircraft to fly around the world without stopping or refueling; its estimated maximum lift to drag ratio was 27, and it was driven by a tractor and a pusher propeller each driven by a different engine. The Global Flyer was built in 2005 and improved on the Voyager design; its estimated maximum lift to drag ratio is 37, and it was driven by a jet engine. Fighter aircraft have lower aspect ratios, and their lift to drag ratio is lower than 10. VTOL jets like the Harrier have a similar lift to drag ratio. Tilt rotors like the V-22 Osprey and the Agusta Westland 609 have lift to drag ratios around 10 because they have higher aspect ratio wings. Helicopters have a lift to drag ratio around 6, passenger jets between 15 and 22, and general aviation aircraft between 9 and 23.

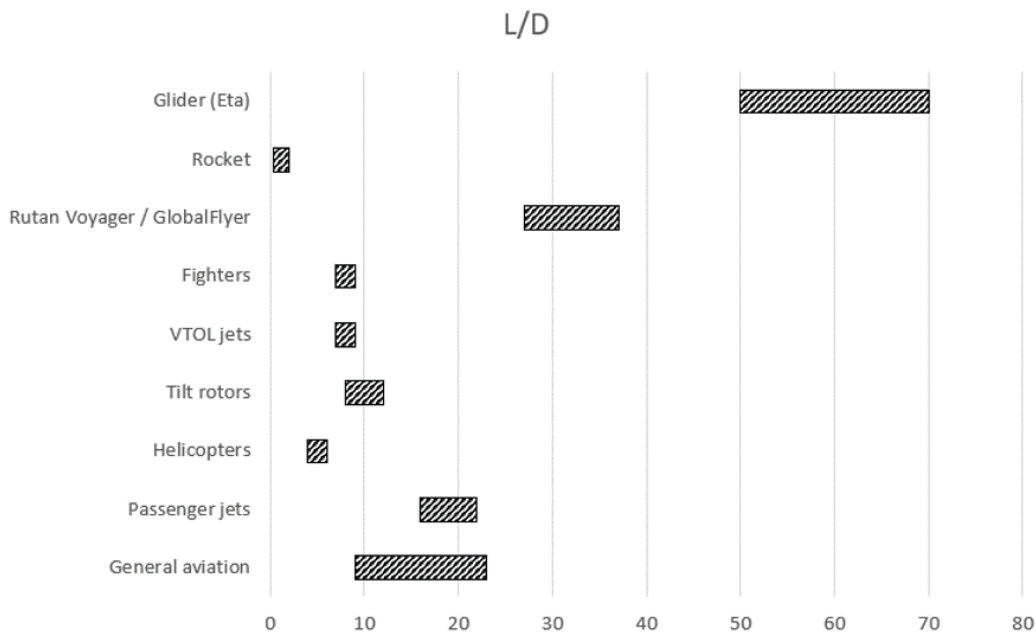


Figure 18: Lift to drag ratios of different aircraft and rotorcraft types [27].

The possibility to increase the lift to drag ratio folding the takeoff propellers inside the fuselage will be discussed in chapter 5.

Figure 19 shows the flight speeds of the aircraft groups analyzed. Fighters are the fastest, flying over Mach 2. The Harrier is not supersonic, but it can fly in the high transonic region. Passenger jets are transonic, and they fly slightly slower. The stall of the retreating blade limits the maximum flight speed of the helicopter at around 300 km/h. The V-22 tilt-rotor can fly up to 500 km/h.

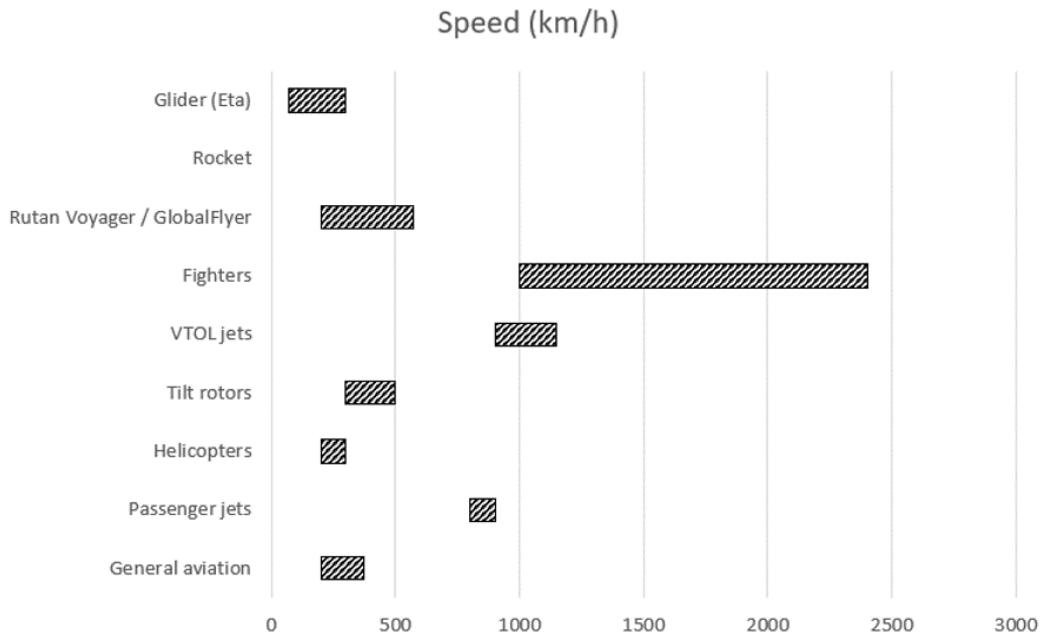


Figure 19: Flight speed of different aircraft and rotorcraft types [27].

The battery specific energy and the possibility to use different power sources other than batteries will be discussed in chapter 4. The propulsive efficiency depends on the electric motor and on the propeller or ducted fan used.

2.2.2 Battery-mass ratio

The designer can control the battery-mass ratio. This parameter can be increased, reducing the payload or improving the technology level of the eVTOL systems. Commonly, the weight of an aircraft is expressed as the sum of payload weight, fuel weight, and empty weight. This same subdivision can be applied to eVTOLs substituting the battery weight for the fuel weight. Figure 20 shows the empty weight, fuel, and payload fraction of existing aircraft, rotorcraft, and VTOLs.

General aviation airplanes are shown first. Their empty weight varies from 77% of the Second World War Spitfire to 40% of the Pipistrel Alpha Electro, which is battery-powered and built using composite materials. The Enfica-FC is a fuel cell powered prototype built in 2010, and its empty weight is 49% [1]. The Alpha Electro is a modified version of the Alpha Trainer powered by batteries. The empty weight of the Electro is lower because the electric motor is lighter, but the batteries are heavier than the fuel carried by the standard version [3] [28]. The Cessna 172, one of the most widespread general aviation aircraft, has an empty weight of 60%. Jet airliners have empty weight fractions in the order of 50%, with narrow-body aircraft serving short-range missions at around 55% and wide-body aircraft around 50%. The third group collects five different helicopters. Their empty weight varies from 65% of the small Robinson R-22 to 49% of the large Chinook. The E-Hang 184 is in this group too, it is an eVTOL, and its empty weight is 44%. The V-22 and AW 609 tiltrotors have an empty weight of about 60%, like the Harrier and Yak-39 jet VTOLs, and the fighters F-22 and Eurofighter Typhoon. The Rutan

Voyager and the Global Flyer are designed to carry as much fuel as possible. Their empty weight is 23% and 16%, and their fuel fraction is 70% and 82%. Rockets have fuel fractions even higher, in the order of 90%, with about 8% empty weight.

This analysis shows that the empty weight depends on the type of aircraft, its dimensions, and the technology level. The effect of the aircraft type is shown by the different empty weights of the various aircraft groups. The impact of the dimensions shows the differences inside the groups, narrow-body vs. wide-body in the commercial jet group, and R-22 vs. Chinook in the helicopter group. The examples showing the effect of the technology level are the reduced weight of composite structures of the Pipistrel aircraft vs. the old Spitfire and the differences in engine weight between electric and internal combustion ones.

Empty weight, fuel and payload fraction

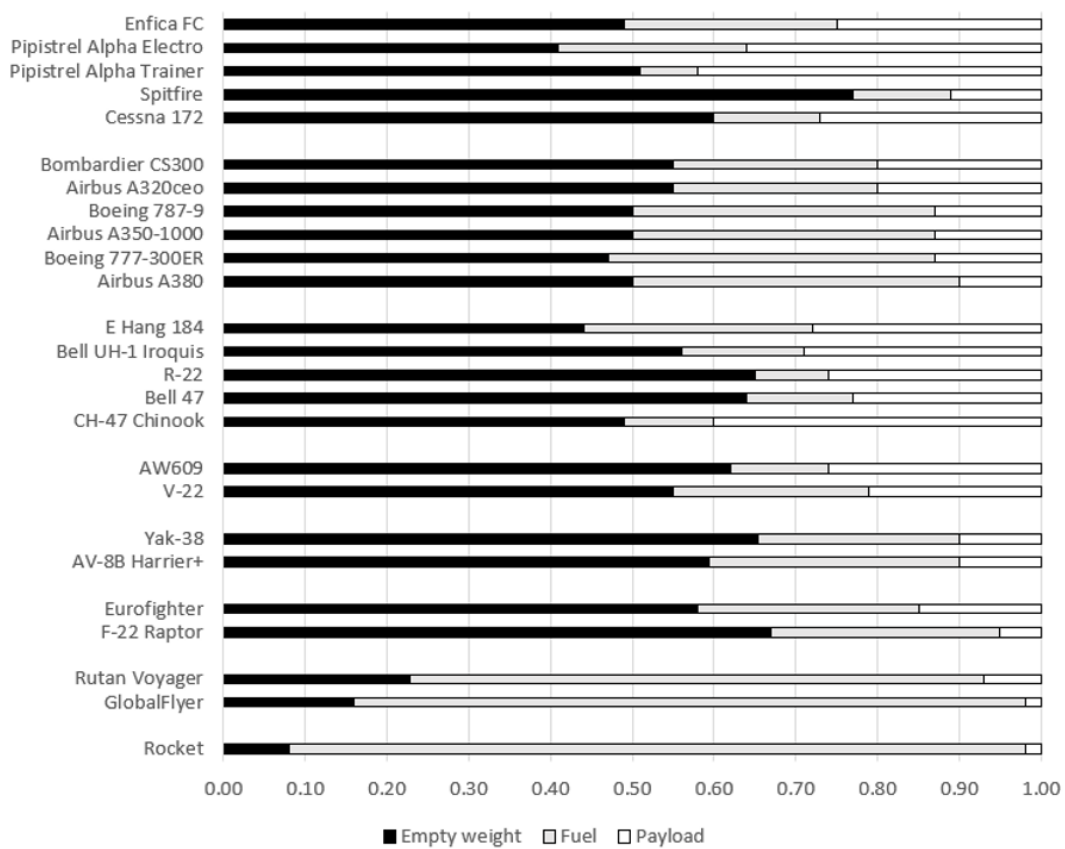


Figure 20: Empty weight, fuel, and payload fraction of existing aircraft, rotorcraft, and VTOLx [27].

Equation (14) and Figure 17 have displayed the importance of the battery-mass ratio and how it can affect the range of the eVTOL. The Empty weight, fuel, and payload fraction analysis showed that the empty weight depends on the type of the aircraft, its dimensions, and the technology level. If the eVTOL configuration and dimensions are chosen, and the technology cannot be improved anymore, the only way to increase the battery-mass ratio is to reduce the payload. If the payload is reduced and the battery-mass is increased, the total mass remains constant, and the range increases. Extended range missions become possible, but the cost of electric energy increases.

2.2.3 Tradeoff between payload and battery mass, and the energy cost of an eVTOL mission.

The tradeoff between payload and battery mass will be analyzed, computing the energy cost of a mission for each passenger of the eVTOL. The payload can be reduced, increasing the battery mass, to increase the range. A reduced payload means fewer passengers and thus a higher cost per passenger.

The payload mass fraction is:

$$\frac{m_{payload}}{m} = 1 - \frac{m_{empty}}{m} - \frac{m_{battery}}{m} \quad (15)$$

A passenger and his luggage is assumed to weight $m_{payload} = 100 \text{ kg}$. The total mass of the vehicle can be computed:

$$m = \frac{m_{payload}}{m_{payload}/m} \quad (16)$$

The battery mass is:

$$m_{battery} = m \cdot \frac{m_{battery}}{m} \quad (17)$$

The cost of the energy required to recharge the battery fully is computed as the total energy storable inside the battery multiplied by the cost of the electric energy for the unit of energy ($c = 0.12 \text{ €/kWh}$) [29] [30]:

$$\text{Energy cost} = m_{battery} \cdot E^* \cdot c \quad (18)$$

$E^* = 200 \text{ Wh/kg}$ is the specific energy of the batteries. The energy cost found is already the energy cost per passenger because the payload is fixed at 100 kg, considering a single passenger. Figure 21 shows the results of computing the energy cost for different empty weight fractions (20%, 30%, 40%, and 50%), varying along the x-axis the battery-mass fraction. The lift to drag ratio is set at 10, and the propulsive efficiency at 0.75. For a given empty weight fraction, the range can be increased, incrementing the battery-mass fraction and the energy cost to perform that mission. As the payload fraction approaches zero, the cost increases dramatically. At that point, increasing the battery fraction stops yielding benefits. The cost becomes too high, and the transportation service at such a high price stops to be desirable. If the battery-mass fraction is too low, it can be increased, improving the range at a little cost.

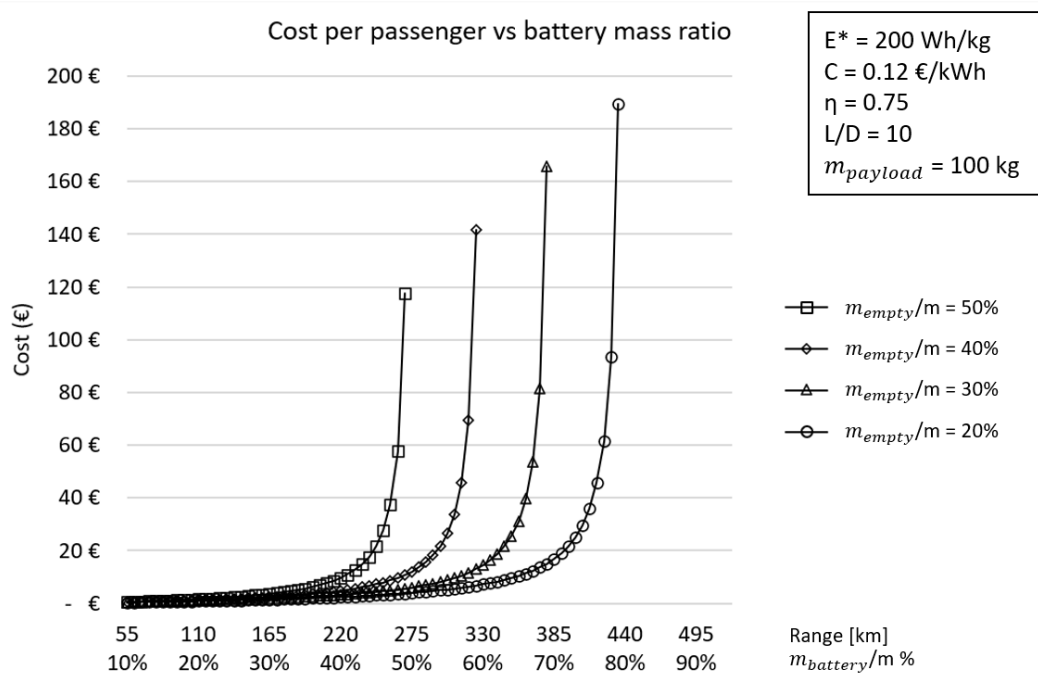


Figure 21: Energy cost to perform the maximum range trip at different empty weight fractions (m_{empty}/m) varying the battery to total mass ratio ($m_{battery}/m$).

2.3 Take-off and landing

During the takeoff and the landing, the eVTOL must produce the force required to stay aloft entirely with its propulsive system because the wing cannot generate lift at zero airspeed. During cruise flight, instead, the wing acts like a force multiplier. The propulsive system generates thrust to propel the aircraft forward, and the wing uses the airflow investing it to generate the lift. The thrust required to keep the cruise altitude and the cruise speed constant is equal to the drag. The lift generated by the wing is the drag multiplied by the lift to drag ratio of the vehicle. High lift to drag aircraft can multiply the thrust generated by the propulsive system by a significant factor producing the lift to stay aloft cheaply. The high lift to drag ratios of the Global Flyer and the Rutan Voyager seen in Figure 18 enable them to have their high ranges.

This section discusses the hover portion of an eVTOL mission. The disk actuator theory [31] [32] gives the power required to produce the thrust required to hover:

$$P = \sqrt{\frac{T^3}{2\rho A}} \quad (19)$$

P is the required power to hover, T is the thrust or the weight of the eVTOL, ρ is the air density, and A is the actuator disk area. Equation (19) shows that the power required to hover decreases as the disk actuator area increases. For this reason, the best vehicles for hover are lightweight helicopters that have large disk actuator area. Internal combustion engines can power these helicopters. Turbines that can produce more power at a given weight enabled the realization of larger and more powerful

helicopters. The effect of density shows that the ceiling of a helicopter is limited by the power required, the lower the density, the more power required to hover.

Table 4: Power required to hover of six popular helicopters.

| Helicopter | Max takeoff weight (kg) | Rotor diameter (m) | Power required theory (kW) | Power available (kW) |
|---------------|-------------------------|--------------------|----------------------------|----------------------|
| Robinson R-22 | 622 | 7.67 | 45 | 93 |
| Bell 47 | 1338 | 11.33 | 96 | 210 |
| AW109 | 2850 | 11 | 306 | 836 |
| UH-1 Iroquis | 4309 | 14.63 | 428 | 820 |
| CH-47 Chinook | 22680 | 18 | 2967 | 7058 |
| AS350 | 2250 | 10.7 | 221 | 632 |

In Table 4, equation (19) is used to compute the power required to hover of six widespread helicopters. The comparison with the power required computed with the disk actuator theory and the maximum power available shows theoretical values close to half the power available. The excess power is since the theory underestimates the power required and there is also a design margin that allows the helicopter to take off from higher altitude heliports. The discrepancy between theory and practice is usually dealt with the figure of merit, a coefficient that describes the efficiency of a rotor to produce thrust in hover. A figure of merit equal to one means that the rotor can generate the same thrust predicted by the theory.

Coaxial rotors or ducted fans can also generate the thrust required to hover. The power required to hover for a couple of coaxial rotors can be estimated with the following modified version of the disk actuator theory:

$$P = k_{int} \frac{T^{\frac{3}{2}}}{2\sqrt{\rho A}} \quad (20)$$

k_{int} is the interference factor, and the possible values computed in [33] are listed in Table 5. Comparing this equation to equation (19), it can be found that the power required by a coaxial rotor couple is $\frac{k_{int}}{\sqrt{2}}$ times the power required by a standard rotor with the same area.

Table 5: Interference factor values for coaxial rotors.

| | Interference factor k_{int} |
|---|-------------------------------|
| Corotation in the same plane at equal thrust | 1.4142 |
| Corotation in the same plane at balanced torques | 1.4142 |
| Equal thrusts with the lower rotor in the slipstream of the upper rotor | 1.2808 |
| Balanced torque with the lower rotor in the slipstream of the upper rotor | 1.2810 |
| Two rotors operated independently but at the same thrust-sharing ratio as found in the torque-balanced case | 1.2657 |

Ducted fans can generate more thrust with the same disk actuator area because the shroud produces thrust too. A modified version of the disk actuator theory for ducted fans is [34]:

$$P = \sqrt{\frac{(T/T_i)^3}{2\rho A}} \quad (21)$$

$T_i = 1.26$ is the thrust increase for ducted fans [34].

2.3.1 Nonideal effects and the figure of merit

In real rotors in hover, several physical effects separating the flow from the ideal case appear, including tip losses, wake swirl, nonuniform flow, and less than ideal wake contraction. These effects and the blades' airfoil drag make the actual power required higher than what can be computed with the disk actuator theory. The figure of merit has been introduced as a form of efficiency factor to evaluate rotors in hover. It is defined as ideal power required to hover divided by actual power required to hover:

$$FM = \frac{\text{Ideal power required to hover}}{\text{Actual power required to hover}} \quad (22)$$

In practice, helicopter rotors have a figure of merit between 0.7 and 0.8, with state-of-the-art rotors reaching a maximum of 0.82.

Introducing the thrust and power coefficients, some nonideal effects can be considered, and the figure of merit can be rewritten. The US customary definition is used as in [32]:

$$C_T = \frac{T}{\rho A (\Omega R)^2} \quad (23)$$

$$C_P = \frac{P}{\rho A (\Omega R)^2} \quad (24)$$

With these coefficients, the disk actuator equation (19) for hover can be rewritten:

$$C_P = \frac{C_T^{3/2}}{\sqrt{2}} \quad (25)$$

This equation is modified to consider the real effects to the following form:

$$C_P = \frac{k C_T^{3/2}}{\sqrt{2}} + \frac{\sigma C_{d0}}{8} \quad (26)$$

k is called induced power factor, and it considers the nonideal effects, including the tip losses, the wake swirl, the nonuniform flow, and the less than ideal wake contraction. The usual value for k is 1.15. The second term has been computed integrating the blades' airfoil drag along the length of the blades. C_{d0} is the section profile drag coefficient, and it is assumed constant to perform the integration. A usual value for C_{d0} is 0.01. These values are normally computed measuring the C_P at different C_T and performing the linear regression on equation (26).

σ is the solidity of the rotor, and it is equal to the area of the blades divided by the area of the disk actuator:

$$\sigma = \frac{N_b c R}{A} = \frac{N_b c}{\pi R} \quad (27)$$

Where N_b is the number of blades, c is the blade chord, R is the radius of the rotor, and A is the area of the disk actuator. Considering the nonideal effects, the figure of merit can be rewritten:

$$FM = \frac{\frac{C_T^{3/2}}{\sqrt{2}}}{\frac{kC_T^{3/2}}{\sqrt{2}} + \frac{\sigma C_{d0}}{8}} \quad (28)$$

Equation (28) shows that, for low thrust coefficients, the figure of merit is low because the profile drag term on the denominator is relevant. The rotor blades are spinning at low angles of attack, and the thrust produced is little while the drag is present. As the angle of attack increases, the profile drag term becomes smaller and smaller compared to the induced power term, and the figure of merit approaches a value of $1/k$. Figure 22 shows experimental and theoretical data of the figure of merit varying the coefficient of thrust. The theoretical lines are computed with equation (28).

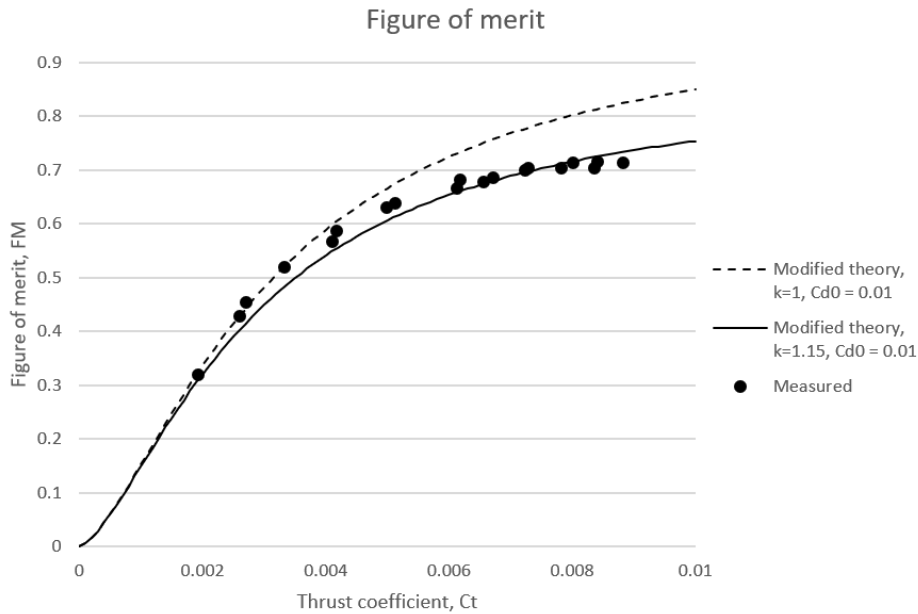


Figure 22: Figure of merit, experimental, and theoretical data at different thrust coefficient. Data source: [35].

Smaller propellers in hover have a lower figure of merit. Table 6 lists motor power consumption, the thrust generated, and the computed figure of merit for data provided by the quadrotor motor manufacturer Cobra Motors [36]. Four motor-propeller combinations are presented for three multirotor motors. The CM 2206/20 $K_v=2100$ is one of the smallest produced by Cobra Motors, and it is designed for drone racing. The K_v rating of a brushless motor is the ratio of the motor's unloaded rpm to the peak voltage on the wires connected to the coils. The figure of merit of this motor is between 42% and 49%. The CM 2217/20 $K_v=950$ is a mid-range motor, and its figure of merit is between 49% and 55%. The CM 4520/18 $K_v=310$

is the largest multirotor motor listed in Cobra Motors website, and its figure of merit is larger. It is comprised between 50% and 64%.

Table 6: Figure of merit of quadrotor motors and propeller computed from the Cobra Motors data.

| Motor | Propeller diameter (inches) | Thrust (grams) | Power (W) | Figure of merit |
|--------------------|-----------------------------|----------------|-----------|-----------------|
| CM 2206/20 Kv=2100 | 5 | 912 | 362.3 | 42% |
| | 5 | 685 | 202.0 | 49% |
| | 5 | 845 | 296.0 | 46% |
| | 6 | 1114 | 367.9 | 46% |
| CM 2217/20 Kv=950 | 10 | 1341 | 266.1 | 51% |
| | 8 | 997 | 199.5 | 54% |
| | 9 | 1160 | 221.1 | 55% |
| | 10 | 1323 | 269.8 | 49% |
| CM 4520/18 Kv=310 | 18 | 4107 | 629.4 | 64% |
| | 15 | 3099 | 630.7 | 50% |
| | 16 | 3604 | 734.4 | 51% |
| | 18 | 3532 | 622.3 | 52% |

Tests have been conducted at Politecnico di Torino to measure the thrust and the figure of merit of the FMS 70 mm model electric ducted fan. Figure 23 shows the figure of merit at different thrust levels. The figure of merit has been computed dividing the ideal power required by the measured power consumed. The ideal power required has been computed with the disk actuator theory modified for ducted fans, equation (21).

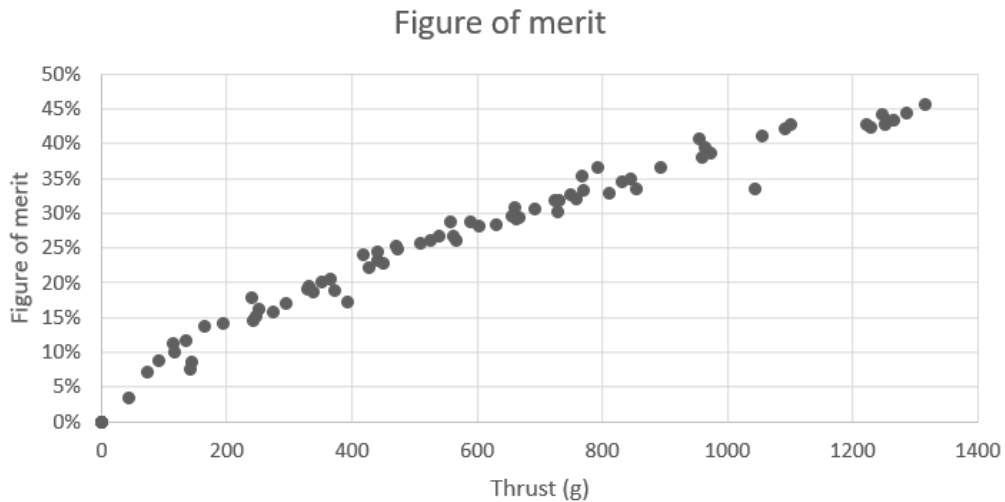


Figure 23: Figure of merit of the FMS 70 mm ducted fan.

2.3.2 Minimum disk actuator area required to hover

The previous section showed that the power required to hover depends on the disk actuator area. A large disk actuator area is efficient for hover because the power required is low, while a small disk actuator area is not because the power required is high. However, a large disk actuator area generates more drag during the cruise phase of an eVTOL, making it less efficient overall. There are many options to reduce the drag generated by the vertical thrust system during the cruise. The main solutions available are to reduce its disk actuator area increasing its power, to retract it inside the fuselage or a fairing, or to use the same system for hover and cruise tilting the direction of the thrust. Lift + cruise eVTOLs are designed to optimize the disk actuator area for the maximum energy efficiency over the design mission. The Krossblade SkyProwler drone can retract its vertical thrust propellers inside the fuselage, increasing its lift to drag ratio in cruise. The Joby aviation S2 and S4 employ foldable propellers that are extended in hover and folded during the cruise. The Lilium Jet takes advantage of the last strategy; it tilts its ducted fans used to generate the vertical thrust to generate the thrust required during cruise too. This same option is used by the V-22 and AW 609 tiltrotors. They can tilt their two large rotors mounted on the tips of their wings.

In this section, the minimum disk actuator area required for hover will be computed from the vehicle mass and the power available. The result will show what the design parameters that affect the disk actuator area required are.

The disk actuator equation (19) can be rewritten for a battery-powered eVTOL:

$$m_{payload} \frac{m_{battery}/m}{m_{payload}/m} k_p = \sqrt{\frac{\left(\frac{T}{W} \frac{m_{payload}}{m_{payload}/m} g\right)^3}{2\rho A}} \quad (29)$$

Where $m_{payload}$ is the payload mass, k_p is the specific power of the batteries, $m_{battery}/m$ is the battery-mass fraction, $m_{payload}/m$ is the payload mass fraction, $\frac{T}{W}$ is the thrust to weight ratio of the vehicle, and g is the gravity acceleration. The left term of the equation is the power available rewritten as battery mass multiplied by the specific power of the battery. The battery mass has been written as total mass times the battery-mass fraction. The total mass is written as payload mass divided by the payload mass fraction. This same expression is used to compute the thrust, which is expressed as thrust to weight ratio times the total mass times the gravity acceleration. The battery technology does not limit the specific power. A hybrid power generator comprising internal combustion engines, turbines, fuel cells, or supercapacitors can be added to the battery. The specific power used considers the specific power of the whole power generation system. The effect of different power systems will be explored more in detail in chapter 4. Rearranging equation (29) to find the disk actuator area required:

$$A = \frac{\left(\frac{T}{W} \frac{m_{\text{payload}}}{m_{\text{payload}/m}} g\right)^3}{\left(\frac{m_{\text{battery}/m}}{m_p \frac{m_{\text{payload}}}{m_{\text{payload}/m}} k_p}\right)^2} \frac{1}{2\rho} \quad (30)$$

$$A = \frac{\left(\frac{m_{\text{payload}}}{m_{\text{payload}/m}}\right)^3}{\left(\frac{m_{\text{battery}/m}}{m_{\text{payload}} \frac{m_{\text{payload}}}{m_{\text{payload}/m}} k_p}\right)^2} \frac{g^3}{2\rho} \left(\frac{T}{W}\right)^3 \quad (31)$$

$$A = \frac{g^3}{2\rho} \left(\frac{T}{W}\right)^3 m_p \left(\frac{1}{k_p}\right)^2 \frac{\left(\frac{1}{\frac{m_{\text{payload}}}{m_{\text{payload}/m}}}\right)^3}{\left(\frac{m_{\text{battery}/m}}{\frac{m_{\text{payload}}}{m_{\text{payload}/m}}}\right)^2} \quad (32)$$

$$A = \frac{g^3}{2\rho} \left(\frac{T}{W}\right)^3 m_p \left(\frac{1}{k_p}\right)^2 \frac{1}{\frac{m_{\text{payload}}}{m} \left(\frac{m_{\text{battery}}}{m}\right)^2} \quad (33)$$

The final formula is:

$$A = \frac{g^3}{2\rho} m \left(\frac{T}{W}\right)^3 \left(\frac{1}{k_p}\right)^2 \frac{1}{\left(\frac{m_{\text{battery}}}{m}\right)^2} \quad (34)$$

The disk actuator area required to hover is directly proportional to the cube of the gravity and inversely proportional to the atmospheric density; this effect will be discussed more in depth in the next section.

The disk actuator area is proportional to the total mass of the eVTOL and proportional to the cube of the thrust to weight ratio. This parameter must be higher than one to enable vertical ascent, but it cannot be very high because the disk actuator area required increases very fast, with its cube. Existing designs cannot be scaled up directly because the mass of the vehicle scales as the cube of the reference length while the disk actuator area scales as the square of the reference length. Equation (19) shows that the power required grows with the mass raised to the 1.5 power, while the available power grows proportionally to the mass of the vehicle if the specific power and the battery-mass ratio are kept constant. E-Hang designed its 184 eVTOL as a bigger quadrotor. They used coaxial rotors, which generate more thrust at the same disk actuator area.

The disk actuator area is inversely proportional to the square of the specific power of the power system, making hover easier for high power systems. Alternative power systems such as fuel cells or hybrids have lower specific power at the present technology level, requiring an eVTOL configuration with a higher disk actuator area. Another possibility to improve the power available is to use supercapacitors. However, their low specific energy reduces the total energy available.

Finally, the $\frac{m_{\text{battery}}}{m}$ ratio is found once again. The disk actuator area is inversely proportional to the square of this parameter, meaning that the higher this

parameter is, the smaller the disk actuator area required is. The $m_{battery}/m$ ratio has also been found in the range analysis. Increasing this parameter improves the range and allows to hover with a smaller disk actuator area.

Some numerical values of the thrust system area required, computed with equation (34), are shown in figures 24, 25, and 26. The values used for the computations are listed in Table 7.

Table 7: Data used for hover computations.

| | Values used for hover computations |
|------------------------|------------------------------------|
| Gravity | 9.81 m/s ² |
| Density | 1.225 kg/m ³ |
| Thrust to weight | 1.3 |
| Total mass | 750 kg |
| Battery specific power | 800 W/kg |
| Battery-mass ratio | 40% |

High specific power, in the order of 800 W/kg, is required to have reasonably small thrust system areas. Batteries have higher specific power than fuel cells, and this is their advantage.

The $m_{battery}/m$ is essential both for hover and range. It should be at least 30% to have a small vertical thrust system area.

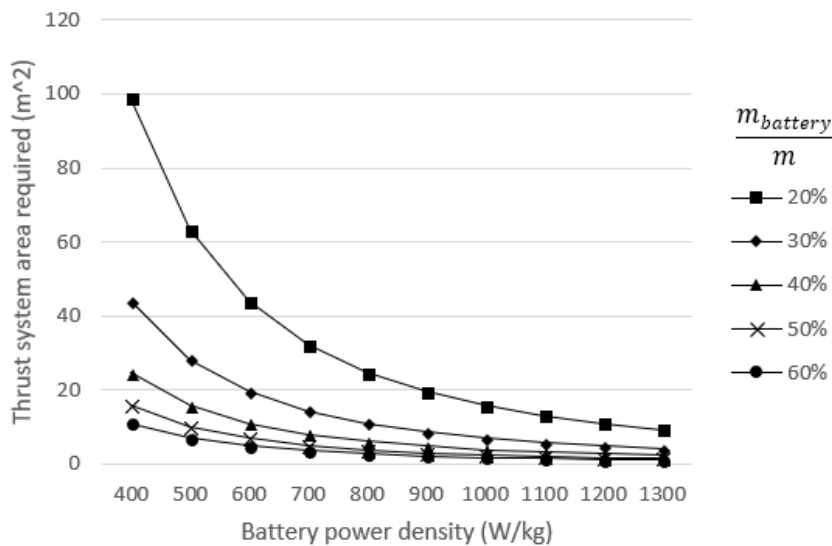


Figure 24: Thrust system area required function of the battery specific power for various battery to total mass ratios.

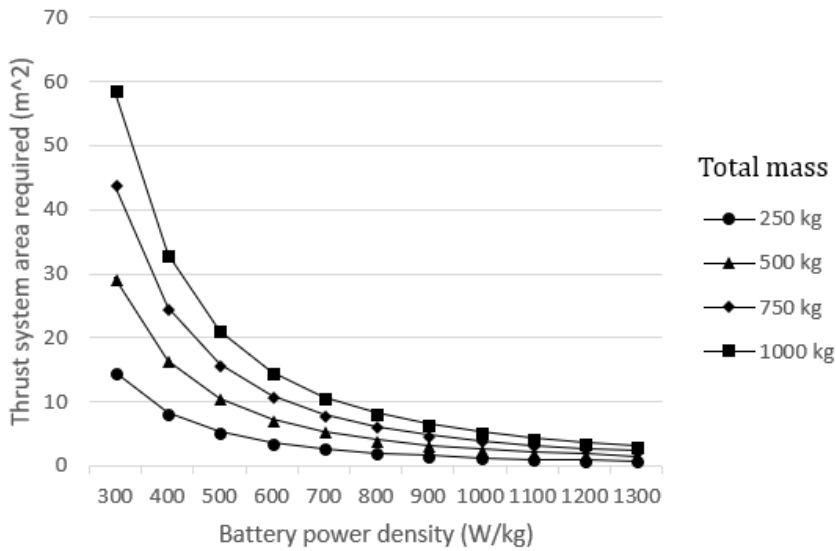


Figure 25: Thrust system area required function of battery specific-power for various total mass.

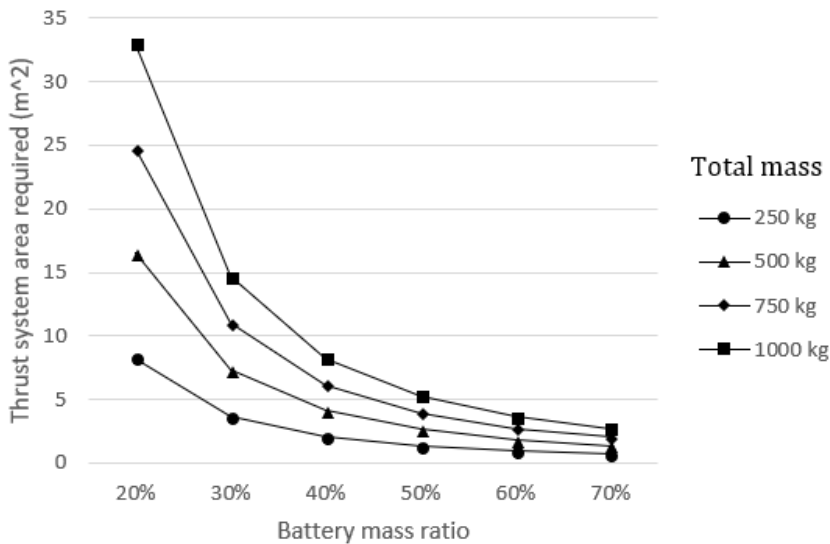


Figure 26: Thrust system area required function of the battery to total mass ratio for various total mass.

2.3.3 Hover on other planets

The disk actuator equation (19) and the minimum area required equation (34) show that on Earth, the higher the altitude, the more difficult it is to hover, and the larger disk actuator area is required. On other planets, the gravity and the atmospheric density change, creating interesting consequences. Equation (34) shows that the disk actuator area required to hover is proportional to the $\frac{g^3}{2\rho}$ parameter, and equation (19) shows that the power required to hover is proportional

to the $\sqrt{\frac{g^3}{2\rho}}$ parameter. The $\frac{g^3}{2\rho}$ parameter at sea level on Mars has the same value it has on Earth at 13400 m altitude, making hovering challenging but possible. A Martian exploration mission could include a quadrotor designed to perform short reconnaissance hops. On Titan, the gravity is about a sixth of Earth's gravity, and the atmospheric density is about five times higher. This makes hovering much easier. Table 8 shows the values of gravity acceleration, atmospheric density, the $\frac{g^3}{2\rho}$ parameter and the $\sqrt{\frac{g^3}{2\rho}}$ parameter on Earth, Mars, and Titan.

Table 8: Gravity acceleration, atmospheric density, the $\frac{g^3}{2\rho}$ parameter, and the $\sqrt{\frac{g^3}{2\rho}}$ parameter on Earth, Mars, and Titan.

| | Earth | Earth 13.4 km | Mars | Titan |
|---------------------------------------|------------------------|------------------------|-------------------------|--------------------------|
| Gravity acceleration | 9.81 $\frac{m}{s^2}$ | 9.77 $\frac{m}{s^2}$ | 3.72 $\frac{m}{s^2}$ | 1.352 $\frac{m}{s^2}$ |
| Pressure | 101325 Pa | 15586 Pa | 610 Pa | 146700 Pa |
| Temperature | 288 K | 217 K | 233 K | 78 K |
| Molar mass | 29 g/mol | 29 g/mol | 44 g/mol | 28 g/mol |
| Atmospheric density | 1.225 $\frac{kg}{m^3}$ | 0.251 $\frac{kg}{m^3}$ | 0.0139 $\frac{kg}{m^3}$ | 6.33713 $\frac{kg}{m^3}$ |
| $\frac{g^3}{2\rho}$ | 385 | 1857 | 1857 | 0.195 |
| $\frac{g^3}{2\rho}$ comparison | 1 | 4.8 | 4.8 | 0.0005 |
| $\sqrt{\frac{g^3}{2\rho}}$ | 19.6 | 43.1 | 43.1 | 0.44 |
| $\sqrt{\frac{g^3}{2\rho}}$ comparison | 1 | 2.2 | 2.2 | 0.022 |

The gravity acceleration of Earth, Mars, and Titan can be found in multiple sources including the NASA website [37] or Wikipedia. The atmospheric density can't be found because it is not measured directly but it is computed from the pressure, the temperature, and the atmospheric composition.

Earth's atmospheric properties at altitude have been computed with the following equations provided by the NASA website [38]:

For $h < 11000$ m (Troposphere):

$$T = 15.04 - 0.00649 h \quad (35)$$

$$p = 101290 \left(\frac{T + 273.1}{288.08} \right)^{5.256} \quad (36)$$

For $11000 \text{ m} < h < 25000$ (Lower Stratosphere):

$$T = -56.46 \quad (37)$$

$$p = 22650 e^{(1.73 - 0.000157 h)} \quad (38)$$

For $h > 25000$ m (Upper Stratosphere):

$$T = -131.22 + 0.00299 h \quad (39)$$

$$p = 2488 \left(\frac{T + 273.1}{216.6} \right)^{-11.388} \quad (40)$$

Altitudes are expressed in meters, temperatures in degrees Celsius, and pressures in Pascal. The number of moles in a cubic meter of air is computed with

the ideal gas law $PV = nRT$. $R = 8.31 \frac{J}{mol K}$ is the gas constant and n is the number of moles. For Earth's atmosphere at sea level, the number of moles in a cubic meter of air is $\frac{n}{V} = \frac{p}{RT} = \frac{101325}{8.31 \cdot 288} = 42.34 \frac{mol}{m^3}$. The atmospheric density can be computed multiplying the number of moles in a cubic meter by the molar mass of air. The molar mass M of air is 29 g/mol because the Earth's atmosphere is composed of about 80% nitrogen N_2 which has a molar mass of 28 g/mol and 20% of oxygen O_2 which has a molar mass of 32 g/mol. The atmospheric density is then $\rho = \frac{n}{V} M = 42.34 \cdot 29 = 1227 \frac{g}{m^3} = 1.227 \frac{kg}{m^3}$ which is in accordance with the standard value of $1.225 \frac{kg}{m^3}$.

The same procedure has been applied to compute the atmospheric density on Earth at 13400 m altitude, on Mars at sea level, and on Titan at sea level. The molar mass of the atmosphere of Mars is 44 g/mol because it is composed of 95% of carbon dioxide which is one atom of carbon (12 g/mol) and two atoms of oxygen (16 g/mol each). The molar mass of the atmosphere of Titan is 28 g/mol because it is composed of 95% of nitrogen N_2 (14 g/mol each atom).

The results of the previous computations show that the minimum area required to hover on Mars is 4.8 times larger than on Earth, and on Titan it is only 0.0005 times.

The difference is so significant that hovering on Mars will require higher power settings and much lower power settings on Titan. Equation (19) shows that the power required to hover is proportional to $\sqrt{\frac{g^3}{2\rho}}$. At the same disk actuator area, hover on Mars is 2.2 times more power demanding than on Earth and hover on Titan only 0.022 times. Hover on Mars is a hundred times more power demanding than hover on Titan.

2.3.4 eVTOL for Titan

This section describes the preliminary computation for an eVTOL for Titan powered by a radioisotope thermoelectric generator.

The MHW-RTG powering the Voyager spacecrafts weighs 37.7 kg and generates 2400 W of thermal power and 157 W of electrical power halving every 87.7 years [39]. Considering an RTG mass fraction of 45%, the total weight would be 83.8 kg. The power available considered for the flight is 80 W because the RTG must provide power not only to the motors but also to the computers and the payload. The mass balance is shown in Table 9.

Table 9: eVTOL for Titan mass balance.

| | Fraction | Mass |
|---------|----------|---------|
| RTG | 45% | 37.7 kg |
| Battery | 5% | 4.2 kg |
| Empty | 40% | 33.5 kg |
| Payload | 10% | 8.4 kg |
| Total | | 83.8 kg |

The configuration considered is the standard quadplane, an airplane with a bolt-on quadcopter. The drag polar is taken from the data gathered during the wind tunnel tests described in chapter 5 on the eVTOL drone realized mounting four propellers on a Mini Talon. The drag polar is defined by its quadratic approximation with a C_{d0} of 0.038 and a k of 0.046. The four propellers have a diameter of 60 centimeters, giving a total disk actuator area of 1.13 m^2 . The power required to hover computed with equation (19), considering a figure of merit of 70% and a thrust to weight ratio of 1.2, is 598 W. The RTG cannot provide enough power for the takeoff, and the battery will provide it. The parameters considered for the battery are those of the Tesla Model S battery pack because it is a commercial product highly tested by all its users. The Tesla Model S 85 kWh battery pack weighs 540 kg and has a maximum power of 397 kW [26]. The specific energy is then 157 Wh/kg, and the specific power is 735 W/kg. Better batteries would probably be available for a future mission. However, the low temperature on Titan would require insulation and a sophisticated thermal management system, so it is not wise to use optimistic values. The battery weighs 4.2 kg and can provide a maximum power of 3 kW, which is much more than enough for takeoff. The total energy available is 658 Wh, and, considering a depth of discharge of 60% to improve the battery life, the eVTOL could hover for 1.2 hours. A depth of discharge of 60% means that the minimum state of charge allowed is 40%. This is a conservative value and considers the degradation of the battery. The battery depth of discharge is detailed in chapter 4.

For cruise flight, the lift will be provided by the wing, which has a surface of 1.2 m^2 , a wingspan of 2.5 m and an aspect ratio of 5.2. The propulsive efficiency η_p of the electric motor and propeller is 75%. Figure 27 shows the power required to fly and the power available at different speeds. To compute the power required, the lift coefficient has been evaluated:

$$C_L = \frac{2W}{\rho S v^2} \quad (41)$$

The drag coefficient is computed with the drag polar:

$$C_D = C_{D0} + k C_L^2 \quad (42)$$

The drag is:

$$D = \frac{1}{2} \rho v^2 S C_D \quad (43)$$

The power required is:

$$P = \frac{D v}{\eta_p} \quad (44)$$

Figure 27 shows that the flight speed can range from 3 m/s to a maximum speed of 6 m/s. Atmospheric disturbances have been assumed negligible. However, strong winds might make such a spacecraft unable to fly safely.

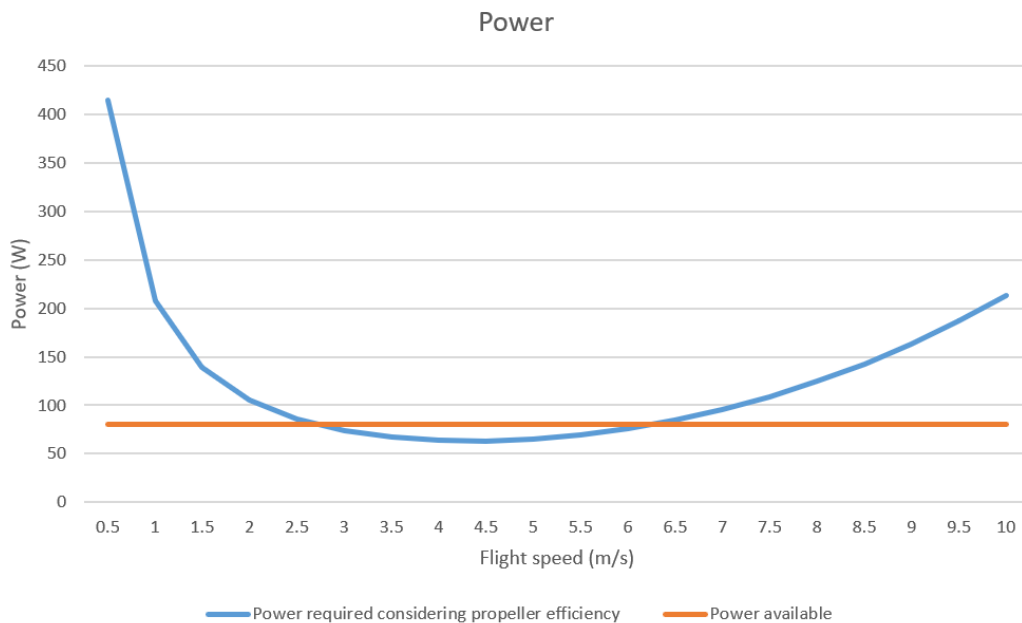


Figure 27: Power required and power available for the eVTOL on Titan.

The speed range using only the power provided by the RTG is not broad. The batteries could provide more power enabling faster airspeeds, and the eVTOL would land periodically to recharge the batteries.

The aerodynamic of flight on Titan differs from the aerodynamic of flight on Earth. The main differences are the Reynolds number and the lift coefficient. The Reynolds number is low because the flight speed that can be reached with the power provided by the RTG is low. This same reason makes the lift coefficient required high. At 5.5 m/s the lift coefficient is 1.

It would be interesting to perform this conceptual exercise knowing the data of the reactor powering the Curiosity rover. Its specific power might be higher.

2.4 Transition from hover to forward flight

The transition is the flight phase in which the VTOL accelerates from hover to cruise flight. Every configuration deals with the transition differently. Helicopters tilt the direction of the vertical thrust with the collective pitch towards the direction in which they want to go, and the horizontal component of the thrust generates the forward acceleration. As the speed increases, the incoming airflow improves the aerodynamics, and the power required decreases. At a certain altitude and flight speed, the helicopter has enough mechanical energy to be able to land on autorotation. This condition is the emergency option in case the engine fails, and no power is provided to the rotor. The rotor keeps spinning with the mechanical

energy stored in it as angular momentum and pushed by the incoming airflow. The helicopter can fly trading the mechanical energy it has in the form of altitude and flight speed to preserve the angular momentum of the rotor.

Multirotors act like helicopters. They tilt the vertical thrust increasing the power of the rear propellers and tilting the whole body. Multirotors cannot fly on autorotation because they cannot control the direction of the thrust with the collective pitch, but six or more propellers ensure enough redundancy to land with the remaining propeller in case one engine fails.

VTOLs with a wing go through a more complex transition phase because, as the airspeed increases, the lift generated by the wing replaces the vertical thrust generated by the takeoff propellers and the surface controls take over the control provided by the propulsion system. The lift plus cruise is probably the more straightforward VTOL configuration. In hover, the vertical thrust and the roll, pitch, and yaw control are provided by the takeoff propellers. As the VTOL reaches the speed at which the wing can provide enough lift, the takeoff propellers are shut down, and the VTOL flies like a conventional aircraft. In the cruise phase, the takeoff propellers do not have a specific function to perform, and some eVTOLs retract them inside the fuselage like the Krossblade SkyProwler or fold them like the Joby Aviation S2 and S4.

Some VTOLs of the fifties and sixties suffered from lack of control power during the transition [40] because the lift provided by the wing and the force the surface controls can produce vary nonlinearly. The prototypes of the Harrier suffered from this problem, and it was overcome adding power to the jet exhausts on the wingtips. Tail-sitters rely on the control provided by the ailerons also in hover because the propellers blow them. The Convair XFY Pogo was a tailsitter VTOL built in 1954, which was powered by a couple of contra-rotating propellers on the nose. Its transition was complicated because the whole vehicle had to tilt. The most complex phase was the landing because the pilot had to sit in an awkward position with a limited view. Today there are some tailsitter drones similar to the Pogo. They usually employ two propellers placed in line with the ailerons to blow them also in hover. This placement is more natural with electric motors than with the big turboprop engine powering the Pogo.

During the transition, the tilt-wing tilts its wing. The blowing effect of the propellers on the wing increases the maximum lift coefficient of the wing. The ducted fans powering the Lilium Jet act similarly, they tilt as the speed increases, and the wing is blown and can generate lift at a high lift coefficient. Tilt-wing has a rotor in the tail that generates pitch control in hover and the first part of the transition until the tail can produce enough forces. In the Lilium Jet, the ducted fans in the nose generate the required pitch control.

The sizing of a VTOL wing is different from that of a conventional aircraft because the VTOL wing is not required for takeoff and landing. The wing of a conventional aircraft is sized to generate enough lift in cruise producing the least possible amount of drag during cruise and to be able to take off and land in as many airports as possible. The first requirement drives the wing surface down because the

lower the wetted area, the lower the drag. The second requirement drives it up because the larger the surface, the lower the stall speed, and the lower the takeoff and landing distance. Usually, a compromise is found in between. The flaps help in this regard because they help a small wing designed for the cruise to generate enough lift during takeoff and landing.

The following section will analyze the effects of the wing dimensions on the energy required to get from hover to cruise. Figure 28 shows a free body diagram of the transition of two different VTOLs.

Configuration A has a smaller wing than configuration B's, and its stall speed is higher. In hover, the free body diagram of the two configurations is the same. At 50 km/h, configuration B generates more lift than configuration A, but neither is enough to keep the eVTOL aloft without the help of the vertical thrust system. At 100 km/h configuration B's lift is enough, and no vertical thrust is required, while the lift generated by configurations A is not equal to the weight of the vehicle yet. At 200 km/h, both the lifts generated by configurations A and B are enough to keep the eVTOL aloft, and the drag generated by the wing of configuration B is higher because its surface is larger. 300 km/h is the cruise speed, both configuration A and B generate enough lift with the wing, and the drag of configuration B is higher because its wing surface is larger.

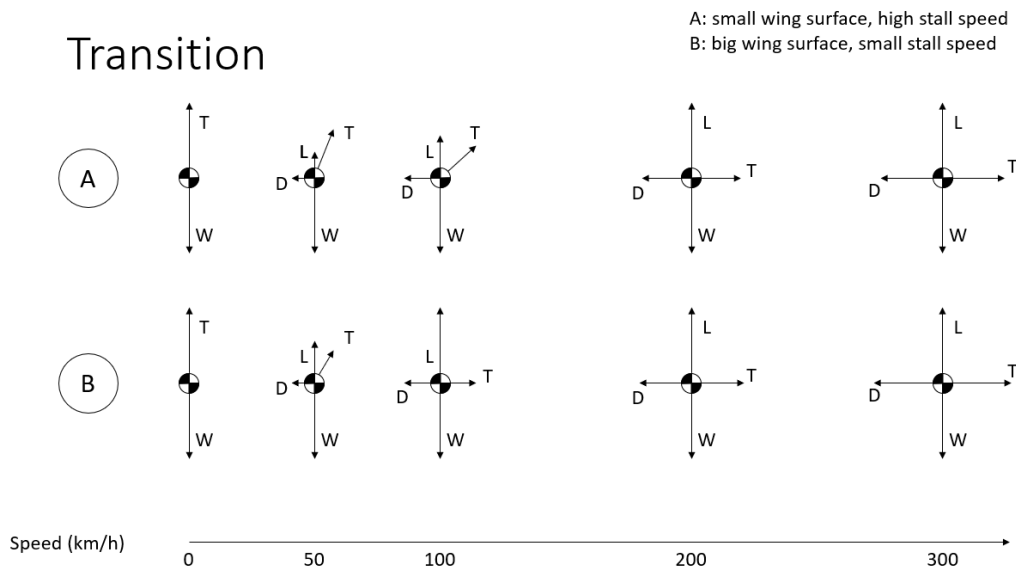


Figure 28: Free body diagram of the transition from hover to forward flight for two VTOLs. Configuration A has a smaller wing surface while configuration B has a bigger wing surface.

2.4.1 Energy required for the transition phase

The energy required to get from hover to cruise is computed for 16 wing dimensions. This analysis builds on the previous conceptual discussion on configurations A and B. The parameters used for these computations are listed in Table 10, the cruise speed is fixed at 300 km/h, and the aspect ratio at 10. Ground effects were not considered in these calculations.

Table 10: Data used for transition computations.

| | |
|---------------------------------|----------------------|
| Total mass | 500 kg |
| Cd0 | 0.022 |
| K | 0.03 |
| Wing surface | 2 m ² |
| Thrust system area | 6 m ² |
| Battery power | 147 kW |
| Total efficiency | 75% |
| Aspect ratio | 10 |
| Cruise speed | 300 km/h @ sea level |
| Maximum horizontal acceleration | 3 m/s ² |

A vectored thrust eVTOL is considered. The thrust system can provide a maximum thrust constrained by the power available, and it can be vectored to produce vertical thrust and horizontal thrust. The vertical thrust required is computed as the weight minus the lift provided by the wing.

$$T_v = W - L \quad (45)$$

It varies from the total weight of the VTOL when it is hovering, to zero after the stall speed. The thrust system is at full power, and it is orientated at an angle that enables it to produce the vertical thrust computed with equation (45). This orientation generates the vertical thrust required and as much horizontal thrust as possible to accelerate the vehicle.

The thrust angle producing the required T_v is computed:

$$\alpha = \sin^{-1} \frac{T_v}{T_{max}} \quad (46)$$

Where T_{max} is the maximum thrust the system can generate. Then the maximum available horizontal thrust is computed:

$$T_{h\ max} = T_{max} \cos \alpha \quad (47)$$

The acceleration generated by this horizontal thrust is checked to keep it small enough to ensure a comfortable passenger experience. A maximum acceleration value is set at $a_{max} = 3\ m/s^2$. The acceleration is computed as maximum available horizontal thrust minus aerodynamic drag divided by the total mass:

$$a = \frac{T_{h\ max} - D}{m} \quad (48)$$

If this value is less than the maximum acceleration allowed a_{max} , the value found of horizontal thrust is kept, else a new value of horizontal thrust is computed as the maximum allowed acceleration times total mass plus aerodynamic drag:

$$T_h = a_{max}m + D \quad (49)$$

To compute the total energy required for the transition, the power required has been integrated in time. This process has been carried out with a simple Euler method that updates the speed at each time step.

$$v_{n+1} = v_n + a \cdot \Delta t \quad (50)$$

Then lift, drag, horizontal thrust, and vertical thrust are computed again for each time step. The energy consumed at each time step is computed multiplying the average power of the two successive time steps by the Δt :

$$E_n = P_{avg} \cdot \Delta t \quad (51)$$

The total energy required to get from hover to cruise is computed adding all the energies of the steps from horizontal speed equals zero to cruise speed.

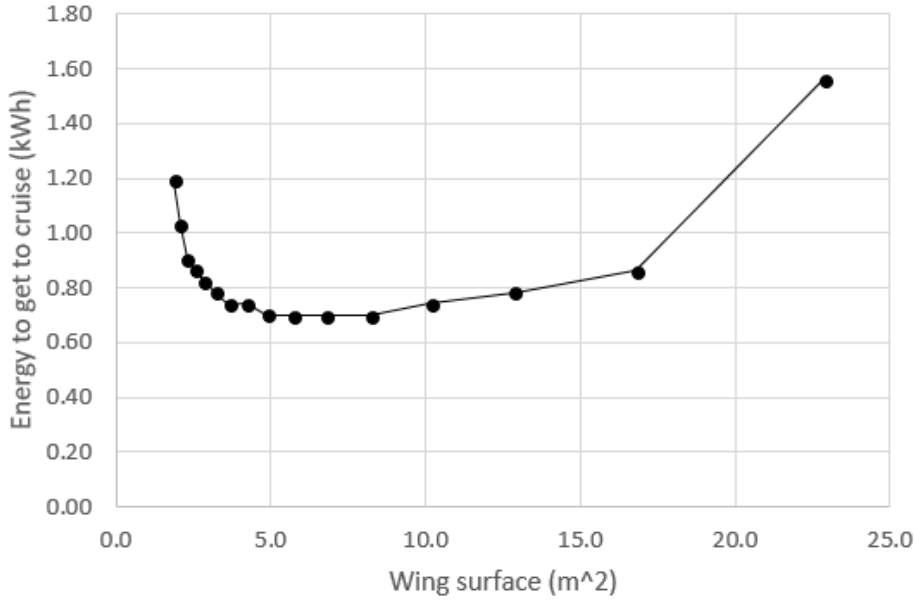


Figure 29: Energy required to get from hover to cruise speed function of the wing surface.

The results of these computations are plotted in Figure 29. This image shows the energy required to get to cruise for different wing surfaces. Configuration A discussed earlier represents VTOLs on the left in Figure 29, configuration B represents VTOLs on the right in that figure. At a low wing surface, the energy required is high because high power is required to supplement the little lift produced by the wing at low speed. The energy required drops as the wing surface increases. Then, the energy required increases again when the increase in the wing surface creates an unnecessary increase in wetted area. The integration with the Euler method is the reason why the curve in Figure 29 is not perfectly smooth.

2.4.2 Power required at every flight speed

With the same data, it is possible to analyze the power required at every flight speed. The power required is the sum of its two components, horizontal and vertical.

$$P_v = \sqrt{\frac{T_v^3}{2\rho A}} \quad (52)$$

$$P_h = D \cdot v \quad (53)$$

The vertical component is computed like in the disk actuator equation (19), with the disk actuator theory. The horizontal component is computed, multiplying the drag by the flight speed. These two sources of power requirements are plotted

in Figure 30. In a vectored thrust VTOL, the balance between vertical and horizontal thrust is achieved tilting the motors, in a lift plus cruise configuration controlling the power given to the motors.

Figure 30 shows that there is no advantage in flying at a speed slower than the stall speed providing the required vertical thrust with the motors instead of the wing. The power required would be higher, and time would be lost flying at lower speeds.

The minimum of the required power is after the stall speed, where $C_L^{3/2}/C_D$ is maximum. The speed that allows having the highest range is the speed at which L/D is maximum, and it is higher than the speed of minimum power required. For commercial applications, the optimal speed might be higher because it would allow saving additional time, perform more missions, and earn more money at a little increase in energy costs.

Another consideration suggested by Figure 30 is that for an electric VTOL, the wing surface should not be designed for takeoff and landing requirements, but it should be designed for cruise and maneuverability, minimizing the total energy required for the mission.

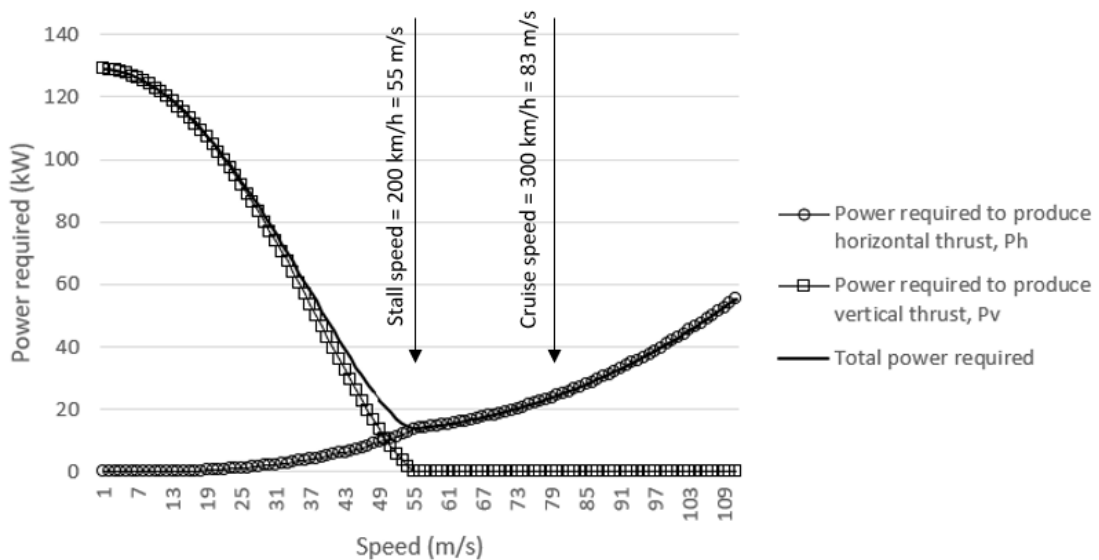


Figure 30: Power required for any flight speed.

2.5 Chapter conclusion

This chapter presented analytical methods to evaluate eVTOL performances in cruise, hover, and transition.

For the cruise portion of the flight, the range is estimated, and the factors affecting it are discussed. The battery-mass ratio is discussed in detail, examining the empty weight of various aircraft and the tradeoff between battery and payload.

The power required to hover is computed with the momentum theory. Coaxial rotors and ducted fans are discussed, and two modified versions of the momentum

theory are presented to evaluate their performances. Non-ideal effects are considered, introducing a figure of merit. Textbook data is presented for large rotors, tests performed by an electric motor manufacturer are presented for small propellers, and we conducted tests at Politecnico di Torino to evaluate the figure of merit of small electric ducted fans. The minimum disk actuator area required for eVTOL takeoff is computed, and the main factors affecting it are discussed.

The power required by a coaxial rotor couple is $\frac{k_{int}}{\sqrt{2}}$ times the power required by a standard rotor of the same disk area, while ducted fans generate 1.26 times the thrust of a standard rotor of the same disk area.

The transition is studied computing the power required to complete it at different wing surfaces and computing the power required at every flight speed.

As the gravity and the atmospheric density affect cruise and hover performances, an interesting conceptual exercise has been carried out. The preliminary design of an eVTOL powered by a radioisotope thermoelectric generator to explore Titan is presented.

This chapter showed that the range of an eVTOL is not only proportional to the specific energy of the power source, but also to the eVTOL lift to drag ratio, and to the battery-mass ratio. Similarly, the battery-mass ratio enables a smaller disk actuator area for hover, which can produce lower aerodynamic drag in cruise and make the eVTOL more efficient overall.

Chapter 3

Configurations

There are many configurations of eVTOL that have been tested and that are being built. This chapter explores the history of the VTOLs designed and tested during the golden era of the VTOL of the fifties and sixties and discusses the present configurations of electric VTOLs. These configurations are compared on disk loading, total hover time, cruise speed, practical range, and flight time, and their performances are evaluated for three reference missions.

3.1 The golden era of the VTOL

The helicopter was the first aircraft capable of vertical takeoff and hover. The first mass-produced helicopter was the R-4 built in 1942 by Igor Sikorsky. The innovation that made the R-4 able to control its direction of flight was the cyclic pitch control. With it, the pilot can adjust the angle of attack of the rotor blades along the cycle of the blade. On one side, the angle of attack is higher, and the blade produces more lift; on the other, it is lower, and the lift produced is lower. With this device, the pilot can control the direction of the thrust produced by the rotor controlling the flight direction. However, this same technology that makes the helicopter perfect for hover makes it limited in forward flight. Its aerodynamic efficiency and its flight speed are lower than those of an airplane.

During the fifties and sixties, many companies tried to build a flying machine combining the vertical takeoff and landing capability of the helicopter and the efficient cruise flight employing a wing of the airplane. The noun VTOL was born to indicate all those flying machines. This section describes the VTOL prototypes designed and tested during that era. The classification follows the V/STOL wheel (Figure 31) published initially by McDonnell Aircraft in the 1960s and then updated by Mike Hirshberg while working on the Joint Strike Fighter program.

V/STOL Aircraft and Propulsion Concepts

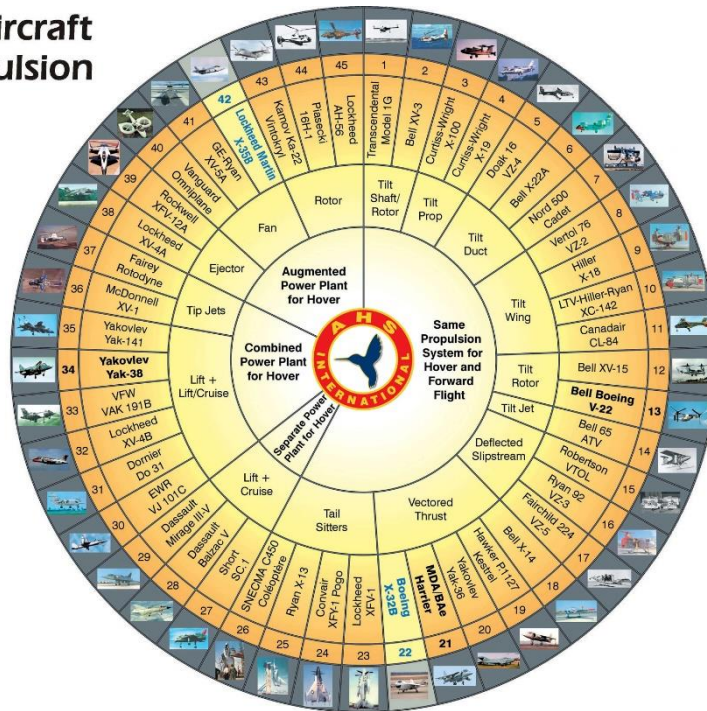


Figure 31: V/STOL wheel [41].

The wheel was accessible until 2018 and has now been replaced by a more conventional website [42]. Mike Hirshberg found in his research [41] that the main issues that impeded the successful development of most V/STOL aircraft were:

- the vast difference in the required thrust for hover and cruise (computed in section 2.4.2),
- the distribution of the thrust around the center of gravity,
- the mechanical complexity,
- and the low fuel efficiency.

These problems were since the efficiency of internal combustion engines, and gas turbines grow with their size. Multiple rotors required multiple engines that were less efficient and less reliable. The new wave of VTOL is powered by electric motors that keep their efficiency constant at different scales.

The information contained in this section is collected from Vertipedia [42], Seth Anderson's NASA report [40], Wikipedia, and documentary videos on YouTube.

3.1.1 Tailsitter

The first subdivision is between VTOLs that use the same propulsion system for hover and forward flight and VTOLs that have a dedicated propulsion system for takeoff and landing. The first VTOLs can rotate the direction of the thrust in different ways. The Convair XFY Pogo (Figure 32) built in 1954 is a tailsitter. It lands on its tail and rotates the whole body to transition from hover to forward flight. It was powered by a turboprop driving a couple of contrarotating propellers

mounted on its nose. The main problems affecting it were the lack of visibility and the danger during landing and the lack of spoilers to slow down from cruise flight to hover. The Lockheed XFV-1 was very similar to the Pogo. It used the same engine and similar coaxial rotors.



Figure 32: Convair XFY Pogo.

Another tailsitter was the Ryan X-13 Vertijet built in 1955, which was powered by a turbojet. The pitch and yaw control in hover were provided by vectored engine thrust while the roll control was provided by puffer jets mounted on the wingtips.

The Snecma C450 Coléoptère was an annular wing jet-powered tailsitter. It first flew in 1954.

3.1.2 Vectored Thrust

The VTOLs in the same group of the Harrier can orientate the direction of its thrust mechanically and for this reason, they are called vectored thrust. In the beginning, vectored thrust VTOLs, like the first Harrier prototypes and the Bell X-14, suffered from suck-down, engine gyroscopic effects, and hot gas re-ingestion [40] [43]. When these problems were solved, the Harrier became the first operational VTOL attack aircraft [44].

The prototype of the Harrier was the Hawker Siddeley P1127, built in 1960 around the newly developed Pegasus engine. This engine has a two-shafts featuring three low-pressure and eight high-pressure compressor stages. The low-pressure compressor supercharges the high-pressure compressor and feeds air to the two forward swiveling nozzles. The two rear swiveling nozzles are driven by the hot exhaust coming from the turbine (Figure 33).

The Hawker Siddeley P1127 was tested from 1960 to 1967 when the first Harrier version flew for the first time. The Harrier Jet (Figure 34) was the only truly successful V/STOL design that emerged during the 1950s and 1960s. It was operated by the RAF, the Royal Navy, the US Marines, and the Indian, Italian, Spanish, and Thai Navies. It played a significant role during the Falkland War in 1982.



Figure 33: Underside view of the Hawker Siddeley P1127 prototype.



Figure 34: The Harrier Jet.

The Bell X-14 (Figure 35) was built in 1957 using existing parts from the Beech Bonanza and the Beech T-34 Mentor. It was powered by two turbojets equipped with thrust deflectors situated in the aircraft's center of gravity. It flew at NASA Ames until 1981 as a testbed for VTOL flight performance, helping Hawker's pilot train before their first flight on the P1127 and Neil Armstrong before its lunar landing. The Yak-36 and the Boeing X-32B are part of the vectored thrust group too. The first was a soviet technology demonstrator first flown in 1963, which led to the Yak-38. It was similar to the X-14. The second was Boeing's competitor to the Lockheed prototype in the Joint Strike Fighter program.



Figure 35: Bell X-14.

3.1.3 Deflected slipstream

The deflected slipstreams use flaps to deflect the slipstream of the propellers. The Ryan VZ3 (Figure 36) first flew in 1958 and achieved excellent STOL performances, but it had no VTOL capabilities [40]. A 1000 shp turboshaft powered two propellers, one under each wing. In hover, the roll was controlled by differential propeller pitch, while engine exhaust, in the tail, controlled yaw and pitch. The Robertson VTOL and the Fairchild 224 VZ-5 Fledgling were similar deflected-slipstream VTOLs



Figure 36: Ryan VZ/3 Vertiplane.

3.1.4 Tilt Jet

The Bell 65 Air Test Vehicle (Figure 37) is the only tilt-jet ever to fly. It was built in 1954 with parts from existing aircraft and was powered by two missile turbojets on each side of the aircraft, mounted under the wing. It had an additional turbo-compressor to power jets in the tail and in the wingtips to provide control in hover. It made partial conversion at altitude, but it had insufficient engine thrust to complete it. The program ended in 1955 and provided data for the subsequent X-14.



Figure 37: Bell 65 Air Test Vehicle.

3.1.5 Tiltrotor

The first tiltrotors to fly were the Transcendental Model 1G and the Bell XV-3. The Model 1G (Figure 38) was the first to fly in 1954 but crashed in 1955. It was a small single-seat monoplane powered by a piston engine driving two three-blade rotors on the wingtips. The Bell XV-3 (Figure 39) powered by a radial engine mounted in the fuselage, driving two two-blade rotors on the wingtips. It flew for the first time in 1955 and performed 110 successful transitions between 1958 and 1962.

The Bell XV-15 (Figure 40) followed the XV-3 and was powered by two turboshafts located in the wingtip pods directly behind the rotors. Like in the V-22 Osprey (Figure 41), who followed it, the engine rotates with the rotor and the pod. The XV-15 first flew in 1977 and was the first tiltrotor to fly faster than conventional helicopters. It led to the development of the V-22, which flew for the first time in 1989. After many tests and refinements, the V-22 was adopted in 2007 by the United States Air Force, the US Navy, and the US Marine Corps. More than 200 V-22 were in service in 2014. The Agusta Westland AW609 (Figure 42) is similar to the V-22 and XV-15, but it is designed for civilian use. It flew for the first time in 2003, and it is expected to enter service in 2020. The Bell V-280 (Figure 43) is a new prototype that flew in 2017 with capabilities like the V-22. The major difference is that the engines sit in the wingtip pods, but they do not tilt, only the rotors tilt.

The main advantages of tiltrotors compared to standard helicopters are the maximum flight speed in the order of 520 km/h and the higher range. The downside is the increased complexity, which required years of testing and resulted in multiple deadly accidents, the last happening as recently as 2015 during the testing of the AW609.



Figure 38: Transcendental Model 1G.



Figure 39: Bell XV-3.



Figure 40: Bell XV-15.



Figure 41: V-22 Osprey.



Figure 42: Agusta Westland AW609.



Figure 43: Bell V-280 Valor.

3.1.6 Tilt-prop

Tilt-props are similar to the tiltrotors. The two prototypes in this category are the Curtiss-Wright X-100 and the Curtiss-Wright X-19 (Figure 44). The X-100 flew in 1959 and performed its only transition in 1960. It had two specifically designed propellers on the wingtips, which differed from the helicopter rotors mounted on the Bell XV-3. The roll was controlled by differential propeller pitch while the yaw and pitch were controlled with engine exhaust jets in the tail. The lift in cruise was generated by the wing and by some “radial force” generated by the propellers [45]. The work on the X-100 led to the development of the X-19, which flew in 1963. The X-19 had two wings, a forward and a rear wing, with two tiltable propellers each wing. A crash in 1965 destroyed the first of the two prototypes built and ended the program.



Figure 44: Curtiss-Wright X-19.

3.1.7 Tilt-duct

Tilt-ducts were like tiltrotors and tilt-props but used ducted fans instead. The Doak VZ-4 (Figure 45), also called Doak Model 16, flew in 1958 and was powered by a Lycoming T-53 turboshaft driving two 4 feet wide ducted fans mounted on the wingtips. This aircraft could transition from hover to 200 kts forward flight in less than twenty seconds. The pitch and yaw were controlled by jets in the tail powered by the engine exhaust, while the roll was controlled with variable inlet guide vanes. It suffered from a lack of control power, but it demonstrated the feasibility of the concept of the ducted fan. The deceleration phase was critical because the lip of the duct could stall if the fans were turned too quickly and because there was a large pitch up moment generated by the ducts that were acting as wings at high angle of attack. The program was ended in 1963 when the US Army announced that its VTOL requirements were met by the helicopter.

The Bell X-22 (Figure 46) was a tilt duct like the Doak VZ-4. It had two wings and four total ducts. It flew for the first time in 1966, and one of the two prototypes crashed that same year due to a failure of the hydraulics controlling a propeller. It was powered by four cross-linked turbines that were able to provide enough power to hover in case one turbine failed. The aircraft was controlled in hover with differential propeller pitch and actuating the elevons across the rear of the ducts. The second prototype performed hundreds of transitions and flew until 1988. The Nord 500 Cadet was a prototype built in 1966, which had two ducted fans on the wingtips. The roll was controlled with differential thrust, and guide vanes at the end of the ducts controlled the pitch and the yaw actuating collectively or differentially. It made static tests and a tethered hover in 1968, and it never flew again.



Figure 45: Doak VZ-4.



Figure 46: Bell X-22.

3.1.8 Tilt-wing

The tilt-wings rotate the entire wing, the engines and the propellers as a single piece. The Vertol 76 VZ-2 (Figure 47) was the first tilt-wing. It was powered by a Lycoming T-53 turbine in the fuselage driving the two three-bladed propellers on the wing. Pitch and yaw were controlled in hover with two ducted fans in the tail. It first flew in 1957 and performed the first transition in 1958. It continued to operate until 1965, making more than 450 flights and 34 complete transitions.

The Hiller X-18 (Figure 48) was a larger tilt-wing powered by two wing-mounted Allison T40 turboshafts with corotating propellers, the same powering the Convair XFY-1 Pogo and the Lockheed XFV-1. An additional turbojet was installed in the tail to provide pitch control in hover. The Hiller X-18 never achieved hover because the turboprops had an electric pitch control too slow to give an adequate response in hover. During the 20th flight test, it had a pitch control problem and entered a spin. The pilot managed to recover it before impact, but it was grounded halting tests.

The Ling-Temco-Vought (LTV) XC-142 (Figure 49) was a larger tilt-wing powered by four cross-linked turboshafts driving four four-bladed propellers. The roll was controlled with differential propeller thrust, the pitch with an 8-foot variable pitch three-blade tail propeller, and the yaw with the ailerons in the propeller slipstream. It first flew in 1964 and completed its first transition in 1965. Five aircraft were built, but four were damaged in hard landings due to mechanical failure to the gearboxes and shaft cross-links due to the deflection of the wing in flight. One crash was due to the collapse of the shaft powering the tail propeller resulting in three fatalities. The XC-142 suffered from excessive vibrations and noise, resulting in a high pilot workload.

The Canadair CL-84 (Figure 50) was a two-propeller tilt-wing. Two cross-linked Lycoming T-53 turboprops drove the two four-bladed propellers. Pitch was

controlled by two counter-rotating horizontal propellers in the tail, roll by differential propeller pitch, and yaw with ailerons. It flew for the first time in 1965 and kept flying until 1974. It was one of the most successful VTOL prototypes, but it was canceled because the end of the Vietnam war meant a significant reduction in military spending and because, as it was built in Canada, making it in an unfavorable position for the US military market. The design was successful because it was simple, and it provided considerable control power. The mechanical problems of the XC-142 were reduced because the cross-linking was between only two turboshafts instead of four. The massive propellers kept the whole wing in the propeller slipstream, protecting it from stalling. Its maximum speed was 520 km/h.

The horizontal tail of tilt wings is deflected at a high angle of attack when they are in hover and transition to avoid the effect of the wing downwash and to reduce aerodynamic interactions with the tail rotor.



Figure 47: Vertol 76 VZ-2.

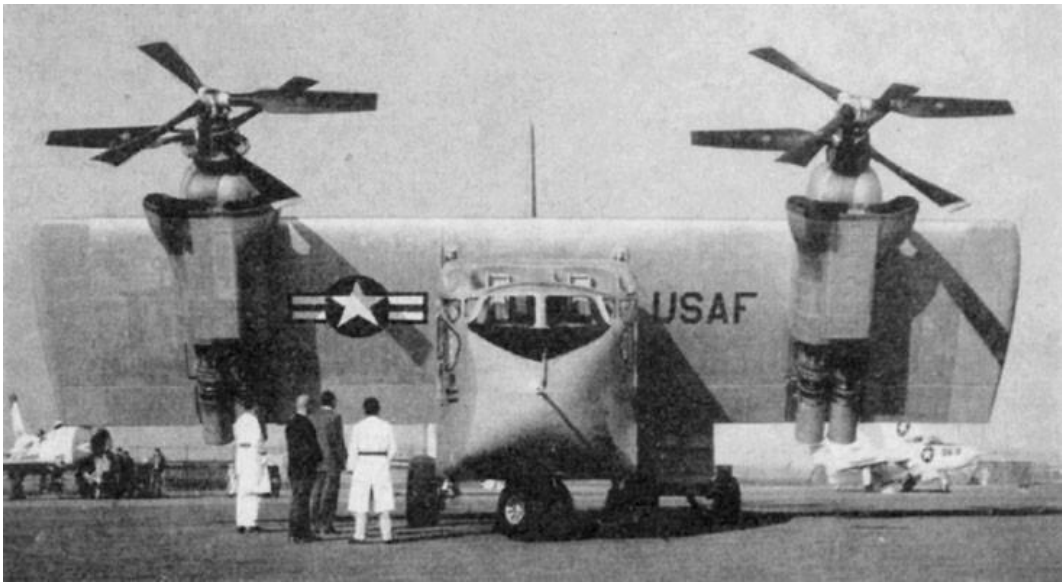


Figure 48: Hiller X-18.



Figure 49: Ling-Temco-Vought (LTV) XC-142.



Figure 50: Canadair CL-84.

3.1.9 Lift + cruise

Other VTOLs like the Short SC.1, the Dassault Balzac V, and the Mirage III V had an additional power plant for hover.

The Short SC.1 (Figure 51) was one of the predecessors of the Harrier. It was built in 1957 and was powered by four Rolls Royce RB108 lift engines in the fuselage and one RB 108 in the rear for the cruise. It completed the first transition in 1960. The fuel consumption of the lift engines was high, and their ignition procedure complicated. It crashed in 1963 due to a control malfunction killing the pilot. It was rebuilt and flew until 1967.

The Balzac is a modified Mirage III with eight RB 108 in the fuselage for takeoff. It flew in 1963 and crashed during one of the first transition attempts killing the pilot. It was rebuilt and crashed again in 1965, killing another pilot.

The Mirage III V (Figure 52) was an improvement on the Balzac with lift engines improved from the RB 108 to the RB 162. It completed the first transition in 1966, and that same year, it reached Mach 2.04, making it the fastest VTOL on record [46]. However, the lift engines reduced the payload and useful load fraction, making it impractical.



Figure 51: Short SC 1.



Figure 52: Mirage III V.

3.1.10 Lift + lift/cruise

The lift + lift/cruise VTOLs use one set of engines for lift only and another set of engines for both lift and cruise.

The Soviet Yak 38 (Figure 53) is one of these VTOLs, it vectored the thrust of the main engine and used two additional engines behind the cockpit for hover. It flew for the first time in 1971, and it remained in service until 1993. It was the Soviet Harrier, and more than 200 were built. The Yak-141 was to succeed to the Yak 38. Its first prototype flew in 1987, but the program was canceled after the collapse of the Soviet Union. It had two lift jets behind the cockpit, and the rear nozzle could be tilted for takeoff. While the Yak 38 had two rear nozzles on the sides of the tail like the rear nozzles of the Harrier, the Yak 141 had a single rear nozzle that could allow afterburning and supersonic speeds.

In the 1960s, German companies developed three main lift + lift/cruise VTOL prototypes. The EWR VJ 101 (Figure 54) first flew in 1963 and was powered by six Rolls Royce RB 145. Two were mounted in the fuselage behind the cockpit and acted as lift engines, and the other four were mounted in couples in wingtip pods that could tilt. Its fuselage was similar to the F-104's fuselage and was intended to be supersonic. The EWR VJ 101 flew until 1968, performing 24 hover flights and 14 complete transitions. It was the first VTOL to break the sound barrier, and it did so during a shallow dive. When they were tilted for hover, the exhaust of the nacelles was close to the ground, and they suffered from hot gas reingestion. Another problem was the erosion of the landing surface, which increased if using afterburners for takeoff. In 1964 one prototype crashed because a roll rate gyro was installed with reversed polarity.

The VFW VAK 191 (Figure 55) was developed as a replacement of the Fiat G91 and used two RB 162 lift engines and an RB 193 vectored thrust engine for lift and cruise. The RB 193 was a scaled-down version of the Rolls Royce Pegasus powering the Harrier and had a reduced frontal size, which reduced the drag. The downside of this solution was the dead weight in cruise of the two RB 162 and the lower thrust in cruise. Ninety-one flight tests were performed until 1975, but mass production never started because of political changes, which pushed to the reduction of military expenditures and the withdrawal of the Italian government from the program.

The Dornier Do31 (Figure 56) was a transport VTOL prototype. It was powered by two Rolls Royce Pegasus vectored thrust engines and eight RB 162 lift engines, four on each wingtip. It made its first hover flight in 1967 and flew until 1970, validating the concept. However, the lift engines' weight and drag reduced the payload and the performance compared to other contemporary conventional transport airplanes.



Figure 53: Yak 38.



Figure 54: EWR VJ 101.



VFW-FOKKER VAK 191B (PAUL NANN)

Figure 55: VFW VAK 191.



Figure 56: Dornier Do 31.

3.1.11 Ejector

Some VTOLs are called augmented power plant for hover because they use additional devices driven by the power plant to generate the vertical thrust. The Lockheed XV-4A (Figure 57) was one of these VTOLs. It was powered by two turbojets on the side of the fuselage. To hover, it turned the engine exhaust into a channel in the middle of the fuselage called augmentor (Figure 58), causing additional ambient air to accelerate through the channel and mix with the engine exhaust. The mixing with the ambient air reduced the temperature of the jet,

eliminating the possibility of erosion problems. The Hummingbird was designed to hover with the nose tilted up by twelve degrees. During the transition, the nose was leveled, and the horizontal component of the thrust accelerated the aircraft. At a specified speed, one of the engine exhausts was turned away from the augmentor and back to the rear, increasing the horizontal speed. When Hummingbird reached a second specified speed, the second engine efflux was diverted from the augmentor and back to its typical setting, and the augmentor doors were closed. The control in hover was provided by reaction jets in the nose, tail, and wingtips. The first flight was in 1962, and the first hover in 1963. The augmentor was expected to produce 40% more thrust than what was generated by the engine exhaust alone, but the tests on the prototypes showed results inferior to laboratory tests. The ambient air could not mix enough with the engine exhaust, producing ram drag [40]. This means that the force generated by the mixed air exiting the augmentor was reduced by the force pushing down the aircraft produced by the ambient air entering the augmentor. The engine exhaust was not mixing enough with the ambient air to accelerate it to sufficient speeds to produce the desired thrust. In 1964, the first prototype was destroyed in a fatal crash. Between 1966 and 1968, the second prototype was modified to the XV-4B standard substituting the augmentor with four lift engines. The XV-4B had a maximum vertical takeoff weight of 12600 lbs., much larger than the 7200 lbs. of the XV-4A. However, the XV-4B prototype crashed in a conventional flight test without ever making a hover.



Figure 57: Lockheed XV-4A Hummingbird in hover.

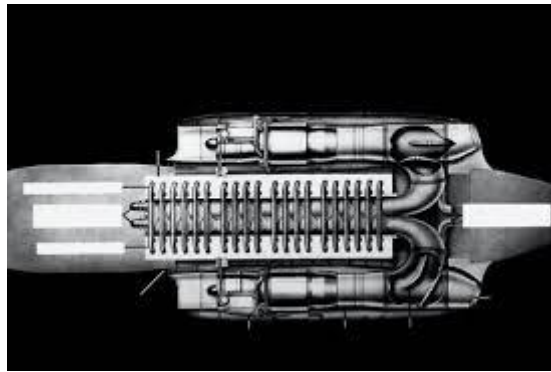


Figure 58: Augmentor system, view of the Hummingbird's fuselage from above.

Rockwell International's XFV-12A (Figure 59) used the augmentor concept to produce its vertical thrust. It was designed to reach Mach 2 and be able to take off and land vertically. Control in hover was provided by controlling differentially the ejector nozzles located in the wing and the canard. Ground testing started in 1977, and tethered tests began in 1978. The results showed less thrust augmentation than expected, and the program ended in 1981.



Figure 59: Rockwell International's XFV-12A.

3.1.12 Fan

Some VTOLs used the powerplant to drive additional fans for hover. A notable example is the F35, which first flew in 2006 and is now in service. For hover, it uses a fan situated behind the cockpit and orientates the engine nozzle downwards, like the Yak 141. The most notable fan VTOL of the golden era was the GE-Ryan XV-5A (Figure 60). The vertical thrust was provided by two five feet diameter fans in the wing. An additional smaller fan in the nose provided extra thrust and pitch control. The fans were driven the exhaust gasses of the engine acting on turbine blades situated on the periphery of the fans. They produced a total of 16000 lbs. thrust while the gross weight was only 12200 lbs. Roll was controlled by differential fan thrust and yaw orientating louvered vanes under the fans. These same vanes orientated the thrust to accelerate the aircraft during the transition. The first prototype flew from 1964 to 1965 when it crashed during a transition attempt when the pilot opened the fan vanes at high speed resulting in pitch down. The second prototype was damaged in 1966 when a fan ingested a horse collar sling for rescue missions, but it was rebuilt, and tests continued until 1971.

The Vanguard Omniplane (Figure 61) was the first fan VTOL. It was powered by a 265 hp Lycoming piston engine driving mechanically two six feet fans in the wing and a pusher propeller for cruise. Tethered tests started in 1959 but the program was discontinued after mechanical failures in 1962.



Figure 60: Ryan XV-5A.



Figure 61: Vanguard Omniplane.

3.1.13 Tip jet and compound helicopter

The remaining VTOLs have a rotor like helicopters. The McDonnell XV-1 (Figure 62) was powered by a piston engine driving a compressor that was providing compressed air to jets located on the tip of the rotor blades. It had a pusher propeller and a wing for forward flight and two small propellers on the tail for yaw in hover. It first flew in 1954, and in 1955 it was the first rotorcraft to reach 200 mph. The program was ended in 1957 because conventional helicopters improved their speed, its advantage over them was too small and the complexity too high, and the noise it produced was too high.

The Fairey Rotodyne (Figure 63) was another tip jet VTOL. It was designed to transport forty passengers, and it had a wing and two propellers for forward flight. Flight tests started in 1957, but the program ended in 1962 when Westland acquired Fairey due to the high noise level produced by the tip jets.

The final group is the compound helicopter, a conventional helicopter with a wing, and a propeller to cruise faster. Notable examples are the Lockheed AH-56 (Figure 64), the Kamov Ka-22 Vintokryl (Figure 65), and the Sikorsky–Boeing SB-1 Defiant (Figure 66). The first flew in 1967 and reached a maximum speed of 277 mph. The program was canceled in 1972 after defense cutbacks and the crash of a prototype. The Kamov Ka-22 was a large convertiplane that flew for the first time

in 1960. It had two rotors on the end of the wing directly over the engines, which were also connected to a propeller for forward flight. The power could be clutched between the two systems to perform the transition. It reached a maximum speed of 221 mph and set multiple altitude payload records. The program ended in 1964 after a crash. The Sikorsky–Boeing SB-1 Defiant is the new air assault compound helicopter designed by Sikorsky and Boeing for the Future Vertical Lift program. It flew for the first time in March 2019. Its coaxial main rotors and pusher propeller enables a maximum speed of 460 km/h and increased efficiency [47].



Figure 62: McDonnell XV-1.



Figure 63: Fairey Rotodyne.



Figure 64: Lockheed AH-64 Apache.



Figure 65: Kamov Ka-22 Vintokryl.



Figure 66: Sikorsky–Boeing SB-1 Defiant.

3.2 Electric VTOLs

After the description of VTOLs from the fifties and sixties, this section describes electric VTOLs designed and tested in the last years. The number of new designs and prototypes is growing exponentially. This chapter will present some of them outlining their characteristics.

The change in the propulsion system from piston engines or turboshafts to electric motors has driven a shift in the design of the VTOL. The most important aspect of electric propulsion is its scalability; small electric motors are as efficient as large ones. The efficiency of internal combustion engines and jets instead depends on the dimension. Larger ones are more efficient. The scalability of the electric motor enables the possibility of large disk actuator areas made by multiple propellers, which can be highly reliable thanks to the redundancy provided by various engines. Previously instead, a single motor driving a single rotor was the only choice for efficient hover.

These new eVTOLs efficient in hover are called wingless because they do not have a wing. eVTOLs with a wing are classified as lift + cruise if they have different power system for lift and cruise or vectored thrust if they use the same system changing its orientation. The last two categories are eHelos, helicopters powered electrically, and hoverbikes, very simple multirotors with a saddle.

3.2.1 Wingless

Wingless VTOLs are multirotors. They have a large disk actuator area which makes them efficient in hover, but they do not have a wing for an efficient cruise. The multiple propellers provide redundancy in case of failure of one of them, making the system reliable.

E-Hang and Volocopter produce the most famous eVTOLs in this class. E-Hang has built the 184 prototype with four couples of coaxial rotors and has now modified it to the 116 and the 216 (Figure 10), which have eight couples of coaxial rotors. The 116 can carry one passenger while the 216 can carry two. They both have sixteen propellers. The cruising speed is 100 km/h, and the maximum speed is 130 km/h. The payload of the 116 is 140 kg, and the payload of the 216 is 220 kg. The design is simple, very similar to a scaled-up multirotor drone, making it easy to pilot by a human and autonomously.

The German company Volocopter has built multiple prototypes called VoloDrone, VoloCity, VC200, and 2X (Figure 67). They have 18 small propellers distributed in a circle over the fuselage. The maximum speed is 110 km/h.



Figure 67: Volocopter VC200 and 2X.

The Australian company Alauda designed the Airspeeder (Figure 68) to create a new motorsport. The design is similar to the E-Hang 184 and the racing quadcopters, which have already established the drone racing sport.

Other wingless eVTOLs are the Alaka'i Technologies Skai, the Astro Aerospace Alta, and the Astro Aerospace Elroy.



Figure 68: Alauda Airspeeder prototype.

Yaw control of large multirotors is more complicated than that of simple small quadcopter drones. For the small ones, it is enough to increase the speed of the right

couple of propellers to make the drone turn. For the larger, manned multirotors, this is not enough; the vehicle is too big. To solve this problem, the lift propellers are placed at a small angle, which gives them the authority to control yaw. This angle can be seen in Figure 1, Figure 2, and Figure 10.

3.2.2 Lift plus Cruise

Lift + cruise eVTOLs are a mix between multirotors and conventional airplanes. Examples of lift + cruise eVTOLs are the Aurora Flight Sciences passenger aerial vehicle (Figure 11) and the Kitty Hawk Cora (Figure 2). They combine good hover efficiency and efficient cruise with a wing. They are easy to operate, and they are mechanically simple. Their main drawback is the substantial drag created by the lift propellers during the cruise.

Ascendance Flight technologies is a startup founded in 2018 by four former members of the E-Fan team from Airbus. Their design, the Atea prototype (Figure 69) is similar to the Ryan XV-5 Vertifan (Figure 60) with two lift fans in the wing and a third lift fan in the nose. A three-bladed propeller in the nose generates forward thrust. They are planning to use a hybrid powertrain.

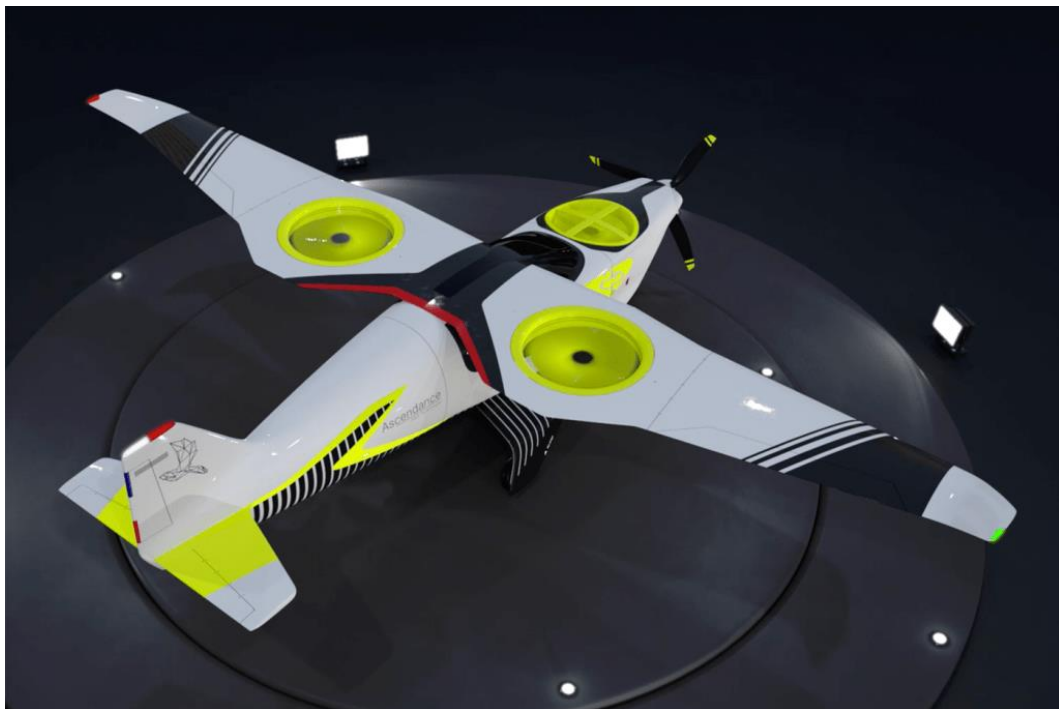


Figure 69: Ascendance Flight Technologies Atea prototype.

AutoflightX is a German startup founded in 2018, their V600 prototype (Figure 70) was presented to the public on the Aero airshow in Friedrichshafen in 2019. It is a scaled-up QuadPlane design with six (or eight as in their website's sketch) lift propellers and a pusher propeller for the cruise.



Figure 70: AutoflightX V600.

Elroy Air is developing a lift plus cruise hybrid electric cargo drone (Figure 71) able to carry 225 kg of cargo with a range of 500 km [48].



Figure 71: Elroy Air cargo drone.

Zuri is a Czech start-up designing a lift plus cruise hybrid-electric VTOL. Their design (Figure 72) looks similar to the Kitty Hawk Cora.



Figure 72: Zuri eVTOL design.

3.2.3 Vectored Thrust

Vectored thrust eVTOLs comprise a wide variety of eVTOLs. They try to solve the lift + cruise problem using the same propulsion system for hover and cruise, and they tilt it in various methods. The Joby Aviation S4 (Figure 7), the Kitty Hawk Heaviside (Figure 4), the Lilium Jet (Figure 9), the Aurora Flight Sciences LightningStrike (Figure 12), the Airbus A³ Vahana (Figure 13), and the NASA Greased Lightning tiltwing (Figure 14) have been presented in the introduction. The Rolls-Royce tilt-wing eVTOL will be presented in chapter 4 (Figure 97).

The Agusta Westland Project Zero (Figure 73) is one of the first eVTOL prototypes, having been revealed in 2013 [49] [50]. It has two large ducts in the wings that can tilt to provide thrust in forward flight.



Figure 73: Agusta Westland Project Puro.

The Mobi-one [51] [52] is a tilt-wing hybrid-electric VTOL design by ASX, Airspace Experience Technologies (Figure 74). The concept is similar to the XC-142.

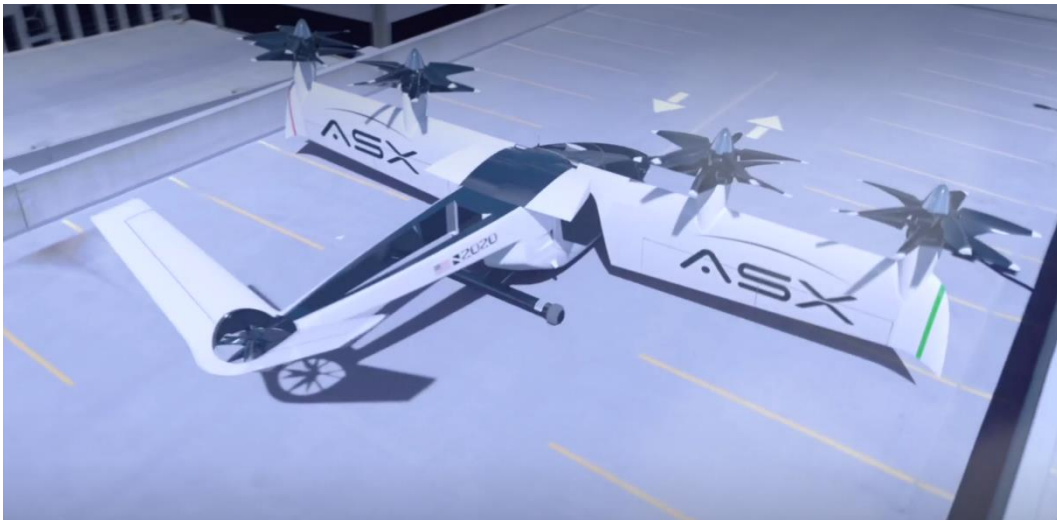


Figure 74: Mobi-one tilt-wing design.

Bell has leveraged his extensive experience with tilt ducts for its eVTOL design. The Bell Nexus (Figure 75) has four tilt-ducts like the X-22 (Figure 46).



Figure 75: Bell Nexus eVTOL.

Kyle Clark founded beta Technologies in Vermont, USA, to transport human organs. Their design (Figure 76) incorporates a wing and four couples of coaxial lift propellers able to tilt. There is little information about their actual design [53], only a YouTube video showing a test on their prototype [54].



Figure 76: Beta Technologies Alia prototype.

The aEro 2 (Figure 77) is the tilt-wing design by the Swiss startup Dufour Aerospace. It is either fully electric or hybrid-electric [55] [56], and it is similar to the CL-84 (Figure 50).



Figure 77: Dufour Aerospace aEro 2.

An interesting concept is the Opener Blackfly (Figure 78) [57]. It has a front and a rear wing with four propellers each. The wings are mounted at approximately 45° to the fuselage and do not tilt. During takeoff, the propellers lift the front of the vehicle first, and the propellers get oriented to provide only vertical thrust [58]. After liftoff, an increase of power to the rear propellers tilts the fuselage back to horizontal, performing a quick transition. It can carry a single passenger. It is not complex, and it is quick and nimble.



Figure 78: Opener Blackfly.

Kareem Aircraft has invested its tiltrotor knowledge in the design of the Butterfly [59] (Figure 79). It has opened a subsidiary called Overair to build it. Its four propellers design resembles the Curtiss-Wright X-19 (Figure 44).



Figure 79: Overair Butterfly.

3.2.4 Hoverbikes

Hoverbikes are small personal flying devices. The pilot sits on a saddle or stands, and the configuration is simple, wingless, and similar to a multicopter. Two of the most famous hoverbike prototypes are the Hoversurf Scorpion (Figure 80) and the Kitty Hawk Flyer (Figure 81). Other hoverbikes are the Jetson Aero Speeder, the Kalashnikov, and the Malloy Hoverbike.



Figure 80: Hoversurf Scorpion.



Figure 81: Kitty Hawk Flyer.

Hoversurf also has patented the Venturi engine [60] which is an electric ducted fan that has a second external duct that collects an additional flow driven by the internal flow of the electric ducted fan. This concept is like Hummingbird's augmentor (Figure 58). They intend to use this engine in their Formula eVTOL.

3.2.5 Electric Rotorcraft

Electric rotorcraft eVTOLs are conventional helicopters powered by electric motors. An example is the Aquinea Volta (Figure 82) [61].

The classic Robinson R44 has been converted to electric power by the company Tier One.



Figure 82: Aquinea Volta.

3.3 Configuration comparison

This section contains the material published in the article “Electric VTOL Configurations Comparison” [15] on the journal Aerospace. The computations performed have been modified, adding the figure of merit of the propellers and ducted fans for takeoff and landing. 70% has been chosen as a figure of merit for all the propellers and fans in this section. This value is in between helicopter rotor hover efficiency, which gets up to 80%, and the model propeller efficiency, which, as we have computed in section 2.3.1, is around 50%. 70% is also the value of the figure of merit of the rotor tested at Nasa by Bagai and Leishman [35], whose theoretical and measured values are plotted in Figure 22.

Wingless, lift+cruise and thrust vectored eVTOLs have been compared evaluating disk loading, total hover time, cruise speed, practical range, and flight time, and their performances for three reference missions. The reference missions are:

- 7 km urban mission
- 30 km extra-urban mission
- 100 km long-distance mission

The time and energy required to perform each mission have been computed. For each configuration, a representative prototype has been selected. The E-Hang 184 has been selected to represent the wingless configuration, the Kitty Hawk Cora represents the lift+cruise, and the Lilium Jet represents the vectored thrust.

3.3.1 Wingless: E-Hang 164

E-Hang 184 data available on the internet [62] is collected in Table 11 and Figure 83.

Table 11: E-Hang 184 specifications from E-Hang’s website.

| | |
|----------------------|------------|
| Maximum total power | 152 kW |
| Number of motors | 8 |
| Total battery energy | 14.4 kWh |
| Propeller diameter | 1.6 m |
| Net weight | 260 kg |
| Total flight time | 25 minutes |
| Rated payload weight | 100 kg |
| Average flight speed | 100 km/h |

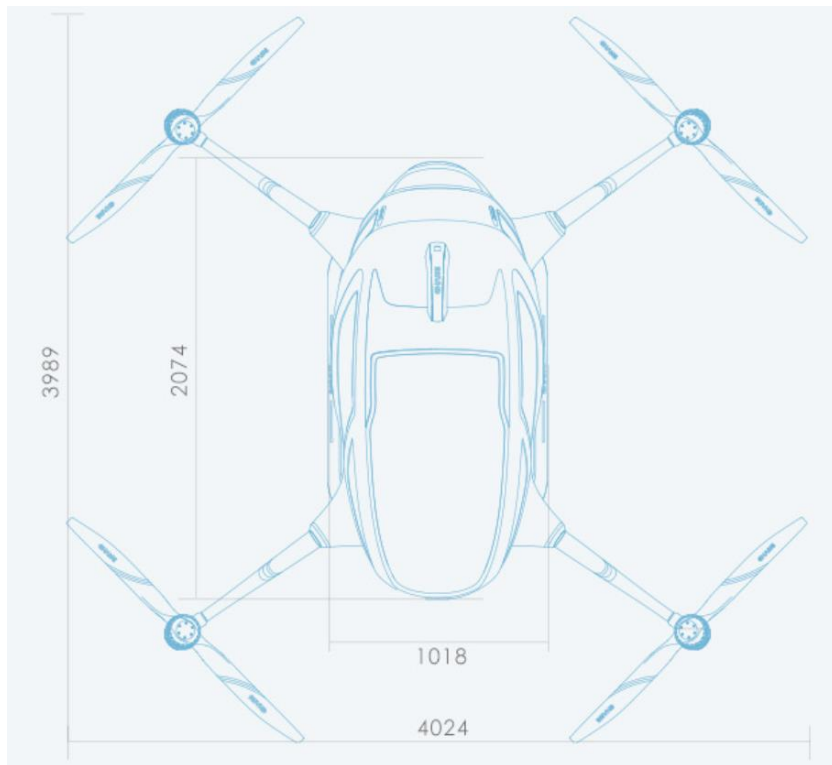


Figure 83: E-Hang 184 specs and dimensions, from E-Hang’s website [62]. Dimensions in the top view are in millimeters.

Table 12: E-Hang 184 data computed with Figure 83 and Table 11 data.

| Geometry | | |
|---------------------------------------|----------------------|--------------------|
| Propeller area | 2.01 m ² | <i>Computed</i> |
| Total disk actuator area | 8.04 m ² | <i>Computed</i> |
| Battery | | |
| Specific energy | 157 Wh/kg | <i>Assumed</i> |
| Specific power | 735 W/kg | <i>Assumed</i> |
| Max power | 67 kW | <i>Computed</i> |
| Mass balance | | |
| Battery mass | 92 kg | <i>Computed</i> |
| Empty weight | 168 kg | <i>Computed</i> |
| Payload weight | 100 kg | <i>E-Hang data</i> |
| Hover performances | | |
| Average power consumption | 34.6 kW | <i>Computed</i> |
| Rotor figure of merit | 70% | <i>Assumed</i> |
| Power required to hover | 60.1 kW | <i>Computed</i> |
| Energy required for 1 minute of hover | 1.0 kWh | <i>Computed</i> |
| Total hover time | 14.4 minutes | <i>Computed</i> |
| Disk loading | 440 N/m ² | <i>Computed</i> |

From the available data, the disk actuator area, the max battery power, the mass balance, and the hover performances have been computed. The results are listed in Table 12.

The E-Hang website specifies a total battery energy of 14.4 kWh. This value has been used to estimate the battery mass, assuming a specific energy of 157 Wh/kg. This is the specific energy of the Tesla Model S battery pack, the same assumption made in chapter 2. This assumption has been explained and supported in chapter 2, and chapter 4 adds more information about batteries and power sources. The resulting battery mass is 92 kg. Assuming the specific power of the Tesla Model, 735 W/kg, the maximum power provided by the battery is 67 kW.

Using the total flight time provided by the E-Hang website and the overall energy available, the average power consumption has been computed, and it is 34.6 kW. The power required to hover has been calculated using the disk actuator theory modified for coaxial rotors, equation (20):

$$P = k_{int} \frac{T^{\frac{3}{2}}}{2\sqrt{\rho A}}$$

The resulting power required to hover, considering a figure of merit of 70%, is 60.1 kW. This value is consistent with the value of average power consumption because, for multirotors as for helicopters, the power required for the cruise is lower than the power required to hover. The airflow on the vehicle generates some lift and reduces the induced drag produced by the rotating blades. Moreover, as shown in [63], the reduction in power required from hover to moderate forward flight is more marked in coaxial rotors than single rotors.

Dividing the energy available by the power required to hover, a total hover time of 14.4 minutes is found.

The E-Hang coaxial rotors have the dual advantage of providing more thrust for the same disk actuator area and being redundant in the case one engine of the couple fails. To ensure redundancy, when one engine fails, the remaining engine and propeller of the coaxial couple must provide the entire thrust provided earlier by the couple. The thrust required by each motor couple is given by the total weight divided by four, the number of coaxial rotor couples. The total weight from table 11 is 360 kg, consisting of 260 net weight and 100 kg of payload. To find the thrust required, the total weight must be multiplied by a margin, which ensures a positive thrust to weight ratio. The value considered is 1.1. The rotor figure of merit is 70%. Applying the formula for coaxial rotors, equation (20), and considering the rotor figure of merit, the power required by the couple found is 17.3 kW. For the contingency scenario, the thrust is provided entirely by a single motor, and the standard disk actuator theory equation (19) is employed.

$$P = \sqrt{\frac{T^3}{2\rho A}}$$

The power required found is 19.5 kW. Both these values are consistent with the specified maximum motor power, which is 19 kW. This last value has been found dividing the maximum power, 152 kW, specified in table 11, by the number of motors, eight. The value found, 19.5 is slightly larger than the maximum motor power. This might mean that the actual figure of merit of the E-Hang rotors is higher, or that the actual thrust to weight ratio margin is smaller. Anyhow, with the 116 and the 216, E-Hang has increased the disk actuator area, improving the hover performances.

3.3.2 Lift plus Cruise: Kitty Hawk Cora

Figure 84 shows the geometry of the Kitty Hawk Cora used as a reference for the lift + cruise configuration. Table 13 lists Cora's data found on the internet [64], and estimated from Figure 84.

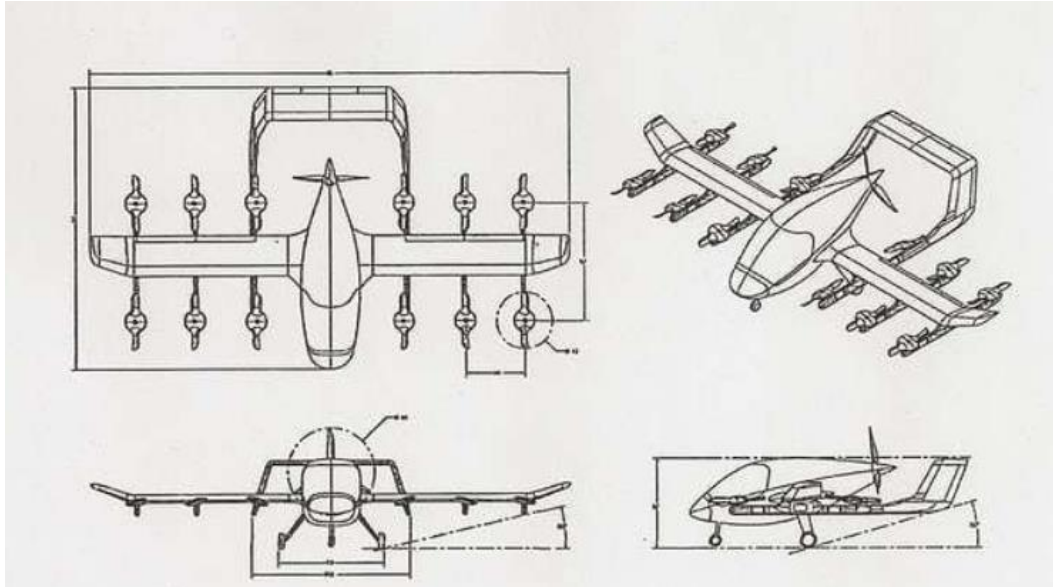


Figure 84: Kitty Hawk Cora geometry.

Table 13: Kitty Hawk Cora specifications from Kitty Hawk's website.

| | | |
|------------------------------------|------------|--------------|
| Wingspan | 11 m | Website data |
| Wing chord | 1 m | Estimated |
| Wing surface | 10 m^2 | Website data |
| Number of lift propellers | 12 | |
| Lift propeller diameter (external) | 1.3 m | Estimated |
| Lift propeller diameter (hub) | 0.5 m | Estimated |
| Cruise propeller diameter | 2 m | Estimated |
| Range | 100 km | Website data |
| Flight time (with 10 min reserve) | 19 minutes | Website data |
| Speed | 180 km/h | Website data |
| Passenger cargo capacity | 181 kg | Website data |
| Rear landing gear – tail angle | 15.9° | Estimated |
| Fuselage – wing angle | 12.4° | Estimated |

With the available data, the propeller area has been computed, and it is presented in Table 14. The external diameter of the lift fans is 1.3 m, its area is 1.3 m^2 . The size of the hub of the propeller hosting the motor is not negligible, and it has been computed and subtracted from the computation of the total disk actuator area. The diameter of the internal hub is 0.5 m, and its area is 0.2 m^2 . Considering all the 12 lift propellers, the total disk actuator area is 13.6 m^2 .

Table 14: Kitty Hawk Cora propeller area.

| | | |
|---|---------------------|-----------------|
| Propeller area (external, single propeller) | 1.3 m ² | <i>Computed</i> |
| Propeller area (internal, single propeller) | 0.2 m ² | <i>Computed</i> |
| Circular crown area (single propeller) | 1.1 m ² | <i>Computed</i> |
| Total disk actuator area | 13.6 m ² | <i>Computed</i> |

The total mass of the Kitty Hawk Cora specified in the eVTOL News article describing it [65] is 1224 kg. With this value, considering a figure of merit of 70%, and the disk actuator theory (equation 19), the minimum power required to hover has been computed. The minimum power required to hover found is 325 kW. The battery specific energy and specific power assumed are again the values of the Tesla Model S battery pack [26]. The minimum battery mass required to produce 325 kW of power at the assumed specific power is 443 kg. This value was the lower boundary to estimating the battery mass on board of the Cora. The final assumed battery mass is 450 kg, which corresponds to 37% of the total mass. The hover computations have been performed assuming an air density of $\rho = 1.225 \text{ kg/m}^3$ and a gravity acceleration of $g = 9.8 \text{ m/s}^2$. The values discussed are presented in table 15.

Table 15: Kitty Hawk Cora mass and battery data.

| | | |
|---------------------------------|-----------|--------------------------|
| Total mass | 1224 kg | <i>Website data [66]</i> |
| Power required to hover | 325 kW | <i>Computed</i> |
| Battery energy specific density | 157 Wh/kg | <i>Assumed</i> |
| Battery power density | 735 W/kg | <i>Assumed</i> |
| Minimum battery mass | 443 kg | <i>Computed</i> |
| Batterymass | 450 kg | <i>Assumed</i> |
| Total battery energy | 71 kWh | <i>Computed</i> |
| Battery-mass ratio | 33% | <i>Computed</i> |

Table 16 lists Cora's hover performances. The energy required for a minute of hover is 5.4 kWh and the total hover time is 13.0 minutes. The disk loading is 550 N/m². The Cora's hover performances are inferior to the E-Hang 184 hover performances. The Cora requires over five times the energy for a minute of hover, its disk loading is double, and the total hover time is lower. Cora, however, can carry four passengers, so the energy required to hover for each passenger is just a bit higher than that of the 184.

Table 16: Kitty Hawk Cora hover performances.

| | | |
|------------------------------|----------------------|-----------------|
| Figure of merit | 70% | <i>Assumed</i> |
| Energy for 1 minute of hover | 5.4 kWh | <i>Computed</i> |
| Total hover time | 13.0 minutes | <i>Computed</i> |
| Disk loading | 880 N/m ² | <i>Computed</i> |

To compute Cora's cruise performances, an aerodynamic study has been carried out. The drag polar of the vehicle has been estimated using the lifting line

theory to compute the lift generated by the wing and using empirical formulas to evaluate the drag generated by the vehicle components.

The airfoil NLF(1)-0115 [67] [68] has been assumed, and its lift and drag coefficients have been computed, using the Xfoil software [69], for a wide range of angles of attack. The lift slope coefficient found is 5.34 rad^{-1} and the zero-lift angle is -3.26° . The aerodynamic drag of the wing and of the horizontal tail are computed integrating the airfoil section contributions. The airfoil used for the tail is the NACA 0012. The drag generated by the other aircraft components is estimated with empirical formulas and the data listed in Table 17.

Table 17: Kitty Hawk Cora geometry data used to compute the drag.

| | | |
|--------------------------|----------------------|------------------|
| Fuselage | | |
| Length | 4.8 m | <i>Estimated</i> |
| Diameter | 1.5 m | <i>Estimated</i> |
| Wet surface | 13 m ² | <i>Computed</i> |
| Horizontal tail | | |
| Surface | 2 m ² | <i>Estimated</i> |
| Thickness to chord ratio | 0.12 | <i>Assumed</i> |
| Chord | 0.75 m | <i>Estimated</i> |
| Vertical tail | | |
| Sweep | 10° | <i>Estimated</i> |
| Thickness to chord ratio | 0.12 | <i>Assumed</i> |
| Height | 1 m | <i>Estimated</i> |
| Chord | 0.75 m | <i>Estimated</i> |
| Wet surface | 1.5 m ² | <i>Computed</i> |
| Number of vertical tails | 2 | |
| Pylons | | |
| Length | 3.5 m | <i>Estimated</i> |
| Width | 0.16 m | <i>Estimated</i> |
| Height | 0.36 m | <i>Estimated</i> |
| Wet surface | 3.76 m ² | <i>Computed</i> |
| Number of pylons | 6 | |
| Propellers | | |
| Length | 1.3 m | <i>Estimated</i> |
| Diameter | 0.3 m | <i>Estimated</i> |
| Wet surface | 0.8 m ² | <i>Computed</i> |
| Number | 12 | |
| Landing gear | | |
| Tire width | 0.15 m | <i>Estimated</i> |
| Tire height | 0.3 m | <i>Estimated</i> |
| Surface | 0.045 m ² | <i>Computed</i> |

The drag of the fuselage is computed using [70]:

$$C_{D0} = \sum C_f FQ [S_{wet}/S_{ref}] \quad (54)$$

where C_f is given, for turbulent flows, by:

$$C_f = \frac{0.455}{(\log Re_c)^{2.58} (1 + 0.144M^2)^{0.65}} \quad (55)$$

And, for laminar flows, by:

$$C_f = \frac{1.328}{\sqrt{Re_c}} \quad (56)$$

F is the form factor:

$$F = 1 + 2.2 \left(\frac{d}{l}\right)^{1.5} - 0.9 \left(\frac{d}{l}\right)^3 \quad (57)$$

Q is the interference factor set at 1. The flow is assumed to be 20% laminar and 80% turbulent. The same procedure has been followed for the vertical tail, computing the form factor, F , with the following equation:

$$F = (F^* - 1)\cos^2\Delta_{0.5c} + 1 \quad (58)$$

where $F^* = 1 + 3.52(t/c)$ and $\Delta_{0.5c}$ is the sweep angle at 50% of the chord. For the vertical tail, the interference factor, Q , is set at 1.2.

The drag of the pylons supporting the vertical lift propellers and the drag of the vertical lift propellers has been computed as the base drag of a 3D body [71] (p. 3-19) computing the base drag coefficient and then scaling it to the reference surface. The base drag coefficient is:

$$C_{DB} = \frac{0.029}{\sqrt{C_f}} \quad (59)$$

it is scaled to the reference surface, corresponding to the wing surface, with the following formula:

$$C_{DB0} = \frac{S_{front}}{S_{ref}} C_{DB} \quad (60)$$

Equations (59) and (60) have been applied for both the pylons supporting the vertical lift propellers and for the vertical lift propellers using their different geometries and different friction coefficients. The drag of the landing gear is computed, supposing a C_{d0} of 0.25, as suggested in [71] and scaling it from the wheel surface to the reference surface. The interference drag between wing and fuselage has been added using the following equation [71]:

$$C_D = \left(0.8 \left(\frac{t}{c}\right)^3 - 0.0003\right) \frac{c^2}{S_{ref}} \quad (61)$$

Computing the lift and drag of the Cora for various angles of attack, various corresponding lift and drag coefficients are found. The drag polar is then computed performing a linear regression on the C_L^2 and C_D couples. The resulting quadratic drag polar is:

$$C_D = 0.0438 + 0.0294 \cdot C_L^2 \quad (62)$$

The speed of maximum L/D and the maximum L/D are given by [72]:

$$V_{maxL/D} = \sqrt{\frac{2}{\rho_\infty} \sqrt{\frac{k}{C_{D0}} \frac{W}{S}}} \quad (63)$$

$$L/D_{max} = \sqrt{\frac{C_{D0}}{k}} \quad (64)$$

where C_{D0} and k are the parameters of the drag polar. This gives a speed of maximum L/D of 145 km/h and a maximum L/D of 13.9. The theoretical range,

computed with equation (14), is 200 km. This approximation is not enough to evaluate the real-life performance of the vehicle. In real life, the Cora will fly at speeds higher than the speed of maximum L/D to save time and complete more missions. In the following computations, we assumed a cruise speed of 180 km/h as specified online [66]. The range equation considers all the energy of the battery used for the cruise. In real life, this is not the case. A battery should not be completely discharged because this would reduce its lifetime [23]. The depth of discharge limit is set at 70%, giving the right amount of energy and preserving the lifetime of the battery. This means that the minimum state of charge is 30%. Finger [73], for a similar application, used two parameters. He considers a degradation to 80% of the battery energy at the end-of-life and an 80% discharge protection which is just another name for the maximum depth of discharge we used. Thus, he is effectively using 64% of the nominal energy of the battery.

15% of the battery energy is allocated for takeoff, the two transitions, and landing. This amount of energy corresponds roughly to two minutes of hover. The power required for the cruise is:

$$P_{req} = \frac{D \cdot v}{\eta} \quad (65)$$

Where D is the aerodynamic drag, $D = \frac{1}{2} \rho_{\infty} S v^2 C_D$, v is the flight speed and η is the total efficiency of the motor, power electronics, and propeller, which has been assumed 75%. The new range found after the computations is 111 km, and the flight time is 37 minutes. These results are in accordance with the performances specified of 100 km range, and 19 minutes flight time plus 10 minutes reserves (Table 13). The difference in the results might be due to one of the many assumptions made. One of the most probable causes might be the sizing of the battery starting from the specific power of the Model S. As very high power is required for takeoff, the Cora might have a higher specific power battery. This would mean a lower total battery mass, and consequently lower range and endurance.

The angle of attack in cruise is 8 degrees. This seems reasonable because, as seen in the drawings, the angle between the wing and the fuselage is 12 degrees. This feature allows a comfortable cruise at high angles of attack that reduces the required wing surface reducing also the aerodynamic drag of the wing. Flight at high angles of attack with low induced drag is possible because Cora has a very high aspect ratio wing. The angle between the wing and the fuselage is also beneficial because turning on the VTOL propellers in flight produces a thrust which has a component opposed to the flight direction, allowing a smooth deceleration and transition between cruise and vertical landing.

3.3.3 Vectored thrust: Lilium Jet

Figure 85 shows the geometry of the two-seat Lilium jet, which represents the vectored thrust category. This image was captured from the video of the first flight of this prototype in April 2017 [74]. Table 18 collects the geometric dimensions estimated from Figure 85.



Figure 85: Lilium jet geometry.

Table 18: Lilium Jet geometry.

| | | |
|-------------------------|--------|------------------|
| Fuselage width | 1.4 m | <i>Estimated</i> |
| Fuselage length | 3.6 m | <i>Estimated</i> |
| Wingspan | 6 m | <i>Estimated</i> |
| Root chord | 0.78 m | <i>Estimated</i> |
| Tip chord | 0.42 m | <i>Estimated</i> |
| Man lying on the tarmac | 1.52 m | <i>Estimated</i> |
| Suitcase | 0.46 m | <i>Estimated</i> |
| Fans diameter | 0.15 m | <i>Estimated</i> |
| Number of fans | 36 | |

In Table 18, there are also the dimensions of the man lying on the tarmac and of the suitcase. They help to crosscheck the validity of the other measures that have been estimated.

Table 19: Lilium Jet mass and battery data.

| | | |
|---------------------------------|-----------|---------------------|
| Total mass | 490 kg | <i>Assumed</i> |
| Power required to hover | 268 kW | <i>Computed</i> |
| Battery energy specific density | 157 Wh/kg | <i>Assumed</i> [26] |
| Battery power density | 735 W/kg | <i>Assumed</i> [26] |
| Battery mass | 240 kg | <i>Computed</i> |
| Total battery energy | 38 kWh | <i>Computed</i> |
| Battery-mass ratio | 49% | <i>Computed</i> |

The total mass is assumed 490 kg. This value was estimated for the article [15] considering the maximum payload of two people and the maximum takeoff weight

of the ultralight aircraft category in Europe (450 + 40) [75] [76]. In February 2020, Wikipedia is specifying an empty weight of 440 kg and a maximum takeoff weight of 640 [77]. This new weight is in accordance with the one previously assumed, and 490 kg has been kept for the computations. The battery mass has been estimated 240 kg, the battery-mass ratio is then 49%. These results are collected in Table 19.

The hover performances have been computed using the disk actuator theory modified for ducted fans (21) [34]. The power required to hover is:

$$P = \sqrt{\frac{(T/T_i)^3}{2\rho A}}$$

where $T_i = 1.26$ is the thrust increase for ducted fans, T is the thrust required or the weight of the vehicle, and A is the disk actuator area of the vertical thrust system. The sea-level air density $\rho = 1.225 \text{ kg/m}^3$ and gravity acceleration $g = 9.8 \text{ m/s}^2$ have been used. The fans figure of merit considered is 70%. The results are listed in Table 20. The power required found is 268 kW, and the maximum power available with 240 kg of batteries and a specific power of 735 W/kg is 176 kW. This means that, with the assumptions made, the Tesla batteries considered are not enough to power the Lilium jet. It requires batteries with a higher specific power. The minimum specific power is 1116 W/kg.

Moreover, the performance of Schuebeler's [78] 15-cm EDF show approximately a 10 kW power consumption for 15 kg thrust. With this data the power required to hover becomes 360 kW Which corresponds to a figure of merit of 50% which is in accordance with the results of the tests on the 70-mm EDF presented in chapter 3.

Table 20: Lilium Jet hover performances

| | |
|------------------------------|-----------------------|
| Figure of merit | 70% |
| Energy for 1 minute of hover | 4.46 kWh |
| Total hover time | 8.4 minutes |
| Disk loading | 7500 N/m ² |

The cruise performances have been computed following the same procedures as for the Cora. Only the resistance of the fuselage and the fans had to be added to the lift and drag computed for the wing with the Prandtl's lifting line theory. The drag polar found is:

$$C_D = 0.0163 + 0.058 \cdot C_L^2 \quad (66)$$

The speed of maximum L/D found with equation (63) is 230 km/h, and the maximum L/D computed with equation (64) is 16.3. The theoretical range, computed with equation (14) [16], is 380 km. The practical range has been computed following the same procedure followed for the Cora. The depth of discharge is limited to 70%. Takeoff and landing account for 15% of the battery energy, corresponding to 1.26 minutes of hover. The remaining 55% of battery energy is dedicated to cruise. The flight speed is 250 km/h. The resulting range is 186 km, with a 44 minutes flight time. The power required for the cruise found is 28 kW, and it looks quite small. The 2-seat Lilium jet is small compared to a general

aviation aircraft, and we could have neglected some sources of drag. For instance, we considered a retractable landing gear, and we didn't add the drag of an external landing gear. The prototype considered is very compact. The width of the fuselage is only 1.4 meter, while most cars are around 1.8 meters wide, and the wing surface is only 3.6 m^2 compared to the 16 m^2 of the Cessna 172. For an additional comparison, the power required for the Cessna 172 to fly at 250 km/h, found in section 2.1.2, is approximately 110 kW (Figure 16 shows the power per passenger, the Cessna 172 can carry four passengers including the pilot).

Lilium flew the 5-seater version of its eVTOL for the first time in May 2019 (Figure 86). Estimating its performance with the same procedures, we find a wingspan of 12 meters, 0.28 m fans diameter, 1700 kg total mass, and 900 kg battery mass. The disk loading of this vehicle is the same as the 2-seater jet, the practical range with 70% depth of discharge, 15% for takeoff and landing, and a cruise speed of 280 km/h is 228 km. The total flight time is 49 minutes. However, it seems that our cruise power required is lower than the one found on the internet, [77].



Figure 86: Lilium Jet 5-seater geometry.

3.3.4 Reference mission performances

The time and energy required by the three eVTOLs to perform the three reference missions have been computed. Each mission consists of:

- 15 seconds of takeoff at hover power;
- acceleration at 2 m/s^2 from zero forward speed to cruise speed at hover power;
- cruise flight;
- deceleration at -2 m/s^2 from cruise speed to zero forward speed at hover power;

- 15 seconds of landing at hover power.
The results are presented in tables 21 to 25.

Table 21: Data used in the computations for the reference missions performances.

| | E-Hang 184 | Kitty Hawk Cora | Lilium |
|---------------------------|------------|-----------------|----------|
| Cruise power | 34.6 kW | 63 kW | 28 kW |
| Cruise speed | 100 km/h | 180 km/h | 252 km/h |
| Takeoff and landing power | 60.1 kW | 325 kW | 268 kW |
| Total battery energy | 14.4 kWh | 71 kWh | 38 kWh |

Table 22: Takeoff, landing, acceleration, and deceleration.

| | E-Hang 184 | Cora | Lilium |
|---|------------|-------------|-------------|
| Takeoff and landing time | 30 s | 30 s | 30 s |
| Takeoff and landing energy | 0.5 kWh | 2.7 kWh | 2.2 kWh |
| Acceleration / deceleration | 2 m/s^2 | 2 m/s^2 | 2 m/s^2 |
| Acceleration time | 14 s | 25 s | 35 s |
| Acceleration energy | 0.23 kWh | 2.26 kWh | 2.6 kWh |
| Acceleration / deceleration distance | 193 m | 625 m | 1225 m |
| Deceleration time | 14 s | 25 s | 35 s |
| Deceleration energy | 0.23 kWh | 2.26 kWh | 2.6 kWh |
| Total time for takeoff, landing, acceleration, and deceleration | 1 minute | 1.3 minutes | 1.7 minutes |
| Total energy for takeoff, landing, acceleration, and deceleration | 1 kWh | 7.2 kWh | 7.4 kWh |

Table 23: Mission 1: 7 km urban mission.

| | E-Hang 184 | Kitty Hawk Cora | Lilium |
|-----------------|-------------|-----------------|-------------|
| Cruise distance | 6.6 km | 5.8 km | 4.6 km |
| Cruise time | 3.9 minutes | 2.0 minutes | 1.1 minutes |
| Cruise energy | 2.3 kWh | 2.0 kWh | 0.5 kWh |
| Total time | 4.9 minutes | 3.3 minutes | 2.8 minutes |
| Total energy | 3.3 kWh | 9.3 kWh | 7.9 kWh |

Table 24: Mission 2: 30 km extra-urban mission.

| | E-Hang 184 | Kitty Hawk Cora | Lilium |
|-----------------|--------------|-----------------|-------------|
| Cruise distance | 29.6 km | 28.8 km | 27.6 km |
| Cruise time | 17.7 minutes | 9.6 minutes | 6.6 minutes |
| Cruise energy | 10.2 kWh | 10.1 kWh | 3.1 kWh |
| Total time | 18.7 minutes | 10.9 minutes | 8.2 minutes |
| Total energy | 11.2 kWh | 17.3 kWh | 10.5 kWh |

Table 25: Mission 3; 100 km long-range mission.

| | E-Hang 184 | Kitty Hawk Cora | Lilium |
|-----------------|------------|-----------------|--------------|
| Cruise distance | | 98.8 km | 97.6 km |
| Cruise time | | 33.0 minutes | 23.2 minutes |
| Cruise energy | | 34.6 kWh | 10.9 kWh |
| Total time | | 34.3 minutes | 24.9 minutes |
| Total energy | | 41.9 kWh | 18.3 kWh |

The three configurations examined have been compared. Their hover and cruise flight parameters are presented in Table 26, and their performances for the three reference missions are presented in Table 27, Figure 87, and Figure 88.

Table 26: Performances comparison.

| | E-Hang 184 | Kitty Hawk Cora | Lilium |
|----------------------------------|------------|-----------------|--------|
| Disk loading (N/m ²) | 440 | 880 | 7500 |
| Total hover time (minutes) | 14.4 | 13.0 | 8.4 |
| Cruise speed (km/h) | 100 | 180 | 252 |
| Practical range (km) | 42 | 111 | 186 |
| Flight time (minutes) | 25 | 37 | 44 |

Table 27: Summary of the energy and time required for the three reference missions.

| | E-Hang 184 | Kitty Hawk Cora | Lilium |
|----------------------------------|--------------|-----------------|--------------|
| 7 km urban mission time | 4.9 minutes | 3.3 minutes | 2.8 minutes |
| 7 km urban mission energy | 3.3 kWh | 9.3 kWh | 7.9 kWh |
| 30 km extra-urban mission time | 18.7 minutes | 10.9 minutes | 8.2 minutes |
| 30 km extra-urban mission energy | 11.2 kWh | 17.3 kWh | 10.5 kWh |
| 100 km long-range mission time | | 34.3 minutes | 24.9 minutes |
| 100 km long-range mission energy | | 41.9 kWh | 18.3 kWh |

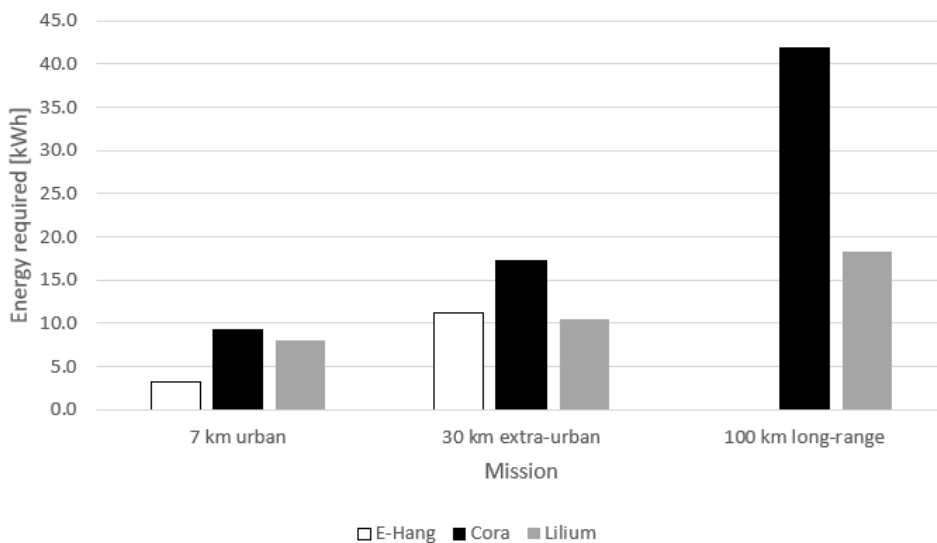


Figure 87: Energy required for the three reference missions.

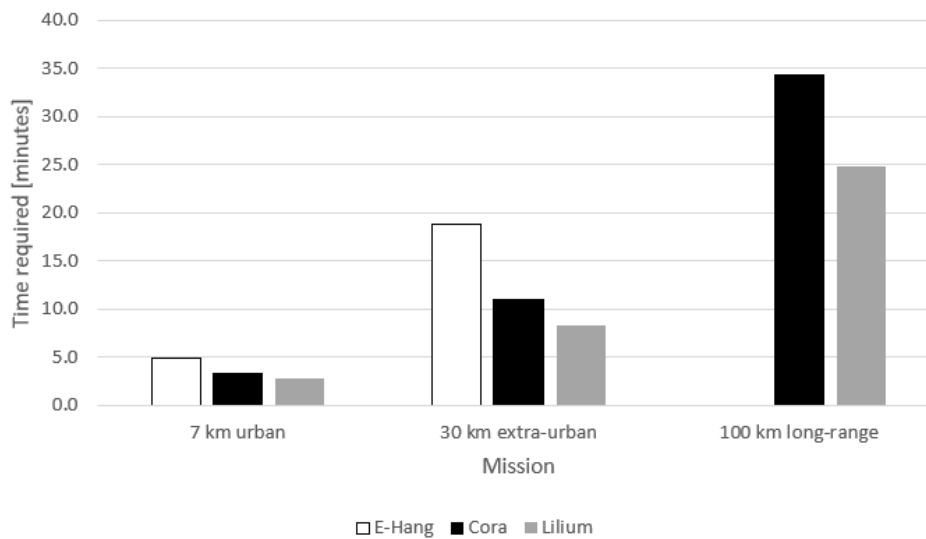


Figure 88: Time required for the three reference missions.

Table 16 shows that the multirotor configuration represented by the E-Hang 184 is the best suited to hover flight while Lilium is the best suited to cruise flight. The lift + cruise Cora is a compromise. It has less range and flight speed than Lilium but good hover performances comparable to the wingless multirotor configuration.

The 7 km urban mission is completed in 4.9 minutes by E-Hang, 3.3 minutes by Cora, and 2.8 minutes by Lilium. E-Hang requires 3.3 kWh, Cora 9.3 kWh, Lilium 7.9 kWh. The 30 km extra-urban mission is completed in 18.7 minutes by E-Hang, 10.9 minutes by Cora, and 8.2 minutes by Lilium. E-Hang requires 11.2 kWh, Cora 17.3 kWh, Lilium 10.5 kWh. The 100 km long-range mission cannot be completed by E-Hang and is almost Cora’s computed maximum range. It is completed in 34.3 minutes by Cora and 24.9 minutes by Lilium. Cora requires 41.9 kWh, Lilium 18.3.

The urban mission comparison shows that multirotors require less energy for short-range missions. In the extra-urban mission, the cruise phase is as crucial as the hover phase, and the energy required by the three configurations is comparable. In the long-range mission, cruise efficiency is more important. E-Hang’s range is insufficient to complete it. Cora’s parasitic drag caused by the pylons and vertical thrust propellers increases its power required in cruise. Its cruise speed is less than Lilium’s, and the energy required is more.

Lilium’s hover is so power demanding that it requires batteries with higher specific power than the Tesla batteries considered for the computations. Higher demands on the batteries and the power electronics balance this configuration aerodynamic advantages.

More practical reasons might influence which eVTOL configuration will be adopted more rapidly in the future. The multirotor configuration seems to be closer to the market and less complex than the lift + cruise and the electric jet. However, the range advantage of the latter two enables missions impossible to the multirotor configuration.

3.4 Chapter conclusion

This chapter explored the most famous eVTOL and classical VTOL configurations. The first part is dedicated to the VTOLs of the fifties and sixties, the second to the present day eVTOLs. The three main eVTOL configurations, the multirotor, the lift plus cruise, and the vectored thrust, are compared on five main parameters, and the energy and time required to perform three reference missions. The values used for the comparison are based on what is currently available in the public domain, and the performances have been computed assuming the inputs unknown and using the tools discussed in chapter 2. The power system values of the real vehicles could differ.

This analysis showed that different configurations perform best on different missions. The multirotors are best suited to short-range missions because they are the most efficient in hover. Vectored thrust is the best configuration for long-range missions because they are efficient in cruise. Lift plus cruise eVTOLs are a compromise, and they are the best suited for medium-range missions.

Chapter 4

Power sources

The power sources available for eVTOL are batteries, fuel cells, and hybrids. Batteries are the most common power source among eVTOLs, fuel cells and hybrids are more complex, but they can enhance the energy available and the range. All power sources can be evaluated on two main parameters: specific power and specific energy. The specific power is the maximum power that the power source can provide divided by the total mass of the power source. The specific energy is the total energy than the power source can provide before being recharged divided by its total mass. The specific power is measured in W/kg and the specific energy in Wh/kg.

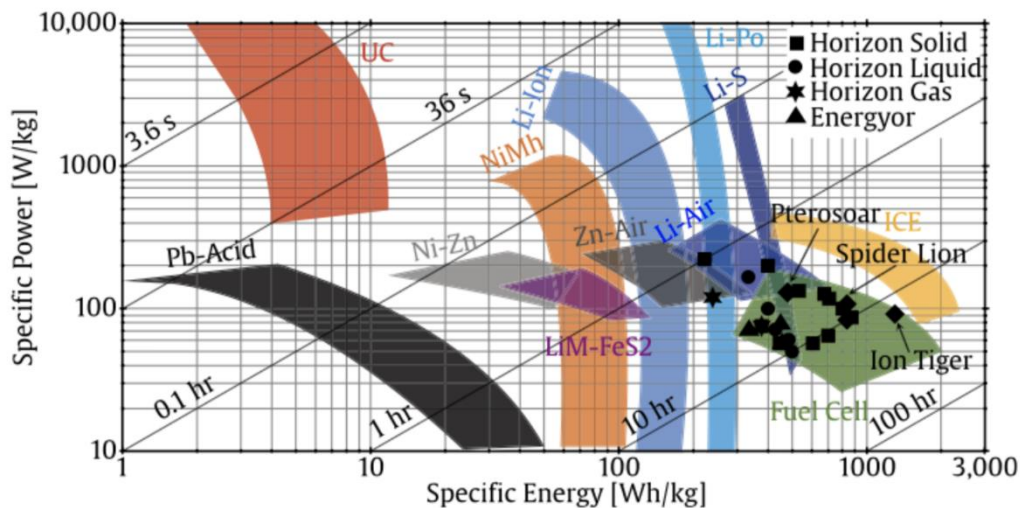


Figure 89: Ragone plot showing specific power and specific energy of different types of batteries, fuel cells, ultra-capacitors, and internal combustion engines. Courtesy of Andrew Gong and Dries Verstraete, [79] [80].

Figure 89 shows a Ragone plot of the different power sources. The Ragone plot has on the x-axis the specific energy, and on the y-axis the specific power. On the top left, there are the ultracapacitors or supercapacitors marked UC. They have high specific power but low specific energy. They can be used coupled with lower specific power sources like fuel cells or internal combustion engines. Lead-acid batteries are in black under the ultra-capacitors. In the middle of the graph, there are different battery types, including nickel-zinc, nickel-metal-hydride, lithium-iron-disulfide, and the most common now lithium-ion and lithium-polymer. Slightly on the right, with higher specific energy, there are zinc air, lithium-air, and

lithium-sulfur batteries. The highest specific energy power sources are internal combustion engines and fuel cells.

In the previous chapters, the specific power and specific energy of the Tesla Model S have been assumed to complete performance computations. In this chapter, different batteries, fuel cells, and hybrids will be discussed. Their specific power and energy densities will be compared, and their effects on eVTOL design will be described.

4.1 Batteries

Batteries convert the chemical energy contained in their active materials into energy through a redox reaction. The reverse process can recharge rechargeable batteries.

Batteries have high coulombic efficiency, in the order of 95% - 98% [23]. This means that for every 100 units of energy used to recharge the battery, 95 to 98 units can be extracted to power the motors. This is a significant advantage over fuel cells, that can extract only a percentage of the energy stored in hydrogen, equal to their efficiency, which is usually around 40%-50%.

Batteries are composed of cells, which are the basic electrochemical unit. Each cell consists of the anode, the cathode, and the electrolyte. The anode is the negative electrode that gives up electrons. The cathode is the positive electrode which accepts electrons. The electrolyte provides the transfer of the charge, as ions, between the anode and the cathode.

Cells are made in different sizes, and they are either cylindrical or flat. Cells are then assembled in battery packs connecting them in series and parallel to reach the voltage and capacity required.

The Tesla Model S battery pack consists of 7104 cylindrical li-ion cells of the size 18650 (Figure 90). The cell shown in the image has a nominal capacity of 3350 mAh, a nominal voltage of 3.7 V, and a weight of 48.5 g [81]. The total energy can be computed multiplying the charge by the nominal voltage; the result is 12.4 Wh. Dividing this value by the weight, the specific energy found is 256 Wh/kg. This value is much higher than the 157 Wh/kg [26] used through this document because the 157 Wh/kg is the specific energy of the battery pack that comprises the weight of the connection between the cells, the packaging, and the thermal management system.

Phones use flat cells because they fit better. Model airplanes use flat cells too, which are sold in small packs of a different number of cell series and different capacities. The battery pack for model airplanes shown in Figure 91 is called 4s. It consists of 4 flat cells connected in series. The number 4 stands for the number of cells, and the letter s stands for series. Each li-ion cell has a nominal potential difference of 3.7 Volts; thus, the 4s battery pack has a 14.8 V voltage. The battery shown in Figure 91 [82] has a total capacity of 8000 mAh, a C-rate of 60C, and a weight of 831 g. The specific energy is computed multiplying the nominal voltage by the capacity; the result is 142 Wh/kg. The C-rate indicates the maximum discharge current that the battery can provide. This maximum current is found

multiplying the battery capacity by the C-rate, the result is 480 A, representing a maximum power of approximately 7 kW.



Figure 90: Li-ion 18650 cell.



Figure 91: Li-ion 4s battery.

4.1.1 Battery classification

There are different kinds of batteries. The main subdivision in batteries is between primary and secondary batteries. Primary batteries cannot be easily or effectively recharged electrically, and so they are discarded when they are completely discharged. Secondary batteries can be recharged electrically, and so they are also called storage batteries. Most primary batteries are used domestically, and they are the cylindrical AA or AAA batteries and the flat button types. The most common primary battery chemistries are zinc-carbon and Alkaline-MnO₂. New high specific energy primary batteries are lithium-based. Primary batteries are not interesting for eVTOLs because the cost of discarding a battery pack for each mission is exceedingly high.

The most common chemistries of secondary batteries are lead-acid, nickel-cadmium, nickel-metal-hydride, and li-ion.

Lead-acid batteries have been used in the automotive industry for engine starting, vehicle lighting, and engine ignition for over a century. Their advantages reside in their low price and their ease of manufacturing, but the specific energy is only around 40 Wh/kg. Lead-acid batteries powered the first batch of General Motors EV1. That battery pack was rated at 53 A, 312 V, for a total weight of 533 kg [83]. The specific energy of this battery pack was 31 Wh/kg providing a range of 60 miles.

Nickel-cadmium are rugged secondary batteries which can withstand electrical and mechanical abuse, and which require little maintenance. They have specific energies between 40-60 Wh/kg, and they have been extensively used in industrial applications. Starting in the 1990s they have lost market share first to the nickel-metal-hydride batteries and to the li-ion batteries.

Nickel-metal hydride batteries are similar to the nickel-cadmium, but they use hydrogen, absorbed in a metal alloy, for the active negative material in place of the cadmium used in the nickel-cadmium battery. Their specific energy is between 60 and 120 Wh/kg. These batteries were used to retrofit EV1. They were rated at 77 Ah, 343V, and a weight of approximately 450 kg. Their energy density was approximately 60 Wh/kg. Their specific power is high, up to 1000 Wh/kg and this is the reason why they have been used for hybrid electric vehicles.

Li-ion batteries are the most popular secondary batteries on the market. They power everything from phones to electric cars, with their high specific power and high specific energy. Most of the discussion on batteries in this thesis has considered li-ion batteries.

Lithium-sulfur batteries a new chemistry that promises even higher specific energy at high specific power. Oxis Energy's ultra-light cell has a specific energy of 400 Wh/kg, but its cycle life is limited to 100 cycles maximum [24].

Sion Power calls their chemistry lithium-metal, and their new product Licerion weighs 158 g, has a 20 Ah capacity, and a nominal voltage of 3.82 V. The resulting specific energy is 480 Wh/kg [84].

While these new products have exciting specific energies, they are still far from being sturdy, reliable mass-market products that can be employed in eVTOLs.

4.1.2 Factors that affect battery life

The main factors that affect the life of the battery are the depth of discharge (DOD), the temperature of operation, and the discharge rate. These variables affect the number of chemical processes that happen during each cycle. Part of these chemical processes are irreversible, and they reduce the total energy that can be stored inside the battery.

Figure 92 and Figure 93 show the effect of the depth of discharge on li-ion batteries. Figure 93 analyzes batteries for LEO satellites, which must endure many cycles because they cycle the Earth every 90 minutes. To be able to withstand such

a high cycle life, the depth of discharge is limited to only 20-30%. This means that the minimum state of charge allowed is 70-80%

Figure 94 shows the effect of the discharge rate on the energy that a 18650 C/LiCoO₂ li-ion battery can provide. High discharge rates reduce the voltage of the cell, reducing the energy provided.

Figure 95 shows the effect of temperature on a 18650-type C / LiCoO₂ battery discharged at 0.2C. As the temperature decreases, the energy available decreases.

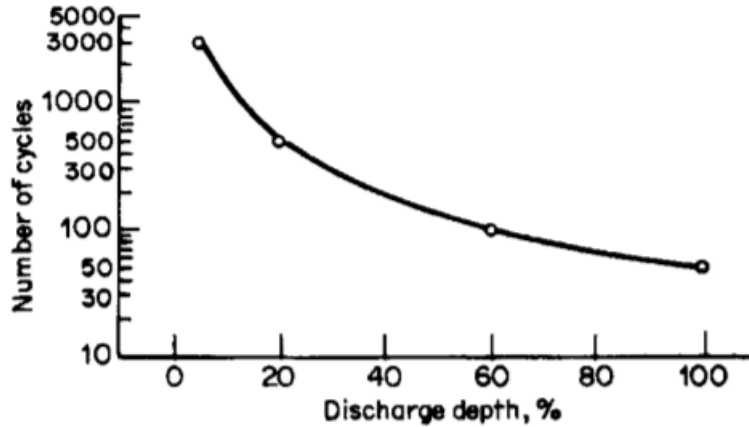


Figure 92: Effect of the depth of discharge on a LiAl / MnO₂ coin-type battery at 20°C from Linden's handbook of batteries, chapter 34 [23].

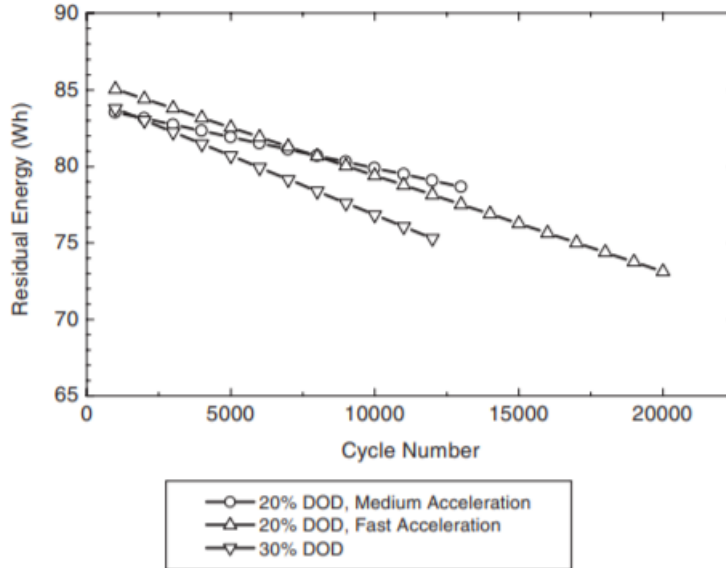


Figure 93: Effect of the number of cycles and the depth of discharge on the residual energy of li-ion batteries from Linden's handbook of batteries, chapter 35 [23].

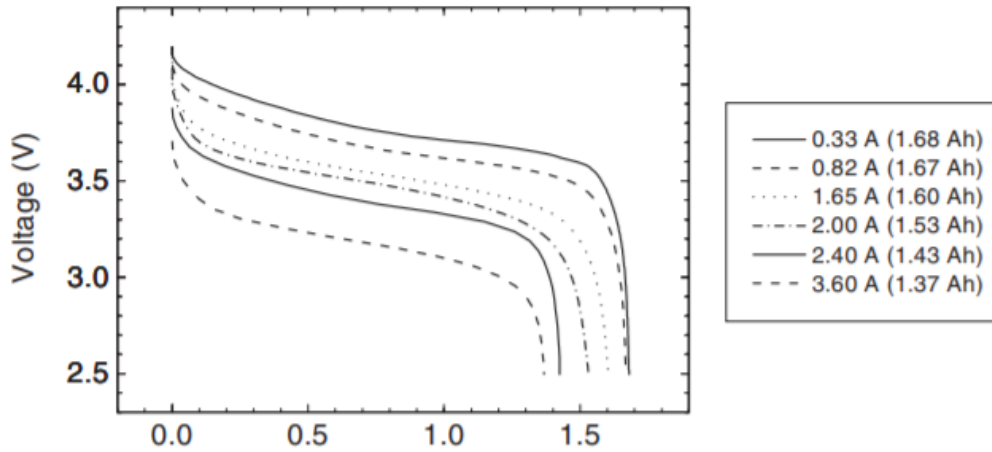


Figure 94: Effect of the discharge rate on the capacity of 18650 type e C/LiCoO₂ li-ion batteries, from Linden's handbook of batteries, chapter 35 [23]. The discharge capacity (Ah) is on the x-axis.

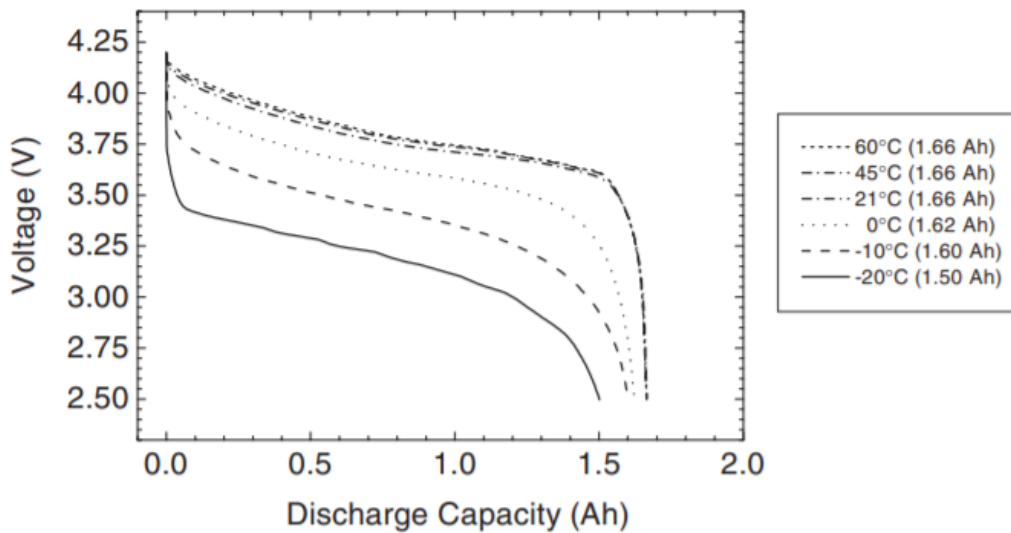


Figure 95: Effect of the temperature on a 18650-type C / LiCoO₂ battery discharged at 0.2C. From Linden's handbook of batteries, chapter 35 [23]

4.1.3 Battery design

The constructional characteristics of the cell affect its performances. Cells designed for high capacity and low or moderate discharge loads have high quantities of active material. On the other end, cells designed for high loads, have large electrodes or reaction surfaces and features to minimize internal resistance and enhance current capacity.

4.2 Fuel Cells

A fuel cell is a galvanic device that converts the chemical energy of a fuel and an oxidant to electrical energy. Like batteries, fuel cells are not subject to the limitations of the Carnot cycle, which applies to thermal engines. The difference

between a fuel cell and a battery is how the source of energy is supplied. In a fuel cell, the fuel and the oxidant are continuously supplied from an external source, in a battery, they are part of the device, and it must be recharged once the reactant is consumed.

Fuel cells have been of interest for the last 150 years and had a useful application in the space program, producing energy for the Apollo and Space Shuttle missions.

There are different fuel cell types, including solid oxide, molten carbonate, phosphoric acid, alkaline, proton exchange membrane, direct methanol, and regenerative fuel cells.

Each fuel cell system consists of a power section composed of one or more stack in series to reach the desired output voltage, a fuel subsystem, and a power converter. For space missions, both hydrogen and oxygen are stored, while for applications on Earth, the oxygen is not required because it can be taken from the atmosphere.

4.2.1 Fuel cell specific fuel consumption

The power provided by the fuel cell depends on the hydrogen consumed. The following procedure shows how to quantify how much hydrogen is required to produce a specific output power, knowing the efficiency of the fuel cell.

The charge contained in a gram of hydrogen is computed knowing that a mole of hydrogen contains $6.022 \cdot 10^{23}$ hydrogen atoms [85] having one elementary charge each. Multiplying the number of hydrogen atoms in a mole by the elementary charge of $1.602 \cdot 10^{-19}$ Coulombs [86], the total charge of a mole of hydrogen, 96472 Coulombs, is found. Knowing that each mole of hydrogen weighs 1.008 grams [87], each gram of hydrogen contains a charge of 95707 Coulombs.

The ideal potential difference of the hydrogen combustion is 1.229 Volts [88], so the energy contained in each gram of hydrogen can be computed multiplying the charge by the potential. The resulting energy is 117624 Joules for each gram of hydrogen, or 32700 Wh/kg. This value cannot be compared to the approximately 200 Wh/kg of the batteries because it does not include all the weight of the cell, of the hydrogen storage, and of the fuel subsystem.

To conclude the analysis of the fuel cell specific fuel consumption, the fuel cell efficiency, and the power required by the compressor that feeds air to it must be considered.

During its combustion, each gram of hydrogen is combined with eight grams of oxygen. As oxygen is 23.14% of the air weight [89], every gram of hydrogen must combine with 34.6 grams of air. Moreover, the fuel cell cannot exploit all the oxygen contained in the air, so the quantity of air must be increased by a factor called cathode stoichiometry. Estimating this parameter at 2.3, the quantity of air required for one gram of hydrogen is 79.5 grams.

The power required by the compressor to compress the air is:

$$P_C = \frac{\dot{m} \cdot C_p \cdot D_T}{\eta_M} \quad (67)$$

Where \dot{m} is the airflow, C_p is the air specific heat capacity $1005 \frac{J}{kg \cdot K}$, η_M is the efficiency of the electric motor driving the compressor, and D_T is the temperature rise due to the adiabatic compression, which can be computed as:

$$D_T = \left(\left(\frac{p_{out}}{p_{in}} \right)^{\frac{\gamma-1}{\gamma}} - 1 \right) \cdot \frac{T}{\eta} \quad (68)$$

p_{out} is the pressure at the exit of the compressor while p_{in} is the input pressure. γ is the air heat capacity ratio, 1.4 because the air is composed of diatomic gases. T is the input air temperature, and η is the efficiency of the compressor.

The fuel cell efficiency depends on the single cell, and it can be measured experimentally. Knowing it and the energy required by the compressor, the specific fuel consumption can be finally computed:

$$SFC = \frac{1}{117624 \cdot \eta_{FC} - P_C} \quad (69)$$

The specific fuel consumption computed with equation (69) is measured in $\frac{g}{W \cdot s}$.

4.2.2 Hydrogen storage

Hydrogen can be stored compressed in gaseous form, as a cryogenic liquid, or in various chemical compounds that may release it upon heating, including metal hydrides and organic compounds [90].

The efficiency of hydrogen storage is usually measured with the tank gravimetric efficiency. It is defined as:

$$\eta_{grav} = \frac{W_f}{W_f + W_t} \quad (70)$$

It is defined as the weight of the fuel or hydrogen, W_f , divided by the sum of the weight of the fuel and the weight of the tank, W_t .

Cryogenic liquid storage requires lighter tanks, but it is difficult to keep its temperature under its boiling point, which is approximately 20 Kelvin. Liquid storage is the primary option in space where heat is exchanged radiatively, and there is no convection. For commercial aviation, it requires foam insulation and produces losses for long hold times at the airport before takeoff [91]. It is recognized as the crucial technology to enable liquid hydrogen propulsion in commercial aviation [92], because it provides gravimetric efficiencies, in the order of 0.5 to 0.7 [91], much higher than any alternative technology.

Gaseous storage requires high pressures to keep the tank dimensions limited and robust materials to be able to withstand these pressures.

Other storage methods have been investigated, including storing it in metal hydrides or other chemical compounds.

This section shows the procedure to compute the tension of a cylindrical tank under pressure, and it can be used to verify tanks for hydrogen storage.

The circumferential or hoop stress is [93]:

$$\sigma_{\theta} = \frac{p \cdot R}{t} \quad (71)$$

Where p is the hydrogen pressure, R is the tank radius, and t is the tank thickness.

The axial stress is [93]:

$$\sigma_z = \frac{p \cdot R}{2t} \quad (72)$$

The radial stress is [93]:

$$\sigma_r = -\frac{p}{2} \quad (73)$$

The resulting values can be combined with the Von Mises or Tresca methods and then compared to the material limits applying a safety factor.

To compute the mass of hydrogen stored inside the tank, the ideal gas law can be applied. First, the volume of the tank is computed, then the number of moles contained in the tank can be computed as:

$$n = \frac{p \cdot V}{R \cdot T} \quad (74)$$

Where p is the pressure of the hydrogen, V is the tank volume, R is the gas constant equal to $8.314 \frac{J}{K \cdot mol}$, and T is the hydrogen temperature. The hydrogen mass can then be computed, multiplying the number of moles found by the hydrogen molar mass, which is 2 g/mol .

An example of the application of these equations is the following hydrogen tank made of aluminum Al 2219 T851 with maximum $\sigma_{yield} = 289 \text{ MPa}$ and $\sigma_{rupture} = 393 \text{ MPa}$ and a density of 2000 kg/m^3 . The radius of the tank is 0.3 m , the length of the cylindrical section is 0.3 m , and its total volume is 0.2 m^3 . The hydrogen pressure is 350 bar , and the wall thickness is 47 mm . The tensions are combined applying the Tresca method, and the margins of safety applied are 1.5 for yield and 2 for rupture. The hydrogen mass stored is 5.7 kg , and the weight of the tank is 159 kg . The gravimetric efficiency, computed as the weight of the hydrogen divided by the total weight of hydrogen and tank, is 3.4% .

Better storage systems can be built employing better materials such as carbon composites and cooling the stored hydrogen. The tanks of the fuel cell powered Toyota Mirai car weight 87.5 kg and can store 5 kg of hydrogen, making for a gravimetric efficiency of 5.4% [94] [95].

In the previous section, we computed the ideal specific energy of hydrogen, 32.7 kWh/kg . Considering a storage efficiency of 5.4% , this value drops to 1.77 kWh/kg . To get to the specific energy of the fuel cell system, the weight of the fuel cell and the weight of the fuel subsystem must be considered.

4.2.3 Fuel cell stack weight and efficiency

The weight of the fuel cell depends on the power it can produce because the power depends on the dimension of the proton exchange surface. The weight varies from fuel cell to fuel cell. The fuel cell stack of the Toyota Mirai has a power of 114 kW and a specific power of 2.0 kW/kg [94]. Ballard produces the FCveloCity-MD, which weighs 125 kg plus 40 kg for the air subsystem and has a power of 30 kW [96]. The specific power is 240 W/kg for the stack and 182 W/kg for the stack plus air system. This fuel cell is not optimized for weight because it is designed for buses and light rails.

The efficiency of the fuel cell varies with their load and average around 40-50%.

These values show that the fuel cell system consisting of the stack, the fuel subsystem, and the hydrogen tank can have different specific energy and specific power depending on the relative power of the stack and size of the tank.

Figure 96 shows the specific power and specific energy of different fuel cell configurations. The specific power of the stack is assumed 2 kW/kg, like the Toyota Mirai stack. The weight of the fuel subsystem, including the pipes and the valves to bring hydrogen from the tank to the fuel cell stack, is computed assuming a weight of the fuel cell subsystem weighting 1 kg for every 6 kW of power of the fuel cell stack. The fuel cell efficiency is considered 50%. Two lines have been drawn, one for a tank gravimetric efficiency of 5% and another for 7.5%. This figure shows that the specific power and specific energy vary widely and, to have specific energies much larger than battery specific energy, fuel cells must sacrifice power.

Figure 96 also shows the importance of the tank's gravimetric efficiency. The improvement from 5% to 7.5% increases the specific energy significantly at the same specific power.

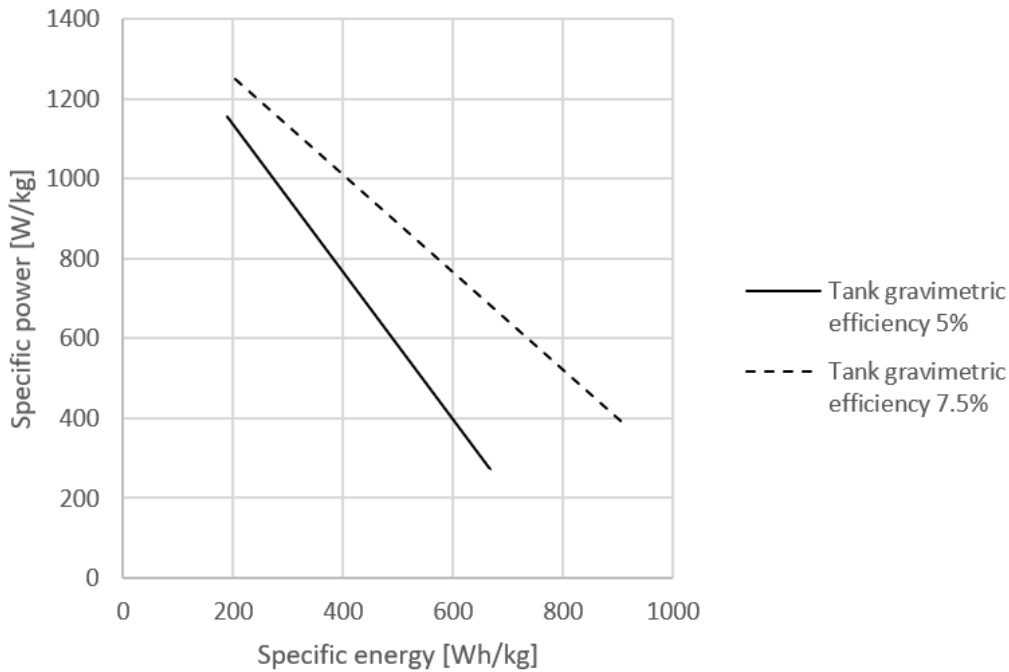


Figure 96: Ragone plot of fuel cell configurations at 50% fuel cell efficiency, 2kW/kg stack specific power, 6 kW/kg fuel subsystem. The two lines correspond to a tank gravimetric efficiency of 5% and 7.5%.

4.3 Hybrids

Hybrids combine different technologies to provide the power required by the eVTOL. The leading hybrid combinations available are internal combustion engine and batteries, gas turbine and batteries, fuel cell and batteries. Hybrids increase the specific energy of the power source because liquid propellants can store more energy than batteries in the same amount of weight. However, the specific power is reduced. Supercapacitors can be employed to increase the instantaneous power available. Their main application is the triple hybrid with fuel cells and batteries [79].

4.3.1 Internal combustion engine and battery hybrid

This kind of hybrid powertrain is common in the automotive industry. The internal combustion engine and the electric motor can be connected in two ways [97]. In the parallel hybrid, the internal combustion engine and the electric motor are connected to the same shaft and the torques provided by the two systems add. This is the configuration that has the lowest possible requirements on the electric motor and batteries. In the series hybrid, the internal combustion engine is directly connected to a generator that provides power to the battery. The car is directly driven by an electric motor powered by the battery and the generator connected to the internal combustion engine.

In conventional aircraft, both architectures can be employed because, like in a car, there is only one power shaft. In eVTOLs, distributed propulsion makes the parallel hybrid configuration impossible.

An example of a conventional aircraft powered by a hybrid powertrain is the Diamond DA36 E-Star, which is powered by a Siemens 70 kW electric motor from power generated by a 30 kW Austro Engines Wankel rotary engine and generator. This drivetrain uses the series architecture, and it can take off on electric power only.

An example of eVTOL powered by a hybrid powertrain is the full-scale Greased Lightning (Figure 14). It is designed to be powered by a combination of two 6 kW diesel motors and a lithium-ion battery pack.

One of the most common internal combustion engines for aviation is the Lycoming O-360 [98]. It was certified in 1955, and it is still in production. It powers many aircraft, including the Cessna 172 and the Robinson R-22. Its power is 134 kW, and its dry weight is 117, making for a specific power of 1.15 kW/kg. It uses 91/96 minimum grade avgas as fuel.

Aircraft diesel engines are starting to replace common internal combustion engines for aviation. Their specific power is 0.8 – 0.9 kW/kg [99].

4.3.2 Gas turbine and battery hybrid

Many hybrid-electric fixed-wing aircraft designs are based on electric power generated by an on-board gas turbine [100]. One of the world's biggest gas turbines, Rolls-Royce, is designing a hybrid powertrain based on its M250 gas turbine [101]. Their design is a tilt-wing with four propellers on the wing and two on the tail. It is intended to carry four to five people traveling at 250 mph over a range of 500 miles (Figure 97). The turbine generates 300-400 kW, and the battery generates an additional 300-400 kW for takeoff and landing.

The M250 is a turboshaft engine family developed by the American company Allison at the beginning of the 1960s [102]. In 1995 Rolls-Royce acquired the Allison company, and it has kept on producing the engine. It is one of the best-selling Rolls-Royce engines with nearly 30000 models produced and 16000 still in service. It powers many fixed-wing and rotorcraft, including the Agusta A109 and the Bell 206 helicopters.

The Model 250 has a five-stages axial compressor followed by a centrifugal compressor stage [103]. Two high-pressure turbine stages power the compressor, and two additional turbine stages provide the output power. The Model 250 C20 has a nominal power of 313 kW, and it weighs 72 kg for a specific power of 4.35 kW/kg, and the Model 250 C30 has a nominal power of 485 kW, and it weighs 124 kg for a specific power of 3.91 kW/kg. They are one meter long, and their diameter is 60 cm.

The M250 turbine is so compact that it has also been mounted on a motorcycle, the MTT Y2K Turbine Superbike. It can reach 250 mph or 400 km/h [104].



Figure 97: Rolls-Royce eVTOL.

4.3.3 Fuel cell, battery, and supercapacitor triple hybrid

The fuel cell, battery, and supercapacitor triple hybrid enhances for fuel cell powertrains. Supercapacitors smooth the electric load canceling transients, which would reduce its efficiency and may damage it. Supercapacitors can store only a small amount of energy; thus, they can deal only with a few seconds of a transient load. The addition of batteries provides the power required for longer high-power transient loads and to the supercapacitors for a continuous load smoothing.

Gong's triple hybrid architecture [79] was designed to power a 2.77 m wingspan, 6.5 kg UAV based on a modified 1:6 scale Grob G109 electric glider. It consists of:

- A 150 W Spectronik fuel cell
- A 4S, 1500 mAh, li-ion battery pack
- Two 7F, 25V supercapacitors

The specifications of Gong's triple hybrid are listed in Table 28.

The Spectronik fuel cell consists of 25 cells in series, giving an operating range between 15 V and 23 V. It weighs 320 g, and it has a maximum efficiency specified by the producer of 48%. During his tests [79], Gong found the maximum power exceeding the producer specifications and reaching 200W and the efficiency underperforming them, reaching a maximum value of 40% (Figure 98). The large scatter in the data points is due to the short-circuiting that happens every ten seconds to purge the cell, assisting it in humidification and ensuring long life and high performances.

Hydrogen is stored with metal hydride technology. Liquid storage is impractical as it must be stored at -253 °C, and compressed hydrogen storage was not an option due to the lack of Australian regulatory approval for composite

hydrogen storage tanks and the unavailability of high-pressure hydrogen compressors. Metal hydride storage exploits the hydrogen reaction with a metal hydride under moderate pressures. This reaction is reversed to release the hydrogen. The gravimetric efficiency of this method of storage is inferior to compressed hydrogen, and hydrogen flow rates are limited due to the reaction kinetics, but the system operates at lower pressure ensuring safer operations. The commercial metal hydride tank is called hydrostik, and it weighs 105 g and can hold up to 10 L of hydrogen, corresponding to 1.6 g at 1 atm and 20°C [105]. Gong's tests show a total storage for eight hydrostik cartridges varying from 27.2 L to 36.8 L depending on the flow rate. Considering the data provided in the datasheet, the gravimetric efficiency of this hydrogen storage is 1.5%. Considering the data provided by Gong, 36.8 L of total hydrogen available from eight canisters assembled in a 1 kg pack corresponds to 3 g of hydrogen, and a gravimetric efficiency is 0.3%. The energy available is 39.5 Wh, and it is computed multiplying the ideal energy available with one gram of hydrogen, 32.9 Wh, by the total hydrogen available, by the fuel cell efficiency.

The battery is a LiPo 4s Turnigy 65C, 1500 mAh weighting 343 g. The total energy stored is 22.2 Wh.

The two Yunasko supercapacitors employed have a maximum voltage of 25 V and a capacity of 7 Farad each, which corresponds to a 0.6 Wh energy at 25V. Each supercapacitor weighs 279 g. Their maximum continuous power is 750 W each for a specific power of 2.7 kW/kg. The specific energy is 2.2 Wh/kg

The total system weighs 2220 grams, has a power of 3140 W, and a total energy of 122.2 Wh. The specific power is 1414 W/kg, and the specific energy is 28.3 Wh/kg. The low specific energy is due to the low gravimetric efficiency of the tank. If it had the 5.4% gravimetric efficiency of the Toyota Mirai tanks, it could have hold 54 g of hydrogen for a total of 1 kg of weight resulting in 712 Wh at 40% fuel cell efficiency. This would have meant a total system energy of 735 Wh and a total system specific energy of 331 Wh/kg.

Table 28: Gong's triple hybrid architecture specifications.

| | |
|---|------------|
| Spectronik fuel cell | |
| Maximum power | 200 W |
| Efficiency | 40% |
| Weight | 320 g |
| Hydrogen storage | |
| Gravimetric efficiency | 0.3% |
| Hydrogen | 3 g |
| Energy considering fuel cell efficiency | 39.5 Wh |
| Weight | 1 kg |
| Battery | |
| Nominal voltage | 14.8 V |
| Capacity | 1500 mAh |
| Energy | 22.2 Wh |
| Weight | 343 g |
| Max power | 1440 W |
| Supercapacitors | |
| Total energy | 1.2 Wh |
| Total weight | 558 g |
| Total power | 1500 W |
| Total power system | |
| Weight | 2220 g |
| Power | 3140 W |
| Energy | 122.2 Wh |
| Specific power | 1414 W/kg |
| Specific energy | 28.3 Wh/kg |

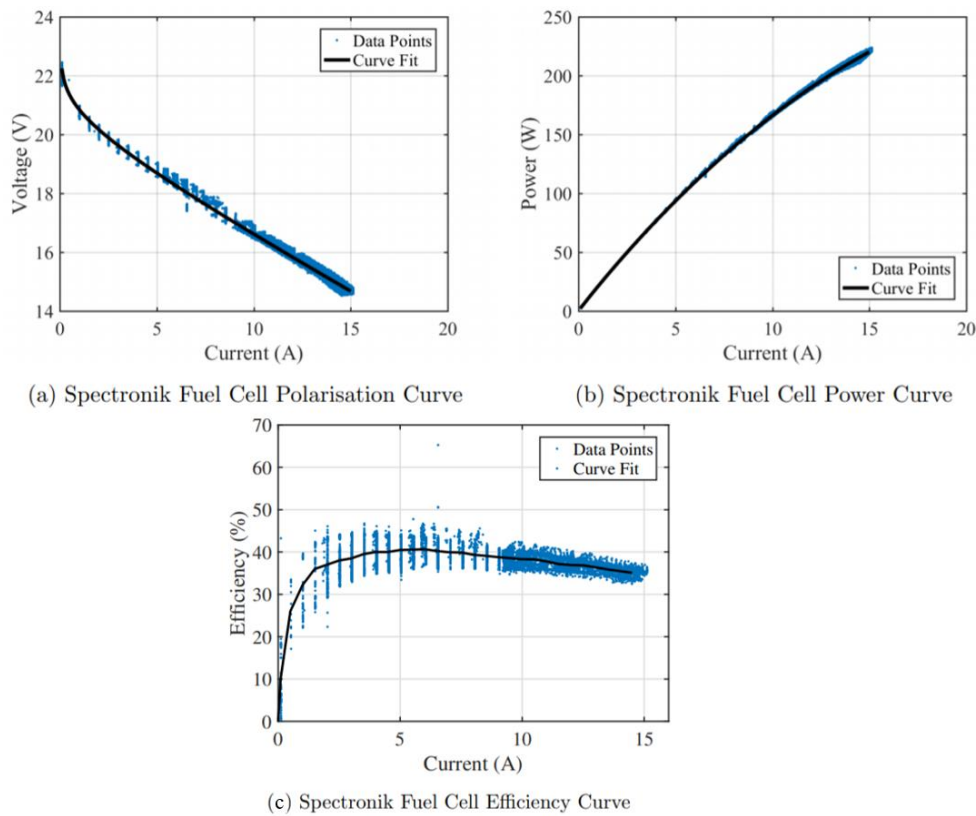


Figure 98: Spectronik fuel cell characteristics. Courtesy of Andrew Gong [79].

4.3.4 Supersonic electric jet

This section explores the feasibility of a supersonic electric jet, applying the necessary computations for hover and cruise performance discussed in chapter 2. The objective of these computations is to find the required battery and electric motor technology level to realize a supersonic electric VTOL jet. Many of the assumptions made here are coarse, and the results will only suggest the required technology level.

The configuration considered is the F 35 configuration with a rear swiveling nozzle and a lift fan used only for takeoff and landing. The data about this supersonic eVTOL is collected in Table 30. The cruise lift to drag at supersonic speed is 7, like the Concorde's [106]. The propulsive efficiency is 75%. Table 29 lists the mass breakdown showing a total mass of 3000 kg. The mass of the battery is 1500 kg, the payload 200 kg for a pilot and a passenger in tandem, the mass of the engines is 350 kg, and the mass of the structure and the remaining systems is 950 kg.

Table 29: Supersonic electric jet mass breakdown.

| Mass breakdown | |
|-----------------|----------------|
| Battery | 1500 kg |
| Payload | 200 kg |
| Engines | 350 kg |
| Remaining parts | 950 kg |
| Total | 3000 kg |

The cruise performances are computed reversing the electric range equation (14) to find the battery specific energy to have the range desired. The power system producing the required performances is now called battery. The range desired is assumed 600 km because it is the distance between San Francisco and Los Angeles, two of the wealthiest cities in the world which host the people more likely to buy such an aircraft. 75% of the battery is assumed for the cruise, and the rest is needed for takeoff, landing, transitions, and reserves.

$$E^* = \frac{R \cdot g}{\eta_{total} \cdot \frac{L}{D} \cdot \frac{m_{battery}}{m}} \cdot \frac{1}{75\%} \quad (75)$$

The specific energy required found is 790 Wh/kg.

The hover performances are computed with the disk actuator theory modified for ducted fans (equation 21), applying a hover figure of merit of 70%. Both the lift fan and the rear fan have a 1.1 m diameter. The power required to hover found is 2.7 MW provided by the two fans. The engine driving the lift fan is designed for a maximum power of 1.35 MW while the engine driving the rear fan has a maximum power of 2.7 MW to be able to take advantage of the maximum power provided by the battery. The energy required for one minute of hover is 45 kWh. The total battery energy is found multiplying the battery specific energy found earlier by the battery mass, and it is 1.2 MWh. The total hover time is 26 minutes. Considering an energy cost of 0.12 €, the total cost of the energy storable in this battery is 140 €.

The maximum speed is computed, finding the cruise drag dividing the weight of the aircraft by the lift to drag ratio. The value found is 4.2 kN. Then the thrust produced at maximum power is computed for every airspeed applying the disk actuator theory [31]:

$$T = 2\rho A \cdot (v + u_e)u_e \quad (76)$$

Where ρ is the air density at cruise, A is the disk actuator area, v is the flight speed, and u_e is the induced speed at the disk. As this last parameter is unknown, it must be assumed and changed until the power required to produce that induced speed is equal to the power available [31]:

$$P = T(v + u_e) \quad (77)$$

The actual thrust produced is computed multiplying the thrust found by the propulsive efficiency. The flight altitude is assumed at 10 km, and the air density is 0.414 kg/m³. The maximum flight speed is the speed for which the drag is equal to the available thrust and, in this case, it is 480 m/s, corresponding to M=1.6.

To complete the study, the remaining battery and motor properties are computed. The battery specific energy has already been computed, and it is 790 Wh/kg, Its specific power is found dividing the 2.7 MW maximum power by the 1500 kg battery mass. The result is 1.8 kW/kg. The motor specific power is found dividing the total motor power, 2.7 MW plus 1.35 MW by the total motor mass. The result is 11.6 kW/kg. The supersonic eVTOL data is collected in Table 30.

Table 30: Supersonic eVTOL data.

| Supersonic eVTOL data | |
|------------------------------------|-------------------------|
| Cruise lift to drag ratio | 7 |
| Propulsive efficiency | 75% |
| Figure of merit for hover | 70% |
| Fans diameter | 1.1 m |
| Power required to hover | 2.7 MW |
| Range | 600 km |
| Battery for cruise | 75% |
| Flight altitude | 10 km |
| Air density at altitude | 0.414 kg/m ³ |
| Air density for hover computations | 1.225 kg/m ³ |
| Cruise speed | 480 m/s |
| Cruise Mach | 1.6 |

The battery and motor values found previously are far from reasonable, and for this reason, the same procedure has been repeated for a high subsonic eVTOL based on the same configuration. The high subsonic eVTOL data are collected in Table 31. The mass breakdown is unchanged. The new lift to drag ratio is 15 because this eVTOL flies at lower speeds. The propulsive efficiency and the figure of merit for hover are unchanged. The range required is again 600 km. Applying equation (75), and assuming 75% of the battery for cruise, the battery specific energy found is 400 Wh/kg.

The lift fan and the rear fan have a 1.6 diameter to reduce the power requirements for hover. The power required to hover found is 1.9 MW and it is provided by the two fans driven by equal engines of 0.95 MW each. The energy for one minute of hover is 31 kWh, the total battery energy is 590 kWh, and the total hover time is 19 minutes. The total energy cost is 70 €. The drag at cruise speed decreases to 2 kW due to the increase in the lift to drag ratio. The resulting flight speed computed with the same procedure applied earlier is 300 m/s or Mach 1. However, knowing the nature of transonic flight, the drag increase approaching the speed of sound would make the drag equal to the thrust at $M=0.8$ or 240 m/s.

The remaining battery and motor properties are computed. The battery specific power is found dividing the maximum power required for hover, 1.9 MW, by the battery mass 1500kg. The result is 1.27 kW/kg. The motor specific power is found dividing the power required for hover by the motor mass, 350 kg. This time the rear engine power is not at the maximum battery power, but it is sized to be half the power required for hover. The engine specific power found is 5.4 kW/kg.

Table 31: High subsonic eVTOL data.

| High subsonic eVTOL data | |
|------------------------------------|-------------------------|
| Cruise lift to drag ratio | 15 |
| Propulsive efficiency | 75% |
| Figure of merit for hover | 70% |
| Fans diameter | 1.6 m |
| Power required to hover | 1.9 MW |
| Range | 600 km |
| Battery for cruise | 75% |
| Flight altitude | 10 km |
| Air density at altitude | 0.414 kg/m ³ |
| Air density for hover computations | 1.225 kg/m ³ |
| Cruise speed | 210 m/s |
| Cruise Mach | 0.7 |

Table 32: Summary of the battery and motor properties required for the supersonic and the high subsonic eVTOL, and the present values.

| | Supersonic | High Subsonic | Present |
|-----------------|------------|---------------|-------------|
| Specific energy | 790 Wh/kg | 400 Wh/kg | 157 Wh/kg |
| Specific power | 1.8 kW/kg | 1.27 kW/kg | 0.735 kW/kg |
| Motor | 11.6 kW/kg | 5.4 kW/kg | 5.22 kW/kg |

Table 32 collects the battery and motor properties computed for the supersonic and the high subsonic eVTOL and the present values. The present values considered are taken from the Tesla Model S battery [26], and the Siemens SP260D electric motor for airplanes [107]. The supersonic eVTOL values are far from the present level technologies. The high subsonic eVTOL values are higher than the present technology, but years of constant technological progress might make them achievable. Maybe the triple hybrid discussed in section 4.3.3 could provide the required technology.

Maybe an eVTOL similar to this high subsonic design might be used as an amusement park attraction to have kids feel the same experience of flying a fighter aircraft. The attraction might consist of 5 minutes flights with vertical takeoff, transition, and some aerobatic maneuvers, and it could be sold for about 50 €. The requirement on the battery specific energy would be much lower because the battery could be switched every flight having five or six additional packs charging.

4.4 Chapter conclusion

The power sources available to eVTOLs are battery, fuel cells, and hybrids. Batteries are easily scalable; they have high specific power and coulombic efficiency. They are the most common option for eVTOLs, but the range achievable with them is limited because their specific energy is limited. Fuel cells and hybrids have higher specific energies because they store the energy in hydrogen or hydrocarbon fuels like kerosene, avgas, or diesel. The main problem hindering fuel cell adoption is hydrogen storage. The best option is cryogenic liquid storage, but the temperature required is -253°C , and it poses many technical challenges. Other possibilities are compressed gas and storing hydrogen in chemical compounds like metal hydrides. The gravimetric efficiencies of these options are much lower, in the order of 5%. Another drawback of the fuel cells is that only a fraction of the energy used to create hydrogen is extracted to power the motors. Hybrids include internal combustion engines plus batteries, gas turbines plus batteries, and fuel cells plus supercapacitors plus batteries. The first two are conceptually similar to the hybrid propulsion systems used in the automotive industry, while the third takes advantage of the merits of the fuel cells and uses supercapacitors to provide the peak power fuel cells cannot provide.

Finally, this chapter hosts the supersonic eVTOL conceptual exercise. The specific power and specific energy required for a supersonic eVTOL having an external configuration similar to the F35 are computed. The results are far from the present technology. Repeating the exercise for a similar but slower high subsonic eVTOL, the values found are higher than the present technology, but they look achievable in the future.

Chapter 5

Wind tunnel tests

This chapter describes the wind tunnel tests performed on a lift plus cruise eVTOL model based on the commercial Mini Talon drone that we built to evaluate the performances of a takeoff propellers retraction system. The tests were performed at the University of Sydney under the supervision of professor Dries Verstraete. The Krossblade Aerospace company kindly provided us a fuselage of one of their Skyproglers, and we were able to test a model built around that fuselage. After a description of the problem investigated, the experimental setup and the test results are presented. The chapter ends with the analysis of the result and the implications they have on the performances of a lift plus cruise eVTOL like the Kitty Hawk Cora and on a surveillance drone quadplane Mini Talon.

5.1 Problem statement

Chapter 3 showed all the electric and non-electric VTOL configurations tested up until now. The lift plus cruise configuration emerged as a compromise between multirotor eVTOLs, which are excellent in hover but perform poorly in cruise flight and vectored thrust, which has poor hover performances but excellent flight speed and range. The lift-plus-cruise main problem is the drag generated by the takeoff propellers, which slow down the eVTOL in cruise and reduce its range.

Vectored thrust eVTOLs solve this problem using the same system for hover and cruise, but some problems emerge. Tilt rotors are highly complex, and they are more suited to turbine than electric propulsion. Two different kinds of tilt wings exist. Small propellers tilt wings like the Nasa Greased Lightning have a reduced disk actuator area, and their efficiency in hover is reduced. Large propellers tilt wings like the old Canadair CL-84, the XC-142, and the new Rolls-Royce eVTOL lose the redundancy, which might save them in case of failure of one rotor or propeller. The XC-142 had a mechanical cross-link between the four turbines and rotors to ensure safety in case of failure, but it proved unreliable due to high vibrations. New ducted fans eVTOL like the Lilium Jet have poor hover efficiency.

A way to reduce the drag generated by the takeoff propellers in lift plus cruise eVTOLs is to retract these propellers inside the fuselage or the wing. A similar option is to fold the propellers as the Joby Aviation eVTOLs do. Propeller retraction or folding solves the drag problem, ensures redundancy, and provides a large disk actuator area for efficient hover.

Retracting the takeoff propellers inside the fuselage resembles the retractable landing gear for commercial jets. The first airplanes, from the Wright brothers, through World War I, to the 1920s, employed fixed landing gears. It was the era of strut-and-wire biplanes, which were maneuverable and robust, but also slow. During the 1920s, aircraft designers improved the standard design moving from biplane to monoplane, covering the radial piston engines with the cowling developed by the NACA, adopting the variable-pitch propeller, and introducing the retractable landing gear [72].

Since eVTOL design is still in its beginnings, retractable takeoff propellers might become a reality like the retractable landing gear for airplanes. However, the aeronautical industry shows that the retractable landing gear is an advance not always useful. Not every aircraft employs a retractable landing gear, the Cessna 172, like many other general aviation airplanes, uses a fixed landing gear. Even the Boeing 737, which has a retractable landing gear, does not have landing gear doors to cover the wheels.

The retractable takeoff propeller concept also applies to VTOL drones for surveillance, delivery, and military applications. The most common VTOL drone configuration is the QuadPlane [108], a conventional aircraft with a bolt-on quadcopter. Usually, the takeoff propellers are mounted on beams parallel to the fuselage and attached to the wing. Rods attached to the fuselage would generate more drag because they would be perpendicular to the airflow. Another standard configuration is the flying wing plus quadcopter, like the Delta Quad produced by Vertical Technologies [109]. The Krossblade Aerospace company designed and sells the SkyProwler drone [110], which can retract its takeoff propellers inside its fuselage. Unlike passenger-carrying eVTOLs, surveillance military VTOL drones are designed for watching over the target area for as long as possible. The parameter to maximize is not range and speed but endurance.

To our knowledge, there are no other drones able to retract their propellers, besides Krossblade's SkyProwler. Stahl, Rößler, and Hornung wrote a paper on this topic [111]. They analyzed and tested in the wind tunnel the retraction of the two-blade rotor into a recess in a pod using the bidirectional rotation of a threaded rotor shaft. They estimated an increase in cruise endurance between 1% and 6% for small uncrewed aircraft and 10% for passenger eVTOLs.

To study whether the improvement in flight speed and range produced by retractable takeoff propellers overcomes the increase in weight and complexity or not, we designed and tested inside the wind tunnel a VTOL drone able to retract its propellers inside the fuselage. The Mini Talon drone was selected as the starting point of the design, and two new fuselages have been designed and 3D printed, a clean version, and a version with the retraction system. The wings of the standard Mini Talon have been used to complete the model. The Krossblade Aerospace company provided us with a fuselage of a SkyProwler, and we were able to test also a model realized with that fuselage and a wing and a tail we 3D printed.

5.2 Experimental setup

5.2.1 Model selection

The tests were intended to measure experimentally, in the wind tunnel, the drag of a quadplane model, with and without takeoff propellers. Then modify it to have a propeller retraction system and measure its aerodynamic properties with the propellers out and retracted.

The quadplane model was realized by modifying an existing commercial drone. The Skywalker x8, the Mini Sky Hunter, the Sky Surfer x8, and the Mini Talon were considered and compared. The first is a flying wing, and it is used as the basis for the Delta Quad [109]. The second and the third are standard configuration fixed-wing drones with a wing and a conventional tail. They are often used as the basis for quadplane conversions [112]. The last is based on the Desert Hawk military drone [113], it has a large fuselage, a pusher motor, and a V-tail. The Mini Talon was selected because its large fuselage may host the retracted propellers, and the tail in the rear provides additional stability for a test flight compared to the Skywalker flying wing design. The Mini talon has already been converted to VTOL multiple times, including the design called Mozzie by PerthUAV [114].

5.2.2 Motors and propellers

The takeoff motors and propellers were sized using the software eCalc. Table 33 shows the mass budget performed to compute the takeoff mass required to size the takeoff motors and propellers. The 1 m carbon bar was supposed to be divided to support the four propellers.

The motors selected for hover are the CM-2217/20 Multirotor motor, $K_v=950$ [115] [116], which drive APC electric 10x4.5 multirotor propellers [117]. The K_v rating of a brushless motor is the ratio of the motor's unloaded rpm to the peak voltage on the wires connected to the coils. The numbers following the name of the propeller are the diameter and the pitch measured in inches. The hover performances computed with eCalc are presented in Figure 99. Figure 100 shows the motor performances when coupled with different propellers. The first line corresponds to the motor, coupled with the propeller selected and shows a maximum thrust of 1.3 kg.

The motor selected for the cruise, to be mounted in pusher configuration, is the Cobra Motors 2820/14 $K_v=840$ [118] [119], driving an APC electric 10x8 propeller [120]. Its performances computed with eCalc are shown in Figure 101, and the motor performances coupled with different propellers are shown in Figure 102.

Table 33: Mini Talon VTOL mass budget

| | Mass (g) | Pieces | Total (g) |
|-------------------------------------|----------|--------|-------------|
| Mini Talon | 562 | 1 | 562 |
| Carbon Bar for QP Arms (1m) | 27 | 1 | 27 |
| Quad Motor CM 2217/20-950 | 76 | 4 | 304 |
| Quad ESC ZTW Spider Pro HV 30A F390 | 6 | 4 | 24 |
| Fwd Motor Cobra C-2820/14 Kv 840 | 140 | 1 | 140 |
| 40A ESC (with Brake) | 50 | 1 | 50 |
| Fwd prop APC 10x8 | 21 | 1 | 21 |
| Hover prop APC 10x5 | 15 | 4 | 60 |
| Battery MultiStar LiHV 4S 10Ah | 794 | 1 | 794 |
| UBEC ZTW 6A | 12 | 1 | 12 |
| Power cables | 50 | 1 | 50 |
| Pixhawk | 39 | 1 | 39 |
| GPS Neo-M8N | 18 | 1 | 18 |
| Digital Airspeed with Pitot | 3 | 1 | 3 |
| I2C Hub | 4 | 1 | 4 |
| Power Module and Sensor | 22 | 1 | 22 |
| Comms | 96 | 1 | 96 |
| Companion Pi | 30 | 1 | 30 |
| Retraction mechanisms | 200 | 1 | 200 |
| Total | | | 2456 |

| | | | | | | | | | |
|---------------------|---|--------------------------------|--|--------------------------|--|--------------------------------|--|------------------------|--------------------|
| General | Model Weight: 2456 g (incl. Drive) / 86.6 oz | # of Rotors: 4 | Frame Size: 500 mm / 19.69 inch | FCU Tilt Limit: no limit | Field Elevation: 500 m ASL / 1640 ft ASL | Air Temperature: 25 °C / 77 °F | Pressure (QNH): 1013 hPa / 29.91 inHg | | |
| Battery Cell | Type (Cont. / max. C) - charge state: LiPo 10000mAh - 15/25C - normal | Configuration: 4 S 1 P | Cell Capacity: 10000 mAh / 10000 mAh total | max. discharge: 85% | Resistance: 0.0025 Ohm | Voltage: 3.7 V | C-Rate: 15 C cont. / 25 C max | Weight: 217 g / 7.7 oz | |
| Controller | Type: max 30A | Current: 30 A cont. / 30 A max | Resistance: 0.008 Ohm | Weight: 40 g / 1.4 oz | Accessories | | | Current drain: 0 A | Weight: 0 g / 0 oz |
| Motor | Manufacturer - Type (Kv) - Cooling: Cobra - CM-2217/20 (950) - good | KV (w/o torque): 950 rpm/V | no-load Current: 0.53 A @ 12 V | Limit (up to 15s): 300 W | Resistance: 0.188 Ohm | Case Length: 33 mm / 1.3 inch | # mag. Poles: 14 | Weight: 76 g / 2.7 oz | |
| Propeller | Type - yoke twist: APC MultiRotor MR - 0° | Diameter: 10 inch / 254 mm | Pitch: 4.5 inch / 114.3 mm | # Blades: 2 | PConst. / TConst: 1.09 / 1.0 | Gear Ratio: 1 : 1 | <input type="button" value="calculate"/> | | |



Remarks:

| | | | | | |
|-----------------------------|-----------------------------------|---------------------------|---------------------------|----------------------------|---|
| Battery | Motor @ Optimum Efficiency | Motor @ Maximum | Motor @ Hover | Total Drive | Multicopter |
| Load: 6.93 C | Current: 6.43 A | Current: 17.32 A | Current: 8.28 A | Drive Weight: 1465 g | All-up Weight: 2456 g |
| Voltage: 14.11 V | Voltage: 14.49 V | Voltage: 13.97 V | Voltage: 14.40 V | Thrust-Weight: 51.7 oz | add Payload: 86.6 oz |
| Rated Voltage: 14.80 V | Revolutions*: 12519 rpm | Revolutions*: 9910 rpm | Revolutions*: 6979 rpm | Current @ Hover: 33.14 A | max Tilt: 31 ° |
| Energy: 148 Wh | electric Power: 93.2 W | electric Power: 242.0 W | Throttle (log): 59 % | P(in) @ Hover: 490.5 W | max. Speed: 53 km/h |
| Total Capacity: 10000 mAh | mech. Power: 77.1 W | mech. Power: 175.7 W | Throttle (linear): 68 % | Efficiency @ Hover: 70.4 % | est. rate of climb: 4.8 m/s |
| Used Capacity: 8500 mAh | Efficiency: 82.7 % | Power-Weight: 394.1 W/kg | electric Power: 119.3 W | P(out) @ Hover: 345.1 W | 945 ft/min |
| min. Flight Time: 7.4 min | | 178.8 W/lb | mech. Power: 86.3 W | Current @ max: 69.29 A | Total Disc Area: 20.27 dm² |
| Mixed Flight Time: 13.0 min | | Efficiency: 72.6 % | Power-Weight: 199.7 W/kg | P(in) @ max: 1025.5 W | with Rotor fail: ✘ |
| Hover Flight Time: 15.4 min | | est. Temperature: 51 °C | mech. Power: 90.6 W/lb | P(out) @ max: 702.8 W | |
| Weight: 868 g / 30.6 oz | | 124 °F | Power-Weight: 199.7 W/kg | Efficiency @ max: 68.5 % | |
| | | Wattmeter readings | est. Temperature: 38 °C | | |
| | | Current: 69.28 A | 100 °F | | |
| | | Voltage: 14.11 V | specific Thrust: 5.15 g/W | | |
| | | Power: 977.5 W | 0.18 oz/W | | |

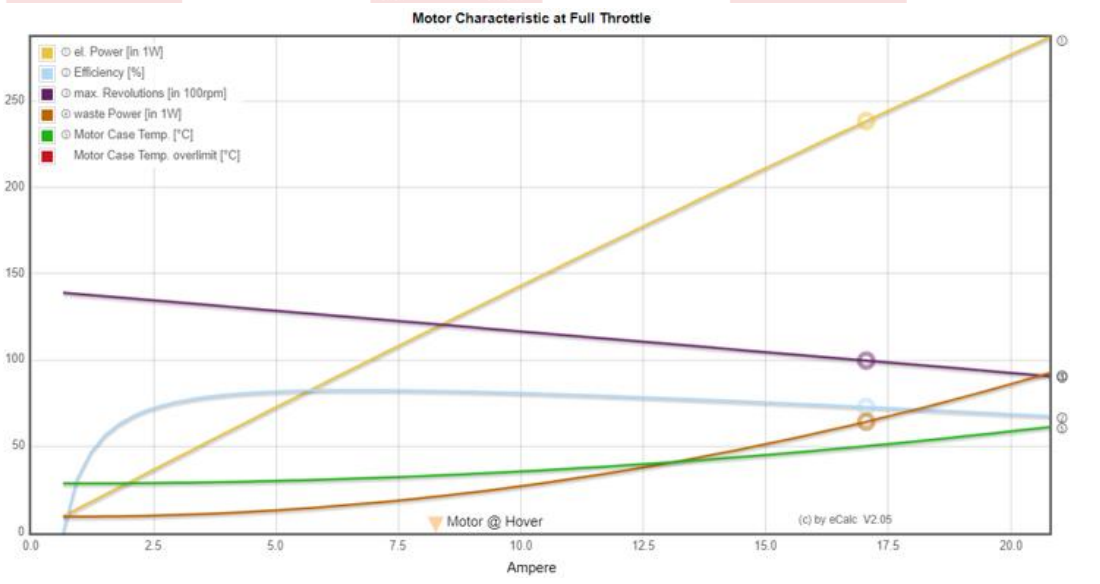





Figure 99: Mini Talon hover performances computed with eCalc.

| Prop Manf. | Prop Size | Li-Po Cells | Input Voltage | Motor Amps | Input Watts | Prop RPM | Pitch Speed in MPH | Thrust Grams | Thrust Ounces | Thrust Eff. Grams/W |
|------------|-----------|-------------|---------------|------------|-------------|----------|--------------------|--------------|---------------|---------------------|
| APC | 10x4.5-MR | 4 | 14.8 | 17.98 | 266.1 | 9,185 | 39.1 | 1341 | 47.30 | 5.04 |
| APC | 11x4.5-MR | 4 | 14.8 | 20.42 | 302.2 | 8,504 | 36.2 | 1506 | 53.12 | 4.98 |
| GemFan | 8x4.5-MR | 4 | 14.8 | 13.48 | 199.5 | 10,170 | 43.3 | 997 | 35.17 | 5.00 |
| GemFan | 9x4.7-MR | 4 | 14.8 | 14.94 | 221.1 | 9,847 | 43.8 | 1160 | 40.92 | 5.25 |
| GemFan | 10x4.5-MR | 4 | 14.8 | 20.22 | 299.3 | 8,603 | 36.7 | 1389 | 49.00 | 4.64 |
| GemFan | 10x4-MR-W | 4 | 14.8 | 18.23 | 269.8 | 9,180 | 34.8 | 1323 | 46.67 | 4.90 |
| GemFan | 11x4-MR-W | 4 | 14.8 | 19.17 | 283.7 | 8,876 | 33.6 | 1426 | 50.30 | 5.03 |

 The prop is too small to get good performance from the motor. (Less than 50% power)

 The prop is sized right to get good power from the motor. (50 to 80% power)

 The prop can be used, but full throttle should be kept to short bursts. (80 to 100% power)


 The prop is too big for the motor and should not be used. (Over 100% power)

Figure 100: Cobra Motors CM-2217/20 Multirotor motor, Kv=950, motor propeller performances specified by the producer.

General Model Weight: 2456 g (incl. Drive) 86.6 oz # of Motors: 1 Wing Area: 30 dm² 465 in² Drag: 0.05 Cd Cross Section: 0 dm² 0 in² Field Elevation: 500 m ASL 1640 ft ASL Air Temperature: 25 °C 77 °F Pressure (Z(NH)): 1013 hPa 29.91 inHg

Battery Cell Type (Cont. / max. C) - charge state: LiPo 10000mAh - 15/25C - normal Configuration: 4 S 1 P Cell Capacity: 10000 mAh max. discharge: 85% Resistance: 0.0025 Ohm Voltage: 3.7 V C-Rate: 15 C cont 217 g 25 C max 7.7 oz

Controller Type: max 40A Current: 40 A cont. 40 A max Resistance: 0.006 Ohm Weight: 50 g 1.8 oz Battery extension Wire: AWG10-5.27mm² Length: 0 mm Motor extension Wire: AWG10-5.27mm² Length: 0 mm

Motor Manufacturer - Type (KV) - Cooling: Cobra C-2820/14 (840) medium KV (w/o torque): 840 rpm/V no-load Current: 1 A @ 10 V Limit (up to 15s): 530 W Resistance: 0.071 Ohm Case Length: 40 mm # mag. Poles: 14 Weight: 140 g 4.9 oz

Propeller Type - yoke twist: APC Electric E 0° Diameter: 10 inch 254 mm Pitch: 8 inch 203.2 mm # Blades: 2 PConst / TConst: 1.08 / 1.0 Gear Ratio: 1 : 1 Flight Speed: 0 km/h 0 mph calculate



Remarks: • The airflow at the propeller blade will stall. Therefore the static thrust and max. current may not be reached. On ground you will measure 'Stall Thrust' as maximum.
• 53.0kmh / 32.9mph - above this airspeed stall at the propeller blade will have disappeared completely.

| | | | | | |
|--|---|---|---|---|--|
| Battery Load: 2.84 C Voltage: 14.52 V Rated Voltage: 14.80 V Energy: 148 Wh Total Capacity: 10000 mAh Used Capacity: 8500 mAh min. Flight Time: 18.0 min Mixed Flight Time: 25.9 min Weight: 868 g 30.6 oz | Motor @ Optimum Efficiency Current: 15.10 A Voltage: 14.56 V Revolutions*: 10857 rpm electric Power: 219.8 W mech. Power: 184.4 W Efficiency: 83.9 % | Motor @ Maximum Current: 28.37 A Voltage: 14.35 V Revolutions*: 9801 rpm electric Power: 407.0 W mech. Power: 327.4 W Efficiency: 80.4 % est. Temperature: 62 °C 144 °F | Propeller Static Thrust: 2068 g 72.9 oz Revolutions*: 9801 rpm Stall Thrust: 1502 g 53 oz aval Thrust @ 0 km/h: 1502 g 53 oz aval Thrust @ 0 mph: 53 oz Pitch Speed: 120 km/h 75 mph Tip Speed: 469 km/h 291 mph specific Thrust: 3.69 g/W 0.13 oz/W | Total Drive Drive Weight: 1164 g 41.1 oz Power-Weight: 171 W/kg 78 W/lb Thrust-Weight: 0.84 : 1 Current @ max: 28.37 A P(in) @ max: 419.9 W P(out) @ max: 327.4 W Efficiency @ max: 78.0 % Torque: 0.32 Nm 0.24 lbf ft | Airplane All-up Weight: 2456 g 86.6 oz Wing Load: 82 g/dm² 82 g/in² Cubic Wing Load: 14.9 26.9 oz/ft³ est. Stall Speed: 43 km/h 27 mph est. Speed (level): 108 km/h 67 mph est. Speed (vertical): - km/h - mph est. rate of climb: 6.7 m/s 1319 ft/min |
|--|---|---|---|---|--|

Motor Partial Load

| Propeller rpm | Throttle % | Current (DC) A | Voltage (DC) V | el. Power W | Efficiency % | Thrust g | oz | Spec Thrust g/W | Pitch Speed km/h | Speed (level) km/h | Motor Run Time (85%) min | |
|---------------|------------|----------------|----------------|--------------|--------------|------------|-------------|-----------------|------------------|--------------------|--------------------------|-------------|
| 1400 | 12 | 0.2 | 14.8 | 2.3 | 40.8 | 42 | 1.5 | 18.1 | 0.64 | 17 | 322.4 | |
| 2100 | 19 | 0.4 | 14.8 | 5.4 | 59.1 | 95 | 3.3 | 17.5 | 0.62 | 26 | 1385.1 | |
| 2800 | 25 | 0.7 | 14.8 | 10.9 | 69.9 | 169 | 6.0 | 15.5 | 0.55 | 34 | 690.0 | |
| 3500 | 32 | 1.3 | 14.8 | 19.6 | 75.9 | 264 | 9.3 | 13.5 | 0.48 | 43 | 383.4 | |
| 4200 | 38 | 2.2 | 14.8 | 32.4 | 79.3 | 380 | 13.4 | 11.7 | 0.41 | 51 | 231.5 | |
| 4900 | 45 | 3.4 | 14.8 | 50.2 | 81.2 | 517 | 18.2 | 10.3 | 0.36 | 60 | 149.0 | |
| 5600 | 52 | 5.1 | 14.7 | 74.1 | 82.1 | 675 | 23.8 | 9.1 | 0.32 | 68 | 100.8 | |
| 6300 | 60 | 7.2 | 14.7 | 104.9 | 82.5 | 854 | 30.1 | 8.1 | 0.29 | 77 | 43 | 71.0 |
| 7000 | 67 | 9.9 | 14.7 | 143.9 | 82.6 | 1055 | 37.2 | 7.3 | 0.26 | 85 | 53 | 51.6 |
| 7700 | 75 | 13.2 | 14.7 | 192.0 | 82.4 | 1276 | 45.0 | 6.6 | 0.23 | 94 | 58 | 38.6 |
| 8400 | 83 | 17.3 | 14.6 | 250.3 | 82.0 | 1519 | 53.6 | 6.1 | 0.21 | 102 | 64 | 29.5 |
| 9100 | 91 | 22.2 | 14.6 | 320.0 | 81.5 | 1783 | 62.9 | 5.6 | 0.20 | 111 | 69 | 23.0 |
| 9800 | 100 | 28.0 | 14.5 | 402.4 | 81.0 | 2067 | 72.9 | 5.1 | 0.18 | 120 | 74 | 18.2 |
| 9801 | 100 | 28.4 | 14.5 | 407.0 | 80.4 | 2068 | 72.9 | 5.1 | 0.18 | 120 | 74 | 18.0 |

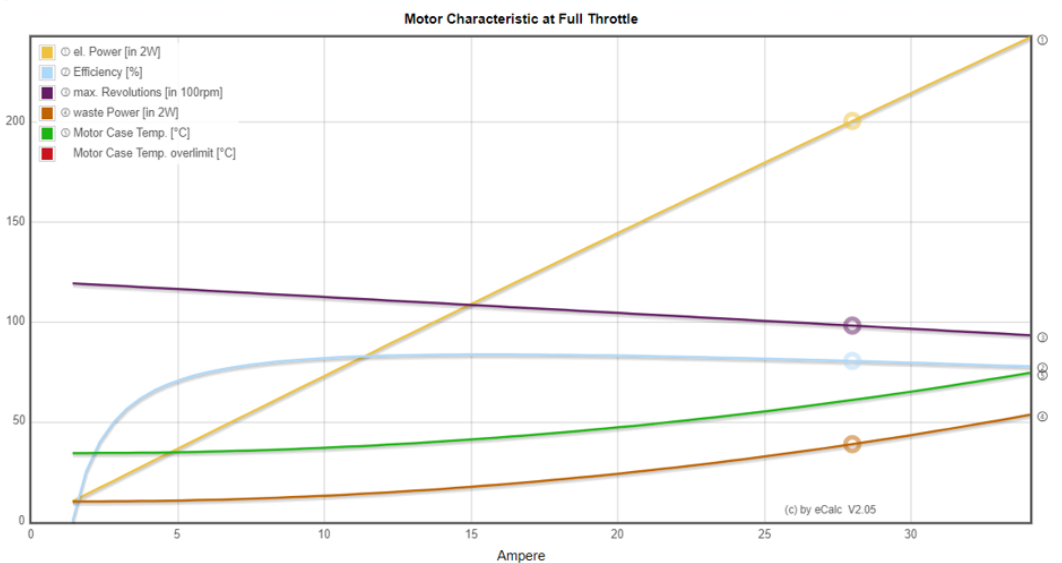


Figure 101: Cruise motor performances computed with eCalc.

| Prop Manf. | Prop Size | Input Voltage | Motor Amps | Watts Input | Prop RPM | Pitch Speed | Thrust Grams | Thrust Ounces | Thrust Eff. Grams/W |
|------------|-----------|---------------|------------|-------------|----------|-------------|--------------|---------------|---------------------|
| APC | 8x8-E | 14.8 | 20.46 | 302.8 | 10,166 | 77.0 | 921 | 32.49 | 3.04 |
| APC | 9x6-E | 14.8 | 16.36 | 242.1 | 10,442 | 59.3 | 1164 | 41.06 | 4.81 |
| APC | 9x7.5-E | 14.8 | 25.09 | 371.3 | 9,794 | 69.6 | 1257 | 44.34 | 3.39 |
| APC | 9x9-E | 14.8 | 28.43 | 420.8 | 9,510 | 81.1 | 1249 | 44.06 | 2.97 |
| APC | 10x5-E | 14.8 | 20.29 | 300.2 | 10,171 | 48.2 | 1497 | 52.80 | 4.99 |
| APC | 10x6-E | 14.8 | 21.85 | 323.3 | 10,048 | 57.1 | 1594 | 56.23 | 4.93 |
| APC | 10x7-E | 14.8 | 25.37 | 375.4 | 9,767 | 64.7 | 1706 | 60.18 | 4.54 |
| APC | 10x10-E | 14.8 | 35.47 | 525.0 | 8,939 | 84.6 | 1476 | 52.06 | 2.81 |
| APC | 11x5.5-E | 14.8 | 27.57 | 408.0 | 9,583 | 49.9 | 1984 | 69.98 | 4.86 |
| APC | 11x7-E | 14.8 | 32.00 | 473.7 | 9,207 | 61.0 | 2061 | 72.70 | 4.35 |
| APC | 11x8-E | 14.8 | 34.53 | 511.0 | 9,010 | 68.3 | 1980 | 69.84 | 3.87 |
| APC | 11x8.5-E | 14.8 | 36.74 | 543.8 | 8,829 | 71.1 | 1974 | 69.63 | 3.63 |
| APC | 11x10-E | 14.8 | 41.20 | 609.7 | 8,361 | 79.2 | 1728 | 60.95 | 2.83 |
| APC | 12x6-E | 14.8 | 35.11 | 519.6 | 8,960 | 50.9 | 2407 | 84.90 | 4.63 |
| APC | 12x8-E | 14.8 | 41.58 | 615.4 | 8,405 | 63.7 | 2060 | 72.66 | 3.35 |
| APC | 13x4-E | 14.8 | 27.58 | 408.2 | 9,582 | 36.3 | 2269 | 80.04 | 5.56 |

Figure 102: Cobra Motors 2820/14, Kv=840, motor propeller performances specified by the producer.

5.2.3 CAD models

The next step in the design was the digitalization of the Mini Talon model purchased by the X/UAV company. After the CAD model of the original drone was ready, it was modified to host a propellers retraction system. During this process, the fuselage turned out to be not large and strong enough to host the retracted propellers. The cuts required to open a passage would have weakened the structure, and the motors would not be entirely retracted. A new fuselage was designed, and it was then 3D printed for the wind tunnel tests. Figure 103 shows the CAD models of the original Mini Talon produced by X-UAV and the modified Mini Talon with the propellers retraction system.

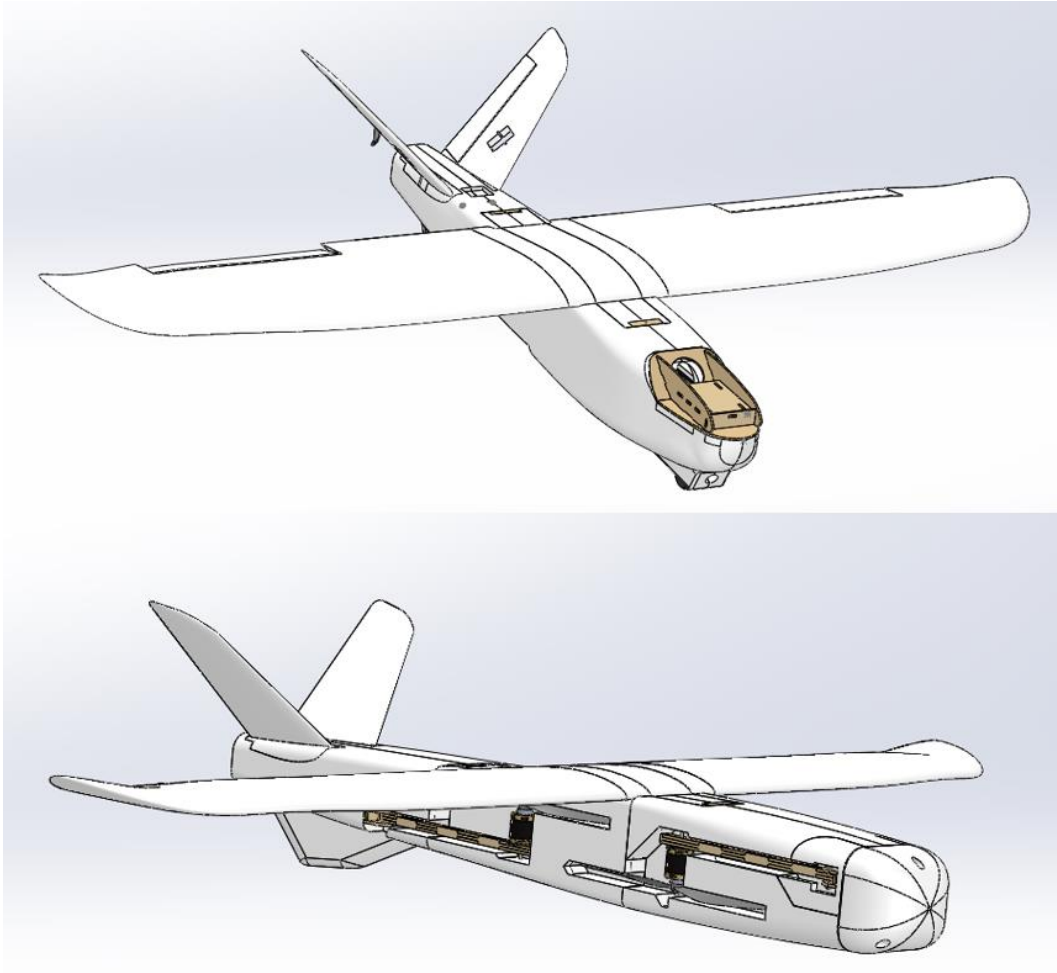


Figure 103: CAD models of the original Mini Talon produced by X-UAV and the modified Mini Talon with the propellers retraction system.

5.2.4 Wind tunnel tests

Three different versions of the Mini Talon were tested:

- The Mini Talon 1 is the clean configuration without hover propellers. Its fuselage has no holes to host the retracted propellers, but it is as big as the fuselage with the holes. Its fuselage has been 3D printed in three sections, and the tail has been 3D printed in four total parts. The different parts have been glued with epoxy. The original X-UAV wings and fuselage central hatch have been used. The nose has been 3D printed, and it is glued with epoxy.
- The Mini Talon 2 is the configuration with the retraction propeller system. A new fuselage with holes for the retracted propellers has been 3D printed. The fuselage parts and the tail parts are glued with epoxy. The second set of X-UAV Mini Talon wings have been used. The retraction system has been realized with laser-cut plywood parts attached with superglue. The beams supporting the motors consist of 4 plywood parts glued together. The

motors are connected to the beams with two M3 bolts for each motor. The beams insert in two plywood supports, one in the front and one in the rear. There is no actuator moving the beams, and they are manually opened and retracted. The beams are locked by an M3 bolt acting as a hinge and secured to one of four possible holes in the supports which correspond to angles of retraction of 0°, 30°, 60°, and 90°. The supports are fastened to the fuselage with M3 bolts. The nose has been 3D printed, and it is fastened to the fuselage with M4 bolts.

- The Mini Talon 3 represents the standard quadplane conversion. It was realized modifying the Mini Talon 1 after having performed tests on it. Two 80 cm aluminum bars were glued with epoxy to the wings, parallel to the fuselage. The VTOL motors and propellers were fastened on these bars with M3 bolts.

Figure 104 shows the assembled models. The Mini Talon 2 with the retraction system is on top, the clean version Mini Talon 1 on the low left, and the Mini Talon 3 quadplane conversion is on the low right.

Another model was realized with the fuselage provided by the Krossblade Aerospace company. This fuselage had the VTOL propellers and their support connected to hinges, but the mechanisms and the actuators were not present. The propellers were fixed in the open or closed position during the tests with small wooden parts and tape. The fuselage is made out of foam with an exterior carbon fiber shell.

We 3D printed the parts not provided by Krossblade. The tail was 3D printed in a single piece and fastened to the fuselage with M2 bolts. It doesn't have an aerodynamic shape, its thickness is constant. The nose was 3D printed too, and it was glued to the fuselage with epoxy. The wing was 3D printed in four total parts. Each half wing was assembled connecting its two 3D printed components with epoxy using two plywood beams attached with superglues as guides. The two halves of the wing were inserted into the fuselage and connected with two four plywood plates, two over and two under the two connections. The plywood plates were fastened to the wing sections with M3 bolts. Figure 105 shows the parts used to realize this model. From the top left and proceeding clockwise there are the 3D printed tail, the 3D printed wings, the fuselage provided by Krossblade, and the wing junction inside the fuselage. The plywood beams were extending out of the surface of the 3D printed wing parts. To reduce aerodynamics problems, the parts in excess were filed and covered with tape.

All the 3D printed parts listed above were printed by Benjamin Van Magill, Ph.D. student designing 3D printable military drones at the University of Sydney. He managed to print all the parts precisely at the first try in an incredibly short time.



Figure 104: Assembled models. The Mini Talon 2 is on top, the Mini Talon 1 is on the low left and the Mini Talon 3 on the low right.

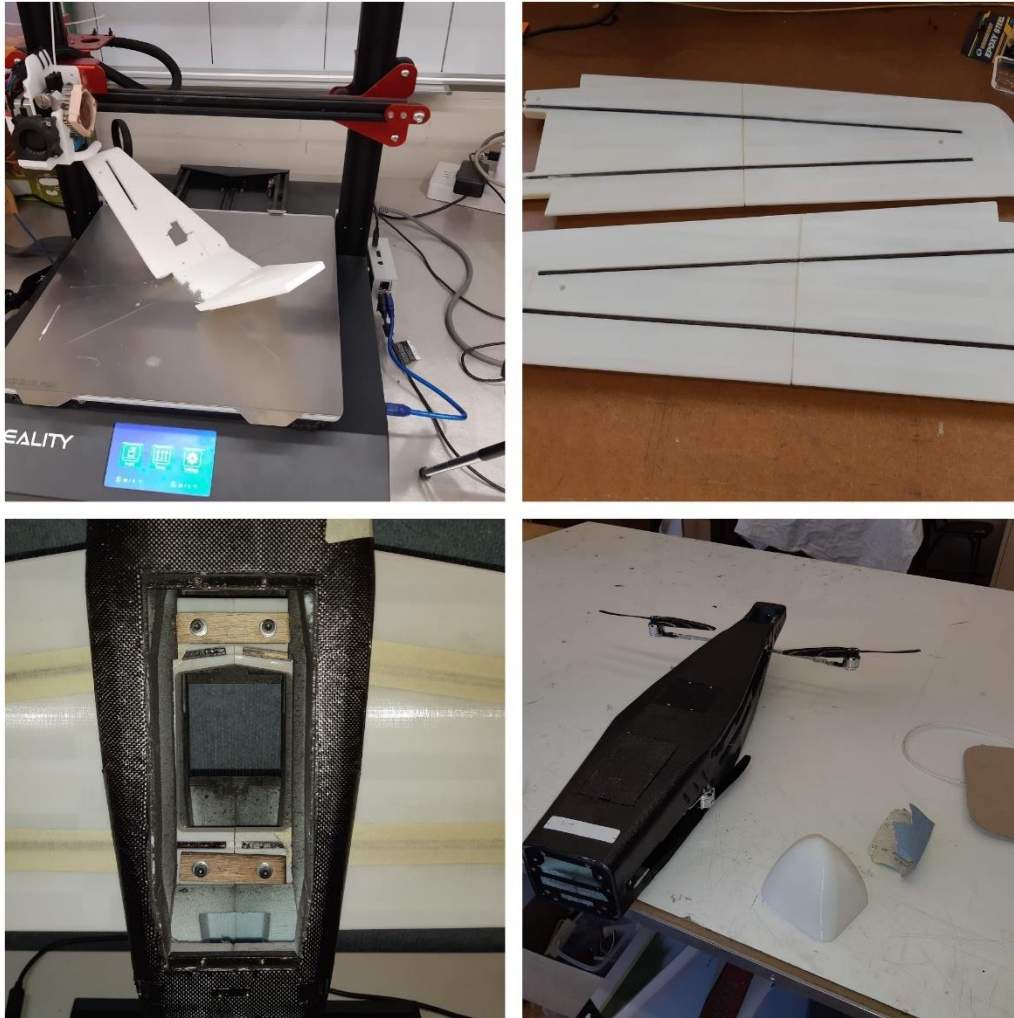


Figure 105: Parts used to assemble the fourth model. Starting from the top left and proceeding clockwise there are the 3D printed tail, the 3D printed wings, the fuselage provided by Krossblade, and the wing junction inside the fuselage.

The tests were conducted at the University of Sydney 7 ft by 5 ft low-speed wind tunnel. It has an operating range of 1 to 38 m/s. Models are attached to a white fairing covering the angle of attack actuation assembly. A turntable in the floor provides the angle of sideslip. Data is sampled at 2000Hz for 2 seconds with an ATI mini 45 6-component load cell capable of measuring XYZ moments and forces up to 10 Nm and 290 N, respectively. To account for the vehicle mass and gravity vector at different angles of attack, the load cell is first biased, before running a tare angle of attack sweep. Figure 106 shows the University of Sydney 7 ft by 5 ft low-speed wind tunnel.

Tamas Christiaan Bykerk, Ph.D. student in hypersonic vehicle aerodynamic stability at the University of Sydney, guided me in the operation of the wind tunnel and taught me how to use it. He was able to find the load cell and the bolts scattered around the campus, and he supported me through the tests.

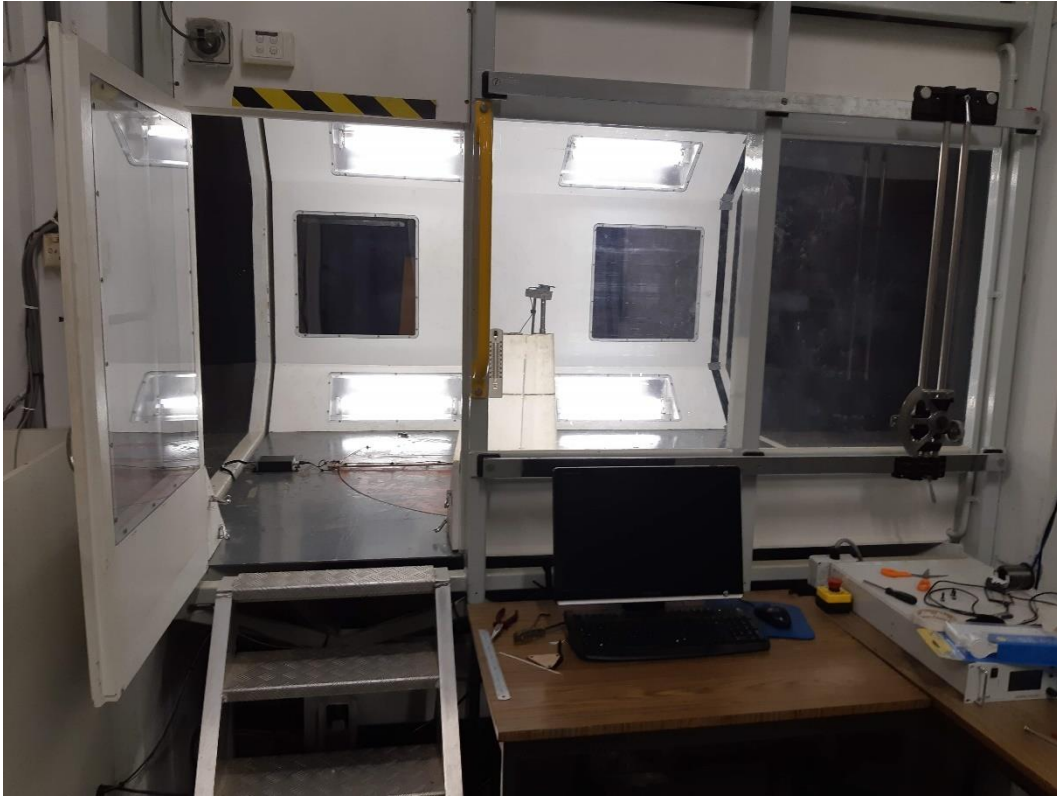


Figure 106: University of Sydney 7 ft by 5 ft low-speed wind tunnel

The four models tested were the Mini Talon 1, Mini Talon 2, Mini Talon 3, and the Krossblade SkyProwler. From this point on, the last model tested will be called SkyProwler, but it does not represent the real SkyProwler for the evident differences due to the 3D printed parts we realized. The aerodynamic performances we measured are inferior to the actual SkyProwler's performances.

Figure 107 shows the Mini Talon 1 in the wind tunnel bolted to the angle of attack actuation assembly. Figure 108 to Figure 111 show the Mini Talon 2 with the propellers in the four positions applied during the tests. The Mini Talon 3 was not tested only in its basic configuration, but the propellers were rotated first and then removed to measure the drag they generate when they are parallel to the airflow and when they are perpendicular to it. Finally, also the motors were removed, and the Mini Talon 3 was tested to measure the drag of the motors. Figure 112 to Figure 115 show the Mini Talon 3 in the wind tunnel in the four configurations tested. In Figure 112 the propellers are parallel to the airflow, in Figure 113 they are perpendicular to it, in Figure 114 they have been removed, and in Figure 115 also the motors have been removed. Figure 116 and Figure 117 show the SkyProwler in the wind tunnel, with the propellers extracted in the former and retracted in the latter.



Figure 107: Mini Talon 1 in the University of Sydney 7 by 5 wind tunnel.



Figure 108: Mini Talon 2, propellers retracted.



Figure 109: Mini Talon 2, propellers out 30°.



Figure 110: Mini Talon 2, propellers out 60°.



Figure 111: Mini Talon 2, propellers out 90°.



Figure 112: Mini Talon 3, propellers parallel to the airflow.



Figure 113: Mini Talon 3, propellers perpendicular to the airflow.



Figure 114: Mini Talon 3 without propellers.



Figure 115: Mini Talon 3 without propellers and motors.



Figure 116: Krossblade Skyproowler, propellers out.



Figure 117: Krossblade SkyProwler, propellers retracted.



Figure 118: Me in the wind tunnel with the SkyProwler model.

5.3 Test results

The tests were performed on the four models Mini Talon 1, Mini Talon 2, Mini Talon 3, and Krossblade Skyproowler in the configurations described above. The results are presented from Figure 119 to Figure 162. They are divided into three groups. The first two groups are dedicated to the Mini Talons and the last to the SkyProwler. The Mini Talon 1 results are presented in the first group with the Mini Talon 2 results and in the second group with the Mini Talon 3 results because they serve as a reference. For each group, we reported the lift coefficient, the drag coefficient, the lift to drag ratio, and the drag polar at various speeds.

The first group (Figure 119 to Figure 134) collects the results of the Mini Talon 1, and the Mini Talon 2 at the four retraction angles. Data has been sampled at four flight speeds, 10 m/s, 12.5 m/s, 15 m/s, and 17.5 m/s. The results at 10 m/s are useful because they allow a larger angle of attack range, from -10° to 10° at 10 m/s, without risking any damage to the structure. At higher speeds, we limited the angle of attack excursion, from -8° to 3° , because of the presence of vibration and because these models were under stress for the first time, and a structural failure might have damaged the entire wind tunnel. At 10 m/s, the angle of attack was increased over the stall, and its effects can be seen.

The second group (Figure 135 to Figure 150) collects the results of the Mini Talon 1 and the four versions of the Mini Talon 3. The same flight speed and angle of attack strategy applied to the first group was applied to the second.

The third group (Figure 151 to Figure 162) collects the results of the SkyProwler. As this airframe is flight-proven, we could confidently raise the flight speeds. The data was sampled at 10 m/s, 20 m/s, and 30 m/s. The low 10 m/s speed allowed us to measure the effects of the stall. At 30 m/s, the range of the angle of attack sweep was restrained for caution.

The figures portraying the lift coefficient of the three groups (Figure 119, Figure 120, Figure 121, Figure 122, Figure 135, Figure 136, Figure 137, Figure 138, Figure 151, Figure 152, and Figure 153) show that the lift coefficient is not affected by the external motor and propellers. Figure 119, Figure 135, and Figure 151 show the lift coefficient at 10 m/s. For this low speed, the angle of attack sweep was extended to high angles of attack, and the stall is visible. The lift coefficient is very high for angles of attack normally considered low. This is due to an offset in the load cell and its connection to the models. The measured data have been reported without changes.

After having discussed the lift coefficient figures of the three groups together, we will now discuss the remaining figures group by group.

Figure 123 to Figure 126 show the drag coefficient of the Mini Talon 2 with the propellers at various positions. The drag coefficient of the Mini Talon 1 is the lowest, closely followed by the Mini Talon 2 with propellers retracted. As the propellers open at 30° , 60° , and 90° , the drag increases progressively. The drag of the motors and propellers produce the first increase at 30° . The successive gradual increase is due to the increase in the frontal area of the supporting beams. The flight speed does not affect the drag coefficient because the variation in the Reynolds

number is marginal. The lines in the 10 m/s image, Figure 123, look closer to each other. This is only due to the wider angle of attack sweep that includes the stall region, which has much higher drag coefficients. These higher values increase the maximum value of the drag coefficient on the y-axis, making the low drag coefficient part look more compact. In all four images, the Mini Talon 1 results and the Mini Talon 2 with propellers retracted are very close. At certain flight speeds and angle of attack, the Mini Talon 2 drag coefficient is even lower than the Mini Talon 1's.

Figure 127 to Figure 130 show the lift to drag ratio of the Mini Talon 1 and the Mini Talon 2 with propellers at four angles. Here the effect of the propellers retraction system is substantial. The Mini Talon 1 and Mini Talon 2 with propellers retracted reach maximum lift to drag ratios from 16 to 18 while the Mini Talon 2 with propellers extracted reaches only lift to drag ratios from 6 to 9.

Figure 131 to Figure 134 show the Mini Talon 1 and 2 drag polars. Similar qualitative considerations apply to these graphs as to the drag coefficient graphs. The propellers create a significant drag that affects the whole range of lift coefficients uniformly. The polar has the advantage that it allows us to find the drag coefficient quickly for a cruise setting. The lift coefficient can be computed from the weight, and the drag coefficient is directly found from the graph. With this procedure, the cruise drag coefficient of the Mini Talon with open propellers and retracted propellers has been found, and the reduction in drag has been computed. Table 34 shows the Mini Talon reference data. The cruise speed is 17.5 m/s which corresponds to 63 km/h. The mass is 2.45 kg, slightly less than the mass budget because not all the instruments would be mounted at the same time. The wing surface is 0.314 m^2 and the air density 1.225 kg/m^3 . The resulting cruise lift coefficient is 0.4. Table 34 collects the Mini Talon reference data.

Table 34: Mini Talon reference data.

| | | |
|-------------------------|--------|-----------------|
| Airspeed | 17.5 | m/s |
| Reynolds number | 280000 | |
| Takeoff mass | 2.45 | kg |
| Air density | 1.225 | kg/m^3 |
| Reference surface | 0.314 | m^2 |
| Wingspan | 1.28 | m |
| Chord | 0.245 | m |
| Cruise lift coefficient | 0.4 | |

Inserting a lift coefficient of 0.4 in Figure 134, a drag coefficient of 0.079 is found for the Mini Talon 2 with propellers out at 90° , a drag coefficient of 0.029 is found for the Mini Talon 2 with propellers retracted, and the same value for the Mini Talon 1.

The drag reduction, D_r , is defined as the difference between the initial drag C_{D_i} and the final drag C_{D_f} , divided by the initial drag:

$$D_r = \frac{C_{D_i} - C_{D_f}}{C_{D_i}} \quad (78)$$

The drag reduction from the Mini Talon 2 with propellers out to the Mini Talon 2 with propellers retracted is 63%.

Figure 135 to Figure 150 show the data collected during the tests performed on the Mini Talon 3 model compared to the Mini Talon 1 data. These tests are important because the Mini Talon 3 represents the standard quadplane. The drag reduction measured above is not enough because the Mini Talon 2 with propellers retracted must not be compared to itself with propellers open but with the standard quadplane represented by Mini Talon 3. These data give also precious insights on the drag produced by the propellers, on the influence of the propellers orientation, on the drag produced by the motors, and on the drag produced by the propellers supporting beams parallel to the fuselage.

Figure 135 to Figure 138 show the lift coefficient of the Mini Talon 3. The different configurations tested do not present any noticeable difference in the lift coefficient.

Figure 139 to Figure 142 present the drag coefficient of the Mini Talon 3 configurations at various angles of attack. The effect of the propellers' orientation is significant. Propellers perpendicular to the airflow generate much more drag than propellers parallel to the airflow. This is an important indication for standard quadplanes, their takeoff propellers must be free to rotate and to align to the airflow. The difference between propellers parallel to the airflow and without propellers is modest. The drag produced by the motors is significant. We did not choose the motors paying attention to their size and their drag, but we focused on finding motors that were suited to provide the required performances. The VTOL propellers of a standard quadplane should be as aerodynamic as possible. The motors for quadrotor competitions are already aerodynamic and look suited for lighter quadplanes. Finally, the drag produced by the means is limited.

Figure 143 to Figure 146 show the lift to drag ratio of the Mini Talon 3 configurations. The results follow the indication provided by the four figures above, The Mini Talon 3 with propellers perpendicular to the airflow has the lowest lift to drag ratios, with a maximum value around 9. Its performances are similar to the Mini Talon 2 with propellers out. The propellers perpendicular to the airflow perform like the Mini Talon 2's supporting beams. The Mini Talon 3 with propellers parallel to the airflow and without propellers perform significantly better, with a maximum lift to drag ratios around 13. The performance of the configuration without motors is close to the Mini Talon 1's with a maximum lift to drag ratio around 17.

Figure 147 to Figure 150 show the drag polars of the Mini Talon 3 configurations. For a cruise C_l of 0.4, and 17.5 m/s airspeed, the drag coefficient of the standard VTOL configuration with propellers parallel to the airflow is 0.044. The drag reduction achievable is found using this as the initial value in equation (78) and the drag of the Mini Talon 2 with retracted propellers at a C_l of 0.4 and airspeed of 17.5 m/s, or 0.029, as the final value. The drag reduction found is 34%.

Figure 151 to Figure 162 show the data collected during the tests on the model realized with the fuselage provided by Krossblade aerospace. This SkyProwler was tested at 10, 20, and 30 m/s with propellers out and with propellers retracted.

Figure 151 to Figure 153 depict the lift to drag ratio of the Skyproowler. At 10 and 20 m/s, the effect of the propellers is negligible, and it becomes noticeable but still limited at 30 m/s. At this speed, the lift coefficient curve is pushed to the left, meaning that the same lift is generated at a lower angle of attack. The comparison with the lower speeds means that the difference in Reynolds number from 10 m/s to 30 m/s is important. At 30 m/s the flow might be turbulent, and the extracted propellers might generate some additional lift.

Figure 154 to Figure 156 show the SkyProwler’s drag coefficient. The propellers increase the drag coefficient over all the angles of attack, and their effect no difference can be noticed for the three different speeds.

Figure 157 to Figure 159 show the SkyProwler’s lift to drag ratio. The maximum value with propellers retracted is around 11s and it is around 8 with propellers extracted. At 30 m/s the angle of attack reached is not enough to measure high lift to drag ratios. The maximum values measured at this airspeed are 5 for propellers retracted and 3 for propellers extracted.

Figure 160 to Figure 162 show the SkyProwler’s drag polars. The 20 m/s drag polar has been used to compute the drag reduction with the procedure described above. A lift coefficient of 0.4 has been assumed. The drag coefficient with propellers extracted is 0.088, and the drag with propellers retracted is 0,062. The drag reduction is 30%. The drag reduction found for the SkyProwler is inferior to the one found for the Mini Talon 2. The SkyProwler’s VTOL propulsion system generates less drag because it is already optimized. The supporting bars are made of aluminum, and they are thin, while the Mini Talon 2’s bars are sturdy. The motors are smaller, and they generate less drag.

The drag reduction values found for the Mini Talon 2, Mini Talon 3, and SkyProwler are collected in Table 35.

Table 35: Drag reduction values found.

| | Drag reduction |
|---|----------------|
| Mini Talon 2 propellers extracted vs retracted | 63% |
| Mini Talon 3 vs Mini Talon 2 propellers retracted | 34% |
| SkyProwler propellers extracted vs retracted | 30% |

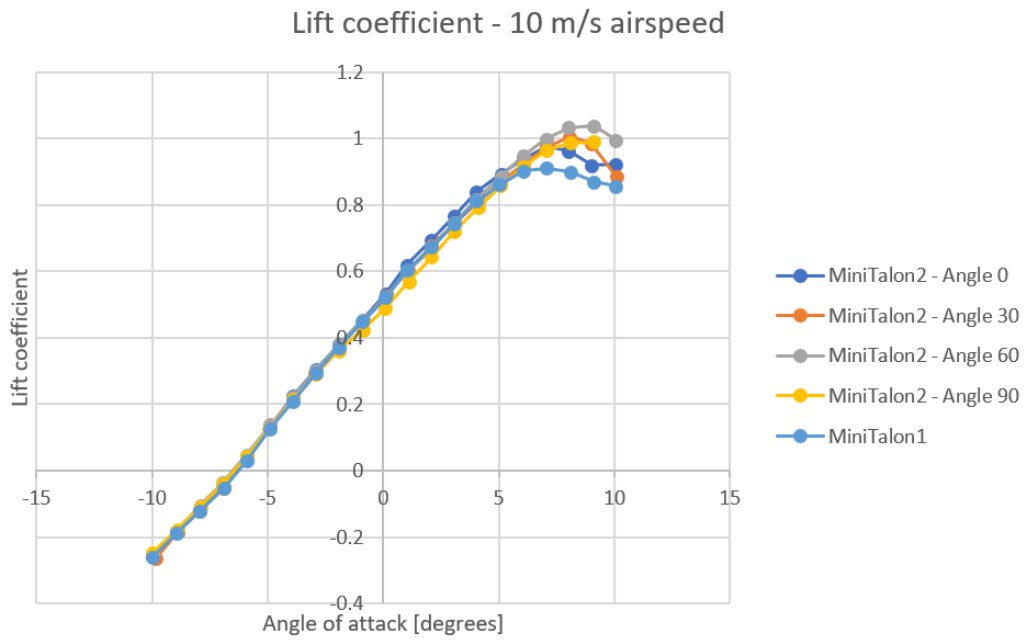


Figure 119: Mini Talon 2, lift coefficient, 10 m/s.

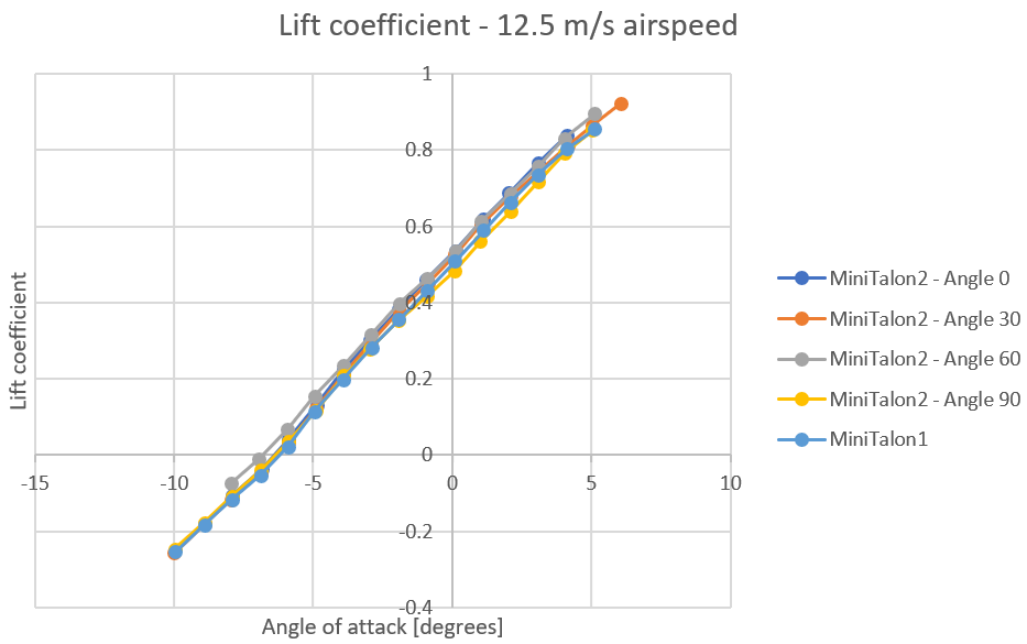


Figure 120: Mini Talon 2, lift coefficient, 12.5 m/s.

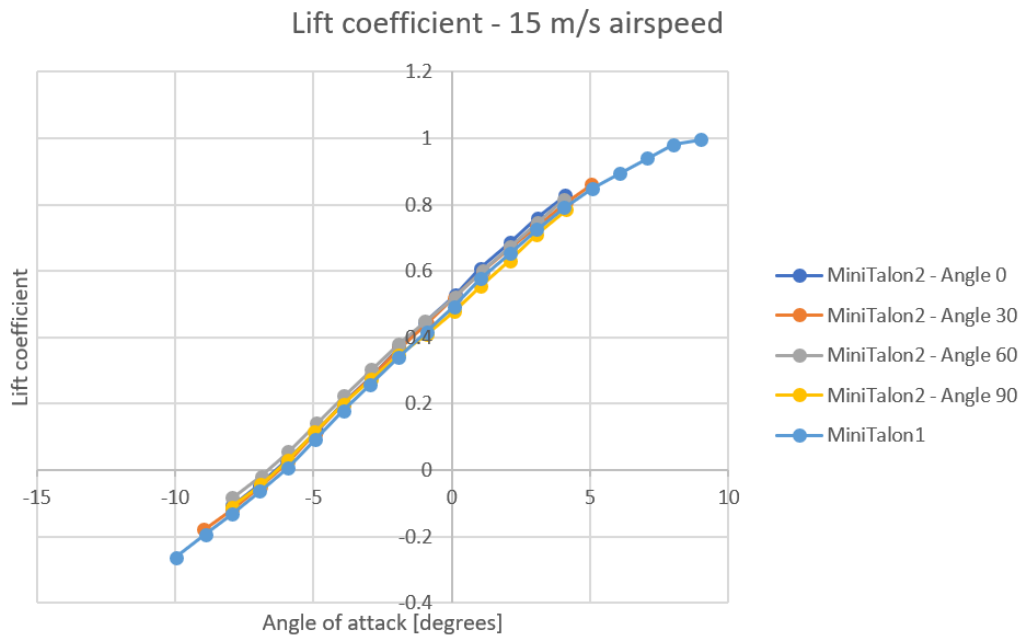


Figure 121: Mini Talon 2, lift coefficient, 15 m/s.

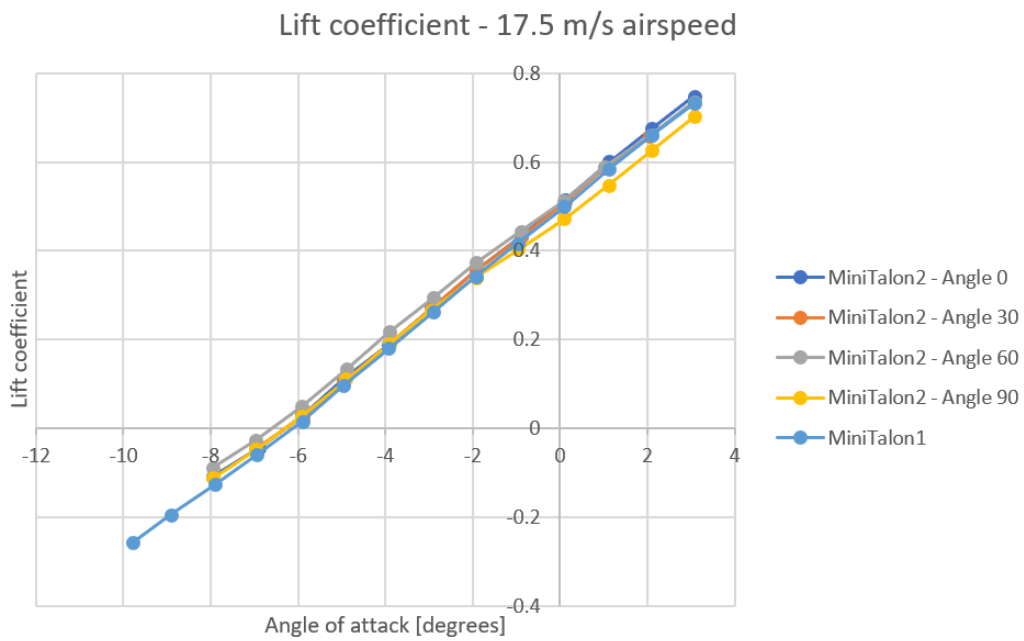


Figure 122: Mini Talon 2, lift coefficient, 17.5 m/s.

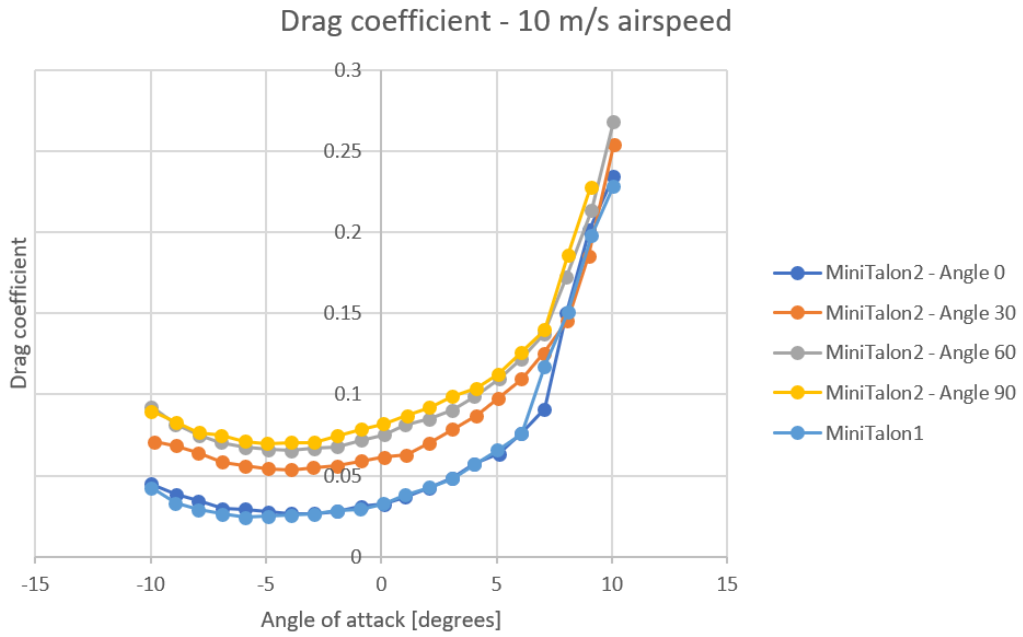


Figure 123: Mini Talon 2, drag coefficient, 10 m/s.

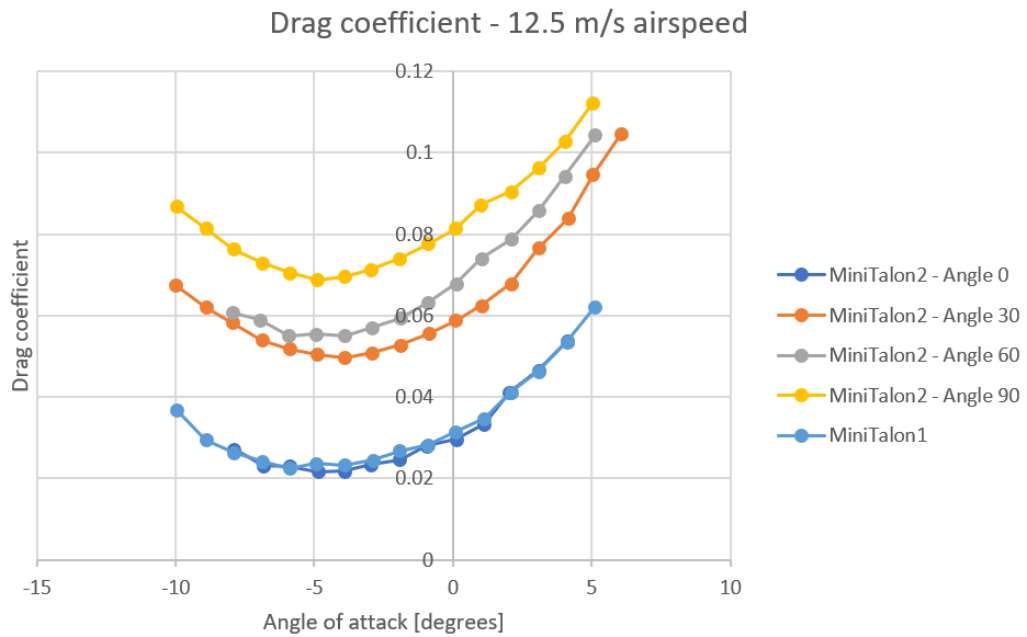


Figure 124: Mini Talon 2, drag coefficient, 12.5 m/s.

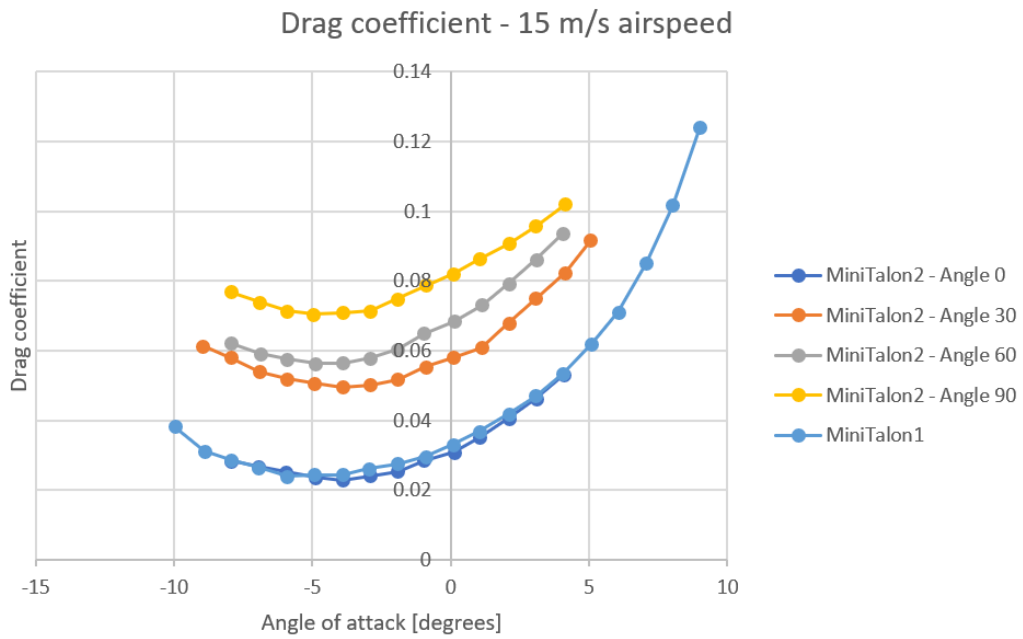


Figure 125: Mini Talon 2, drag coefficient, 15 m/s.

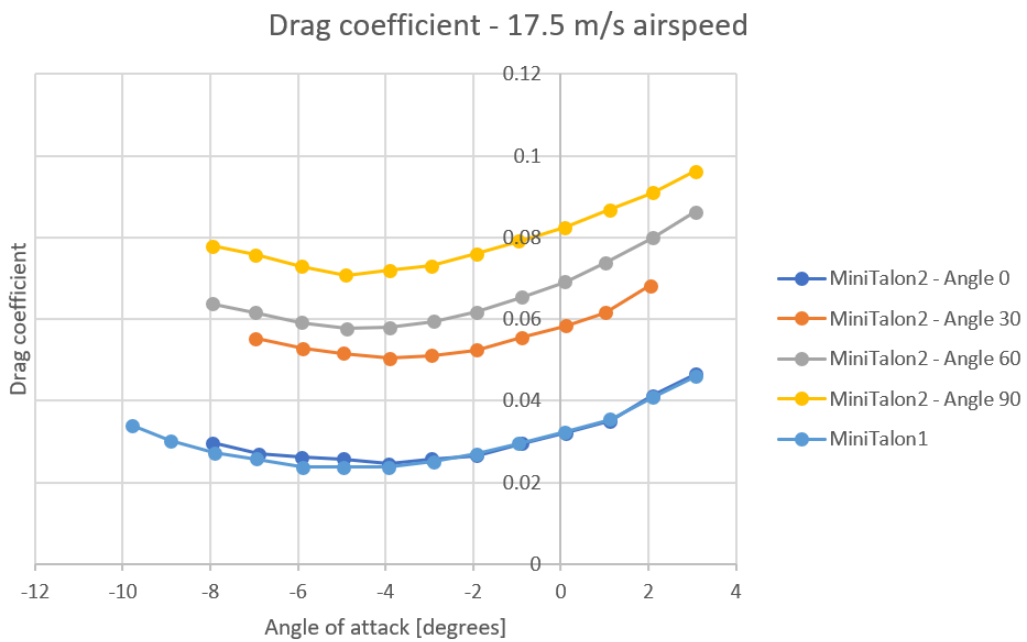


Figure 126: Mini Talon 2, drag coefficient, 17.5 m/s.

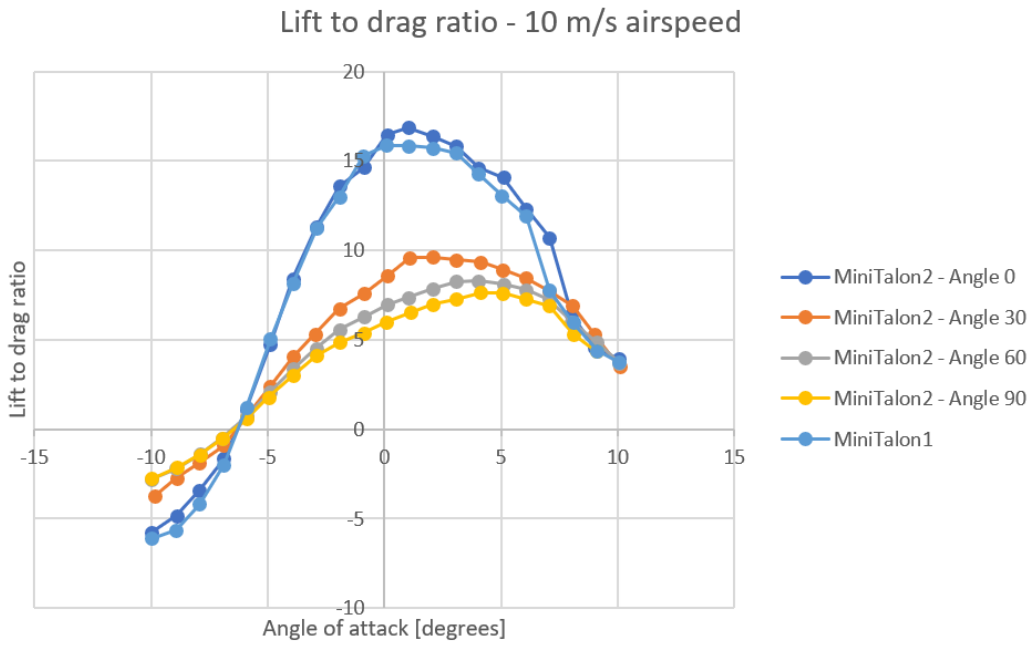


Figure 127: Mini Talon 2, lift to drag ratio, 10 m/s.

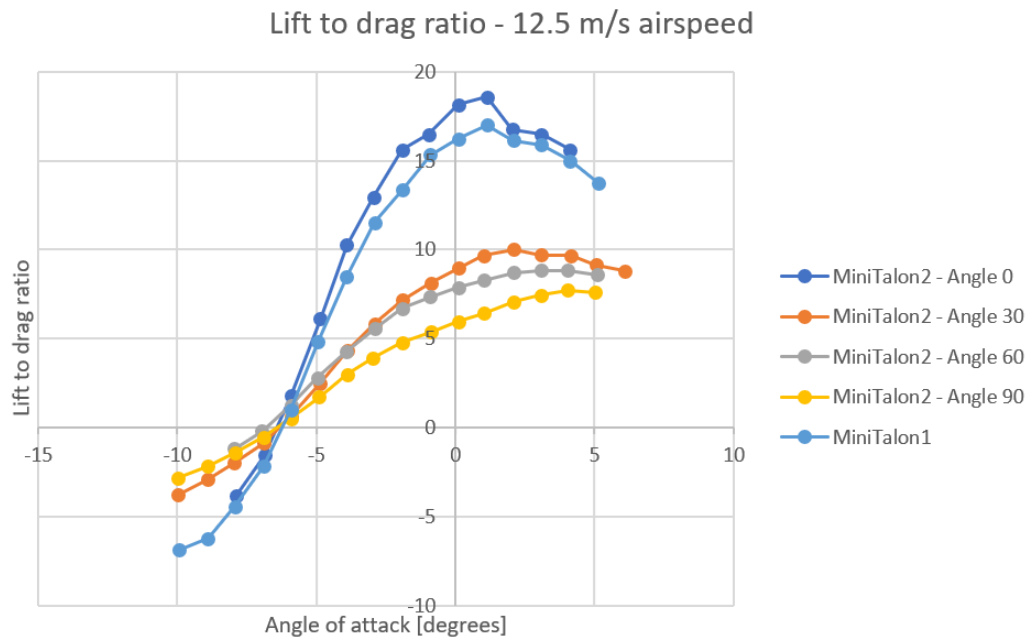


Figure 128: Mini Talon 2, lift to drag ratio, 12.5 m/s.

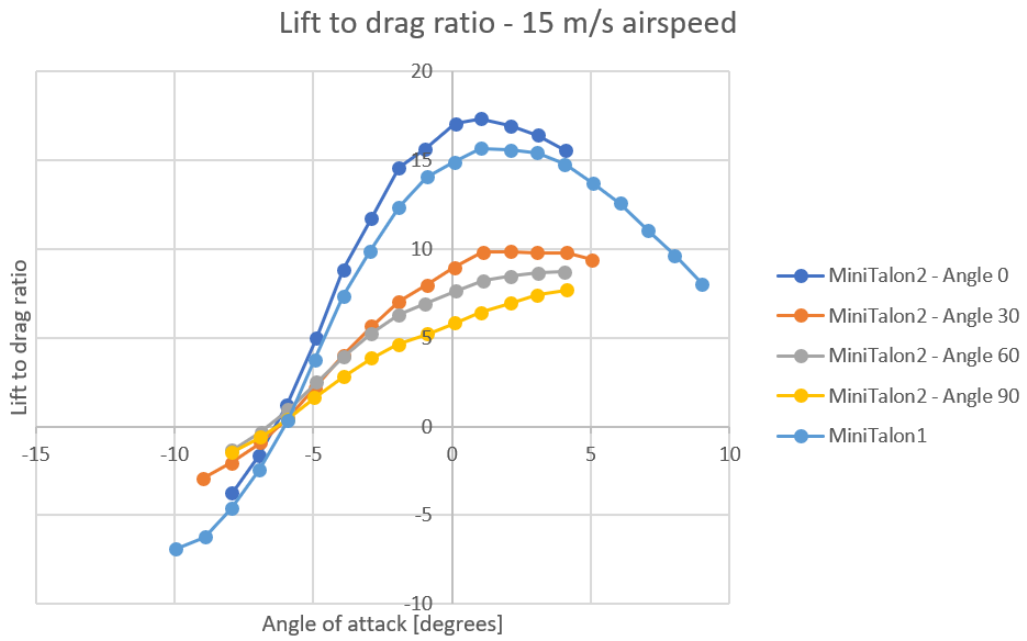


Figure 129: Mini Talon 2, lift to drag ratio, 15 m/s.

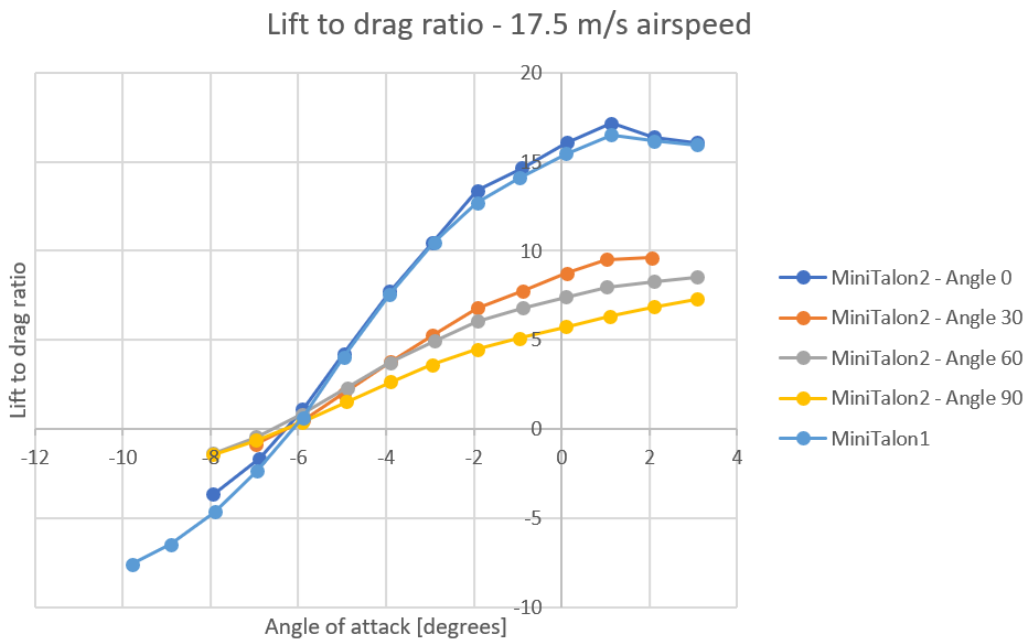


Figure 130: Mini Talon 2, lift to drag ratio, 17.5 m/s.

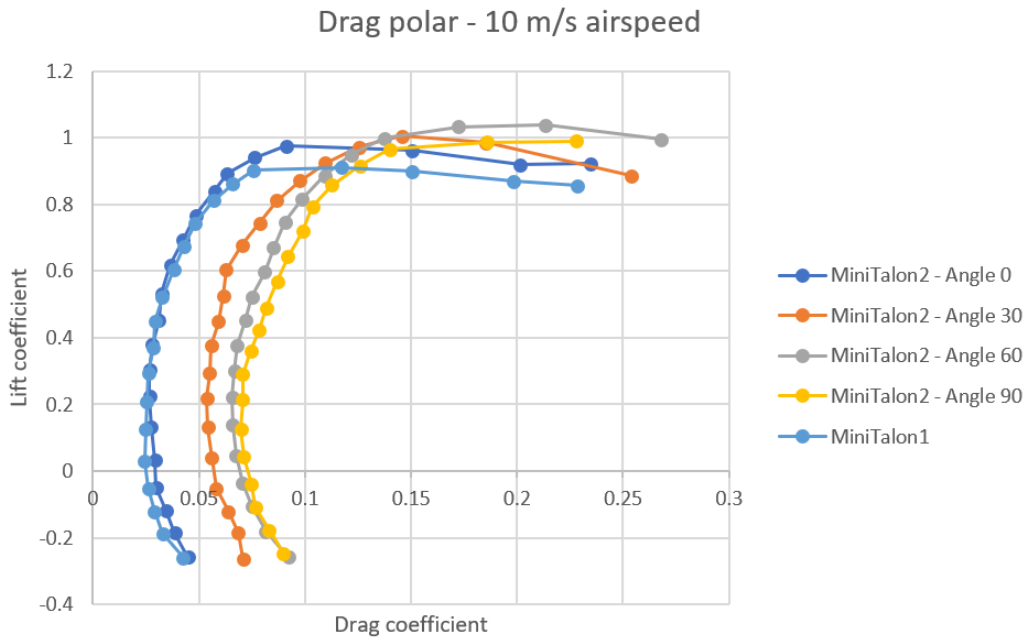


Figure 131: Mini Talon 2, drag polar, 10 m/s.

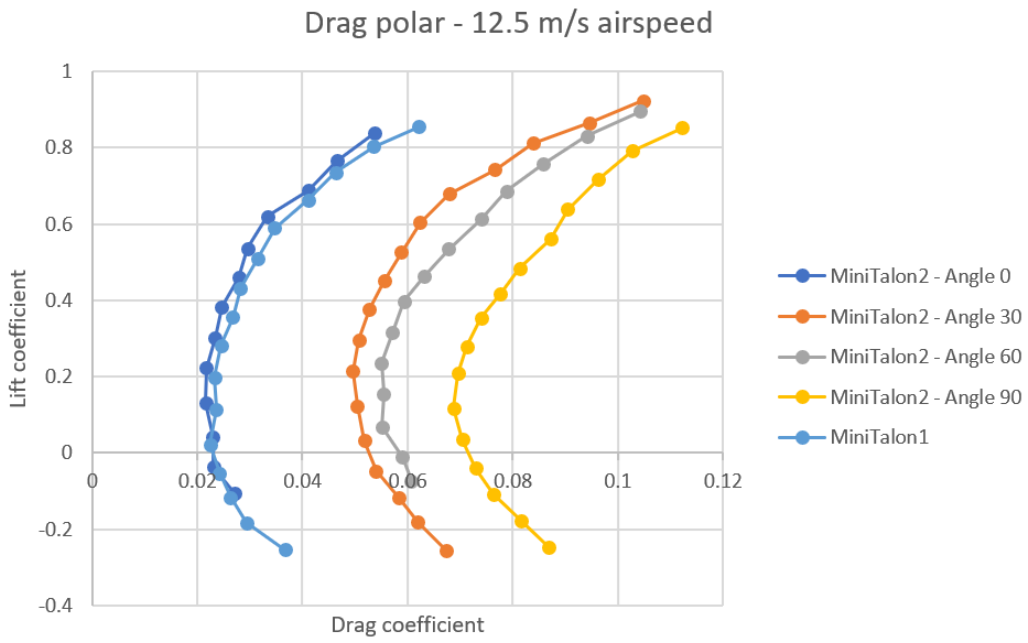


Figure 132: Mini Talon 2, drag polar, 12.5 m/s.

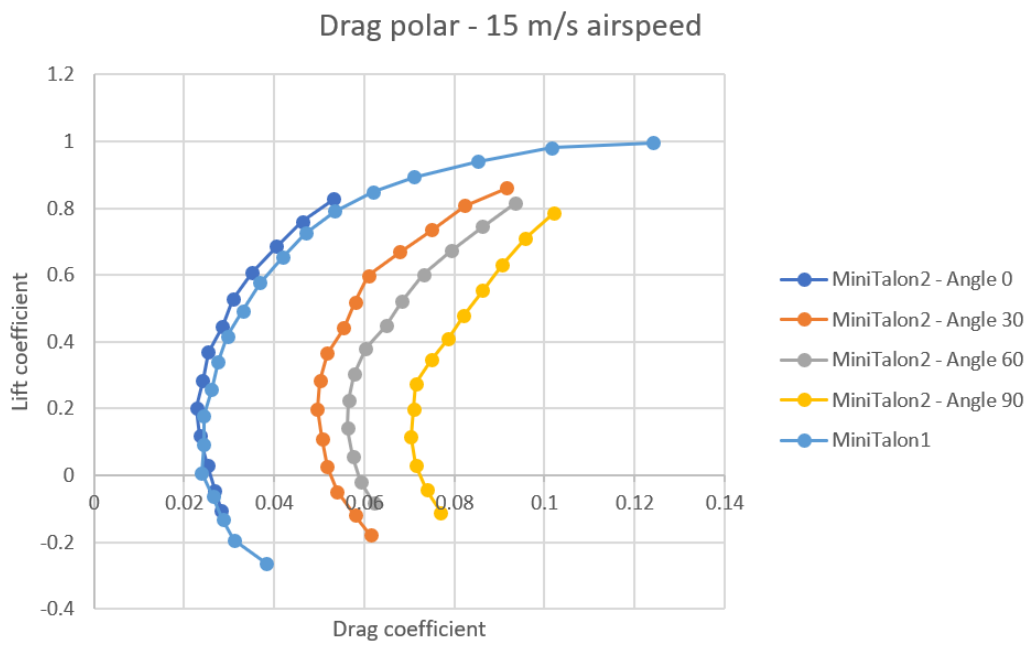


Figure 133: Mini Talon 2, drag polar, 15 m/s.

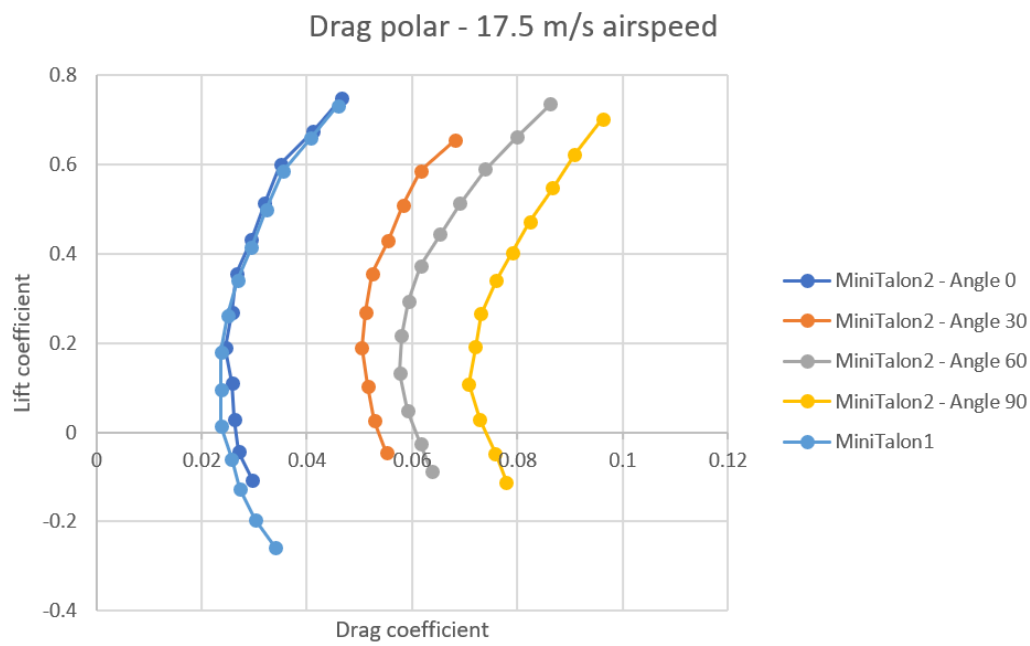


Figure 134: Mini Talon 2, drag polar 17.5 m/s.

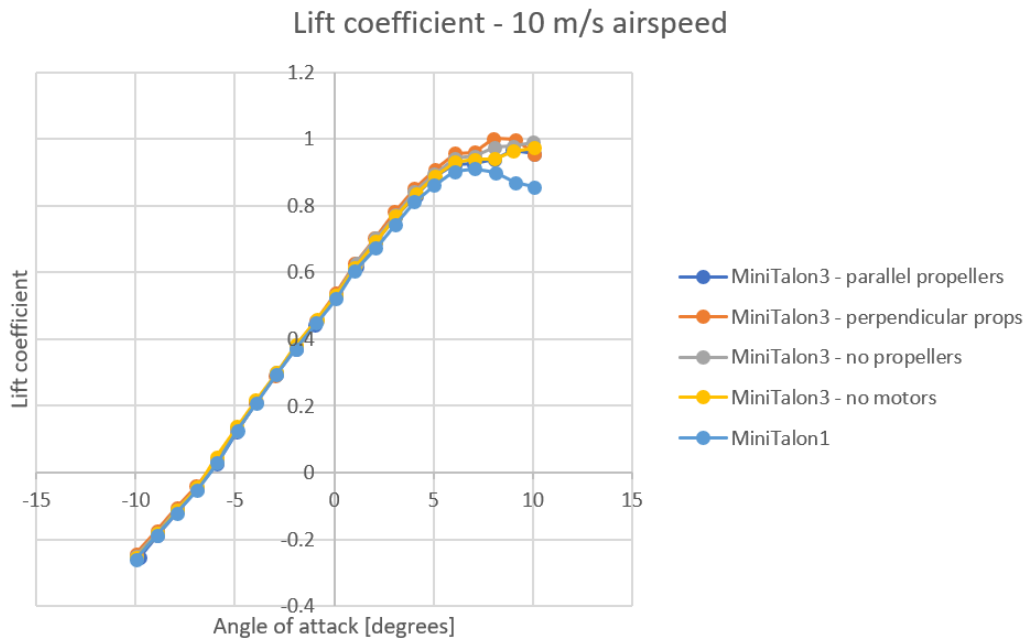


Figure 135: Mini Talon 3, lift coefficient, 10 m/s.

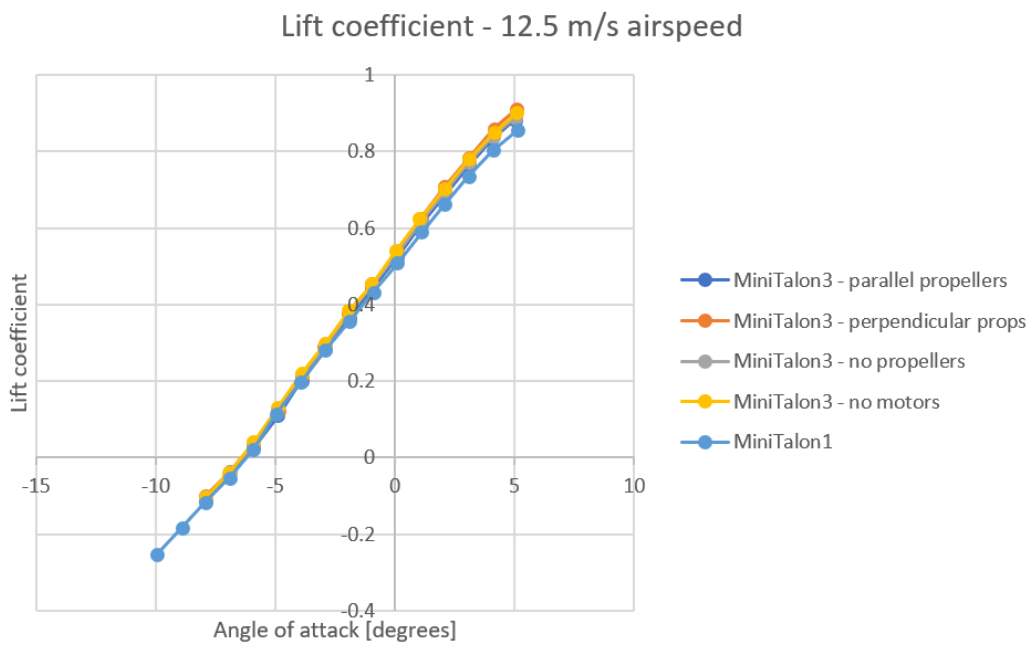


Figure 136: Mini Talon 3, lift coefficient, 12.5 m/s.

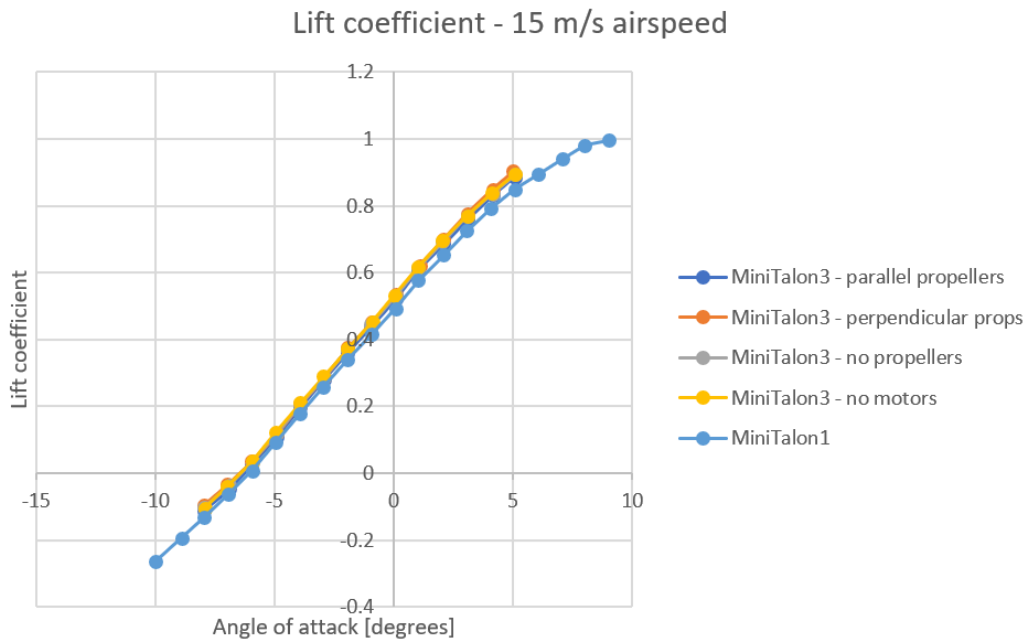


Figure 137: Mini Talon 3, lift coefficient, 15 m/s.

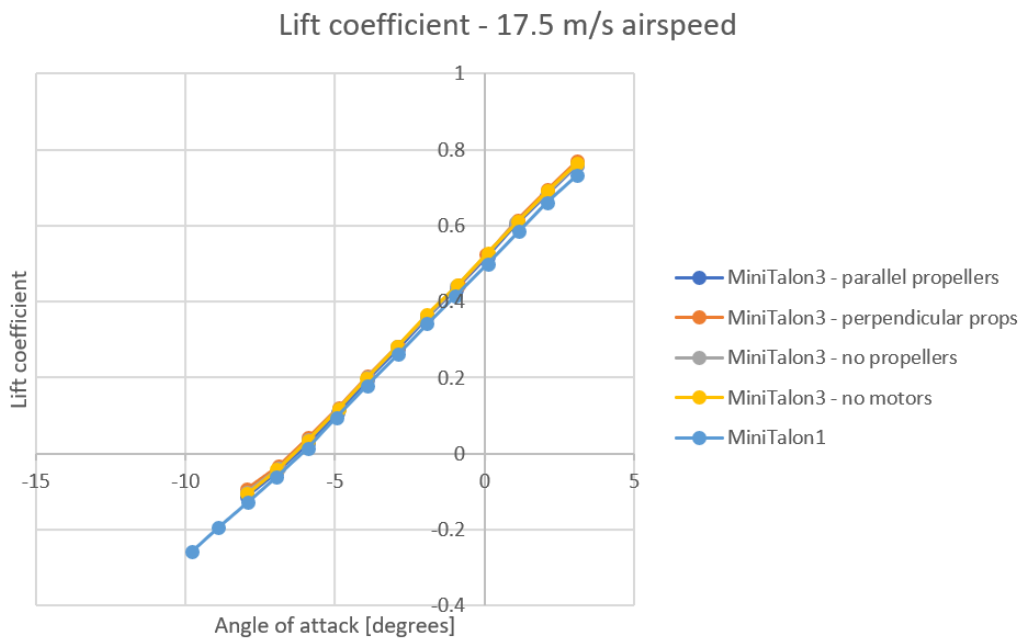


Figure 138: Mini Talon 3, lift coefficient, 17.5 m/s.

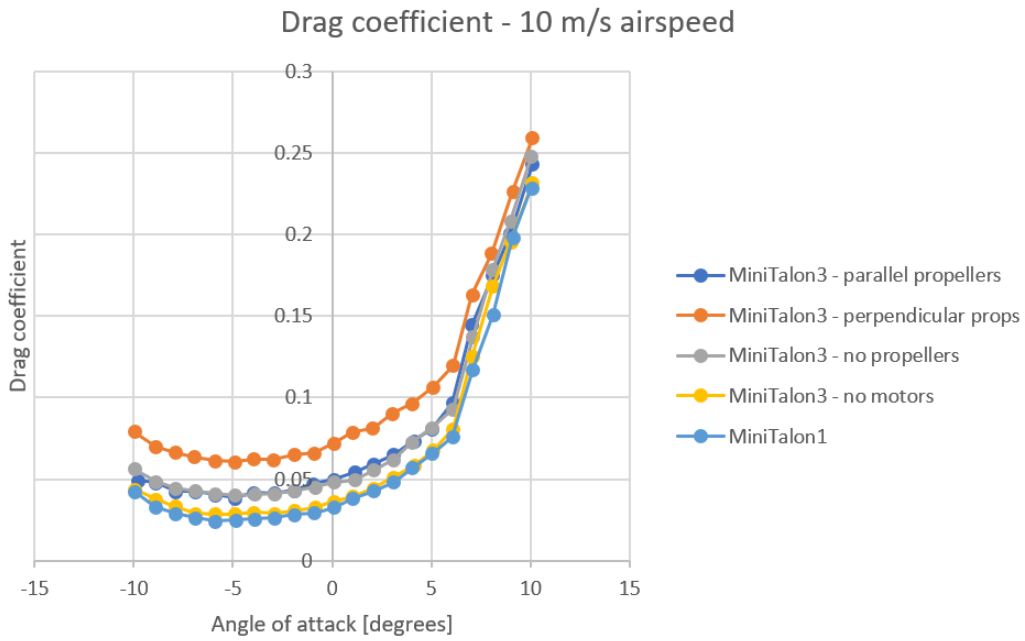


Figure 139: Mini Talon 3, drag coefficient, 10 m/s.

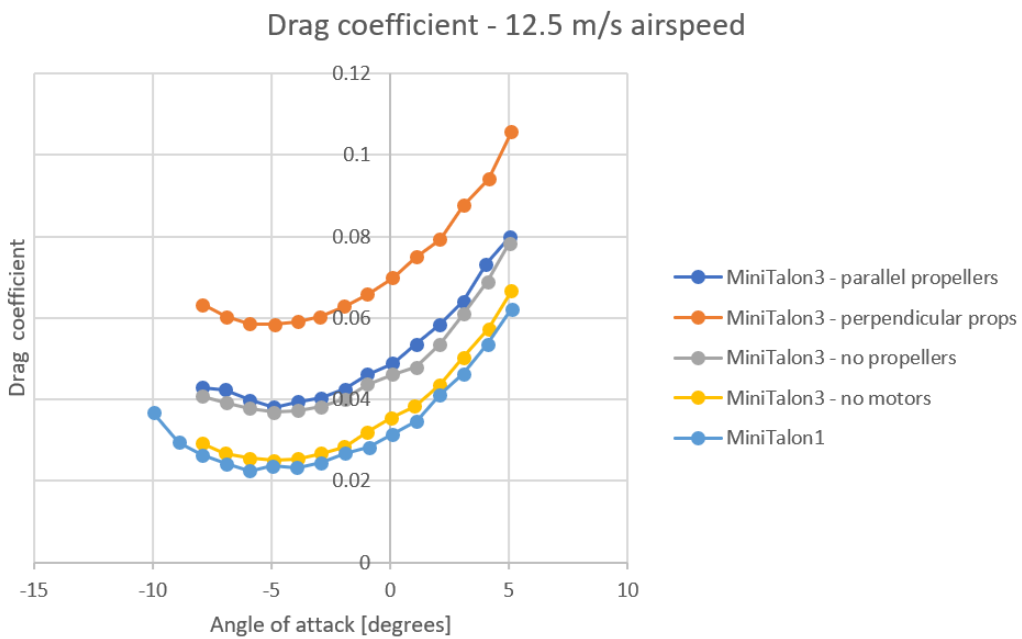


Figure 140: Mini Talon 3, drag coefficient, 12.5 m/s.

Drag coefficient - 15 m/s airspeed

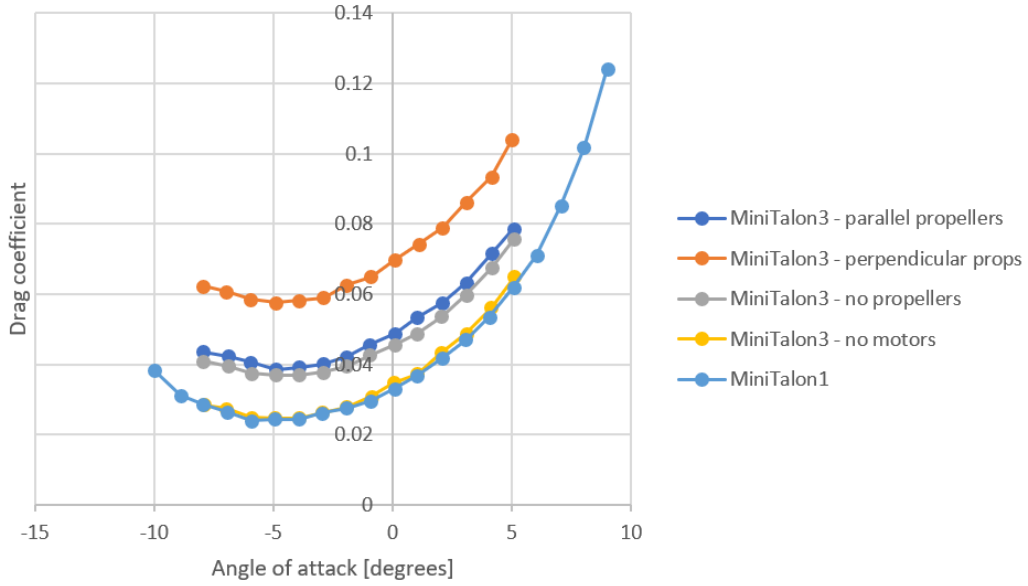


Figure 141: Mini Talon 3, drag coefficient, 15 m/s.

Drag coefficient - 17.5 m/s airspeed

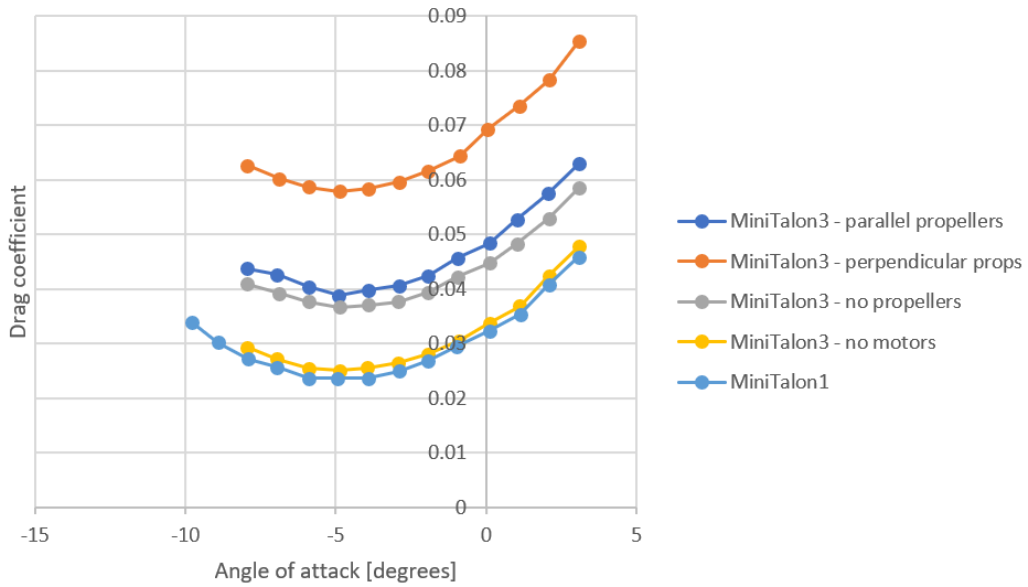


Figure 142: Mini Talon 3, drag coefficient, 17.5 m/s.

Lift to drag ratio - 10 m/s airspeed

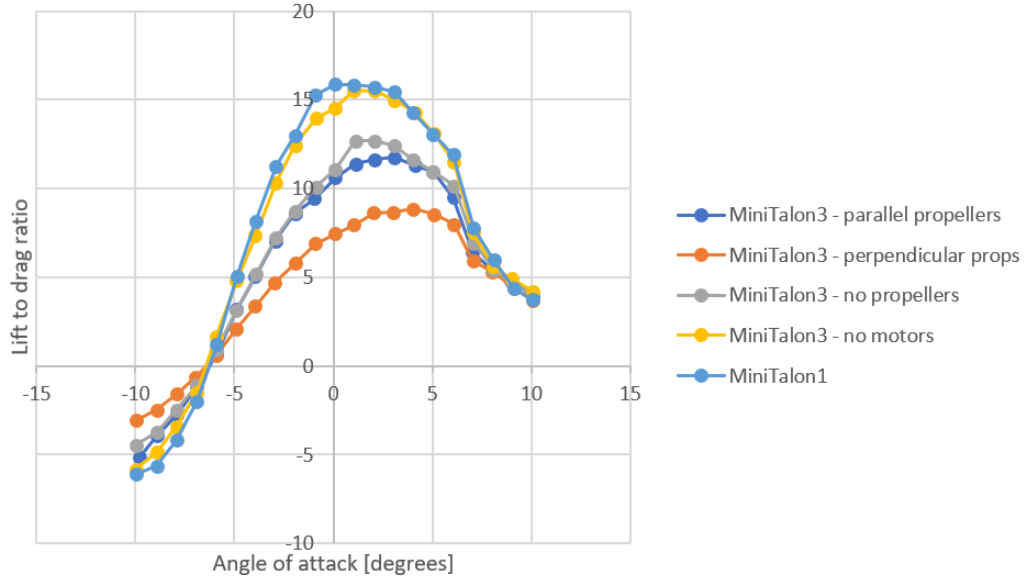


Figure 143: Mini Talon 3, lift to drag ratio, 10 m/s.

Lift to drag ratio - 12.5 m/s airspeed

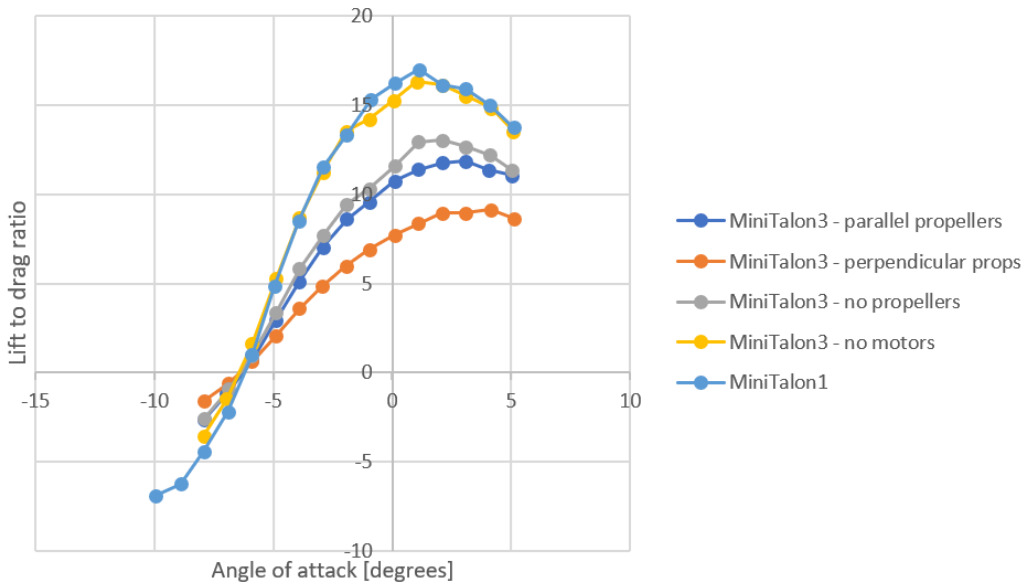


Figure 144: Mini Talon 3, lift to drag ratio, 12.5 m/s.

Lift to drag ratio - 15 m/s airspeed

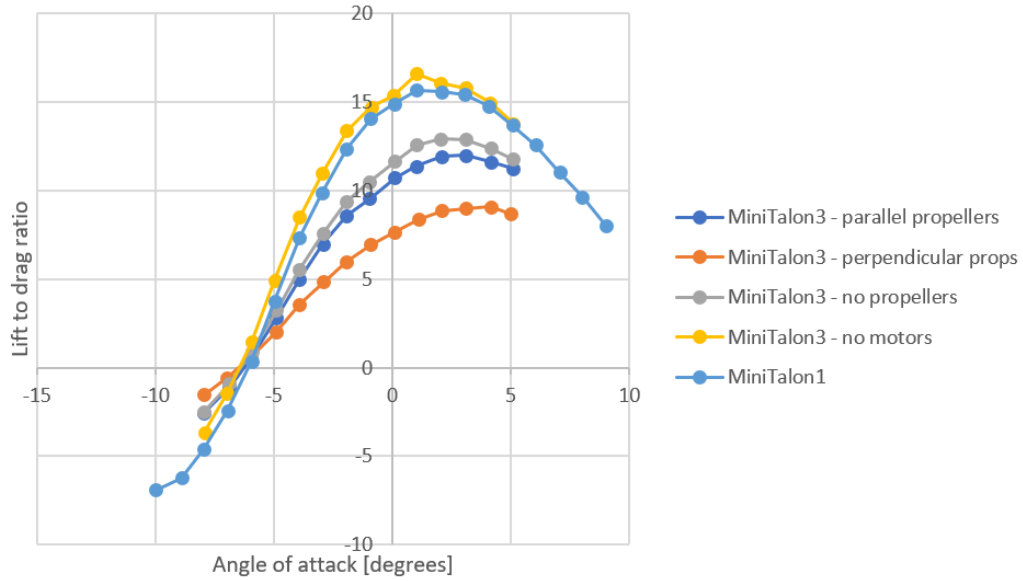


Figure 145: Mini Talon 3, lift to drag ratio, 15 m/s.

Lift to drag ratio - 17.5 m/s airspeed

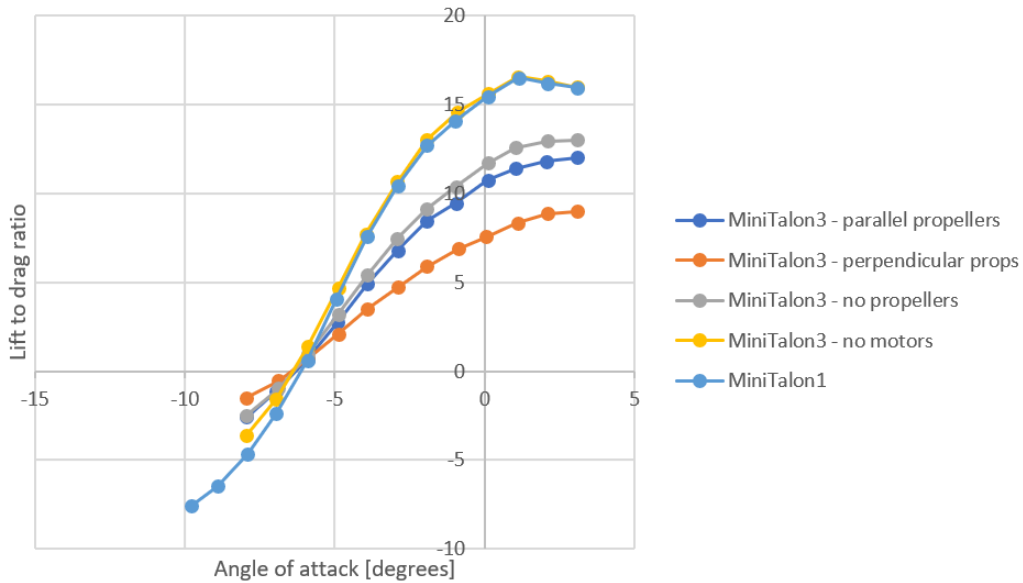


Figure 146: Mini Talon 3, lift to drag ratio, 17.5 m/s.

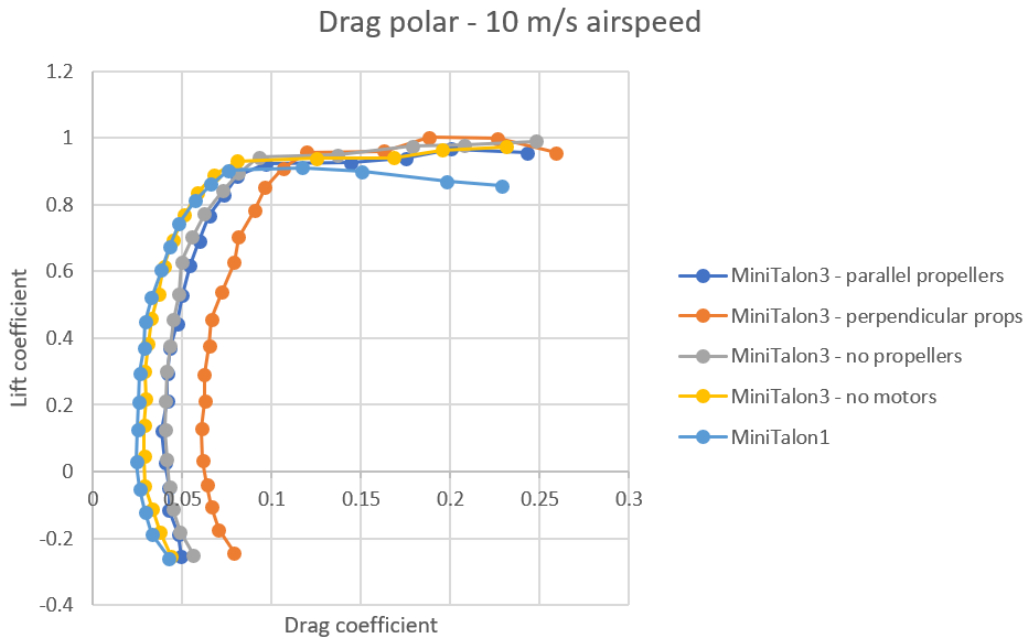


Figure 147: Mini Talon 3, drag polar, 10 m/s.

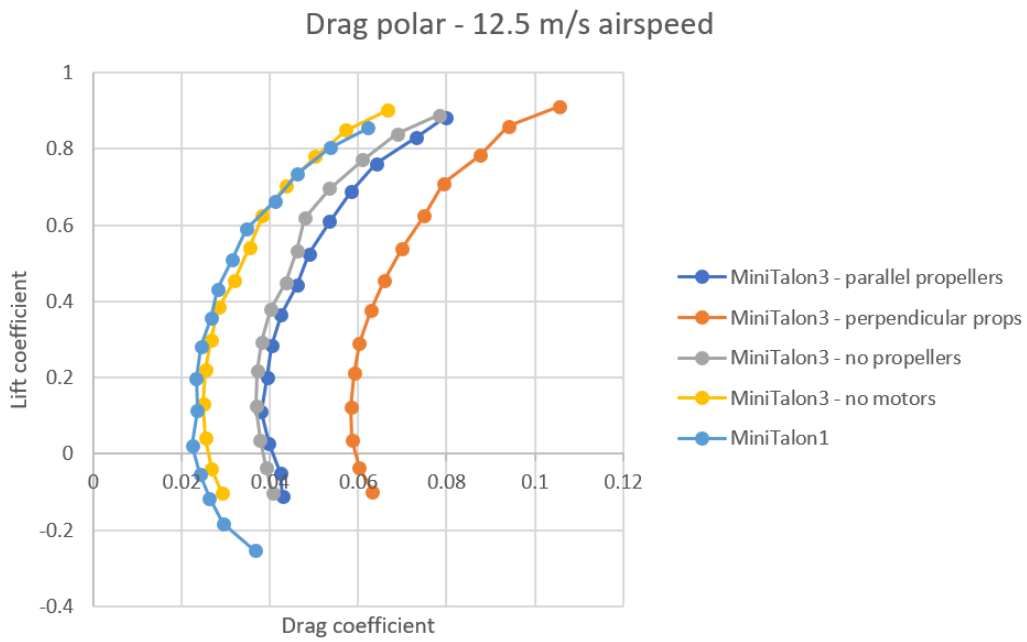


Figure 148: Mini Talon 3, drag polar 12.5 m/s.

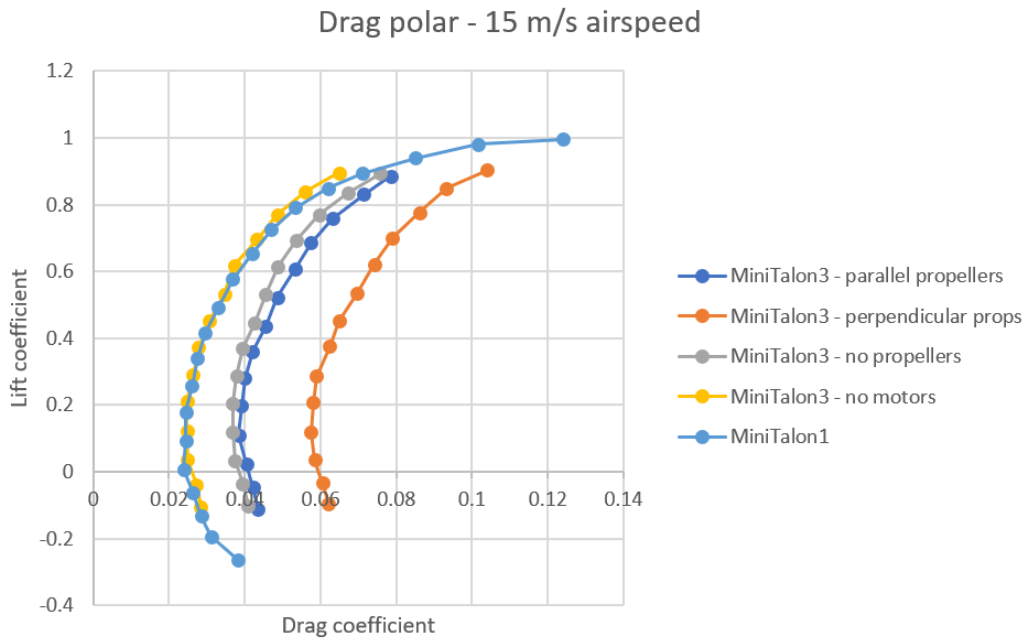


Figure 149: Mini Talon 3, drag polar, 15 m/s.

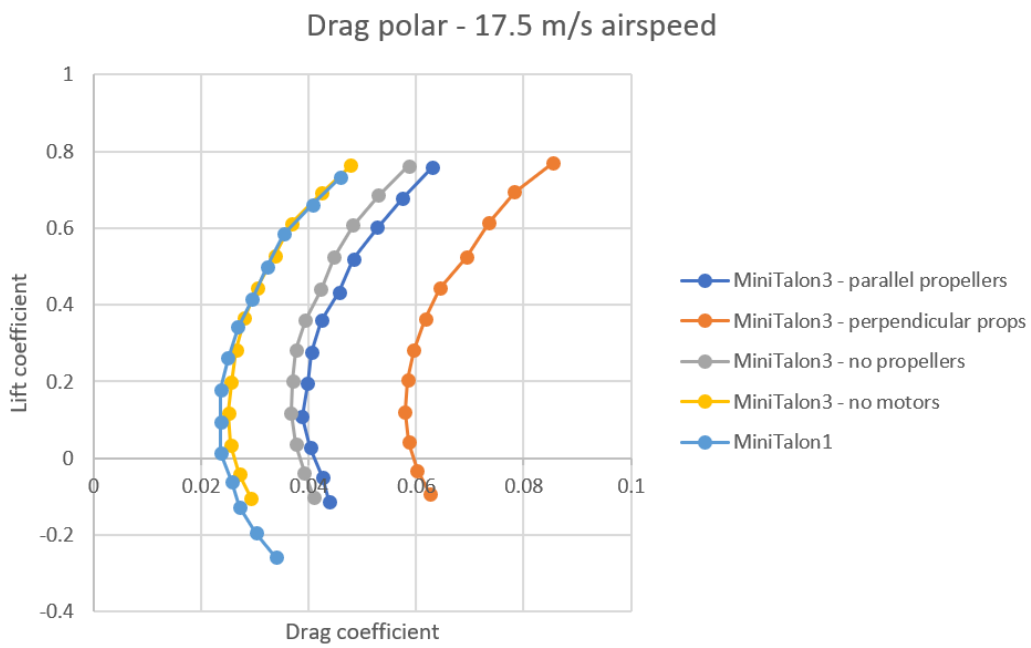


Figure 150: Mini Talon 3, drag polar, 17.5 m/s.

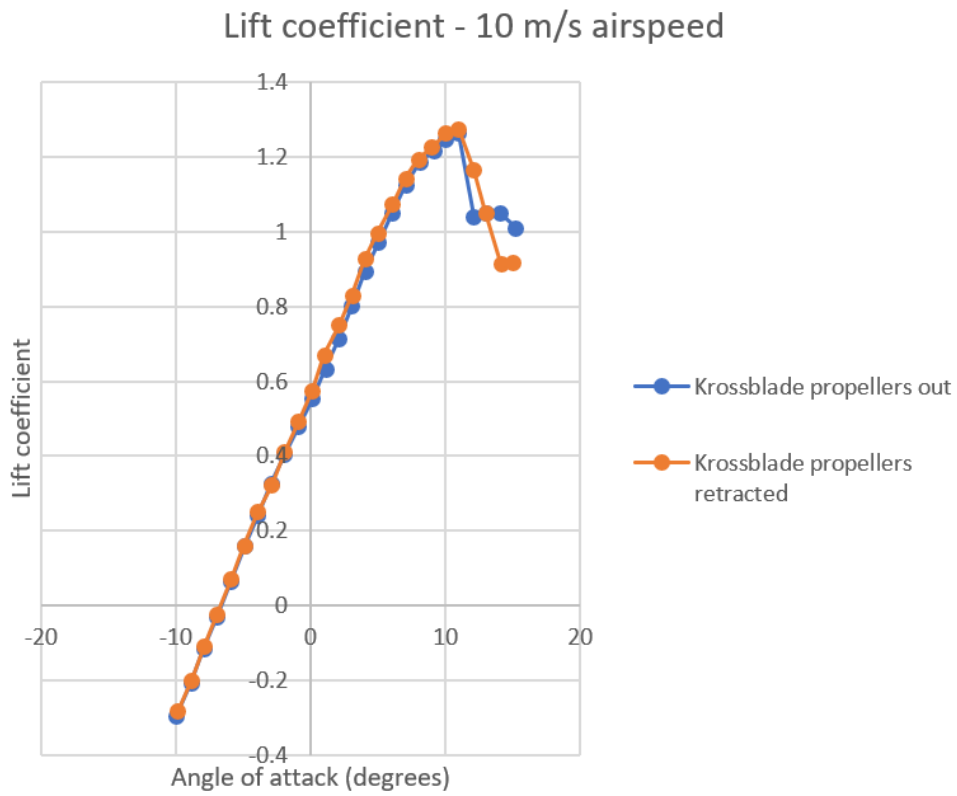


Figure 151: Krossblade SkyProwler, lift coefficient, 10 m/s.

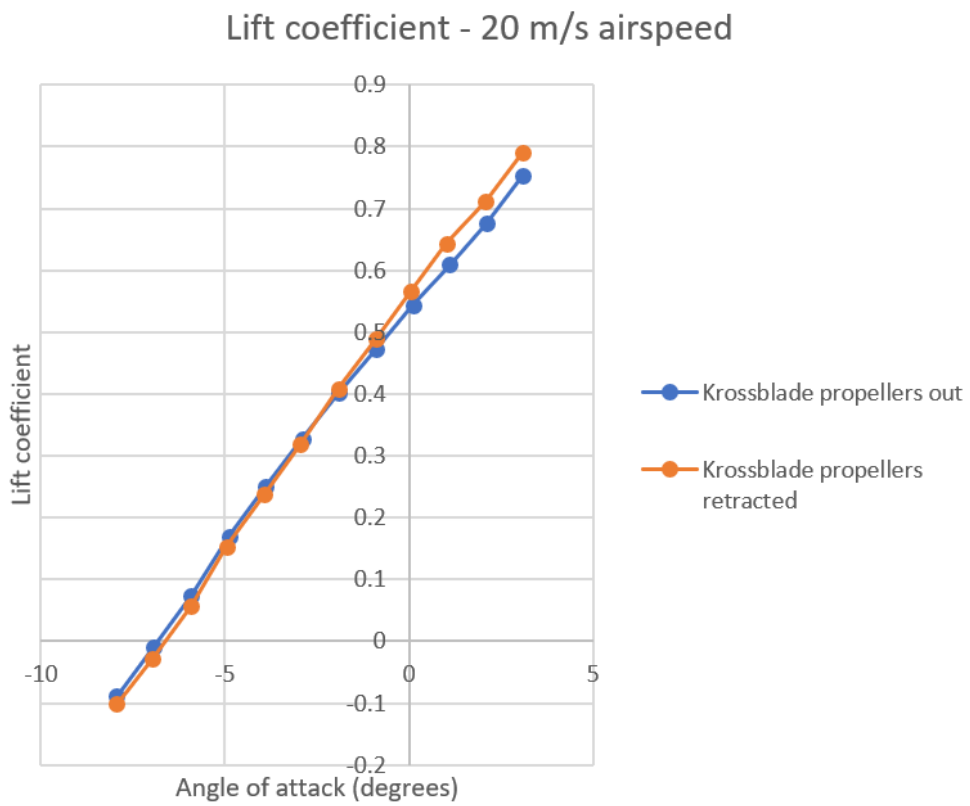


Figure 152: Krossblade SkyProwler, lift coefficient, 20 m/s.

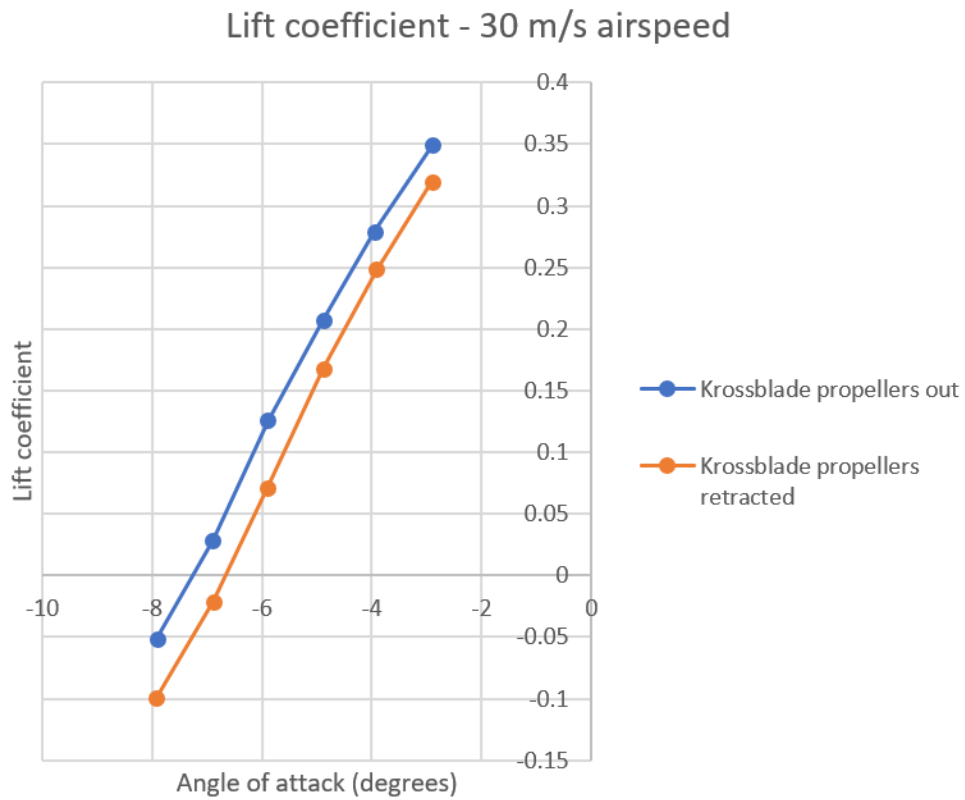


Figure 153: Krossblade SkyProwler, lift coefficient, 30 m/s.

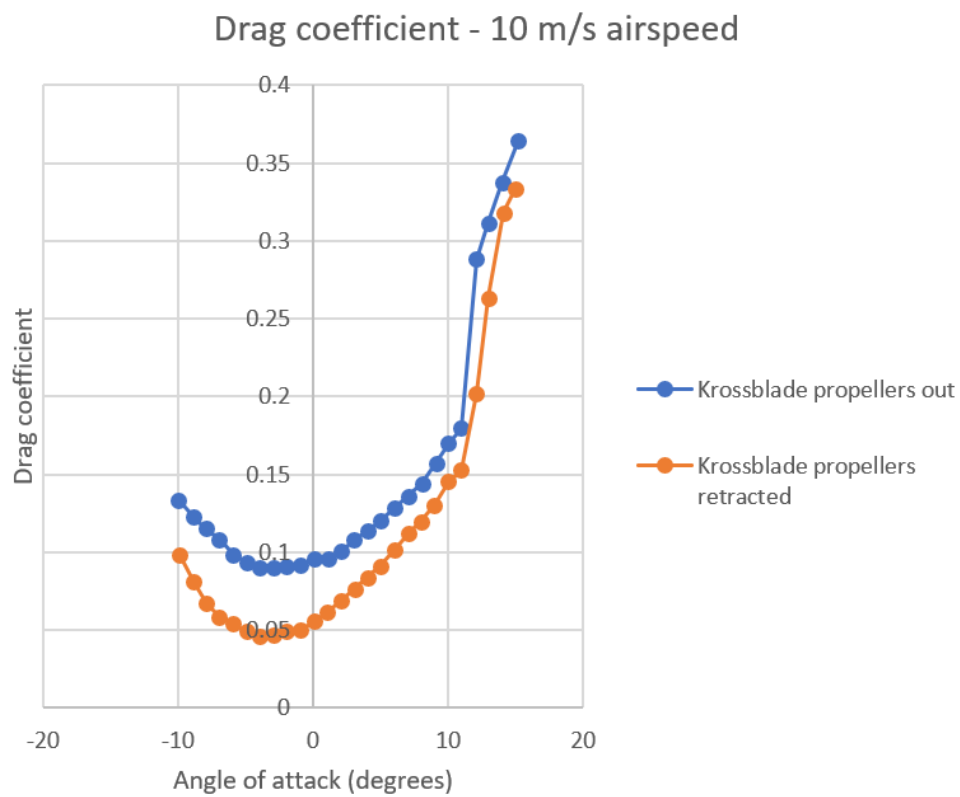


Figure 154: Krossblade SkyProwler, drag coefficient, 10 m/s.

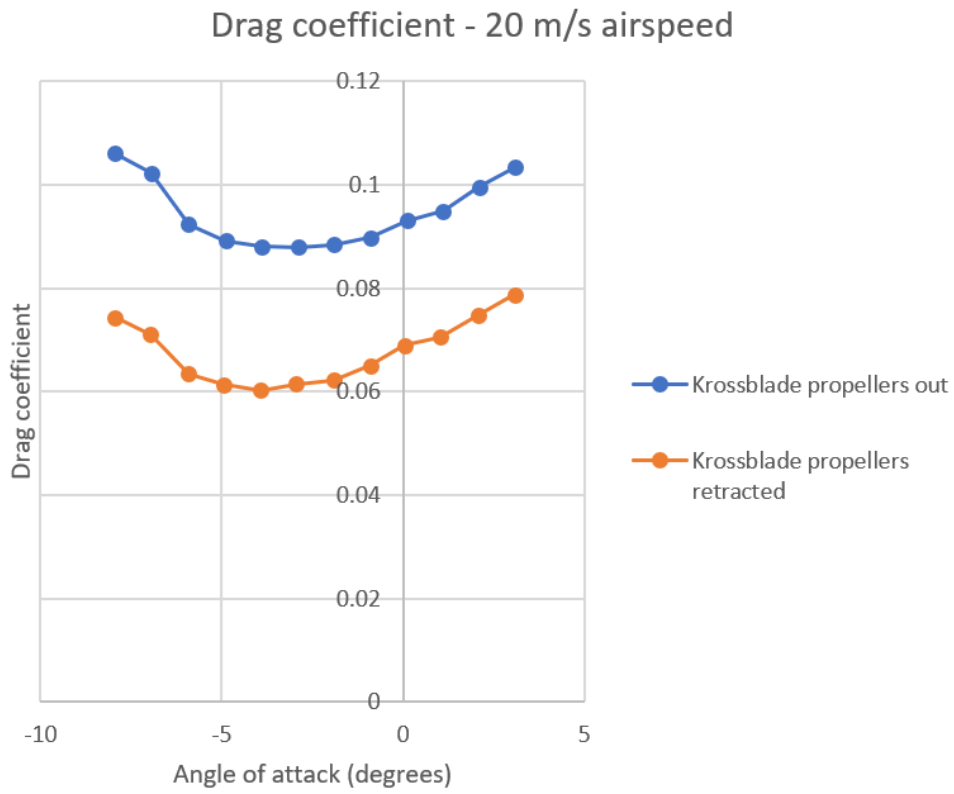


Figure 155: Krossblade SkyProwler, drag coefficient, 20 m/s.

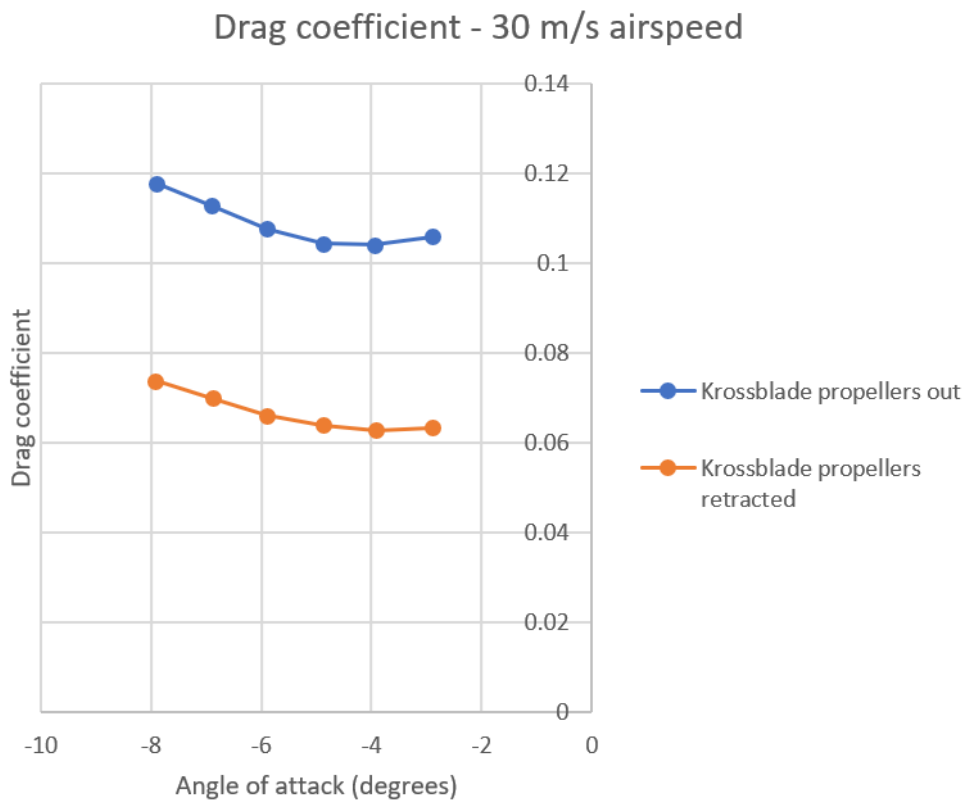


Figure 156: Krossblade SkyProwler, drag coefficient, 30 m/s.

Lift to drag ratio - 10 m/s airspeed

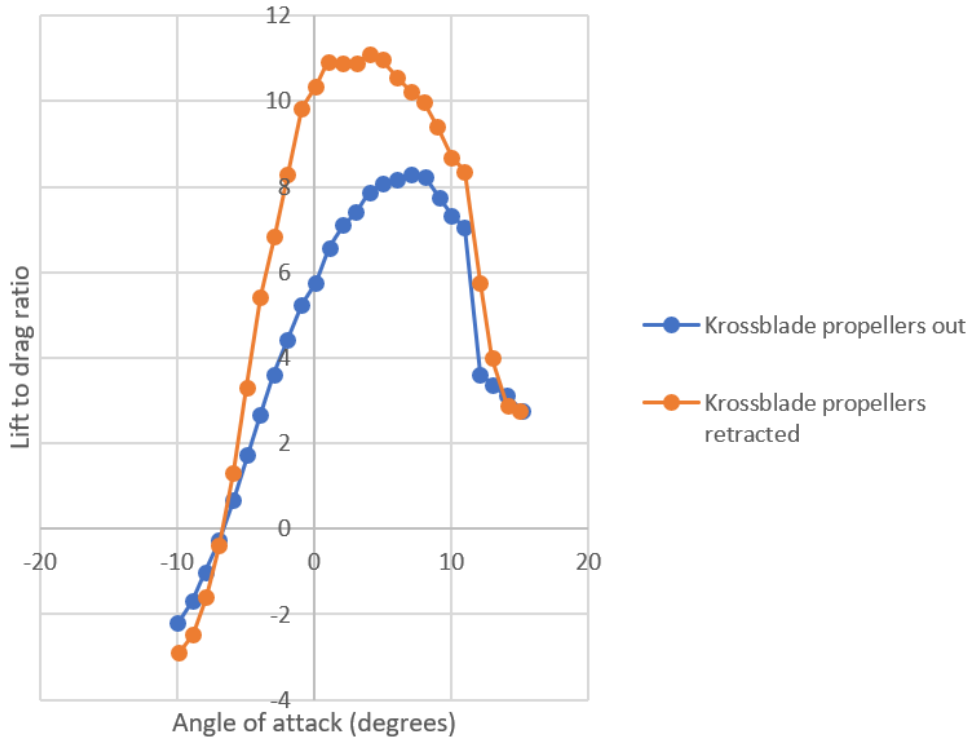


Figure 157: Krossblade SkyProwler, lift to drag ratio, 10 m/s.

Lift to drag ratio - 20 m/s airspeed

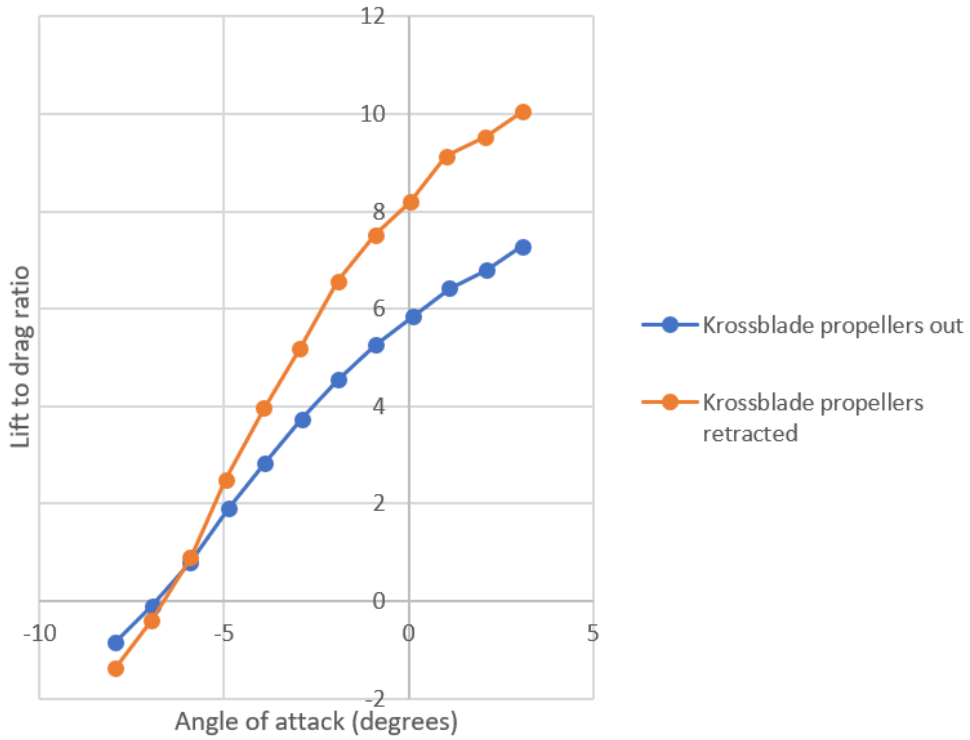


Figure 158: Krossblade SkyProwler, lift to drag ratio, 20 m/s.

Lift to drag ratio - 30 m/s airspeed

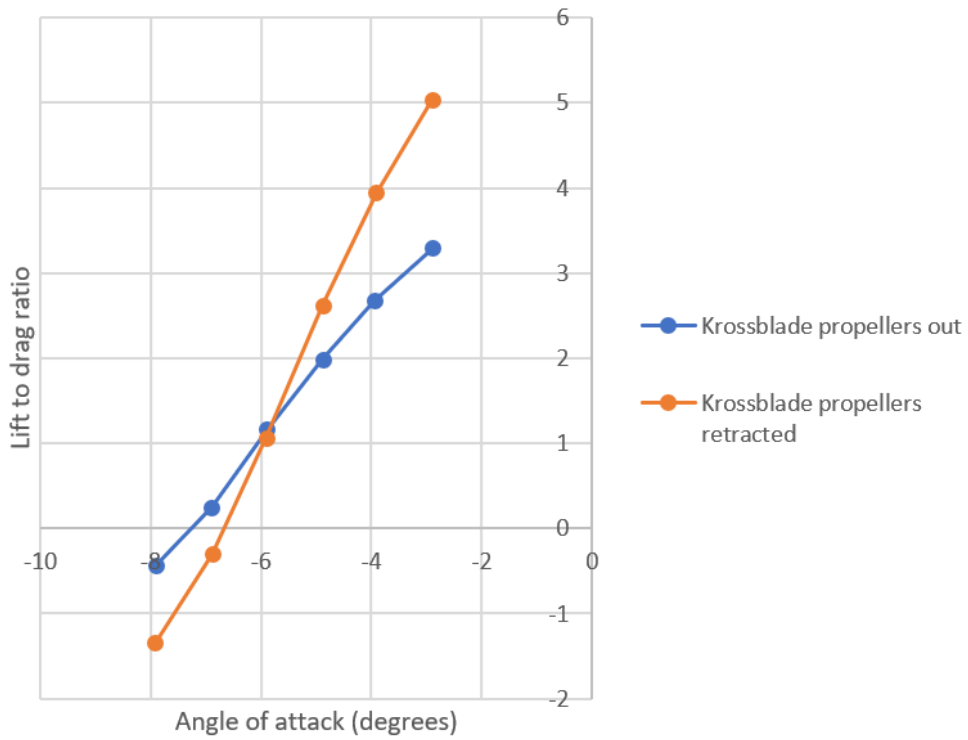


Figure 159: Krossblade SkyProwler, lift to drag ratio, 30 m/s.

Drag polar - 10 m/s airspeed

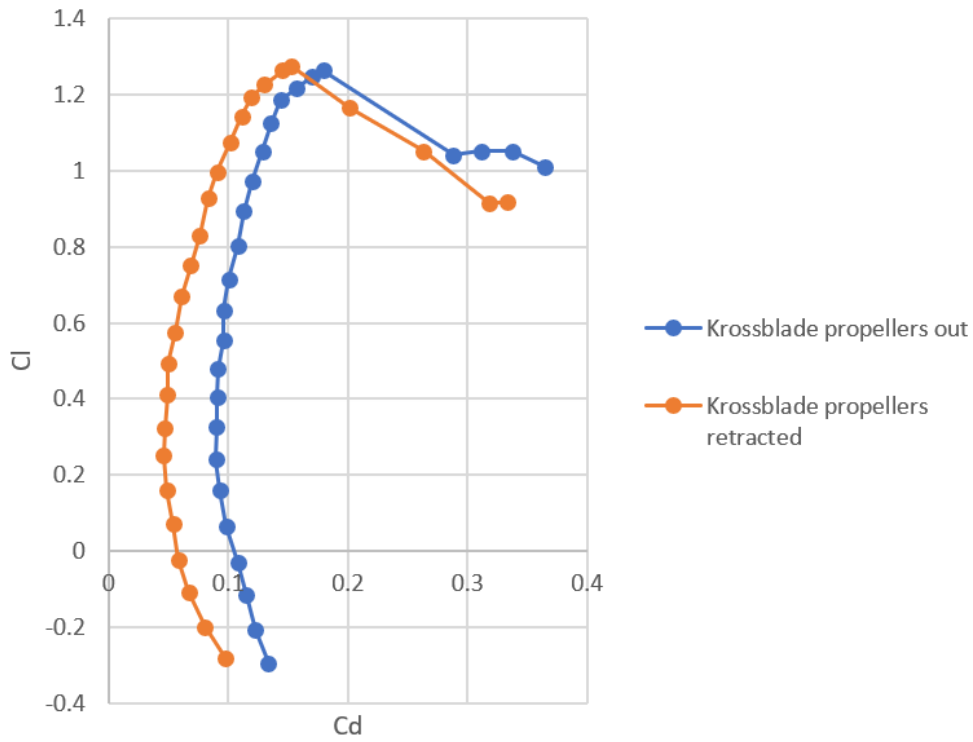


Figure 160: Krossblade SkyProwler, drag polar, 10 m/s.

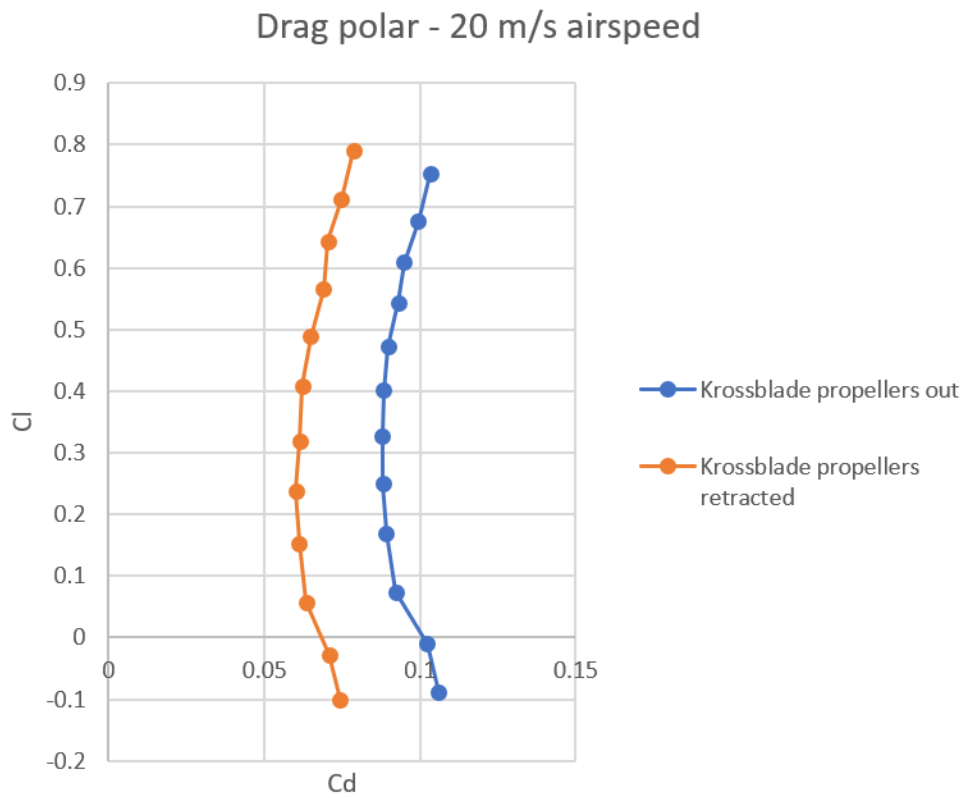


Figure 161: Krossblade SkyProwler, drag polar, 20 m/s.

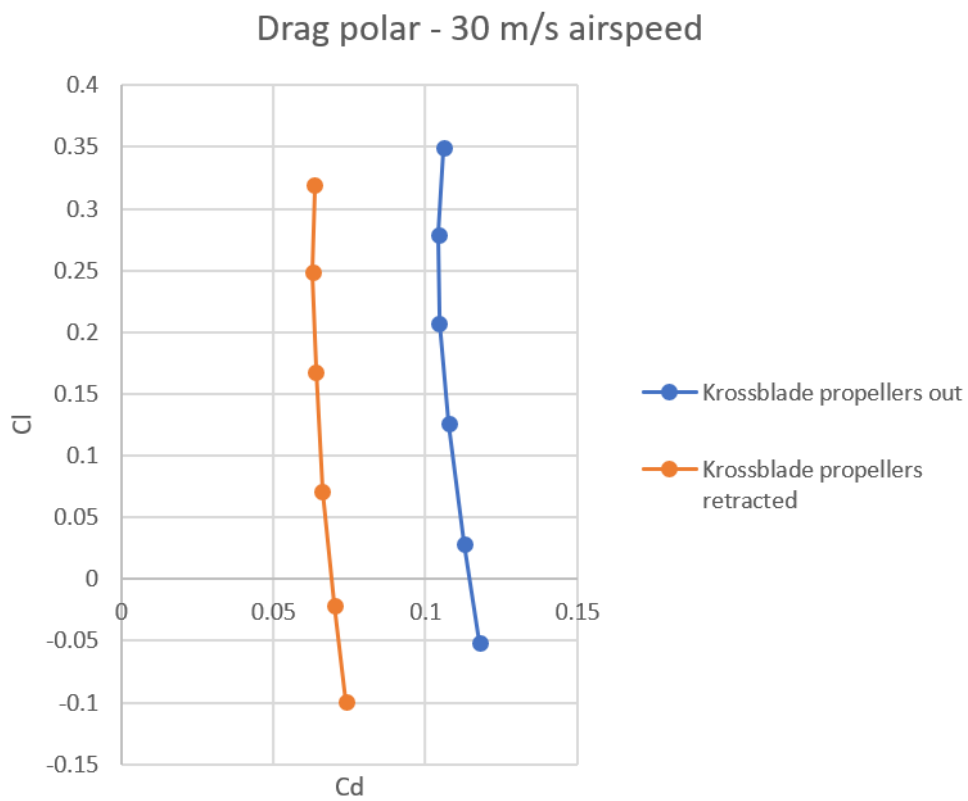


Figure 162: Krossblade SkyProwler, drag polar, 30 m/s.

5.4 Effect of the drag reduction on passenger eVTOLs and surveillance drones

5.4.1 Effect of the drag reduction on passenger eVTOLs

The results listed in Table 35 show a drag reduction of 34% between the Mini Talon 3 standard VTOL configuration and the Mini Talon 2 with retracted propellers, and a 30% drag reduction between the Skyproowler with propellers out and with propellers retracted. These results have been used to estimate the performances of the Kitty Hawk Cora eVTOL and the Mini Talon VTOL drone employing the propellers retraction system. The Kitty Hawk Cora data from chapter 3 are collected in table 36. C_{D0} and k are Cora's drag polar coefficients expressed in the quadratic form: $C_D = C_{D0} + kC_L^2$.

Table 36: Kitty Hawk Cora data used to compute the eVTOL with propellers retraction system performances.

| | |
|--|------------------------|
| C_{D0} | 0.0438 |
| k | 0.0294 |
| Wing surface, S | 10 m^2 |
| Total mass, m | 1224 m^2 |
| Gravity, g | 9.8 m/s^2 |
| Density, ρ | 1.225 kg/m^3 |
| Propulsive efficiency, η_{total} | 0.75 |
| Battery energy density, E^* | 157 Wh/kg |
| Battery-mass ratio, $\frac{m_{battery}}{m}$ | 33% |
| C_{Lmax} | 1.3 |
| Battery energy fraction for cruise, $\frac{E_{cruise}}{E_{total}}$ | 60% |

Figure 163 shows the range function of the flight speed for different drag reductions and retraction system weights. The black line represents the Cora baseline without the propeller retraction system. The different line shapes represent different drag reductions, and the different line colors represent different retraction system weights.

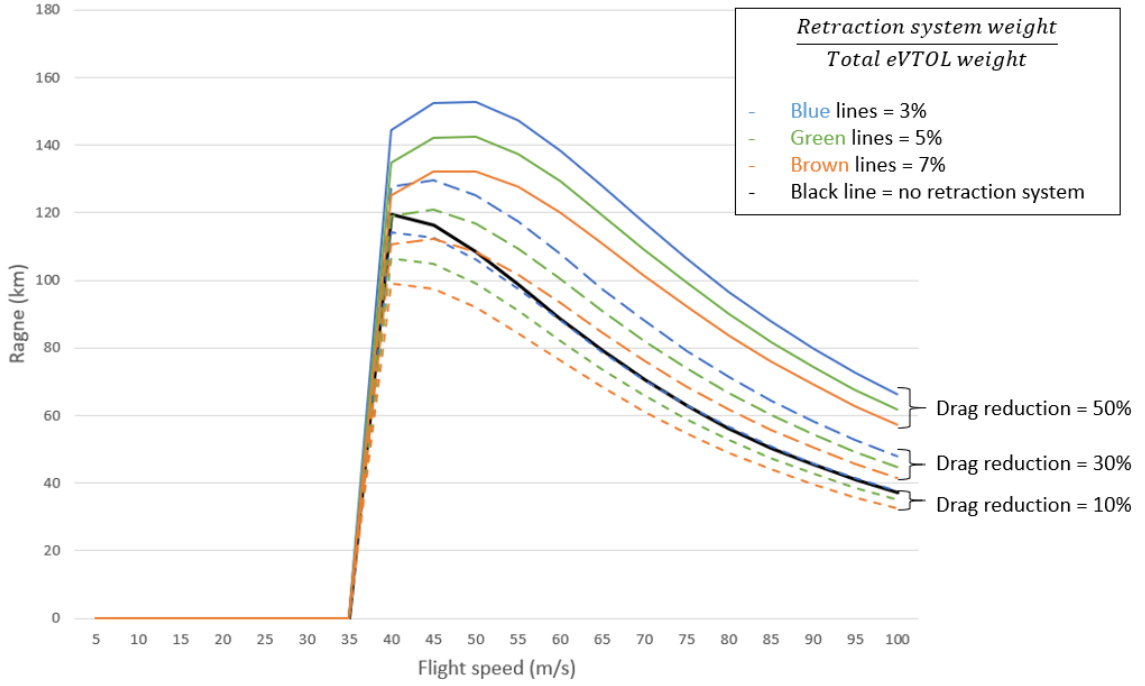


Figure 163: Range function of the flight speed for different drag reductions and retraction system weights, computed using Kitty Hawk Cora's data.

For each flight speed, the lift coefficient was computed equating the lift to the weight of the vehicle:

$$C_L = \frac{2 m g}{\rho v^2 S} \quad (79)$$

The drag coefficient has been computed using the quadratic approximation of the drag polar and considering the drag reduction:

$$C_D = C_{D0}(1 - D_r) + k C_L^2 \quad (80)$$

The drag reduction D_r affects only the C_{D0} because the VTOL propellers and motors produce only a small amount of lift, and their induced drag is negligible.

The range has been computed using a modified version of the electric range equation (14):

$$R = E^* \cdot \eta_{total} \cdot \frac{1}{g} \cdot \frac{L}{D} \cdot \left(\frac{m_{battery}}{m} - \frac{m_{retraction}}{m} \right) \cdot \frac{E_{cruise}}{E_{total}} \quad (81)$$

E^* is the battery energy density, η_{total} is the propulsive efficiency, g is the gravity acceleration, $\frac{L}{D}$ is the lift to drag ratio, $\frac{m_{battery}}{m}$ is the battery-mass ratio, $\frac{m_{retraction}}{m}$ is the retraction system mass divided by the total mass of the vehicle, and $\frac{E_{cruise}}{E_{total}}$ is the battery energy fraction for the cruise phase.

Some lines show a range lower than the baseline, and this because, in equation (81), the retraction system weight is supposed to reduce the battery mass. If the retraction system weights 50 kg, we consider a battery 50 kg smaller than the baseline. This assumption has been made because the battery is the only part of the eVTOL that can be changed without affecting everything else. Reducing the

payload might make the vehicle unable to complete its design mission. Adding the retraction system without changing anything else might worsen the hover performances significantly.

From the wind tunnel tests, a drag reduction of 30% can be selected, and the curves corresponding to 10% and 50% drag reduction can be neglected. The three remaining curves show that the advantages of the drag reduction outnumber the disadvantages of the weight added. With a 5% retraction system mass over the total eVTOL mass fraction, the maximum range increases slightly from 119 km to 121 km. However, the great advantage is that the speed that maximizes the range has increased by 5 m/s. An 80-km range mission can be flown 10 m/s faster. Higher flight speed is a great advantage for commercial air taxi operations. It means being able to perform more missions in the same duration, significantly reducing mission costs. The costs of air taxi operations consist of the fixed costs of the vehicle and infrastructure and the operating costs of the electricity and the pilot if needed [121]. The cost of electricity to recharge the Cora battery by 70%, which is the maximum discharge considered for a mission, considering an electric energy price of 0.12 €/kW, is just 5.50 €. Pilots are paid by the hour, so the more missions they can accomplish in a given time, the cheaper the missions can be. Similarly, if the fixed costs of building the eVTOL are spread on more missions, the cost of each mission decreases.

5.4.2 Effect of the drag reduction on surveillance drones

Surveillance drones are best evaluated on their flight endurance because their typical mission is to patrol an area for as long as possible. The flight time has been computed to evaluate the performances of a VTOL drone employing the retraction system. The endurance is energy available for cruise divided by the power consumed:

$$Endurance = \frac{E_{cruise}}{P_{required}/\eta_{total}} \quad (82)$$

The energy available is:

$$E_{cruise} = m \cdot \left(\frac{m_{battery}}{m} - \frac{m_{retraction}}{m} \right) \cdot E^* \cdot \frac{E_{cruise}}{E_{total}} \quad (83)$$

The power required is drag multiplied by flight speed:

$$P_{required} = \frac{1}{2} \rho S v^2 C_D \cdot v \quad (84)$$

The drag coefficient C_D is computed with equation (80).

Table 37: Mini Talon VTOL data used to compute the eVTOL drone with propellers retraction system performances.

| | |
|--|------------------------|
| C_{D0} | 0.0396 |
| k | 0.0378 |
| Wing surface, S | 0.314 m^2 |
| Total mass, m | 2.45 kg |
| Gravity, g | 9.8 m/s^2 |
| Density, ρ | 1.225 kg/m^3 |
| Propulsive efficiency, η_{total} | 0.65 |
| Battery energy density, E^* | 157 Wh/kg |
| Battery-mass ratio, $\frac{m_{battery}}{m}$ | 32% |
| C_{Lmax} | 1.3 |
| Battery energy fraction for cruise, $\frac{E_{cruise}}{E_{total}}$ | 60% |

Table 37 collects the Mini Talon VTOL data used to compute the eVTOL drone with propellers retraction system performances. Figure 164 shows the endurance function of the flight speed for different drag reductions and retraction system weights. As in Figure 163, the black line represents the baseline without the retraction system. Figure 164 shows that the advantages in time of flight for surveillance drones are smaller than the advantages for eVTOLs that must complete an air taxi mission. For maximum flight time, the aircraft must fly as close as possible to the condition of maximum $\frac{C_L^{3/2}}{C_D}$, which is at low flight speed. The reduction in C_D brought by the propellers retraction system is less effective at this low speed and becomes more effective as the flight speed increases.

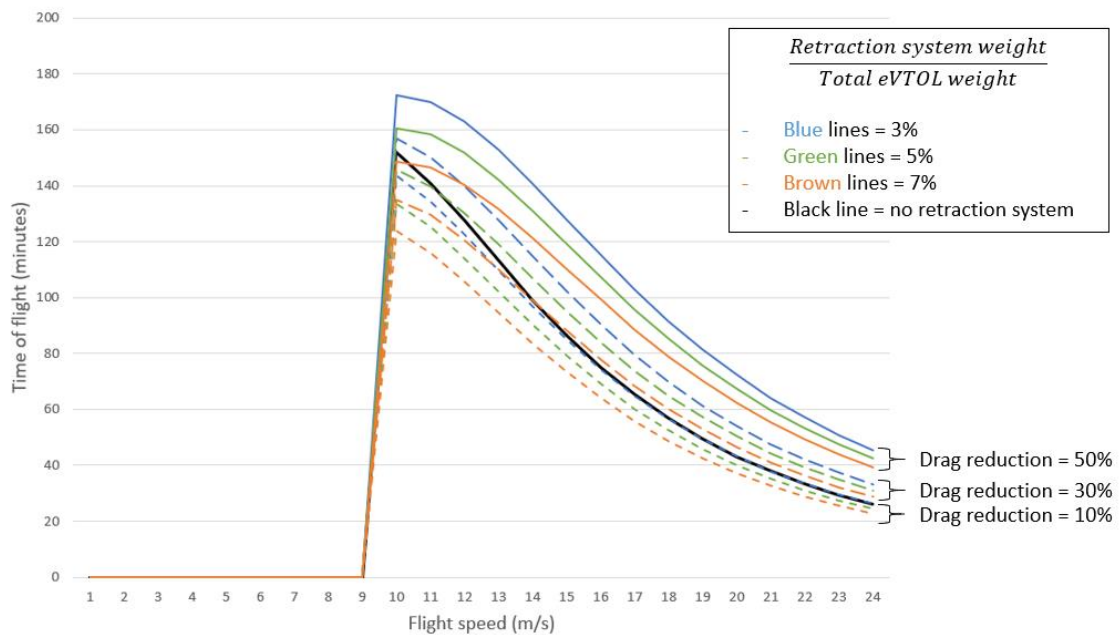


Figure 164: Endurance function of the flight speed for different drag reductions and retraction system weights.

5.4.3 Considerations regarding scaling up the drag reduction from model to full-size eVTOLs

In this discussion, the drag reduction has been considered constant for the small size Mini Talon model and the scaled-up Kitty Hawk Cora. We consider this assumption conservative because, as shown in chapter 2, scaling up an eVTOL, the propeller area must grow to keep the same hover performances. The total hover time is:

$$t = \frac{m_{battery}}{m} \cdot E^* \cdot \sqrt{\frac{2\rho}{g^3}} \cdot \sqrt{\frac{A}{m}} \quad (85)$$

The first three factors are constant between the model and the scaled-up version. The last factor shows that the total hover time is proportional to the square root of the ratio between the disk actuator area and the total mass. The disk actuator area of the propellers for hover scales with the square of the reference length because it is an area. On the other hand, the total mass of the vehicle scales as the cube of the reference length because it is proportional to the volume. This means that, in order to keep the same hover performances, the geometry cannot be directly scaled up, but it must be modified, increasing the disk actuator area of the propellers for hover. A bigger disk actuator area of the hover propellers means higher drag and higher drag reduction when they are retracted.

5.5 Chapter conclusion

The test performed in the University of Sydney 7 ft by 5 ft wind tunnel showed a drag reduction of 34% for the Mini Talon model and of 30% for the SkyProwler model. The retraction of the propellers does not affect the lift coefficient, but it reduces the drag coefficient improving the lift to drag ratio. Applying these results to the estimation of eVTOL performances, an increase in flight speed is found. With the Cora data estimated in chapter 3, an 80-km mission can be flown 10 m/s faster at the same energy consumption. For a surveillance drone, the advantages of a propellers retraction system are limited because their objective is to watch over their target area for as long as possible, and a flight speed increase is not required.

Chapter 6

Conclusion

Electric VTOLs promise to revolutionize transportation. Their capability to take off and land vertically, their low cost, and the low cost of electric energy they use might make them a convenient means of transport for everybody.

This work has provided a comprehensive investigation into the design of eVTOLs. Chapter 1 has introduced these machines presenting the most famous prototypes. Chapter 2 has described the analytical tools needed to compute their performance in cruise, hover, and transition. Chapter 3 has analyzed the main VTOL configurations tested from the 1950s up to now, evaluating their advantages and disadvantages. Three present eVTOL configurations have been further analyzed using the tools introduced in chapter 2. Chapter 4 has discussed the power sources available to eVTOLs, including batteries, fuel cells, and hybrids. Chapter 5 investigated more in detail the design of the lift plus cruise configuration. This type of eVTOL has lift propellers that create unwanted drag in cruise. A system to retract these propellers inside the fuselage to reduce drag during the cruise was investigated building and testing in the wind tunnel scale models. The measured results were applied to the estimation of the performance of the lift plus cruise passenger eVTOL Cora and to a surveillance drone showing that the retraction system can increase the cruise speed significantly.

6.1 Contributions to knowledge

The main contributions of this research project into the design of electric VTOL presented in this dissertation are:

- *First wind tunnel test of the impact of takeoff propellers drag on the performance of lift plus cruise eVTOL aircraft.* This new idea may allow lift plus cruise eVTOLs to take advantage of their excellent hover efficiency, increasing their cruise speed and range.
- *Presentation of the analytical tools required to evaluate the performances of any eVTOL.* The electric range equation, the momentum theory for hover, and all their variants have been discussed, and efficiency data has been provided for multiple eVTOL components to enable the reader to estimate the performances of any eVTOL
- *First comprehensive catalogue and analysis of the VTOL configurations.* This dissertation presents, discusses, and compares the different configurations from the 1950s up to now.

- *Discussion of the power source available to eVTOLs, including batteries, fuel cells, and hybrids.* The battery technology is presented, discussing the main factors affecting battery performances. Fuel cells are presented, and the hydrogen storage is analysed. Difference hybrids are discussed, including internal combustion engine and battery, gas turbine and battery, fuel cells, batteries, and supercapacitors.
- *Preliminary design of an eVTOL drone for Titan exploration powered by a nuclear power source.* This exotic eVTOL design has been investigated with the tools described in chapter 2.
- *Investigation on the specific energy and specific power of the battery required to power a supersonic eVTOL.* This futuristic topic has been investigated with the tools described in chapter 2 to provide a new application for the futuristic technologies presented in chapter 4 other than an increase in range on the known designs.

Based on the work presented in this dissertation, the following conclusions can be drawn:

The wind tunnel tests showed that the drag reduction achievable retracting the takeoff propellers inside the fuselage is in the order of 30%. This reduction enables passenger eVTOLs to increase their cruise speed substantially. With the propellers retraction system, the Cora could fly an 80-km mission 10 m/s faster. Surveillance drones receive limited advantages from a propellers retraction system because their objective is to watch over a prescribed area for as long as possible.

The configuration comparison in chapter 3 showed that different configurations are best suited to different missions. Multirotors are efficient in hover and suited to short-range missions. Vectored thrust are efficient in cruise and best suited to long-range missions. Lift plus cruise combine high over efficiency like the multirotors with a wing for an efficient cruise, but the takeoff propellers create a considerable unwanted drag.

Chapter 2 presented the tools required to compute the range and the power required to hover. Range is affected not only by the specific energy of the batteries, but also by the battery-mass ratio, and by the lift to drag ratio. The power required to hover is inversely proportional to the square root of the disk actuator area. Hover efficient eVTOLs have large disk actuator area.

Chapter 4 showed that batteries provide the required specific energy and specific power for urban air mobility eVTOL. Hybrids could improve the range, but their reduced specific power excludes some power demanding eVTOL configurations. The fuel cell triple hybrid looks promising.

The exotic study showed that the eVTOL for Titan powered by an RTG like the one powering the Voyagers could fly for years.

The investigation on the specific energy and specific power of the battery required to design a supersonic eVTOL shoed that the required technology level is far, but the technology level for a high subsonic eVTOL with the same configuration of the F-35 is higher than the present level, but it may be achievable in the future.

6.2 Future Work

This research has entered the vast area of eVTOL design. Every single configuration presented here requires the hard work of the engineers trying to transform that concept into a market product. Other than the detailed design on the single configuration, also the detailed design on the single propulsion system could be investigated, providing additional data on their figure of merit for hover and their propulsive efficiencies during the cruise.

This dissertation focused on the propeller retraction system for lift plus cruise eVTOLs. The flight of a model with the propellers retraction system is not so interesting from a research perspective because Krossblade has been flying their models for years. The next step is to scale up the system to the size of a passenger eVTOL. This step requires capital investments that are probably out of the reach of most universities and better suited to companies. The work in this thesis and the results found provide a measure of the performance enhancement that this system provides. It is useful to the people deciding whether to invest in the realization of a full-scale propeller retraction system. They could evaluate the costs and use this dissertation to evaluate the operational cost savings and increased productivity to take a reasoned choice.

Adding a small fairing to the motors, like small general aviation aircrafts have for the wheels of the landing gear, could also be studied.

The work in this dissertation could be helpful also for eVTOL operators and city planners because they would have tools to estimate the performances of eVTOLs that are yet to be tested.

References

- [1] Giulio Romeo, F. Borello, G. Correa, E. Cestino. ENFICA-FC: Design of transport aircraft powered by fuel cell & flight test of zero emission 2-seater aircraft powered by fuel cells fueled by hydrogen. *International journal of hydrogen energy*, 38(1):469–479, 2013.
- [2] Laurent Juvé, Julie Fosse, Emmanuel Joubert and Nicolas Fouquet. Airbus Group Electrical Aircraft Program, The E-Fan Project. *52nd AIAA/SAE/ASEE Joint Propulsion Conference*, July 25-27, 2016, Salt Lake City, UT, <https://doi.org/10.2514/6.2016-4613>.
- [3] Pipistrel Alpha Electro. <https://www.pipistrel-aircraft.com/aircraft/electric-flight/alpha-electro>. Accessed on 10/02/2020.
- [4] Internal combustion engine, Wikipedia. https://en.wikipedia.org/wiki/Internal_combustion_engine. Accessed on 15/02/2020.
- [5] Mark Moore. NASA Puffin Electric Tailsitter VTOL Concept. *10th AIAA Aviation Technology, Integration, and Operations (ATIO) Conference*, Fort Worth, Texas, 13 September 2010 - 15 September 2010. <https://doi.org/10.2514/6.2010-9345>
- [6] Mark Moore. Misconceptions of Electric Propulsion Aircraft and Their Emerging Aviation Markets. *52nd AIAA Aerospace Sciences Meeting*, National Harbor, MD, 2014.
- [7] Electric VTOL News, Zee Aero. <https://evtol.news/aircraft/zee-aero>. Accessed on 15/02/2020
- [8] Pranay Sinha, Alex M. Stoll, Edward V. Stilson and JoeBen Bevirt. Design and Testing of the Joby Lotus Multifunctional Rotor VTOL UAV. *15th AIAA Aviation Technology, Integration, and Operations Conference*, Dallas, TX, 22-26 June 2015.
- [9] Alex M. Stoll, Edward V. Stilson, JoeBen Bevirt and Percy P. Pei. Conceptual Design of the Joby S2 Electric VTOL PAV. *Aviation Technology, Integration, and Operations Conference*, Atlanta Georgia, 2014.
- [10] Alex M. Stoll, JoeBen Bevirt, Mark D. Moore, William J. Fredericks and Nicholas K. Borer. Drag Reduction Through Distributed Electric Propulsion. *Aviation Technology, Integration, and Operations Conference*, Atlanta, Georgia, 2014.
- [11] Jeff Holden, Nikhil Goel. Fast-Forwarding to a Future of On-Demand Urban Air Transportation, *Uber Elevate*, October 27, 2016.
- [12] Robert G. McSwain, Louis J. Glaab, Colin R. Theodore. Greased Lightning (GL-10) Performance Flight Research – Flight Data Report NASA/TM–2017-219794, NASA, 2017.

- [13] Tine Tomažič, Vid Plevnik, Gregor Veble, Jure Tomažič, Franc Popit, Sašo Kolar, Radivoj Kikelj, Jacob W. Langelaan, Kirk Miles. Pipistrel Taurus G4: on Creation and Evolution of the Winning Aeroplane of NASA Green Flight Challenge 2011. *Journal of Mechanical Engineering*, vol. 57, n. 12, pp. 869-878, 2011.
- [14] Electric VTOL News, Pipistrel 801. <https://evtol.news/aircraft/pipistrel-801-evtol>. Accessed on 20/01/2020.
- [15] Alessandro Bacchini, Enrico Cestino. Electric VTOL Configurations Comparison. *Aerospace*. 2019, 6, 26.
- [16] Alessandro Bacchini, Enrico Cestino. Key aspects of electric vertical take-off and landing conceptual design, *Proceedings of the iMechE, Part G: Journal of Aerospace Engineering*, 2019. <https://doi.org/10.1177/0954410019884174>.
- [17] Alessandro Bacchini, Enrico Cestino, Giulio Romeo. A reduced order model to estimating propeller&wing interaction in solar powered aircraft preliminary design. *7th EASN international conference, Innovation in European Aeronautics Research*, Warsaw, Poland, 2017.
- [18] New York Airways, Wikipedia. https://en.wikipedia.org/wiki/New_York_Airways. Accessed on 23/12/2019.
- [19] Bloomberg Businessweek. The life and death of helicopter commuting. <https://www.youtube.com/watch?v=8nbz5VFilxY>. Accessed on 23/12/2019.
- [20] Pieter Abbeel, Adam Coates and Andrew Y. Ng. Autonomous helicopter aerobatics through apprenticeship learning. *The International Journal of Robotics Research* OnlineFirst, published on June 23, 2010 as doi:10.1177/0278364910371999.
- [21] John D. Anderson. *Introduction to Flight*, equation 6.28 p. 462: McGraw-Hill, 1978.
- [22] Giancarlo Genta. *Introduction to the Mechanics of Space Robots*. Springer. Equation 5.9 p. 243, ISBN 978-94-007-1796-1, 2012.
- [23] David Linden, Thomas Reddy. *Handbook of batteries*. McGraw-Hill, 2002.
- [24] Oxis Energy. Ultra Light Lithium Sulfur Pouch Cell. <https://45uevg34gwlltnbsf2plyua1-wpengine.netdna-ssl.com/wp-content/uploads/2019/07/OXIS-Li-S-Ultra-Light-Cell-spec-sheet-v4.2.pdf>. Accessed on 24/06/2020.
- [25] Martin Hepperle. Electric flight – potential and limitations. German Aerospace Center DLR, Braunschweig, Germany, 2012.
- [26] Tesla Model S, Wikipedia. https://en.wikipedia.org/wiki/Tesla_Model_S. Accessed on 20/12/2018.
- [27] Wikipedia. <https://www.wikipedia.org>.
- [28] Pipistrel Alpha Trainer. <https://www.pipistrel-aircraft.com/aircraft/flight-training/alpha>. Accessed on 04/03/2020.

- [29] Electricity Pricing, Wikipedia.
https://en.wikipedia.org/wiki/Electricity_pricing. Accessed on 24/06/2020.
- [30] US Energy Information Administration. Electric Power Monthly – Average Retail Price of Electricity to Ultimate Customers by End-Use Sector, by State. Archived from the original on 7 October 2010. Retrieved 14 May 2017., 7 October 2010.
- [31] John. m. Seddon, *Basic Helicopter Aerodynamics*, Chatham, Kent: Mackays, 1990
- [32] J. Gordon Leishman, *Principles of Helicopter Aerodynamics*. New York: Cambridge University Press, 2006.
- [33] J. Gordon Leishman, Monica Syal. Figure of Merit Definition for Coaxial Rotors. *Journal of the American Helicopter Society*, Volume 53, Number 3, 1 July 2008, pp. 290-300(11).
- [34] Renato Tognaccini. *Lezioni di aerodinamica dell'ala rotante*. Università degli studi di Napoli, Napoli, 2008.
- [35] A. Bagai, J. Gordon Leishman. Experimental Study of Rotor Wake/Body Interactions in Hover. *Journal of the American Helicopter Society*, Volume 37, Number 4, 1 October 1992, pp. 48-57(10)
- [36] Cobra Motors. <https://www.cobramotorsusa.com/multirotormotors.html>. Accessed on 10/01/2020.
- [37] NASA. Planetary Fact Sheet.
<https://nssdc.gsfc.nasa.gov/planetary/factsheet/index.html>. Accessed on 24/06/2020.
- [38] NASA Earth Atmosphere Model. <https://www.grc.nasa.gov/www/k-12/airplane/atmosmet.html>. Accessed on 24/06/2020.
- [39] Multihundred-Watt radioisotope thermoelectric generators, Wikipedia.
<https://en.wikipedia.org/wiki/MHW-RTG>. Accessed on 27/01/2020.
- [40] Seth B. Anderson. Historical Overview of V/STOL Aircraft Technology. NASA Ames Research Center, Moffett Field, California, 1981.
- [41] Mike Hirshberg. Electric VTOL Wheel of Fortune. *Vertiflite*, March/April 2017.
- [42] Vertipedia. <https://vertipedia.vtol.org/aircraft>. Accessed on 25/06/2020.
- [43] Richnrd J. Margason. Review of propulsion-induced effects on aerodynamics of jet/stol aircraft. NASA, Washington, D.C., 1970.
- [44] Harrier Jet, Wikipedia. https://en.wikipedia.org/wiki/Harrier_Jump_Jet. Accesd on 13/12/2019.
- [45] Curtiss-Wright X-100. Vertipedia.
<https://vertipedia.vtol.org/aircraft/getAircraft/aircraftID/810>. Accessed on 24/06/2020.
- [46] Dassault Mirage III V, Wikipedia.
https://en.wikipedia.org/wiki/Dassault_Mirage_IIIIV. Accessed on 12/12/2019.
- [47] Sikorsky–Boeing SB-1 Defiant, Wikipedia.
https://en.wikipedia.org/wiki/Sikorsky-Boeing_SB-1_Defiant. Accessed on 24/06/2020.

- [48] Electric VTOL News, Elroy Air Chapparral. <https://evtol.news/aircraft/elroy-air-chapparral/>. Accessed on 24/06/2020.
- [49] Electric VTOL News, Project Zero. <https://evtol.news/2013/05/01/project-zero>. Accessed on 24/06/2020.
- [50] Mike Hirshberg. The exclusive story of AgustaWestland’s all-electric technology incubator. *Vertiflite*, May/June 2013.
- [51] Airspace Experience Technologies. <https://www.iflyasx.com/mobi-one>. Accessed on 24/06/2020.
- [52] Electric VTOL News, Airspace Experience Technologies (ASX) MOBi-One. <https://evtol.news/aircraft/airspacex>. Accessed on 24/06/2020.
- [53] Electric VTOL News, Beta Technologies Alia. <https://evtol.news/aircraft/beta-technologies-alia>. Accessed on 24/06/2020.
- [54] Youtube, Beta Technologies eVTOL Air Taxi Prototype. <https://www.youtube.com/watch?v=GBcLIr-pc4k>. Accessed on 24/06/2020.
- [55] Electric VTOL News, Dufour aEro 2. <https://evtol.news/aircraft/dufour-aero2>. Accessed on 24/06/2020.
- [56] Dufur Aerospace. <https://dufour.aero/team>. Accessed on 24/06/2020.
- [57] Electric VTOL News, Opener BlackFly. <https://evtol.news/aircraft/opener-blackfly>. Accessed on 24/06/2020.
- [58] YouTube, BlackFly – Flight. <https://www.youtube.com/watch?v=FI8AemQcclY>. Accessed on 24/06/2020.
- [59] Electric VTOL News, Overair (Karem) Butterfly. <https://evtol.news/aircraft/karem-butterfly>. Accessed on 24/06/2020.
- [60] Venturi Engine, Hoversurf. <https://www.hoversurf.com/technology>. Accessed on 24/06/2020.
- [61] Electric VTOL News, Aquinea Volta. <https://evtol.news/aircraft/aquinea-volta>. Accessed on 24/06/2020.
- [62] E-Hang 184. <http://www.ehang.com/ehang184/specs>. Accessed on 01/12/2018.
- [63] Colin P. Coleman. A Survey of Theoretical and Experimental Coaxial Rotor Aerodynamic Research. NASA, 1997.
- [64] Kitty Hawk. <https://kittyhawk.aero>. Accessed on 01/12/2018.
- [65] Mike Hirshberg. Meet Cora. <https://evtol.news/2018/04/19/meet-cora/>. *Vertiflite*, May/June 2018.
- [66] Electric VTOL News, Wisk (Kitty Hawk) Cora. <http://evtol.news/aircraft/kitty-hawk-cora>. Accessed on 24/06/2020.
- [67] M. Selig, M. Maughmer and D. Somers. Natural-Laminar-Flow Airfoil for General-Aviation Applications. *Journal of Aircraft*, vol. 32, p. 710–715, 1995.
- [68] Airfoil tools, <http://airfoiltools.com/airfoil/details?airfoil=nlf0115-il>. Accessed on 28 January 2019.
- [69] Mark Drela. Xfoil. <https://web.mit.edu/drela/Public/web/xfoil/>. Accessed on 28 January 2019.

- [70] L. R. Jenkinson. *Civil Jet Aircraft Design*. London: Arnold, a member of the Hodder Headline Group, 1999.
- [71] S. F. Hoerner, *Fluid-dynamic drag*, Brick Town, N.J., 1965.
- [72] John D. Anderson, *Aircraft performance and design*, McGraw-Hill, 1999.
- [73] D. Felix Finger, Falk Götten, Carsten Braun, Cees Bil. Initial Sizing for a Family of Hybrid-Electric VTOL General Aviation Aircraft. *Deutscher Luft - und Raumfahrtkongress*, Friedrichshafen, 2018.
- [74] Lilium. lilium.com. Accessed on 28/01/2019.
- [75] Ultralight Glider. <http://www.ultralight-glider.fr/en/european-exemptions>. Accessed on 10/12/2018.
- [76] *Official Journal of the European Union*. Volume 61, 22 August 2018. <https://eur-lex.europa.eu/legal-content/EN/TXT/PDF/?uri=OJ:L:2018:212:FULL&from=FR>. Accessed on 24/06/2020.
- [77] Lilium Jet, Wikipedia. https://en.wikipedia.org/wiki/Lilium_Jet. Accessed on 16/01/2020.
- [78] Schuebeler. <http://www.schuebeler-jets.com/en/products/hst-en>. Accessed on 10/05/2020.
- [79] Andrew Tian You Gong. Impact of Supercapacitors on a Fuel-Cell-Based Triple Hybrid for Small Unmanned Aircraft, Sydney: The University of Sydney, March, 2018.
- [80] Andrew Gong, Dries Verstraete. Fuel cell propulsion in small fixed-wing unmanned aerial vehicles: Current status and research needs. *International Journal of Hydrogen Energy*, p. 42:21311–21333, 2017.
- [81] Batteryspace.com. Panasonic Lithium Ion NCR18650B. <https://www.batteryspace.com/prod-specs/NCR18650B.pdf>. Accessed on 24/06/2020.
- [82] Zop Power, Banggood. https://www.banggood.com/it/ZOP-POWER-14_8V-8000mAh-60C-4S-Lipo-Battery-With-XT60-Plug-p-1334197.html?gmcCountry=IT¤cy=EUR&createTmp=1&utm_source=googleshopping&utm_medium=cpc_union&utm_content=xibei&utm_campaign=xibei-ssc-it-all-0508&ad_id=34725706. Accessed on 24/06/2020.
- [83] EV1, Wikipedia. https://en.wikipedia.org/wiki/General_Motors_EV1#Battery. Accessed on 06/03/2020.
- [84] Sion Power. Licerion. <https://sionpower.com/products>. Accessed on 06/03/2020.
- [85] Avogadro constant, Wikipedia. https://en.wikipedia.org/wiki/Avogadro_constant. Accessed on 06/03/2020.
- [86] Elementary charge, Wikipedia. https://en.wikipedia.org/wiki/Elementary_charge. Accessed on 06/03/2020.

- [87] Hydrogen, Wikipedia. <https://en.wikipedia.org/wiki/Hydrogen>. Accessed on 06/03/2020.
- [88] Electrolysis, Wikipedia. <https://en.wikipedia.org/wiki/Electrolysis>. Accessed on 06/03/2020.
- [89] Engineering toolbox. Air composition. https://www.engineeringtoolbox.com/air-composition-d_212.html. Accessed on 06/03/2020.
- [90] Hydrogen storage, Wikipedia. https://en.wikipedia.org/wiki/Hydrogen_storage. Accessed on 06/03/2020.
- [91] D. Verstraete, P. Hendrick, P. Pilidis, K. Ramsden. Hydrogen fuel tanks for subsonic transport aircraft. *International Journal of Hydrogen Energy*, vol. 35, pp. 11085-11098, 2010.
- [92] Abe Silverstein, Eldon Hall. Liquid hydrogen as a jet fuel for high-altitude aircraft. Lewis flight propulsion laboratory, Cleveland Ohio. NASA, RM-E55C28a, 1955.
- [93] Cylinder stress, Wikipedia. https://en.wikipedia.org/wiki/Cylinder_stress. Accessed on 06/03/2020.
- [94] Toyota Mirai, Wikipedia. https://en.wikipedia.org/wiki/Toyota_Mirai. Accessed on 06/03/2020.
- [95] Wanyi Ng and Anubhav Datta. Hydrogen Fuel Cells and Batteries for Electric-Vertical Takeoff and Landing Aircraft. *Journal of Aircraft*, vol. 56, n. 5, pp. 1765 - 1782, September–October 2019.
- [96] Ballard. Heavy duty motive modules. https://www.ballard.com/docs/default-source/motive-modules-documents/hd_motive_brochure_pgs_072517-01.pdf?sfvrsn=2&sfvrsn=2. Accessed on 24/06/2020.
- [97] Hybrid vehicle drivetrain, Wikipedia. https://en.wikipedia.org/wiki/Hybrid_vehicle_drivetrain. Accessed on 06/03/2020.
- [98] Lycoming O-360, Wikipedia. https://en.wikipedia.org/wiki/Lycoming_O-360. Accessed on 06/03/2020.
- [99] Aircraft diesel engine, Wikipedia. https://en.wikipedia.org/wiki/Aircraft_diesel_engine. Accessed on 06/03/2020.
- [100] L. Trainelli, F. Salucci, N. Rossi, C. Riboldi, A. Rolando. Preliminary sizing and energy management of serial hybrid-electric airplanes. *Italian Association of Aeronautics and Astronautics, XXV International Congress*, Rome, Italy, 2019.
- [101] Rolls Royce Air Taxi. <https://www.rolls-royce.com/innovation/propulsion/air-taxis.aspx>. Accessed on 06/03/2020.
- [102] Allison Model 250, Wikipedia. https://en.wikipedia.org/wiki/Allison_Model_250. Accessed on 06/03/2020.
- [103] Rolls Royce M250 250, Wikipedia. <http://www.fipowerweb.com/Engine/Rolls-Royce-M250.ht>. Accessed on 06/03/2020.

- [104] Hannah Klot Jake Callahan. This \$270,000 ‘Superbike’ is one of the fastest motorcycles in the world, <https://www.cnbc.com/2017/10/30/y2k-superbike-is-one-of-the-fastest-motorcycles-in-the-world.html> . Accessed on 06/03/2020.
- [105] Horizon educational. Hydrostik Pro datasheet. <https://www.horizoneducational.com/wp-content/uploads/2014/09/LWH22-10L-5-datasheet.pdf>. Accessed on 06/03/2020.
- [106] Lift to drag ratio, Wikipedia. https://en.wikipedia.org/wiki/Lift-to-drag_ratio. Accessed on 06/03/2020.
- [107] Siemens SP260D, Wikipedia. https://en.wikipedia.org/wiki/Siemens_SP260D. Accessed on 06/03/2020.
- [108] Ardupilot. Quadplane support. <http://ardupilot.org/plane/docs/quadplane-support.html>. Accessed on 06/03/2020.
- [109] Vertical technologies. DeltaQuad. <https://www.deltaquad.com>. Accessed on 06/03/2020.
- [110] Krossblade Aerospace. SkyProwler. <https://www.krossblade.com>. Accessed on 06/03/2020.
- [111] Philipp Stahl, Christian Rössler and Mirko Hornung. Benefit Analysis and System Design Considerations for Drag Reduction of Inactive Hover Rotors on Electric Fixed-Wing VTOL Vehicles. *AIAA Aviation Technology, Integration and Operations Conference*, June 2018.
- [112] Haowei Gu, Ximin Lyu, Zexiang Li, Shaojie Shen, Fu Zhang. Development and experimental verification of a hybrid vertical take-off and landing (VTOL) unmanned aerial vehicle (UAV). *2017 International Conference on Unmanned Aircraft Systems (ICUAS)*. 13-16 June 2017. Miami, FL, USA.
- [113] Lockheed Martin. Desert Hawk. https://www.lockheedmartin.com/content/dam/lockheed-martin/rms/documents/desert-hawk/Desert_Hawk_Brochure.pdf. Accessed on 06/03/2020.
- [114] Perth UAV. Mozzie. <https://mozzie.readthedocs.io/en/latest/GettingStarted.html>. Accessed on 06/03/2020.
- [115] Cobra Motors. CM-2217/20. <http://www.cobramotorsusa.com/multirotor-2217-20.htm>. Accessed on 06/03/2020.
- [116] Cobra Motors. CM 2217/20 test data. <http://www.innov8tivedesigns.com/images/specs/Cobra-CM-2217-20-Specs.htm>. Accessed on 06/03/2020.
- [117] APC. Electric 10x4.5 propeller, <https://www.apcprop.com/product/10x4-5mr-b4>. Accessed on 06/03/2020.
- [118] Cobra Motors. C 2820/14. <http://www.cobramotorsusa.com/motors-2820-14.html>. Accessed on 06/03/2020.

- [119] Cobra Motors. C 2820/14 test data,
http://www.innov8tivedesigns.com/images/specs/Cobra_2820-14_Specs.htm. Accessed on 06/03/2020.
- [120] APC. Electric 10x8 propeller, <https://www.apcprop.com/product/10x8e>.
Accessed on 06/03/2020.
- [121] A. Kopitzke. EVTOL urban air mobility: analysis of fleet configuration and route planning. Michigan State University, MSc Thesis, 2019.